The application of linear-scaling Density Functional Theory to large metal oxide nanotubes.

Thesis submitted in accordance with the requirements of the University of Liverpool for the degree of Doctor of Philosophy by

Joshua David Elliott

July 2016

The application of linear-scaling density functional theory to large metal oxide nanotubes.

Joshua David Elliott

The aim of this Thesis is to provide a characterisation of Imogolite nanotubes and investigate their photocatalytic potential by means of innovative linear-scaling Density Functional Theory methods. Imogolite nanotubes are an emerging and rapidly growing class of aluminosilicate materials easily synthesised from cheap materials under aqueous conditions.

The first Chapter discusses the potential of photo-catalysis for Sustainable Chemistry, the requirements for efficient photo-catalysis, the factors governing electron transfer between the photo-catalyst and reactant and an overview of the current state of research in the field. The Chapter also introduces Imogolite Nanotubes, and based on the properties known to date, suggests a potential photocatalytic strategy that will be investigated in this Thesis. Chapter 2 provides a description of linear-scaling Density Functional Theory (LS-DFT) as implemented in the ONETEP code. The Chapter also gives a brief overview of Many-Body Quantum Theory and Kohn-Sham Density Functional Theory. In addition to the theoretical underpinning, an outline of some of the practical aspects of LS-DFT simulations are discussed. Leveraging the introduction to LS-DFT in Chapter 2, Chapter 3 investigates the tunable parameters and accuracy-viability trade offs associated with performing this type of simulation.

The electronic properties and emergence of surface polarisation are explored for the recently discovered inner surface methyl functionalized AlSi NTs in Chapter 4. Although

the relative vacuum alignment of the valence and conduction band edges and ensuing band gap is found to be constant for differently sized nanotubes, the computed polarisation is found to decrease with increasing diameter. It is uncovered in Chapter 4 that this is a result of a geometric dependence, generalisable to other (Imogolite) nanotubes, that could be used to direct the engineering of materials with high surface polarisations for enhanced electron-hole separation. Chapter 5 extends the research to Imogolite nanotubes with different compositions and investigates the potential for polarisation-enhanced photocatalytic water splitting (with respect to TiO_2). Based on the computed energy drive for photo-oxidation and photo-reduction, Imogolite nanotubes emerge as promising candidate for this processes.

The final Chapter reports on the optimisation of Hubbard-U corrections in LS-DFT for more accurate simulation of materials with correlated electrons. The work represents the initial steps in a wider study of transition metal doped Imogolite nanotubes. The results indicate, consistent with experimental spectra, a visible light band gap as well as a separation of the valence and conduction band edges in real space. These elements, although promising, require substantial further investigation, which could not be carried out due to time constraints.

Acknowledgements

At this point I would like to express my gratitude to several people who have made this work possible. Firstly, I thank my supervisor Dr. Gilberto Teobaldi for the constant "ball-breaking" that has brought this work to fruition, for the guidance and support that he has provided along the way and for leaving me in a position to tackle the next challenge in my career path... *I've got mayo on me.*

Una delle persone a cui sono maggiormente grato è Emiliano. È stato difficile scrivere questa tesi avendo la tua scrivania vuota dietro di me. Semplicemente questo lavoro non sarebbe stato possibile senza il tuo aiuto, senza le nostre discussioni e senza il tuo tempo dedicato ad ascoltare le mie presentazioni. Ci sono alcune cose di questi quattro anni che non mi dimenticherò mai, in primis lo sguardo che hai fatto quando ho guidato sul lato sbagliato della strada... *taa lad!*

I wish to thank everyone with at The Stephenson Institute for Renewable Energy and Surface Science Research Centre, for it is here that I have had the pleasure of sharing coffee breaks with a diverse spectrum of people. As a result, my outlook on life has been changed for the better, this is something that I will miss on leaving the University. It is not possible to include everyone, however I would like to pay special tribute to those that I have worked closely with over the last few years: Iván, Lorena and Stefano, I wish you all of the best for the future.

I cannot escape without thanking my parents and my nan for their continued support and unwavering belief in my ability to get to this point. I have to thank them for their patience and consideration during the last few months, I know that I must have been unbearable. If I could, I would thank my grandad. Out of everyone, I felt like he believed in me the most and it saddens me deeply that I am not able to share one of my proudest achievements with him. For almost the entire time that I have been working

towards this PhD, I have lived with Lynda and Tom, I am eternally grateful to them for welcoming me into their family.

Two years ago I became part of the CrossFit community, this is also something that has changed my life. I would like that thank everyone at CrossFit Wirral for providing me with somewhere to completely forget about the stresses of work, for pushing me to achieve more and for helping me demand better of myself. These effects have translated to all aspects of my life, and I am sure that they are reflected in this work.

Finally, I wish to express my gratitude to my wonderful girlfriend Gemma. Over the last ten years you have shared with me all of the ups and downs that led to this point. During this time, you have kept me grounded and focused and getting here would not have been possible without you. I cannot thank you enough for continuing to support in spite of the massive uncertainties in our future. I owe you this... *will you marry me?*

Contents

List of publications

Poli, E., Elliott, J. D., Teobaldi, G. and Lopez-Sanchez, A. *Water-splitting by inorganic nanotubes under near-UV irradiation: the Imogolite case.* In preparation.

Elliott, J. D., Scivetti, I., Poli, E. and Teobaldi, G. *Polarised amine-functionalized inorganic nanotubes for use in photo-catalysis.* In preparation.

Amara, M. S., Rouzire, S., Paineau, E., Poli, E., Elliott, J. D., Teobaldi, G. and Launois., P *Quantitative X-ray resolution of the atomic structure of metal oxide nanotubes: the Imogolite case.* To be submitted.

Wang, D., Liu, H., Elliott, J. D., Liu, L.-M. and Lau W.-M. *Robust Vanadium Pentoxide Electrodes for Sodium and Calcium Ion Batteries: Two-Phase Thermodynamic and Diffusion Mechanical Insights.* Accepted July 2016 *J. Mater. Chem. A*

Elliott, J. D., Poli, E., Scivetti, I., Ratcliff, L. E., Andrinopoulos, L., Dziedzic, J., Hine, N. M., Mostofi, A. A., Skylaris, C.-K., Haynes P. D. and Teobaldi G. *Polarisation Enhanced Photo-catalysis without Ferroelectrics and with Tunable Selectivity: the Unrealised Potential of Hybrid Inorganic Nanotubes.* Accepted July 2016 *Advanced Science*

Poli, E., Elliott, J. D., Ratcliff, L. E., Andrinopoulos, L., Dziedzic, J., Hine, N. M., Mostofi, A. A., Skylaris, C.-K., Haynes P. D. and Teobaldi G. *The potential of Imogolite nanotubes as (co-)photo-catalyst: a linear-scaling Density Functional Theory study. J. Phys.: Condens. Matter* 2016 **25** 074003

Poli, E., Elliott, J. D., Hine, N. M., Mostofi, A. A., Teobaldi G. *Large-scale density functional theory simulation of inorganic nanotubes: a case study on Imogolite nanotubes. Mater. Res. Innov.* 2015 **19** S272

List of Figures

List of Tables

Chapter 1

Advances & challenges in photo-catalysis

Abstract

This Chapter provides the background and theoretical framework upon which the remainder of this Thesis is built. It first aims to introduce the reader to the requirements for efficient photo-catalysis from the perspective of electron and hole formation and migration within the photo-catalyst, and then the electron transfer between photo-catalyst and reactant. The second Section of the Chapter describes three relatively recent, disconnected breakthroughs in the field, which have all been driven by design of the photo-catalyst based on its properties. Specifically, they leverage the effects of nanoconfinement of reactants within the photo-catalyst, the permanent polarisation of photoferroelectrics for polarisation enhanced photo-catalysis and one dimensional (nano)structuring for effective electron-hole separation. In the final Section, Imogolite Nanotubes are introduced as a candidate material potentially capable of combining these three avenues of research in one cheap solution comprised of light molecular weight atoms. Finally, an extensive review of the experimental and theoretical literature relating to Imogolite Nanotubes is provided. Overall, the elements presented suggest a potential photocatalytic mechanism that will be investigated in this Thesis.

1.1 Motivation

According to a recent report published by the United Nations the global population is forecast to reach 9.6 billion people by the year 2050 [1]. This represents a 30% increase

on top of the current population (estimated at 7.4 billion people [2]), and anticipate future significant pressure on resources availability and distribution such as energy, fresh water, fuels and food.

In response to this, by treaties such as the Kyoto protocol (1992), and more recently the Paris agreement (2015), the United Nations and European Commission have recognised the urgent need to reduce the negative impact that mankind is having on the planet and its climate. Such initiatives have started to produce beneficial impact: as recently as June of this year, reports have indicated that the wide spread banning of chlorofluorocarbons during the 1980s and 90s has contributed to a healing of the Antarctic Ozone layer [3]. However, greenhouse gas (CO_2, CH_4, NOx) emissions, which are widely recognised as being the leading cause of human driven climate change [4], have yet to be curbed.

Animal agriculture represents the largest contributor to greenhouse gas emissions, estimated as being responsible for between 18 and 51% of all CO_2-equivalent emissions [5,6], and is expected to rise by a further 80% by 2050 [7]. Fossil fuel consumption for energy production (read carbon-fuelled power stations) represents another sizable contribution to global greenhouse gas emissions. Combustion of carbon, natural gases and crude and refined oil releases carbon dioxide into the atmosphere whilst simultaneously (and irreversibly) depleting the planet of its natural resources. From a cultural perspective, dietary changes with a shift towards more carbon neutral food sources would undoubtedly help in reducing greenhouse gas emissions [8], however, rather than on socio-political aspects of food production, the work presented in this Thesis is focused on contributing to ameliorate concerning over-reliance on fossil fuels.

Fossil fuel combustion increases the concentration of greenhouse gases within the atmosphere. Greenhouse gases play an important role in modulating the surface temperature of the Earth by reducing the amount of solar radiation reflected back into space [9]. However, the current (human influenced) steady accumulation of greenhouse gases in the atmosphere is coupled to further trapping of heat and a net warming of the Earth's surface. Global temperature rises could have a large detrimental impact on society, with predictions of mass extinctions and losses of land mass due to sea level rises [10]. Furthermore, in the shorter term the prospect of a complete depletion of natural resources has been associated with soaring living costs, with 2.34 million households in the United Kingdom already considered to be below the fuel poverty line [11].

For these reasons significant time and resources are being devoted to the development of methods capable of harnessing clean and renewable energy sources such as solar or geothermal energy and wind or hydro-power [12].

Scientific investigations have begun to focus on the discovery and development of new functional materials and technologies to answer these energy concerns. For example, the Materials Genome Initiative [13] represents a large undertaking with the goal of providing a database of all known inorganic materials and their respective properties. The database provides researchers at the forefront of materials discovery with complete access to properties of different materials screening via high-throughput simulations [14]. Of particular interest for renewable energy applications are photo-active semiconductors that can be used to convert solar radiation into chemical fuels. Interest in these types of materials has grown immeasurably since the discovery of water splitting by TiO_2 [15]. TiO_2 is able to absorb a photon, and then via charge-transfer, catalyse the chemical decomposition of H_2O molecules in a processes known as photo-catalysis. If engineered in such a way that the photo-catalyst remains non-toxic and cost effective, then photo-catalysis is widely accepted as a viable approach for many processes including photolysis, pollutant decomposition and solar fuel generation.

As the field of heterogeneous photo-catalysis has expanded, many different candidate materials have been investigated. However, given that over four decades of research has culminated in a less than 3% efficiency for visible-light photolysis [16], significant changes to the design of photo-catalysts must be considered. Investigations into new avenues of (visible-light) photo-catalysis have begun to appear in the literature, see Section 1.3 and references therein. This Chapter provides a description of practical and theoretical considerations for the discovery and continued development of photocatalytic materials and strategies. Of key relevance is the following question: if high throughput approaches are to be deployed in screening photo-catalytic materials and solutions, what physical properties of the substrate are to be pursued? Can libraries of properties and predictions on bulk-materials (as targeted by the Materials Genome project and generously funded over the world, UK included) be rationally used to screen photo-catalysts? What materials and properties could make photo-catalytic strategies more efficient and scalable? In short, what controls the efficiency of a photo-catalyst and how to enhance it?

1.2 Introduction to photo-catalysis

1.2.1 The requirements for viable photo-catalysis

A photo-catalyst is a material with the capability of using light to produce reactive species that initiate chemical reactions. The photo-catalyst absorbs photons producing reactive electron and hole pairs (e-h) that can be transferred independently or jointly to reagents. The former can be utilised in order to produce alternate fuel sources, in feed stocks or to aid in pollutant degradation. As outlined in several reviews and research articles on the matter [17–29], the electronic structure, surface reorganisation and interface structuring of the photo-catalyst and solvent are critical components in photocatalytic performance and viability. On this basis, the opportunity for photo-catalysis can be maximised if the following criteria is met:

(i) The band gap and band structure of the photo-catalyst should permit the absorption of light through electronic excitation, without the need for phonon absorption or emission. From the perspective of renewable energy consumption, sunlight (and artificial visible light) should to be used, therefore the band gap must match the visible range of the electromagnetic spectrum, which is 1.6 to 3.1 eV and ideally the sun radiance peak at 1.6 to 2.1 eV [30].

(ii) Upon electronic excitation or during the de-excitation pathway there should be an effective separation of the e-h that should minimise the possibility of recombination.

(iii) For photo-assisted surface redox reactions to take place on the photo-catalyst surface the e and h must diffuse independently towards the surface.

(iv) Redox chemistry demands transfer of the separated e or h to reactants with high efficiency. This rests on a favourable alignment between the photo-catalyst and reactant electronic energy levels as well as charge-transfer kinetics faster than any other competing processes that might lead to recombination or catalyst degradation.

(v) The oxidative and reductive transfer of e and h should lead to the formation of desirable products.

(vi) The quantum yield, which is the ratio of absorbed photons to product formed, should be as high as possible.

(vii) The photo-catalyst should present a high reaction selectivity that can be tailored to specific reactants in multi-component media [31].

Over one hundred years of research [17–29, 32–35], focused on the discovery and development of new photo-catalysts, has yet to produce materials that simultaneously fulfil each of the attributes (i)-(vii). Serious challenges arise in the engineering of materials that combine appropriately sized band gaps with the energetic alignment of the valence and conduction band edges and the highest occupied and lowest unoccupied molecular orbitals of the reagents they will catalyse. Furthermore, in cases where there is favourable alignment of the electronic states, other factors still present significant challenges. For example slow photo-catalyst-to-reactant charge transfer kinetics relative to e-h recombination, interface restructuring in response to different media and the ensuing shifts to the photo-catalyst band edges and changes to the fine structure of the catalyst due to defects that introduce trap states or recombination centres in the structure.

The most common strategies to build upon and improve the performance of photo-catalysts rest on the modulation of the band gap via valence band engineering, conduction band engineering or joint engineering of both band edges [36–61]. These are carried out with the aim of tailoring the photo-catalyst to specific oxidation and reduction potentials. Recently, innovative approaches to overcome the challenges outlined have begun to emerge, these include encapsulation of the reactants inside photo-catalyst pores [31, 62–64], nano-structuring of the photo-catalyst [33–35, 65–80] and using internal polarisations [81–107]. These different approaches will be described in more detail in the coming sections.

1.2.2 Underlying theory of photo-catalysis by semiconductors

In any photocatalytic reaction, the initial step is the absorption of light by the catalyst, which generates *e*-*h* pairs that (subject to relaxation) are situated close to the conduction and valence band edges, see **(1)** Figure 1.1. The adsorption process may then be followed by radiative or non-radiative recombination of the charge carriers (**(2)** Figure 1.1) or, under the right conditions, to an effective separation of the *e*-*h* pair. If the excitation is long lived, there is sufficient chance that the *e*-*h* might (independently) migrate to the semiconductor surfaces (**(3a)** & **(3b)** Figure 1.1) where they can take part catalytically in redox electron transfer reactions **(4a)** & **(4b)** Figure 1.1).

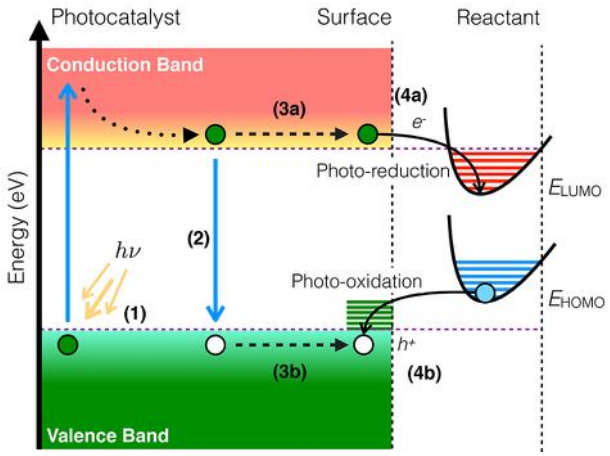

Figure 1.1: A schematic representation of the photocatalytic process. Absorption and emission of electromagnetic radiation ($h\nu$) is depicted with the solid blue vertical lines (1) and (2) respectively. Broken arrows represent relaxation and migration of the charge carriers within the photo-catalyst (3). The vibronic-relaxation coupled charge transfer is represented by the solid black arrows (4). Suitable alignment of the reactant HOMO and LUMO with the VBE and CBE is a necessary, yet not sufficient (see text), condition for photo-catalysis.

1.2.2.1 Absorption by direct and indirect gap semiconductors

The absorption of light by the material relies on several factors: the size and shape of the catalyst, the quality of crystal and the presence of defects in the photo-catalyst structure. Each of these plays a part in determining the opto-electronic structure and properties of the material. External factors such as the light source, temperature, medium and presence of magnetic fields can also impinge the photon absorption. Full discussion regarding the absorption of light by semiconductors can be found in several references [108, 109],

When a model semiconducting surface is subject to irradiation by incident light I_0, then each of the individual photons may be absorbed, reflected or transmitted. The fraction, or intensity of absorbed photons, I_A, can modelled according to the equation,

$$I_A = AI_0, \tag{1.1}$$

where A is a dimensionless coefficient for absorption,

$$A = (1 - R)(I - \mathrm{e}^{-\alpha d}). \tag{1.2}$$

Here, R is the analogous coefficient for reflection, and d is the thickness of the semiconductor. Special consideration is given to the treatment of the linear absorption coefficient α, which describes the interaction of the absorbed photons with the material. In direct band-gap semiconductors, where the crystal momenta of the valence band energy maximum and conduction band energy minimum are coincidental, the excitation energy is,

$$\begin{aligned} h\nu &= E_f - E_i, && (1.3) \\ &\geq E_g. && (1.4) \end{aligned}$$

The photon energy $h\nu$ matches the fundemental band gap, E_g between the final and initial states E_f and E_i. Assuming parabolic band edges, α is,

$$\alpha = A^* \left(h\nu - E_{\mathrm{g}}\right)^{\frac{1}{2}}, \tag{1.5}$$

where A^* is an prefactor that depends on the effective masses of the e and h. As demonstrated by Equation (1.4), the excitation of an electron from the valence band edge to the conduction band edge is exclusively driven by the incident photon in a direct band-gap semiconductor. Other semiconducting materials have indirect band-gaps where the momenta of the band edges do not coincide. Because photons do not carry crystal momentum, the excitation of an electron also requires coupled absorption or emission of phonons in order to maintain energy conservation rules:

$$h\nu = E_f - E_i \pm E_p. \tag{1.6}$$

The additional term corresponds to the energy of the emitted ($+E_p$) or absorbed ($-E_p$) phonon. The absorption coefficient for indirect gap semiconductors is the sum of the absorption coefficients relating to the case of emitted (α_e) and absorbed (α_a) phonons,

$$\alpha = \alpha_e + \alpha_a. \tag{1.7}$$

Each of these components is proportional to the probability of interacting with a phonon of given frequency, calculated from Bose-Einstein statistics, yielding,

$$\alpha = \frac{A^*(h\nu - E_{\mathrm{g}} + E_{\mathrm{p}})^2}{e^{\frac{E_{\mathrm{p}}}{k_{\mathrm{B}}T}} - 1} + \frac{A^*(h\nu - E_{\mathrm{g}} - E_{\mathrm{p}})^2}{1 - e^{-\frac{E_{\mathrm{p}}}{k_{\mathrm{B}}T}}}. \tag{1.8}$$

Equation (1.8) shows that photon absorption is temperature dependent in indirect band gap semiconductors. When the temperature is low, the density of phonons will also

be low and therefore the absorption coefficient will also be reduced. This means that, at room temperature direct gap semiconductors usually absorb more electromagnetic radiation making them more appealing for photo-catalysts.

1.2.2.2 Further considerations for electron-hole formation

After absorption of photons the *e*-*h* pair should migrate to the photo-catalyst surface and interfaces for further charge-transfer reactions to occur. For each of the *e*-*h* pairs created this is not always the case. In some instances the *e* and *h* are bound together as an exciton or naturally decays back to the ground state. The implications of exciton's and radiative and non-radiative recombination within semiconductors are discussed within this Section.

The absorption of photons by semiconductors may also result in the formation of excitons [108, 110]. These are neutral quasi-particle states where the *e*-*h* pair are Coulombically bound to one another and do not behave in the same way as free charge carries. The exciton has a low effective mass and moves through the crystal as an *e*-*h* pair lowering the energy of the associated states and bringing them underneath the conduction band edge as shown in Figure 1.2. The translational velocities of the *e* and *h* must be equal despite differences in their relative masses. This restricts the *k*-space distribution of the exciton to regions that satisfy the condition [108],

$$\left[\frac{dE_{\mathrm{CB}}}{dk}\right]_{\mathrm{electron}} = \left[\frac{dE_{\mathrm{VB}}}{dk}\right]_{\mathrm{hole}}. \tag{1.9}$$

For the purpose of this discussion, the two most important fates of the exciton are its recombination and its dissociation. Bound (Coulombically attracted) *e*-*h* pairs have a higher propensity to recombine than free charge carriers so the exciton lifetime is relatively short. When the exciton recombines it emits a photon with energy,

$$h\nu = E_{\mathrm{g}} - E_{\mathrm{x}}, \tag{1.10}$$

where E_{x} is the energy difference between the exciton state and the conduction band edge, see Figure 1.2. Instead, in materials where there are large internal local fields (such as in highly doped semiconductors or materials with a largely anisotropic potential leading to internal polarisation gradients and ensuing electrostatic fields) the resultant forces can be larger than the Coulomb interaction between the *e* and *h* pair. Under these conditions the exciton will dissociate leaving free charge-carriers.

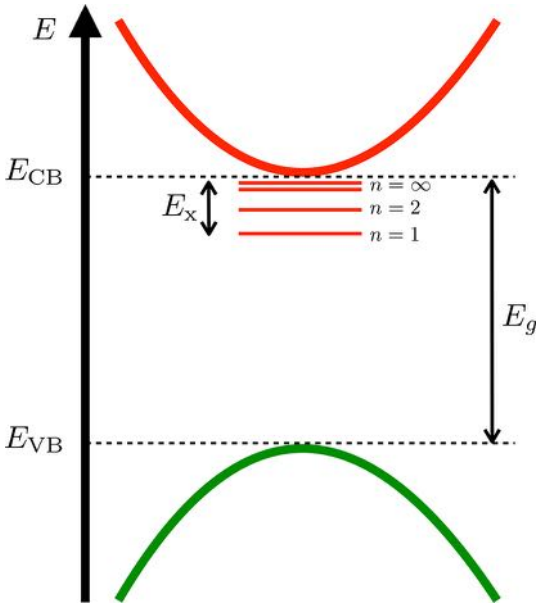

Figure 1.2: An energy level plot for the excited states of the exciton. The exciton states are given by $n = 1, 2, ...$ whilst the conduction band edge is taken as the continuum state, $n = \infty$.

In general, exciton formation occurs most readily in materials with high crystallinity at low temperatures because anisotropies within the system can lead to local polarisation gradients that cause exciton-dissociation; nevertheless, excited e-h pairs also radiatively recombine. The decay of free charge-carriers and emission of photons mirrors the absorption processes outlined in the previous section. In direct gap semiconductors recombinative transitions occur between e and h states with the same crystal momentum. The photon emission energy is the same as the photon absorption energy given by Equation (1.4). A radiative transition connecting two states with different crystal momentum in indirect gap semiconductors must also be accompanied by the emission or absorption of a phonon(s). Thus the emitted photon energy is given by Equation (1.6).

Recombination of the e-h pair can also occur non-radiatively, that is without the emission of photons. Several non-radiative recombination mechanisms exist including the Auger effect, mediated by surfaces and defects sites and through a cascade of phonon emissions.

Non-radiative recombination can occur when two photo-generated electrons or holes collide. The excitation energy of one of the pair can be transferred to the other, and results in an e (h) decaying back to the ground state and the other being excited deep into the conduction (valence) band. This is the Auger effect, that relies on collisions between two excited particles and is therefore is strongly dependent on the carrier concentration. Surfaces and defects introduce high energy dangling bonds that can act as recombination centres into the semiconductor by providing a decay pathways for excited e-h pairs. Recombination can also occur if the systems emits a multitude of (high probability) phonons as a dissipation of excess energy. Multiple phonon emissions are required because of the large difference between band gap energies and the energies of the vibrational modes of the lattice.

1.2.2.3 Theoretical rate constant for non-adiabatic charge-transfer processes

After the charge-carrier generation and migration through the photo-catalyst, one can now turn attention to the basic theory of non-adiabatic charge transfer at the interface between the photo-catalyst, reactant and electrolyte. To date, one of the most poorly understood areas in the design of photocatalytic materials is the link between the atomic-scale structuring and electronic properties of the catalyst surface, the solvent-electrolyte and reagent interface, and the observed photocatalytic activity and selectivity. Simulations that aim to target these problems complement ongoing experimental work and inform the engineering of new photochemically active materials.

The fundamental process which drives the surface redox reactions is the electron transfer, where either an electron from the semiconductor (photo-catalyst) conduction band hops to an empty reactant state, or from the filled molecular HOMO to the photo-catalyst valence band. Electron transfer at the photo-catalyst-reactant-electrolyte interface involves non-covalently bonded states that are typically separated by just a few Ångstroms (i.e. weak electron coupling). Marcus theory states that the redistribution of charge density by the electron transfer process requires reorganisation of the nuclei involved, which has an associated *reorganisation energy*, λ. The Marcus mechanism is shown in Figure 1.3 and discussed at length in reference [111]. In this model, the reaction is facilitated by reconfiguration of the nuclei into an arrangement convenient for electron transfer: (1) Figure 1.3. Subsequently the charge transfer event can take place: (2) Figure 1.3, followed by relaxation into a nuclear ground state: (3) Figure 1.3. The arrangement of the photo-catalyst, solvent and reactant, which is governed

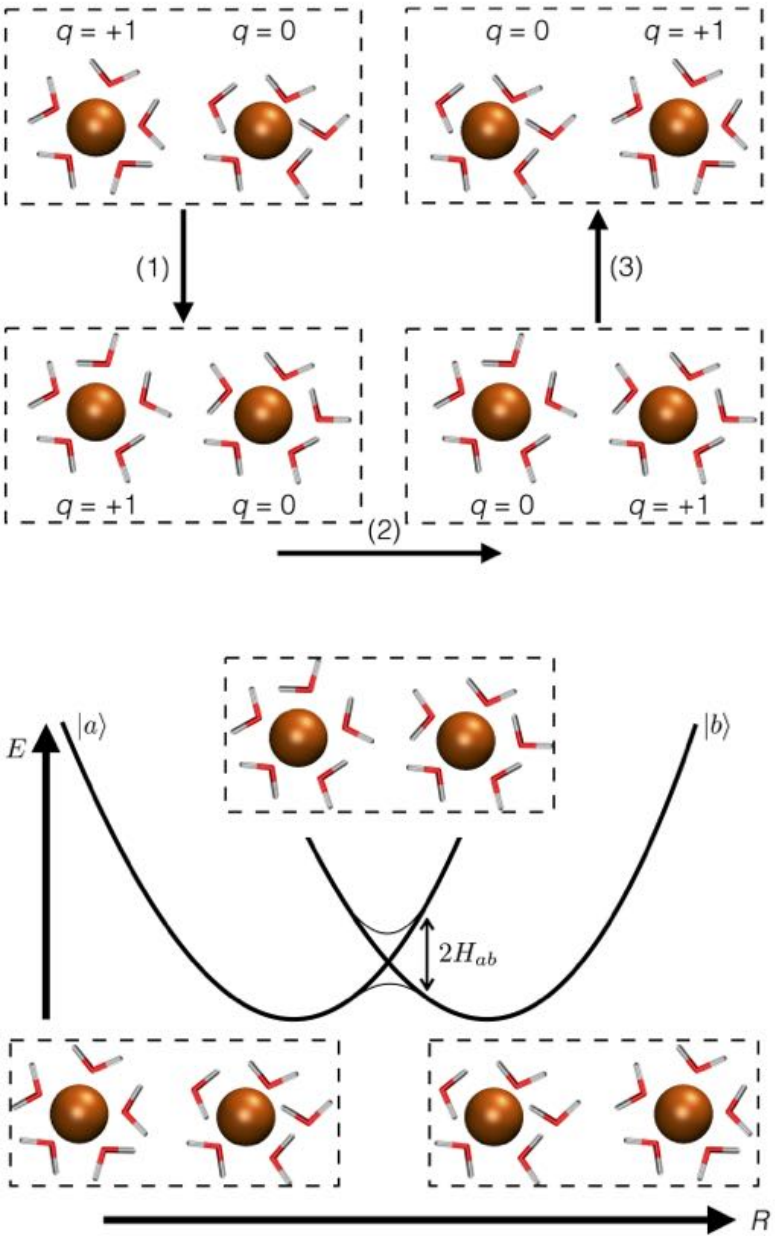

Figure 1.3: An example of electron transfer for solvated ions within the Marcus model. In the upper schematic instantaneous charge transfer cannot occur directly and must proceed via three steps: (1) Fluctuations in the solvent cause a reorganisation of the molecules. (2) Electron transfer from the atom ($q = 0$) to the positively charged ion ($q = 1$) can occur. (3) The solvent relaxes in response to the charge transfer. The lower diagram is an energetic representation along the reaction coordinate, R, demonstrating the parabola hopping required for charge transfer to occur.

by long ranged hydrogen bonding and van der Waals forces, means that the electron transfer can be described by the weak coupling regime. The kinetics of such a process are best described by Fermi golden rule for transitions between two states [111]. By simply stating the resulting theoretical rate constant, it is possible to dissect the important physical contributions that should be taken into account when aiming to develop efficient photo-catalyst-reactant charge transfer. The interested reader is referred to Chapters 16 and 17 in reference [111] for a full derivation. The non-adiabatic weakly coupled charge transfer rate constant between two electronic states $|a\rangle$ and $|b\rangle$, $k_{b\leftarrow a}$, can be written as the integral

$$k_{b\leftarrow a} = \int_{\text{band}} \Gamma(E) f(E - E_{\text{Fermi}}) F(E, \Delta G, \lambda, \omega^{\text{eff}})\ \mathrm{d}E. \tag{1.11}$$

Where $f(E - E_{\text{Fermi}})$ is the Fermi-Dirac distribution, providing the probability that a given state is populated. $F(E, \Delta G, \lambda, \omega^{\text{eff}})$ is the the Franck-Condon integral, which includes the terms arising from the reorganisation of the nuclei (λ) and the frequencies of the vibrational modes (ω^{eff}). $\Gamma(E)$ is a function that describes the electron transfer omitting the nuclear vibrational motion (considered by F)

$$\Gamma(E) = \frac{2\pi}{\hbar} |H_{ab}|^2 \delta(E_a - E_b). \tag{1.12}$$

Here, H_{ab} are the off-diagonal elements of the perturbed Hamiltonian matrix that correspond to the electronic coupling of the diabatic donor and acceptor states, $|a\rangle$ and $|b\rangle$, where the term diabatic refers to a state for which $\vec{\nabla}_{\mathbf{R}} |a\rangle \neq 0$. The vibrational energy levels in the initial and final states are E_a and E_b, thence the term $\delta(E_a - E_b)$ is the energetic alignment of the states a and b.

Inspecting Equations (1.11) and (1.12) three important physical contributions that will affect the rate of charge-transfer at the photo-catalyst-reactant-electrolyte interface can be identified. Firstly, the energetic alignment of the electronic states involved in the transfer. Secondly, the magnitude of the electronic coupling between the states and lastly the Franck-Condon integral. Next, the discussion of the physics governing photo-catalysis by solid state semiconducting materials considering how each of these elements can be maximised for optimal transfer rates will be expanded.

1.2.2.4 Energetic alignment of charge transfer states

Photo-oxidation takes place if an electron occupying a HOMO (donor state) of the reactant molecule (or electrolyte) transfers into the valence band (acceptor state) of the photo-catalyst, as shown in Figure 1.1. The photo-catalyst provides a hole that drives a given chemical reaction, and can be thought of as acting as an electron sink. Photo-reduction takes place if a photo-excited electron occupying a state close to the conduction band minimum (donor state) is transferred into the empty LUMO state (acceptor state) of the reactant (or electrolyte), Figure 1.1. In this case the catalyst acts as an electron source for the desired chemical reaction.

The difference in energy between these acceptor and donor states features explicitly in Equation 1.11 in the form of a Dirac delta function:

$$k_{b\leftarrow a} \propto \delta(E_a - E_b) \tag{1.13}$$

From a physical perspective, this is included as a temperature-dependent smearing of the energy difference. As the rate constant is proportional to the delta function, the overall rate of charge transfer, is zero unless $E_a \rightarrow E_b$. This means that the photo-reaction will not proceed unless the energies of the states a and b are roughly equal within the temperature induced smearing.

The difference in energy of $|a\rangle$ and $|b\rangle$ is related to the energy alignment of the photo-catalyst band edges with respect to the molecular states (HOMO and LUMO). This means that, to maximise $k_{b\leftarrow a}$ for a photo-oxidation process, the energy of the HOMO and the valence band maximum of the reacting species should be aligned, but, the energy of the HOMO should be slightly higher than the valence band maximum in order to promote transfer of the electron to the valence band edge. To maximise $k_{b\leftarrow a}$ for photo-reduction there must be good alignment of the photo-catalyst conduction band minimum and the LUMO state of the molecule, with the energy of the LUMO just below the conduction band minimum favouring transfer from the catalyst to the molecule. These two conditions are displayed in Figure 1.1.

1.2.2.5 Electronic coupling between charge transfer states

On the basis of Equations (1.11) and (1.12), the charge-transfer rate constant in Marcus theory is quadratically proportional to the electronic coupling of the donor and acceptor

states $|a\rangle$ and $|b\rangle$,

$$k_{b\leftarrow a} \propto |H_{ab}|^2. \tag{1.14}$$

Here H_{ab} are the off-diagonal elements of the Hamiltonian matrix expanded on an adiabatic basis ($\vec{\nabla}_{\mathbf{R}} |a\rangle = 0$), expressed here in the simplified two state representation,

$$\begin{pmatrix} \langle a|H|a\rangle & \langle b|H|a\rangle \\ \langle a|H|b\rangle & \langle b|H|b\rangle \end{pmatrix} = \begin{pmatrix} E_a & H_{ab} \\ H_{ba} & E_b \end{pmatrix} \tag{1.15}$$

Put simply, H_{ab} is a measure of the strength of the interaction (coupling) between the initial charge-transfer state $|a\rangle$ and final charge-transfer state $|b\rangle$. Equation (1.11) is valid in the weakly coupled regime, where there are no formal bonding interactions between the donor and acceptor states. That being said, the matrix elements H_{ab} are specifically dependent on the electronic structure of the photo-catalyst and the reagent and subject to surface restructuring, the polarity and arrangement of the nearby solvent molecules and the presence of external magnetic and electric fields. From a theoretical perspective, it is possible to calculate H_{ab} through different approaches. For information on these techniques, which are beyond the scope of Thesis, the interested reader is referred to reference [112]. The overall rate of the electron transfer processes, $k_{b\leftarrow a}$ will be larger if the states interact more strongly, this will occur in systems where the phase space leads to larger coupling.

1.2.2.6 The Franck-Condon factor

Finally, the rate of charge transfer depends also on the Franck-Condon factor, which is the square overlap integral between the initial and final nuclear wavefunctions. Using a single-mode harmonic approximation for the nuclear modes, the solution to the integral can be approximated as

$$F(E, \Delta G, \lambda, \omega^{\text{eff}}) = (4\pi\lambda k_{\text{B}}T)^{-\frac{1}{2}} \sum_{\nu} e^{-S^{\text{eff}}} \frac{(S^{\text{eff}})^{\nu}}{\nu!} e^{-\frac{(E+\Delta G+\lambda+\nu\hbar\omega^{\text{eff}})^2}{4\lambda k_{\text{B}}T}}. \tag{1.16}$$

ΔG is the change in Gibbs free energy for the charge transfer process, λ is the reorganisation energy mentioned above, ω^{eff} is the collected effective frequencies of the quantum modes along the reaction coordinate (this is important when the modes in question have energies lower than the thermal energy, i.e. where the classical limit breaks down [113]) and S^{eff} is the electron-phonon coupling of the effective vibrational modes of the photo-

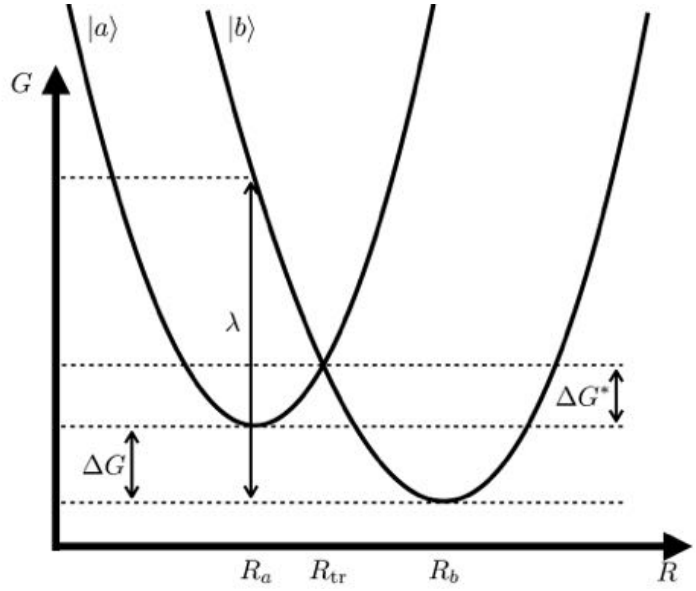

Figure 1.4: Plot of two diabatic potential energy surfaces for states $|a\rangle$ and $|b\rangle$ that transform to one another during electron transfer reactions. The free energy, G, is plotted as a function of the nuclear reactions coordinate R. λ is the reorganisation energy, ΔG^* is the activation energy and ΔG is the free energy difference between the electronic minima E_a and E_b.

catalyst and medium, the so-called Huang-Rhys factor.

The reorganisation energy can be visualised by considering the two (parabolic, since we are within the harmonic approximation for nuclear modes) potential energy surfaces along the one dimensional reaction coordinate, R as shown in Figure 1.4. Upon electron transfer, the two surfaces transform to one another and λ is the ensuing vertical exothermic (endothermic) energy change from a to b (b to a).

1.2.3 Strategies for band engineering

Taking all of the aforementioned elements into account, the main factors that govern the performance and prospective industrial application of a semiconducting photo-catalyst can be reduced to (i) the size of the photo-catalyst band gap, (ii) the energetic alignment of the photo-catalyst band edges with respect to donor and acceptor states in reactant molecules, (iii) the photo-catalyst band structure and (iv) the surface-medium interface structuring. These properties define the absorption process, the rate of e-h

recombination, the migration of the charge carriers within the semiconductor and the energetic drive for charge transfer between the photo-catalyst and reactants. Therefore, the target for research, as outlined in Section 1.2.1, has been to engineer a material with a visible light band gap and suitable alignment between the photo-catalyst valence and conduction band edges and the HOMO and LUMO states in target reagents.

Such tasks have so far proven so difficult that compromises have had to be introduced (i.e. the use of non-visible light sources [114]) that damage the profitability or productivity of the photo-catalyst. Ongoing research attempts to circumvent these compromises through modulation of the semiconductor valence and conduction band edges. In general this is achieved by doping the catalyst lattice or through chemical functionalisation. These approaches can be grouped depending on whether they target the tuning of the valence band or conduction band, or simultaneously modulate the energies of both. By controlling the band edges of the photo-catalyst it is possible to engineer an energy gap capable of visible light absorption or to tune the energy levels of the photo-catalyst to the specific reactants.

Cation doping using $3d$-transition metals is a proven effective strategy for semiconductor band gap narrowing. The introduction, and ensuing hybridisation, of the occupied d orbitals raises the energy of the valence band edge, which is shown to occur in transition metal doped TiO_2 [37–40]. The degree to which the energy of the valence band edge can be altered via cation doping is subject to the dopant atom (i.e. the transition metal), and to the concentration of defect sites introduced into the material. On the other hand, it is also possible to dope semiconductor materials with non-metallic anionic species such as N, O, P and S. In these cases hybridisation occurs between the p-orbitals of the dopant atom and states within the semiconductor lattice. However it remains unclear whether the band gap narrowing observed is brought about directly by the dopant atoms or by induced defects within the native lattice [52].

The introduction of dopant atoms may enable tuning of the semiconductor valence band edge, but it can also have a large negative impact on prospective photocatalytic applications. Firstly, in general, defect sites act as electron-hole recombination centres. Notably, by their nature, localised d-orbitals have been shown to reduce the charge-carrier mobility [36, 53]. In reducing the mobility of the photo-generated e-h pairs, it is likely that migration to the surface charge transfer sites is diminished, which hampers the overall photocatalytic process. Where anionic dopant atoms are used, for meaning-

ful modulation of the valence band edge (> 0.3 eV), a large concentration of impurities are required, this can lead to a destabilisation and decomposition of the semiconductor (photo-catalyst) structure [46, 51].

Different avenues exist for the modulation of the conduction band edge, these include the substitution of transition metal cations whose electronic configuration is d^0 or d^{10}. In the semiconducting materials $InXO_4$ and $BiXO_4$ (X = V^{5+}, Nb^{5+}, Ta^{5+}), a marked change in the energy of the conduction band edge is observed as the composition changes [42, 43, 45, 55, 60]. In particular, the smaller $3d$ states of the V-containing materials are computed to be lower in energy than the Nb- and Ta-containing ones [45]. Along similar lines, d^0 transition cation substitutions in Bi_2GaXO_7 (X = V^{5+}, Sb^{5+}, Nb^{5+}, Ta^{5+}) yield the same results, with the V-containing compound having the smallest (optical) energy gap due to reorganisation of the conduction band edge [44,47,50,61].

The main limitation of all of these band engineering techniques is clear: these approaches only seek to improve existing candidate materials. In these works, target materials have known photocatalytic deficiencies and are tuned in the hope that the severity of their drawbacks can be lessend [58,59]. In addition, the screening of *new* materials for photo-catalysis occurs only as an afterthought, for example on the basis of absorption measurements, rather than being driven by design [41, 57].

More rigorous control over the valence and conduction band edges can be achieved using solid-solution photo-catalysts. These are mixtures of solid materials with continuously tunable compositions. Access to the exact composition of the catalyst simultaneously provides control over the fine tuning of the states at both band edges, making solid-solution photo-catalysts ideal for band tuning.

References [48, 49, 54] explore the photocatalytic splitting of water using the solid-solution photo-catalyst ZnO:GaN, which has the tunable composition $(Ga_{1-x}Zn_x)(N_{1-x}O_x)$. In these works, it is found that increasing the ZnO constituent, within the range $0.05 \leq x \leq 0.22$ narrows the materials band gap from 3.4 eV (UV wavelength) to 2.6 eV (visible wavelength). Analysis reveals that the reduction in the energy gap is brought about by the introduction of $2p$ and $3d$ states (from the ZnO) to the valence band edge [49]. Visible light photolysis is reported for the ZnI:GaN photo-catalyst, however it is suggested that 90% of charge carriers generated recombine rather than participating in the reaction. This is another indication of the further work required in the field. To this end, a

more recent investigation of GaN:ZnO with nanoparticles deposited onto the surface has been carried out, over a six month period the new catalyst performance was still found to be unsatisfactory [56].

These approaches often overlook the fundamental requirements for photo-catalysis because the techniques employed cannot access the atom resolved structure of the photo-catalyst surface or the time resolved evolution of the excited states. These are necessary for the understanding of the charge transfer kinetics that govern photocatalytic processes [111]. In general, band tuning methods also neglect some of the properties of materials which could be beneficial to photo-catalysis. Luckily, in several different avenues, pioneering work has recently begun that focuses on the properties of the photo-catalyst that promote chemical selectivity, e and h separation and the charge transfer reactions to reactants. These are described in the next Section.

1.3 Photo-catalysts by design

The aim of this Section is to introduce the state of the art in current photo-catalyst design. Given the persistent failures of approaches based on band engineering techniques only, that were discussed in the previous Section, research has begun to explore different avenues for the design of photo-catalysis. The methods outlined below instead attempt to achieve photo-catalysis by altering the chemical reactivity and increasing the carrier lifetimes. Three current lines of research will be described in detail.

1.3.1 Photo-catalysis in confined volumes

A series of recent publications have demonstrated that photocatalytic selectivity, albeit in the deep UV range (< 200 nm), is increased when reactants are confined within the cavities of nanoporous zeolites [31, 62–64]. Zeolites are a widely studied family of porous crystalline aluminosilicate; they vary in their atomic composition and pore shapes and sizes, which gives rise to their application as heterogeneous catalysts. Reference [31] reports that zeolites with pore volumes between 0.17 and 0.24 cm^3/g were used in the studies. The evidence presented suggests that the trapping of reagents within the zeolites pores could open up the possibility of new reaction pathways through a combination of catalyst activation, surface absorption and confinement of the reagent in proximity of the excitation centre.

These ideas are explored in reference [31], where the photocatalytic conversion rates of different zeolites are compared. The performance of photo-catalysts of different morphologies and compositions has been contrasted against amorphous silica, finding that the rate of conversion is greater in all of the cases where zeolite is used. In the proposed reaction mechanism it is suggested that silanol (SiOH) groups at the zeolite surface absorb photons at deep UV frequencies and initiate free radical reactions with trapped CH_4 molecules, catalysing the oxidation to low molecular weight hydrocarbons, methanol and other single carbon oxides (see scheme below, for a full list of radical chain reactions see [62]).

$$\mathrm{SiOH} \xrightarrow[\lambda<200\,\mathrm{nm}]{\mathrm{h}\nu} \mathrm{SiO}^{\bullet} + \mathrm{H}^{\bullet}$$

$$\mathrm{SiO}^{\bullet} + \mathrm{CH_3}^{\bullet} \longrightarrow \mathrm{SiOCH_3}$$

$$\mathrm{SiOCH_3} + \mathrm{H_2O} \longrightarrow \mathrm{SiOH} + \mathrm{CH_3OH}$$

Using control experiments (no catalyst present), and by exploring the reactions with different zeolite photo-catalysts several factors were found to impact the photo-oxidation process. (i) There is no conversion of CH_4 to C_1 oxygenates in the control experiment. This means that there is a need for the catalyst [31]. (ii) Photocatalytic activity is severely diminished when non-porous, amorphous silica is used as a catalyst in spite of the fact that silica catalyst has the highest density of silanol groups. This means that the confinement of reagents (in the zeolite pores), close to where free radicals are formed after excitation of the catalysts and relaxation of the e and h pair, has a major role in the observed photocatalytic activity [31]. (iii) Otherwise, the density of silanol groups is proportional to the photo-catalyst activity, zeolites with pores that have more SiOH groups are shown to exhibit greater conversion because of the greater concentration of radicals in the pores and their containment close to the reagents [31]. (iv) Product selectivity depends on the composition of the catalyst [31], tuning the reaction mixture, morphology and composition of the catalyst can favour the formation of certain products during the free radical reaction.

Investigation of the reagent-confined zeolite photo-catalysis has been further extended in [62, 63]. The size of the zeolite pore is found to be a factor in determining the photo-reactivity of the catalyst [62], with smaller pore materials having greater reactivity: zeolite ZSM-5 (5.4 Å × 5.6 Å oval pores and 5.6 Å diameter pores) and zeolite MCM-41 (38 Å diameter pores). When the methane molecules enter the smaller pores their interactions with the surface hydroxyls (via thermal diffusion or surface adsorp-

tion) are increased with respect to larger pores allowing for a larger number of reactions. These results cannot yet be generalised (to other photo-initiated reactions) given the relatively narrow scope of the investigations. However, promising results have also been obtained in [63] where exploration of nanoconfined-photocatalytic oxidation of CH_3CH_3 within zeolite micropores is also observed.

As well as showing a direct enhancement of the photo-catalysed conversion of methane and ethane by confinement inside microporous zeolites, a degree of chemical selectivity is also highlighted. The selectivity of the reaction products is dependent on the reaction conditions, the removal of oxygen from the reaction mixture encourages the formation of low molecular weight hydrocarbons and restricts the formation of oxygenated products [31, 62, 63]. As briefly mentioned above, selectivity is also dependent on the zeolite composition [31] and the distribution of silanol surface coverage [31, 62]. Other photocatalytic reactions have been studied, the conversion of $CO_2 \longrightarrow CH_4$ is found to decrease with respect to the uncatalysed reaction for zeolite based photo-catalysts [64]. However, the reported absorption of CO_2 onto the catalyst surface is in itself a promising result [64]. This is because the induced changes in internal bonding brought about by interactions with the zeolite surface open up new alternative strategies for the reduction of CO_2.

1.3.2 Polarisation enhanced photo-catalysis

Work that targets the use of polarised materials to maximise the electron-hole separation, thereby reducing recombination kinetics will now be discussed. Photoferroelectric materials couple the spontaneous permanent polarisation of ferroelectrics with the ability to absorb photons and to produce free charge carriers. In cases where the resultant force exerted on the *e*-*h* pair by the electric field (brought about by the internal polarisation) is sufficient to overcome exciton binding energies and to influence the carrier diffusion pathways, the photoferroelectric materials become ideal candidates for investigation in the context of photo-catalysis, Figure 1.5, especially if the polarisation can be maintained under irradiation [104].

In more detail, when an *e*-*h* pair are created in the ferroelectric crystal, nanoparticle or thin film, they are subject to the influence of the internal polarisation gradient. The unbound *e*-*h* pair oppositely drift, the *e* towards the positively charged surface, and the

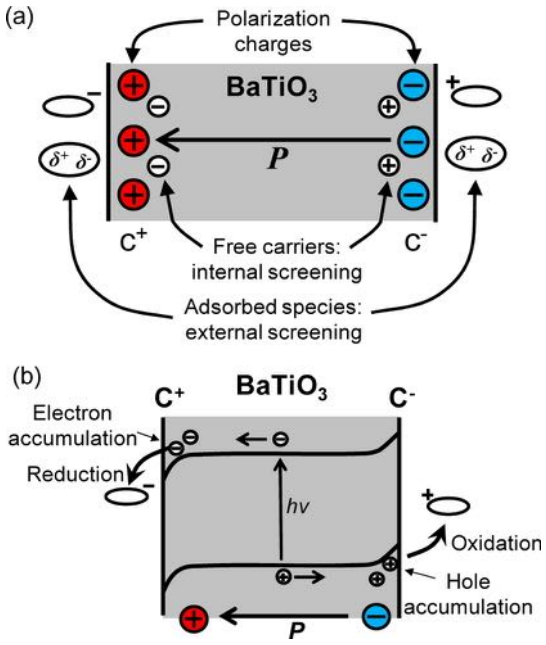

Figure 1.5: Taken from reference [102, 107], (a) a schematic representation of a typical ($BaTiO_3$) ferroelectric material. The internal polarisation, and surface charging is highlighted along with the charge-screening by internal charge carriers and adsorbed molecules. (b) Example of a photoferroelectric photo-catalyst, the separated charge carriers migrate to the surfaces under the influence of the internal polarisation gradient. Spatially separated holes and electrons are available for reduction and oxidation reactions.

h towards the negatively charged surface [93], Figure 1.5. The e-h recombination probability is reduced since in order to decay those particles have to move against the field created by the ferroelectric polarisation. It is suggested in [102] that the ferroelectric polarisation of lithium niobate may be a factor in the relatively long photoluminesence times for the ferroelectric phase (9 μs [87]) in comparison to paraelectric (i.e. a material that becomes polarised in response to an applied electric field) titanium dioxide (0.1 μs [115]). Exploiting polarisation enhanced e-h separation has been used in the development of new photovoltaic applications for the conversion of solar to electrical energy [88,92,94–96,100,101]. Moreover, a recent review highlights that work has begun to develop polarisation enhanced photo-catalysis based on the use of photoferroelectric substrates for the catalyst [106].

The absorption of molecules at the surface of a photo-catalyst is a critical step in the process of heterogeneous catalysis. This allows for the diffusion of the molecule to reactive sites on the catalyst, energetic activation of the molecular states and charge-transfer from the photo-catalyst to the molecule. The presence of the polarised surfaces in ferroelectric materials has been shown to have an impact on the molecular absorption properties as well as to contribute towards the screening of the surface polarisation, Figure 1.5 [89–91,106]. For the ferroelectric phase of $BaTiO_3$, the polarisation of the surface increases the strength of surface-molecule dispersion interactions lowering the energy barrier for physisorption of CH_3OH and CH_3CH_2OH [89,90]. Physisorption is further promoted if the reagent is polar. In [91] it has been shown that 2-fluoroethanol has a lower physisorption activation barrier than less polar alcohols. The net effect is that the interaction between the catalyst surface polarisation and the molecular dipoles facilitates a greater surface absorption. Thence more of the reactant is available for photo-induced charge transfer between the catalyst and molecule.

The first investigations of photo-catalysis by polarised ferroelectrics can be traced back over three decades. The photocatalytic H_2O splitting by TiO_2 deposited on $LiNbO_3$ is reported in [81–83]. Other metal oxide compounds with the perovskite structure ($BaTiO_3$ [97,102–104], $BiFeO_3$ [98,105] and $LiNbO_3$ [99]) have all been shown to photocatalytically decompose the dye molecule Rhodamine B. Their strong polarisation and suitable band gaps (summarised in Table 1.1) are suited to such an application. The degradation of Rhodamine has typically been used as a benchmark for gauging the photocatalytic performance of photoferroelectrics. Whilst promising, these experiments do not provide any insight into the interface structuring between the photoferroelectric cat-

Material	P (C m^{-2})	Band Gap (eV)	Reference
$BaTiO_3$	0.26	3.2	[97]
$BiFeO_3$	1.00	2.6	[98, 105]
$LiNbO_3$	0.78	3.7	[99]

Table 1.1: The reported Polarisation (P) and band gaps of perovskite photoferroelectrics

alyst and reactant molecules, or into their energy alignments for charge transfer, which could also be making a significant contribution to the results obtained.

Investigation of the photocatalytic capabilities of the ferroelectric phase of $BaTiO_3$ has shown that the internal polarisation can be enhanced by annealing. This is a processes whereby the material is heated to allow thermal refinement of the microstructure. As outlined above, higher surface polarisation can lead to increased surface coverage (that is linked to improved photocatalytic performance), which results in greater photochemical degradation of the Rhodamine B molecules [102, 103]. In addition, the decolourising rate can also be improved by depositing metal clusters (e.g. Ag) onto the $BaTiO_3$ surface. In this case, as well as the polarisation enhanced e-h separation, Ag-clusters act as electron traps at the positively charged surface. The e-traps at the catalysts surface increase the availability of the electrons for the photodegredation reaction and therefore the probability of charge-transfer, taking into account the electric field and polarisation brought about by surface e accumulation, far outweighs the recombination [102, 103]. It is worthwhile noting that further investigation into the catalyst morphology has uncovered that zero dimensional nanostructuring, in the form of nanoparticles, to maximise the surface-to-volume ratios leads to a decrease in the surface polarisation and therefore an ensuing loss in the rate of photochemical reactions [103].

Of the perovskites studied, $BiFeO_3$ has the largest polarisation (1.00 C m^{-2} [98, 105]) and a band gap between 2.6 to 2.8 eV, which is ideal for visible light photo-catalysis [98]. However, its performance in the photocatalytic degradation of the rhodamine dye are less promising. The shortcomings are attributed to an energetic misalignment between the dye HOMO and LUMO and photo-catalysts VB and CB edges, inevitably influenced by the polarisation and interface nuclear-dynamics, leading to reduction of the charge-transfer kinetics (see Section 1.2.2.4) [98]. Because of the strong separation of the e-h pair, brought about by the large polarisation, this opens up the potential for secondary

side reactions, and severe degradation of the photo-catalyst is observed when holes (from the solvent) are injected into the CB. These results demonstrate the need for a material to have a balance between properties for viable photo-catalysis.

Finally, photochemical degradation of the Rhodamine B has also been studied using $LiNbO_3$ as the catalyst [99]. As shown in Table 1.1, $LiNbO_3$ absorbs in the UV part of the electromagnetic spectrum and has a lower (-0.22 C m^{-2}) polarisation than the $BiFeO_3$ photo-catalyst. The effect of doping the photo-catalyst has been investigated and is shown through a change to the dielectric screening, to alter the surface polarisation, dye-molecules surface coverage and the rate of decolourising [99]. In spite of p-type (Mg doped $LiNbO_3$) or n-type (Fe doped $LiNbO_3$) doping, no changes to the band gap or absorption properties of the photo-catalyst is reported, most likely due to the fact that these photocatalytic studies are carried out at super band gap wavelengths [99], that is at wavelengths with corresponding energies much larger than the band gap. The photocatalytic activity is enhanced for the n-type material and suppressed for the p-type material with respect to undoped $LiNbO_3$. This was shown not to be related to either the absorption behaviour of the dye in the differently polarising environments or charge carrier concentration. Instead [99] suggests that the change in photocatalytic rate is related to the interaction of charge carriers with the impurity sites influencing recombination. This is in agreement with observations made in studies of cation doping for band engineering, and reinforces the conclusion that for viable photo-catalysis, simply tuning the valence and conduction band edges to obtain enhance absorption properties can lead to faster e-h recombination and overall reduce the rate of photo-catalysis.

For prolonged electron-hole separation it is important that the polarisation is maintained under illumination. Photon absorption by a ferroelectric material can impact the spontaneous polarisation of photoferroelectrics by two mechanisms [85]. Firstly, altering the occupancy of the localised, ordered electronic states can reduce the overall polarisation of the material. Secondly, excitation of the system can induce a change in the ferroelectric phase transition temperature (T_c) with respect to the non-irradiated phase. For liquid crystal photoferroelectrics this has been shown to significantly alter [84–86] or destroy the polarisation altogether and should be taken into account when designing photoferroelectric catalysts [101].

1.3.3 One-dimensional semiconductors for photo-catalysis

The exceptionally large surface area to volume ratio of nanomaterials has led to the investigation of nano-engineered materials for photocatalytic application [33–35, 65–80]. The electronic properties of nanomaterials, that distinguish them from their bulk counterparts, depend on the size and morphology of the particles as well as on the surface and interface structuring with the medium. In addition to the high surface area to volume ratio, one dimensional nanomaterials such as nanotubes, nanowires and nanorods offer large aspect ratios, which in combination with anisotropies brought about by surface reconstructions that lead to internal polarisations and electric fields, could be advantageous for charge carrier separation. Photocatalytic activity has been reported for nanowires of several different compositions, in particular CdS, TiO_2, GaN and ZnO nanowires have all been investigated as photo-catalysts [65,66,70]. In the case of the GaN nanowires, improved photocatalytic performances are observed with respect to other nanostructured morphologies such as nanoparticles in suspension and thin films [66].

A series of publications have investigated photocatalytic H_2O splitting for H_2 production by 100 nm long, 4 nm wide Pt-decorated CdS nanorods [71, 75]. In these investigations, colloidal CdS nanorods are synthesised and sub-nanometer Pt clusters are deposited homogeneously onto the surface [71, 75]. Irradiation under UV-visible light creates e-h pairs in the CdS nanorods, the separation of the charge-carriers and the protection of the catalyst from anodic degradation is assisted by hole-scavengers contained in solution [71, 75]. These are chemicals deliberately added to the reaction mixture in order to react with the holes and reduce the rate of e-h recombination. The photogenerated electrons migrate to the Pt clusters, which act as an electron sink for the H_2 generation process:

$$2H_2O + 2e^- \longrightarrow H_2 + 2\,OH\cdot$$

The dual function of the solvated hole-scavenger molecules has been further investigated in [76]. On the one hand, the hole-scavenger protects the catalyst from degradation and ensures carrier separation. On the other, the use of hole-scavengers dramatically reduces the rate of electron migration to the Pt-clusters and the rate of H_2 production. This ultimately means that there is a trade-off between higher photocatalytic production in the short term (with degradation of the catalyst mediated by the holes) and a lower photocatalytic production (but no degradation of the catalyst). This can be offset somewhat via the choice of hole-scavenger. Scavenger molecules with more negative redox

potentials remove holes at a faster rate, this further reduces recombination kinetics and results in increased H_2 production [77].

The deposition of Pt-clusters on the nanowires likely contributes to the anisotropy of the electrostatic potential and formation of local polarisations that favour e-h separation. To investigate how the Pt-cluster coverage of the CdS surface is linked to photocatalytic activity three coverage regimes have been considered [78].

(i) **Low Coverage** (< 15 clusters per rod): H_2 production is low because the transfer of photo-generated electrons is out-competed by recombination processes.

(ii) **Medium Coverage** ($15 \rightarrow 30$ clusters per rod): H_2 production dramatically increases as coverage increases. There are more Pt sites for the photo-generated electrons to transfer to allowing for more photocatalytic H_2O splitting.

(iii) **High Coverage** (> 30 clusters per rod): H_2 production is saturated above this coverage because the increasing number of Pt sites compete for the electrons.

Within the high coverage regime, carefully controlling the size of the Pt clusters has also been shown to enhance the H_2 output by tweaking the energy of the unoccupied molecular orbitals with respect to the H_2O molecules [78]. Pt clusters with exactly 46 atoms have the highest H_2 quantum efficiencies [78, 79].

1.4 Imogolite nanotubes

The final Section of this Chapter introduces the family of materials that will become the focus for the remainder of this Thesis. This represents a first attempt to unify the different concepts outlined in Sections 1.3.1, 1.3.2 and 1.3.3 in an emerging class of cheap, easily synthesised and functionalized metal oxide nanotubes, namely Imogolite nanotubes (Imo NTs).

Imo is a naturally occurring open-ended aluminosilicate nanotube found in volcanic clay soils [116–118], the structure of which is shown in Figure 1.6. To understand its potential relevance to materials for photo-catalysis, the following Sections discuss its physical and electronic properties, the synthesis of functionalized derivatives and elements suggesting the occurrence of an integrated mechanism for effective e-h separation across the tube wall.

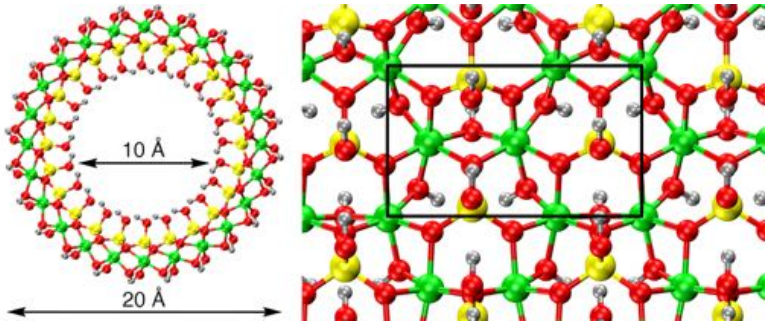

Figure 1.6: The structure and geometry of the pristine single walled, open-ended Imogolite nanotube (N = 24) as viewed along the nanotube axis (left) and from inside the cavity (right). The approximate inner and outer diameter, as experimentally obtained, and the hexagonal Gibbsite unit are marked. Al: Green, Si: Yellow, O: Red, H: Silver.

1.4.1 Structure and geometry of natural Imogolite

During the late 1960's and early 1970's the structure of Imo was the subject of considerable debate [119–123]. The earliest diffraction experiments accounted for the size of the NT repeat unit [119, 120], but it was not until the availability of electron micrographs that it was shown that Imo is formed from bundles of fine individual aluminosilicate nanotubes [121]. The first complete picture of the nanotube composition and geometry, taking into account the tubular structure, is provided in reference [122] and confirmed in [123], these works form the basis for the following discussion of the natural Imo NTs.

The Imo NTs have the empirical formula $(Al_2SiO_7H_4)_N$, where the subscript N is the number of radially nonequivalent aluminium atoms in the circumference [122] (this provides a measure of the number of repeated units within the nanotube unit cell). As displayed in Figure 1.6, Imo NTs are single walled structures; the outside layer of the nanotube wall is Gibbsite (aluminium hydroxide: $\gamma-AlOH_3$) with pendant silanol ($SiO_3(OH)$) moieties bonded on the inner surface. The curved nature of the NT arises from the relative difference between Si−O and Al−O bond strengths and lengths. The influence of the shorter Si−O bonds exclusively on one side induces a curvature in the Gibbsite layer enabling the formation of NTs [122, 123]. In terms of the local geometry, the Al atoms are octahedrally coordinated and joined to one another by oxygen bridges, with (acidic) Al−OH groups facing outwards from the surface. The Si atoms are tetrahedrally coordinated with Si−OH lining the cavity surface, which is shown in Figure 1.6.

Along the NT-axis (**c**), the Imogolites are distinguishable by six-membered Al-rings (Figure 1.6), this is similar to the arrangement of C atoms in carbon NTs (CNTs). The **c** axis repeat length is approximately 8.4 - 8.7 Å (marked by the black rectangle in Figure 1.6). Owing to the formation of H-bonds along the inner surface and in analogy with CNTs, the Imo NTs have a zig-zag (n,0) configuration. This is commensurate with the lattice parameters of the Gibbsite unit cells as noted in [119, 120, 122]. Reports indicate that the diameter of the nanotube pore is approximately 10 Å and the thickness of the tube wall is 5 Å, this corresponds to tubes with N in the interval 20 - 24 [122]. To date, to the best possible knowledge, no quantitative atomically resolved structural data exists to determine exactly the value of N for natural Imo.

1.4.2 Synthetic aluminosilicate nanotubes and their derivatives

1.4.2.1 The synthesis of aluminosilicate nanotubes

More recently, synthetic routes to Imo-like Aluminosilicate (AlSi) NTs have been uncovered [124–130]. Advantageously, these are fairly straight-forward one-pot syntheses, involving the mixture of tetraethoxysilane and aluminium *sec*-butoxide at low temperature and entirely within aqueous media. As outlined in [126, 128], the synthesis of AlSi NTs requires five steps:

(i) Vigorous mixing of reagents under aqueous conditions.

(ii) Stepwise addition of base (NaOH) to increase the pH.

(iii) Stepwise acidification (HCl) to gradually lower the pH.

(iv) Equilibration of the reaction mixture under ambient conditions.

(v) Final reaction under reflux to obtain nanotubes.

After this process, a highly mono-disperse NT powder can be obtained by drying the reaction mixture [126]. Analysis of the structure suggests that the composition of the synthetic AlSi and natural Imo NTs are equivalent. However, there is a discrepancy in the size of the two: high resolution transmission electron microscopy suggests that AlSi NTs have N = 24, whereas (in the absence of quantitative evidence) this is only an upper bound for Imo.

Controlling and fine-tuning the length and diameter of the NTs produced is a key component in diversifying any prospective applications. For instance, in the case of

photo-catalysis, the ability to synthesise NTs with predetermined pore sizes can restrict substrate access to the inner cavity thereby increasing reaction selectivity. Additionally, increasing the aspect ratio, by growing longer NTs could conceivably lead to superior *e*-*h* separation along the NT-axis. However, these avenues cannot be explored without a comprehensive understanding of the NT formation mechanism, which has been elucidated in [131]. Meticulous investigation by liquid- and solid-state ^{27}Al NMR and solid-state ^{29}Si NMR have shown that the AlSi NT self-assembly proceeds in several distinct steps, Figure 1.7 [131].

(i) The Al- and Si-containing reagents combine to form small, curved protonanotube precursors composed of $Al_{1-3}Si_x$ clusters.

(ii) The small curved clusters combine, and after passing through medium sized fragments under dynamic equilibrium, eventually form large curved protonanotube fragments with stoichiometries ranging $Al_{8-12}Si_x$.

(iii) External heating of the equilibrium mixture promotes the aggregation of the larger curved protonanotube fragments in the condensation processes.

(iv) Once aggregation begins, rearrangement of the individual clusters and the formation of chemical bonds between them yields the aluminosilicate nanotubes.

On the basis of the mechanism proposed it has been shown that the dimensions of the synthetic AlSi NTs are tunable; careful control over the synthesis enables the production of the NTs with specific N and therefore radii [130]. The control is achieved by integrating different anions during the reaction, which influence the shape and curvature of the protonanotube precursors through cooperative complexation. The difference in the precursor curvature is then manifested in the size of the AlSi NT synthesised. As mentioned above, the ability to specifically tune the size of the nanotube cavity offers the opportunity for size-specific substrate separation, and as shown later in this Thesis, can be used to control the cavity electrostatics for fixed compositions. Furthermore, it allows for the fine tuning of confinement effects, which have very recently been shown to drastically change the properties of solvents such as water [132].

The self-assembly of sterically controlled, highly mono-disperse nanotubes composed of cheap elements, under mild aqueous conditions makes AlSi NTs an attractive prospect, especially if their properties can be optimised for the points (i)-(vii) outlined in Section 1.2.1.

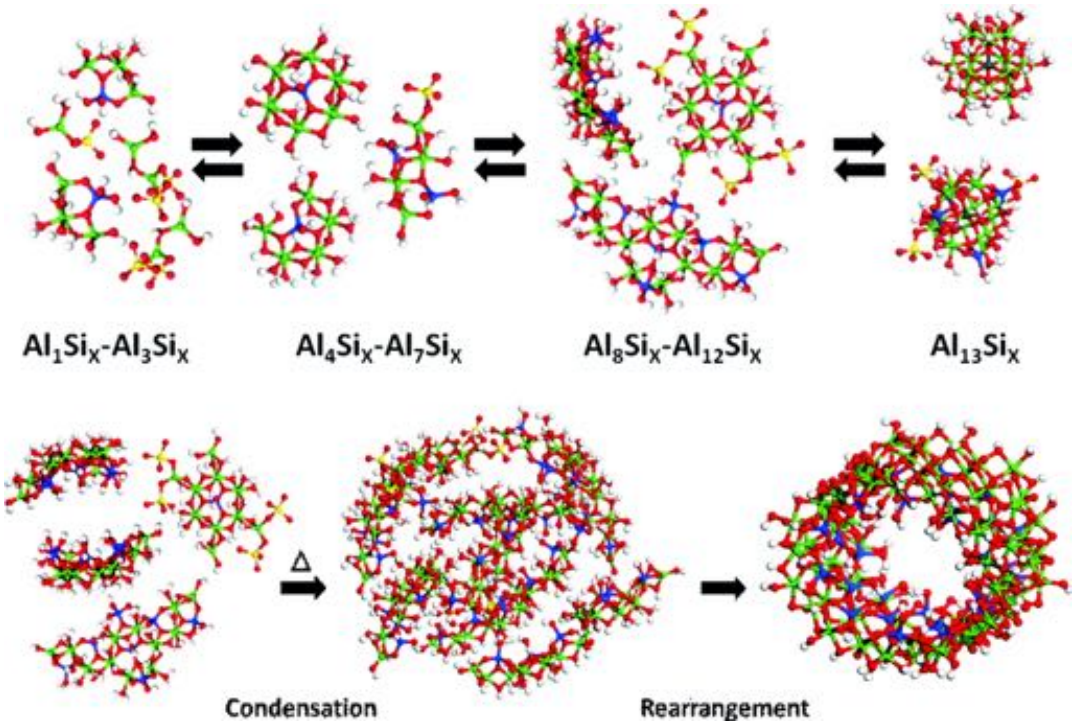

Figure 1.7: The self-assembly mechanism for the formation of AlSi NTs. Small curved protonanotube precursors form large NT fragments. The fragments aggregate and rearrange forming highly mono-disperse NTs. This Figure is reproduced from [131]

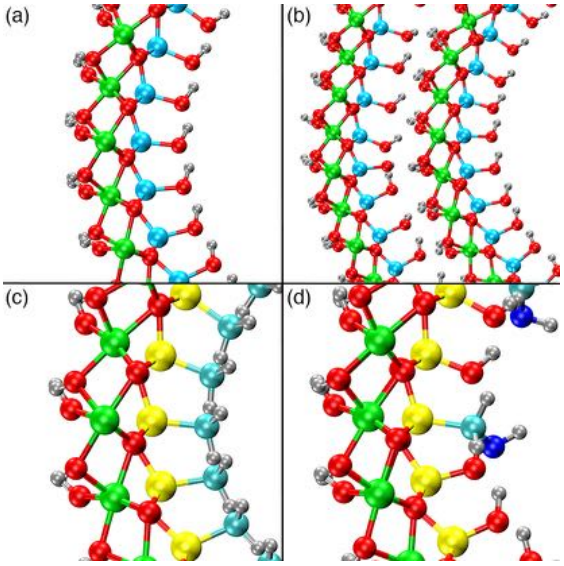

Figure 1.8: Close up view of the different composition Imo-type NTs that have been reported in the literature. (a) SW-AlGe NTs have substitution of Si atoms for Ge. (b) DW-AlGe NTs have one smaller NT encapsulated within another. (c) AlSi-Me NTs have complete inner surface methyl functionalization. (d) AlSi-Am NTs have partial substitution of inner hydroxyls by alkyl amine groups.

1.4.2.2 Imo-type nanotubes of different composition

Control over the experimental conditions is not the only approach available for the synthesis of Imo NTs with tuned dimensions. Compositional changes, such as atomic substitutions and in-situ functionalization, provide an avenue for obtaining differently sized NTs. Moreover, they also potentially lead to changes in the chemistry and physics of the inner and outer NT surfaces, their interaction with different solvents and molecules and the global electrostatic properties of the NTs.

By substituting the tetraethoxysilane, which is the source of Si for the reaction, for Ge containing reagents such as tetraethylorthogermanate, it is possible to synthesise single-walled aluminogermanate (SW-AlGe) NTs [126–128, 133–142]. These are analogous to the AlSi NTs and have the chemical formula $(Al_2GeO_7H_4)_N$, the only difference is the substitution of the inner surface silanol for germanol (GeOH) groups, as shown in Figure 1.8a. The larger Ge atoms and longer Ge−O bond lengths have a smaller disparity with the Al−O bonds, however the H-bonding network between adjacent Ge-OH groups along the inner NT surface is unaffected. Consequently, SW-AlGe NTs have a

larger inner NT radii, which is roughly 13 Å (AlSi NTs: 10 Å) corresponding to N = 18 units in the circumference of the tube [137]. Further refinement of the NT dimensions by compositional substitutions has been achieved by modulating the ratio of Si/Ge in the reaction mixture. Leveraging the different curvatures induced in the AlOH layer brought about by the shorter (longer) Si−O (Ge−O) bonds, it is possible to engineer hybrid aluminosilicate-germanate AlSi/Ge NTs with compositions $(AlSi_xGe_{1-x}O_7H_4)_N$ [142]. It has been shown that subtle changes to the Si:Ge ratio allow control of the radius and length of the NTs.

A route towards controlled formation of double walled aluminogermanate (DW-AlGe) NTs has also been realised [135, 137, 138]. SW- and DW-AlGe NTs can be selectively synthesised by varying only the initial concentrations of the reagents. The DW-AlGe NTs have one small AlGe NT encapsulated within a non-covalently bonded larger one. They are joined by H-bonding interactions between the hydroxyl groups on the inner surface of the outer tube and outer surface of the inner tube as displayed in Figure 1.8b. The synthesis and production of high quality SW- and DW-AlGe NTs has been exhaustively investigated [135–140, 143]. However, there has not yet been any experimental investigation into the mechanical, chemical or electronic properties of the AlGe NTs that would impact on their potential use as novel photo-catalysts.

The synthesis of differently modified AlSi NTs is perceived by the experimental community as a way to enhance the absorption selectivity of the tubes towards specific molecules [144–147]. This would improve the outlook of Imo-type NTs for applications involving gas sensing and chemical separation. Reports of partial and complete substitution of the inner surface hydroxyls by organic functional groups are beginning to emerge [144–151].

An interesting example of this are the selectively inner surface methylated aluminosilicate (AlSi-Me) NTs, see Figure 1.8c and [145, 146, 148–151]. Successful incorporation of $SiCH_3$ was first reported in [145]. A loss of the inner surface H-bonding network, in combination with the repulsive effects of the sterically larger groups results in AlSi-Me NTs that have larger NT diameters than AlSi NTs (10 Å). On the basis of N_2-absorption isotherms, the AlSi-Me NT inner diameters fall within the range of 15 to 25 Å. AlSi-Me NTs have an intrinsically hydrophobic surface inside the NT cavity and hydrophilic outers surfaces and interstitial cavities. The occurrence of a hydrophobic cavity in an otherwise hydrophilic NT has already been linked to superior chemical separation

performances [145, 146], which provides a starting point for their possible integration of chemical separation and photocatalytic strategies in one material. This Thesis will explore the changes in NT diameter as well as the ensuing changes to the electronic properties of the AlSi-Me NTs and their behaviour towards polar solvent molecules.

The partial substitution of the SiOH groups on the inside surface for $SiCH_3NH_2$ groups has been described in reference [147]. These partially aminated Imo NTs (AlSi-Am), which are shown in Figure 1.8d, have a 16% substitution ratio, with the functional groups distributed randomly throughout the NT. The partial substitution raises questions over the extent of the H-bonding along the NT inner surface. It will be reported elsewhere [152] that the amine lone pairs are able to contribute to the H-bonding network, however, the introduction of non H-bond compatible functional groups at low concentrations may present a strategy for the destabilisation of inner surface hydroxyls and therefore VB edge tuning. Incidentally, AlSi-AM NTs favour CO_2 absorption over CH_4 and N_2 [147]. This could be due to the potential for nucleophillic addition by the NH_2 lone pair into the CO_2 molecule [147].

Finally, Fe atoms can be incorporated into the aluminosilicate (germanate) framework [141,153–157]. Adding $FeCl_3$ to the reaction mixture makes it possible to synthesise Fe-doped AlSi and AlGe NTs with the structure $Al_{2-x}Fe_xSi(Ge)O_4H_7$ [141,153,158]. Although no other substituents have been reported, these syntheses open up for an array of transition metal doped Imo NTs, which could be considered for the band tuning of the material. It is thought that the Fe ions enter into the Imo framework as point defect substitutions for Al ions, however questions have been raised over the possible formation of Fe^{3+} species or clusters adsorbing onto the NT surfaces [153, 155]; it has been found that for dopant concentrations greater than $x = 0.025$ the formation of Fe-doped NTs is accompanied by Fe_2O_3 clusters as a side product [155].

Structurally, the Fe-containing NTs are equivalent to the pristine AlSi and AlGe NTs, with the same reported high monodispersity and pore sizes [141, 153–155, 158]. Experiments suggest that the Fe-AlSi NT has a significantly lower band gap (1.9-2.8 eV) than any other Imogolite NT [153, 155, 158], the absorption of visible light suggest that Fe-AlSi NTs could be more suited to photocatalytic applications provided that the Fe atoms do not act as *e*-*h* recombination centres. The emergence of paramagnetism in the Fe-AlSi NTs is also reported in [155] with the indirect, i.e. not directly validated by techniques such as magnetic atomic force microscopy, suggestion that high spin Fe^{3+}

ions are incorporated into the aluminosilicate framework.

1.4.3 Theoretical insight into Imogolite nanotubes

1.4.3.1 Simulation of AlSi NTs

In the previous Section, it was shown that the experimental Imo community has been able to uncover synthetic routes to AlSi [124] and AlGe NTs [133,134,140], identify their formation mechanism [126, 128, 131, 136, 138, 139] and thence synthesise NTs of specific controlled dimensions [130], outline effective strategies to doped and functionalized AlSi and AlGe NTs [144, 145, 147, 155, 158, 159] and begun to explore a wide range of applications [142, 145–147, 160–165]. Investigation of Imo NTs by computational approaches has been much less prominent. This is a consequence of the difficulty associated with electronic structure calculations of systems with large numbers of atoms. This has led to an over-reliance on the transferability of parametrised Density Functional Tight Binding (DFTB) for similar (non-curved) materials [166]. To date, theory-based contributions have been used to contribute to the debate over the number of radial units, N, contained in the NT circumference, investigate the electronic properties of idealised models of the pristine AlSi NTs and the inclusion of point defects and single atom substitutions, these will be discussed in this Section.

Atomistic simulations can be (and have been in this Thesis) applied to assess the energetic dependence of the NT radii and identify the minimum energy N. The details of the atomic structure of pristine defect-free AlSi NTs have been studied by different computational approaches in several publications [166–168, 170, 172, 176]. Both DFTB and DFT approaches agree that zig-zag (n,0) Imo NTs are energetically favoured in comparison to armchair (n,n) NTs [166, 172, 176]. The relative stability of the zig-zag conformation is confirmed to be linked to the maximisation of the NTs H-bonding network on the inner surface [176].

Each of the different approaches are however, at odds with each other in the derived N. The results of the different methods are summarised in Table 1.2, DFTB methods present single energetic minimum for Imo NTs with N = 22 and 24 [166, 167], which is similar to the global energy minimum obtained via generalised gradient approximated Density Functional Theory (GGA-DFT) investigation where N = 24 [170]. The GGA-DFT simulations also reveal a second local energy minimum for N = 18. The emergence of the local minima may explain the size difference associated with the natural and

Imo NT	Method	N	Band Gap (eV)	Reference
AlSi	Experiment	-	3.6	[128]
	Experiment	-	4.9	[155]
	NVT-MD	24	-	[127]
	SCC-DFTB	24	9.86	[166]
	SCC-DFTB	22	10.8	[167]
	DFT-PBE	20†	4.8	[168]
	DFT-PBE	24†	3.7	[169]
	DFT-PBE	24	5.3	[170]
	DFT-PW91	24†	4.1	[171]
	DFT-B3LYP	20	7.2	[172]
	LS-DFT-PBE	24†	4.4	[173] & This work
SW-AlGe	SCC-DFTB	28	9.5	[167]
	DFT-PW91	36†	3.9	[171]
	LS-DFT-PBE	36†	4.4	[173] & This work
DW-AlGe	SCC-DFTB	24,42	8.5	[167]
	LS-DFT-PBE	36,54†	2.8	[173] & This work
Fe-AlSi	Experiment	-	2.8	[155]
	DFT-PW91	20	2.6	[174]
	LS-DFT-PBE+U	24†	2.3	This work
AlSi-Me	LS-DFT-PBE	32*	4.7	[175] & This work
AlSi-Am	LS-DFT-D2	24†	4.2	[152]

Table 1.2: Table summarising the results of theoretical investigations for the different AlSi NTs. The values of N marked with † refer to simulations where the size of the Imo NT has not been energetically derived. *In this case, AlSi-Me NTs have been screened with several different exchange-correlation functionals, for those results see [175] and Chapter 4

synthetic Imo NTs and suggests slightly different formation conditions for the natural Imo. At other levels of theory, namely Hybrid-DFT, it is suggested that aluminosilicate nanotubes instead have an energy minimum for N = 20 [172], however the validity of such an approach is also questionable given the arbitrary mixing of exact Hartree-Fock exchange into the DFT functional. A strain energy minimum, calculated on the basis of DFT, is instead reported in reference [176] for N = 16. It should be noted that the results presented all derive from simulations that neglect the role of the solvent, both inside and outside the NT cavity, in stabilising the differently sized NTs.

AlSi NTs are wide gap insulators; inspection of the relevant literature, which is presented in Table 1.2, suggests that the band gap of AlSi NTs is larger than the visible range of the electromagnetic spectrum [128,155,166–173]. The reported band gaps vary significantly depending on the simulation method employed: PBE-DFT simulations yield (expectedly underestimated) energy gaps in the range 3.7 $\rightarrow$ 5.3 eV [168–170], furthermore PW91-DFT calculation (also expectedly underestimated) of the band gap gives 4.1 eV [171]. These values are larger than the experimental band gap obtained (3.6 eV) in reference [128] for an unpurified synthetic solution that may contain unreacted precursor or amorphous materials, but are in general agreement with the value found from UV-Vis spectra (4.9 eV) in [155]. The slight underestimation of DFT results (see Table 1.2) with respect to [155] is expected, whilst Hybrid-DFT (B3LYP) and DFTB approaches grossly overestimate the value of the energy gap.

DFT investigations have uncovered a peculiar separation of the NT band edges in real space [170,171]. The high energy edge of the NT valence band is located at the inner surface and throughout the NT wall, whilst the low energy edge of the conduction band faces outwards from the NT [170,171]. This is coupled with a permanent electrostatic polarisation of the nanotube walls, with a positively charged outer and negatively charged inner surface [166,171,177], resulting in the formation of a surface dipole density across the nanotube wall. This suggests that AlSi NTs, whilst overall dipole free and charge neutral, have local inner-outer polarisations that, subject to screening by different media, may be used to influence the electronic states of nearby molecules.

1.4.3.2 Computational modelling beyond pristine AlSi NTs

With regards to publications involving non-idealised (single unit, vacuum exposed) isolated pristine aluminosilicate nanotubes, there have been very few computational inves-

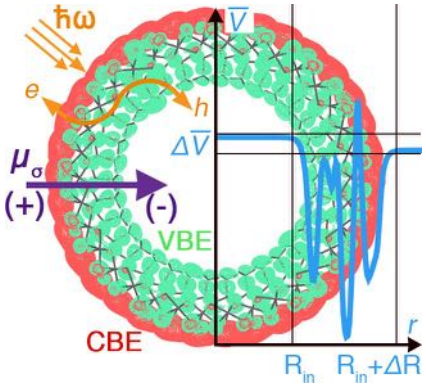

Figure 1.9: Real space plot of the band-decomposed charge density distributions for the Imogolite NTs. The top edge of the VB and bottom edge of the CB are shown in green and red respectively. In blue the average electrostatic potential ($\bar{V}$) across the NT is plotted indicating the formation of a surface dipole density (μ_σ) and polarisation of the NT surfaces. The photo-generated *e*-*h* separation mechanism on different sides of the NT wall is highlighted in yellow.

tigations. A combination of the size and complexity of the systems as well as the lack of atomically resolved experimental data makes theoretical study of the materials and attempts to uncover the structural and electronic properties of other NTs within the Imo family challenging. The key results, along with those that will be discussed in detail throughout this Thesis, have been collected in Table 1.2.

AlGe NTs have received some attention from the computational Imo community. DFTB methods have recently been applied to SW- and DW structures, the SW-AlGe NTs have a global energy minimum [167] for N = 28. Therefore the modified NTs are larger in diameter than the pristine AlSi NTs which is in qualitative agreement with chemical intuition and experimental results. Given the massive disparities between experimental results for both AlSi and AlGe NTs, and the limitations associated with the computational approaches, it is difficult to draw any further conclusions, apart from the urgent need for quantitative X-ray characterisation of these materials. Similarly, results indicate that DW-AlGe NTs have an inner (outer) NT with N = 24(42), that should give a diameter more similar to the AlSi NTs, which is in line with experimental evidence [135, 137, 139].

There is no UV-Vis data available for comparison with the calculated band gaps of SW- and DW-AlGe NTs. Therefore, resting on their application to the AlSi NTs, energy

gaps obtained via DFT (DFTB) represent a lower (upper) boundary to the system band gap. DFT predicts predicts the AlGe (N = 36) NT band gap is 3.9 eV [171], whereas DFTB 9.5 eV [167]. In both cases, this is a narrowing of the band gap (with respect to AlSi). Interestingly, in both works the extent to which the change in the band gap is related to differences in the NT composition and curvature of the tube wall is unexplored. Simulations of DW-AlGe NT (DFTB) suggest that band gap is smaller still (8.5 eV) [167]. As highlighted in Table 1.2, this is also true for those results that will be discussed later in the Thesis. Consistent with results for the AlSi NTs, SW-AlGe NTs exhibit the same real-space localisation of the valence and conduction band edges and polarisation of the nanotube walls [171]. The computed magnitude of the surface dipole density is double that of the AlSi NT for the larger (less curved) but compositionally different SW-AlGe NTs, which calls into question the role of NT composition and NT curvature in the formation of locally polarised NTs. However, as shown in Chapter 4, the formulation of the NT-wall dipole in reference [171] is incorrect and fails to take into consideration any of the geometric factors uncovered in the detailed derivation contained in reference [175]. Therefore, as reported in Chapter 5 and [173] the AlSi and AlGe NTs polarisation is roughly equal to the AlSi NTs.

As seen in Table 1.2, besides the work documented in this Thesis, computational investigation of non-ideal nanotubes are almost non-existent. Barring two publications [171,174], no studies of defect structures or the impact of chemical functionalization or doping have been carried out. In [171] the role of hydroxyl vacancies on both inner and outer surfaces were evaluated. These vacancies are computed to reduce the band gaps of aluminosilicate (1.8 eV) and aluminogermanate (1.1 eV) nanotubes by introducing defect states within the energy gap.

Fe-doped Imo (AlSi and AlGe) NTs have been investigated via theoretical simulations in reference [174]. The effects of the Fe ions inside the NT (as Fe/Al substitutions) and at the surfaces (as solvated ions inside and outside the cavity) are considered for AlSi and AlGe NTs with $N = 20$ by DFT. In qualitative agreement with the reduction of the band gap in experimental reports [153, 155, 158], the DFT band gap for Fe-AlSi NT is computed in the range 1.5 - 2 eV. In this case, the band gap is underestimated, most likely as a result of the adopted DFT exchange-correlation functionals (see Chapter 2). A reduction of the band gap of the Fe-AlGe NTs is also observed, with energy gaps in the range 0.9 - 2.6 eV.

1.4.4 Novel routes to photo-catalysis by aluminosilicate nanotubes

On the basis of all of the evidence presented so far, Imogolite nanotubes offer a set of properties that couple the potential for nanoporous confinement, permanent surface polarisation and one dimensional nanostructuring. This, in addition to the highly tunable nature of the nanotubes through compositional exchange, functionalization and doping marks Imogolite-type nanotubes as potential candidate materials for (co-)photocatalytic applications. This Section proposes a conceivable photocatalytic mechanism that leverages these properties; but also assumes that the factors governing charge transfer kinetics, solvent-catalyst interface structuring and finite sizes effects are favourable for reaction, aspects which will be left for future research.

A photo-induced excitation leads to the formation of an electron and hole pair on opposite sides of the nanotube wall: the electron residing at the valence band edge inside the NT cavity is transferred via direct charge transfer or through migration following electronic decay pathways to the conduction band edge outside the NT wall leaving a hole. Resting on the evidence and arguments presented in Section 1.3.2, the polarisation of the nanotube wall may enhance electron hole separation, see Figure 1.9. Furthermore, the direction of the polarisation in direct opposition of the real space electron and hole recombination path could further increase the effective separation of photo-generated charge carriers. Once the photo-excited electron occupies a state close to the conduction band edge, given the ground-state real-space locations of the band edges, the electron and hole will be available at the wall surface for redox chemistry. With the electron-hole pair at the surface: selective oxidation of reactants outside the nanotube cavity and selective reduction of species inside the nanotube cavity resulting in catalyst regeneration.

Rather than enter into debate about the precise dimensions of the natural and synthetic Imo NTs this work is concerned with the properties that may give rise to such a catalytic mechanism. Namely the impact of changes to the nanotube size, composition and functionality on the polarisation, the real space separation of the valence and conduction band edges, the alignment of band edges with respect to HOMO and LUMO states in technologically relevant molecules and the effects of the nanotube ends.

Chapter 2

Computational Methods

Abstract

This Chapter serves as an introduction to Linear-scaling Density Functional Theory (LS-DFT) [178], and specifically to its implementation within the ONETEP software package [179]. It builds up to the derivation of a linear-scaling theory by first recounting the relevant Many-Body Quantum Theory and Kohn-Sham Density Functional Theory [180, 181]. The Chapter begins with introductory remarks on the use of the Born-Oppenheimer adiabatic approximation. In the description of DFT there is a discussion of the Hohnberg-Kohn theorems, Kohn-Sham equations and the development of approximated, yet viable, exchange-correlation functionals. As well as providing a theoretical foundation, the Chapter also outlines some of the practical aspects that underpin DFT simulations. Specifically, the minimisation of functions for geometry optimisation with the quasi-Newton algorithm, performing simulations under periodic boundary conditions, and with the pseudopotential approximation. The final section of this Chapter explains the evolution of Kohn-Sham (KS) DFT to the LS-DFT implemented within the ONETEP code. A derivation of the linear-scaling theory on the basis of the single particle density matrix, localised basis functions and subspace partitioned Fast Fourier Transforms (FFTs) are recounted. Finally, some of the more specialist aspects related to LS-DFT are introduced such as the calculations of Pulay forces, the optimisation of empty KS states and the ONETEP specific Hybrid MPI-OpenMP parallelisation scheme. Each of these aspects plays a role in the work presented in later Chapters.

2.1 Basic many-body quantum theory

In this work investigations are focused on quantum mechanical systems that have N_e electrons and N_n nuclei. Their respective coordinates are expressed as the set of Cartesian vectors $\{\mathbf{r}_i\}$, and $\{\mathbf{R}_I\}$. In Hartree atomic units ($m_e = e = \hbar = \frac{1}{4\pi\epsilon_0} = 1$), these systems can be described by a Hamiltonian operator of the form

$$\hat{H} = -\frac{1}{2}\left[\sum_{i}^{N_e}\nabla^2_{\mathbf{r}_i} + \sum_{I}^{N_n}\frac{1}{M_I}\nabla^2_{\mathbf{R}_I}\right] + \sum_{i}^{N}\sum_{j>i}^{N}\frac{1}{|\mathbf{r}_i - \mathbf{r}_j|} - \sum_{i}^{N_e}\sum_{I}^{N_n}\frac{Z_I}{|\mathbf{r}_i - \mathbf{R}_I|} + \sum_{I}^{N_n}\sum_{J>I}^{N_n}\frac{Z_I Z_J}{|\mathbf{R}_I - \mathbf{R}_J|}, \tag{2.1}$$

where M_I are nuclear masses and Z_I are nuclear electronic numbers. In (2.1) $\hat{H}$ is a non-relativistic time-independent Hamiltonian that is composed of the kinetic energies of the electrons and nuclei and the electron-electron, electron-nucleus and nucleus-nucleus Coulomb interaction energies.

The wave function, $\Psi(\{\mathbf{r}_i\}, \{\mathbf{R}_I\}, t)$, which completely describes the quantum nature of the system, is an eigenfunction of the time-independent Hamiltonian operator. Given the $\Psi(\{\mathbf{r}_i\}, \{\mathbf{R}_I\}, t)$, it is possible to write the time-dependent Schrödinger equation [182]

$$\hat{H}\Psi(\{\mathbf{r}_i\}, \{\mathbf{R}_I\}, t) = i\frac{\partial}{\partial t}\Psi(\{\mathbf{r}_i\}, \{\mathbf{R}_I\}, t). \tag{2.2}$$

So long as $\hat{H}$ is time-independent, i.e. where the Hamiltonian operator defined in Equation (2.1) contains no time-dependent potential $\hat{V}(t)$, then $\Psi(\{\mathbf{r}_i\}, \{\mathbf{R}_I\}, t)$ may be expressed as a product of the time-independent many-body wave function, that is a function of the electronic and nuclear coordinates, and a time dependent function. This is known as the separation of the space $(\{\mathbf{r}_i\}, \{\mathbf{R}_I\})$ and time (t) variables

$$\Psi(\{\mathbf{r}_i\}, \{\mathbf{R}_I\}, t) = \Phi(\{\mathbf{r}_i\}, \{\mathbf{R}_I\})\Omega(t). \tag{2.3}$$

On this basis, the time-independent Schrödinger equation that makes it possible to calculate the eigenvalues of the Hamiltonian, ε is

$$\hat{H}\Phi(\{\mathbf{r}_i\}, \{\mathbf{R}_I\}) = \varepsilon\Phi(\{\mathbf{r}_i\}, \{\mathbf{R}_I\}). \tag{2.4}$$

Moreover, the time evolution of each ε for a given phase factor, θ, is described by

$$i\frac{\partial}{\partial t}\Omega(t) = \varepsilon\Omega(t), \tag{2.5}$$

where $\Omega(t) = e^{i(\theta-\varepsilon t)}$.

Provided that the electronic ($\{\mathbf{r}_i\}$) and nuclear ($\{\mathbf{R}_I\}$) components are decoupled, the time-independent many-body wave function, $\Phi(\{\mathbf{r}_i\},\{\mathbf{R}_I\})$, may be expressed as a product of the electronic, $\psi(\{\mathbf{r}_i\};\{\mathbf{R}_I\})$, and nuclear $\eta(\{\mathbf{R}_I\})$, wave functions

$$\Phi(\{\mathbf{r}_i\},\{\mathbf{R}_I\}) = \psi(\{\mathbf{r}_i\};\{\mathbf{R}_I\})\eta(\{\mathbf{R}_I\}). \tag{2.6}$$

2.1.1 The Born-Oppenheimer approximation

The electronic wave function depends parametrically on the positions of the nuclei [183]. Typically, the masses of the nuclei are orders of magnitude larger than the masses of the electrons. Thence, the ensuing velocities of the electrons are orders of magnitude larger than those of the nuclei. Comparing the two wave functions, it is anticipated that the electronic response is instantaneous on the time scale of the nuclei; for any given arrangement of the atoms, the electronic wave function can be expected to rapidly relax to its ground state. This is the essence of the Born-Oppenheimer adiabatic approximation [184], which formally separates the electronic and nuclear degrees of freedom according to Equation (2.6). Accordingly, the Hamiltonian can be expressed as a sum of the electronic and nuclear parts: $\hat{H} = \hat{H}_{el} + \hat{H}_{nu}$. Within this approximation, the electrons, described by the electronic wave function, experience a static potential generated by the frozen nuclei. The electronic time-independent Schrödinger equation is

$$\hat{H}_{el}\psi(\{\mathbf{r}\};\{\mathbf{R}\}) = E(\{\mathbf{R}_I\})\psi(\{\mathbf{r}\};\{\mathbf{R}\}), \tag{2.7}$$

where

$$\begin{aligned}\hat{H}_{el} &= -\frac{1}{2}\sum_{i}^{N_e}\nabla^2_{\mathbf{r}_i} + \sum_{i}^{N_e}\sum_{j>i}^{N_e}\frac{1}{|\mathbf{r}_i-\mathbf{r}_j|} \\ &- \sum_{i}^{N_e}\sum_{I}^{N_n}\frac{Z_I}{|\mathbf{r}_i-\mathbf{R}_I|} + \sum_{I}^{N_n}\sum_{J>I}^{N_n}\frac{Z_I Z_J}{|\mathbf{R}_I-\mathbf{R}_J|},\end{aligned} \tag{2.8}$$

and $E(\mathbf{R}_I)$ are the total electronic energy eigenvalues for the nuclear configuration $\mathbf{R}_I$. For treatment of the nuclei, the full Hamiltonian of Equation (2.1) is applied to the

separable wave function of Equation (2.6). Noting the result of Equation (2.7), it can be found that:

$$\hat{H}\Phi(\{\mathbf{r}_i\},\{\mathbf{R}_I\}) = \left[-\frac{1}{2}\sum_I^{N_n}\frac{1}{M_I}\nabla^2_{\mathbf{R}_I} + E(\{\mathbf{R}_I\})\right]\Phi(\{\mathbf{r}_i\},\{\mathbf{R}_I\}) \quad (2.9)$$

$$= \psi(\{\mathbf{r}_i\};\{\mathbf{R}_I\})\left[-\frac{1}{2}\sum_I^{N_n}\frac{1}{M_I}\nabla^2_{\mathbf{R}_I} + E(\{\mathbf{R}_I\})\right]\eta(\{\mathbf{R_I}\})$$

$$-\frac{1}{2}\sum_I^{N_n}\frac{1}{M_I}\left[2\nabla_{\mathbf{R}_I}\psi(\{\mathbf{r}_i\};\{\mathbf{R}_I\})\cdot\nabla_{\mathbf{R}_I}\eta(\{\mathbf{R}_I\}) + \nabla^2_{\mathbf{R}_I}\psi(\{\mathbf{r}_i\};\{\mathbf{R}_I\})\cdot\eta(\{\mathbf{R}_I\})\right]. \quad (2.10)$$

It is note worthy that $E(\{\mathbf{R}_I\})$ is the *adiabatic* potential energy surface, providing the energy contributions from the electrons. The remaining N_n terms

$$-\frac{1}{2M_I}\left[2\nabla_{\mathbf{R}_I}\psi(\{\mathbf{r}_i\};\{\mathbf{R}_I\})\cdot\nabla_{\mathbf{R}_I}\eta(\{\mathbf{R}_I\}) + \nabla^2_{\mathbf{R}_I}\psi(\{\mathbf{r}_i\};\{\mathbf{R}_I\})\cdot\eta(\{\mathbf{R}_I\})\right],$$

are the non-adiabatic contributions to the energy, otherwise known as vibronic coupling terms. These vibronic coupling terms generally provide only very minor contributions to the energy of the system close to its electronic ground state, therefore within the Born-Oppenheimer approximation they are neglected, allowing one to write the nuclear Schrödinger equation

$$\left[-\frac{1}{2}\sum_I^{N_n}\frac{1}{M_I}\nabla^2_{\mathbf{R}_I} + E(\mathbf{R}_I)\right]\eta(\mathbf{R}_I) = \epsilon\eta(\mathbf{R}_I). \quad (2.11)$$

The benefits of the Born-Oppenheimer approximation are clear, it provides a method for separating and treating the electronic and nuclear components of the many-body wave function individually. This Thesis is primarily concerned with solving the electronic Schrödinger equation (Equation (2.7)) for materials of interest. However, being concerned with the development of new photo-catalysts one should also be aware that, due to the inherent neglect of the vibronic coupling terms, the Born-Oppenheimer approximation is inadequate for the description of charge-transfer processes. In Chapter 1, it was highlighted that predictions of the rate of photo-catalysis are intimately linked to (and therefore should take into consideration) the surface-reactant charge-transfer processes that involve transfer between different potential energy surfaces. However, as a first investigation of novel materials for photo-catalysts, using the Born-Oppenheimer approximation to simulate the alignment between the energies of donor, E_d, and accep-

tor, E_a, states $[\delta(E_a - E_d)]$ is a meaningful endeavour.

2.1.2 The electronic density

In the previous Section, the formulation of time-independent Schrödinger equation has been discussed to highlight that it is possible compute properties of quantum-mechanical systems using various operators. So far, the fact that the electronic, nuclear and vibronic wave functions span many variables has only been alluded to. In a position-space representation (neglecting any spin contributions) the many-body electronic wave function $\psi(\{\mathbf{r}_i\};\{\mathbf{R}_I\})$ is a function of $3N$ coordinates, where N is the number of electrons. Expanding $\psi(\{\mathbf{r}_i\};\{\mathbf{R}_I\})$ onto a grid, as is common practice, causes the volume of discretised information pertaining to $\psi(\{\mathbf{r}_i\};\{\mathbf{R}_I\})$ to scale as $\mathcal{O}(M^{3N})$, where M is the number of grid points, and, due to memory constraints, this is prohibitive for systems larger than just a few simple atoms.

This limitation can be overcome by defining the electronic density, $n(\mathbf{r})$, which is the measure of the probability of an electronic charge occupying a point in space, as

$$n(\mathbf{r}) = N_e \int \mathrm{d}\mathbf{r}_2 \ldots \int \mathrm{d}\mathbf{r}_N |\psi(\{\mathbf{r}_i\};\{\mathbf{R}_I\})|^2, \tag{2.12}$$

which, for a normalised wave function ($\langle\psi|\psi\rangle = 1$) in braket notation reads

$$n(\mathbf{r}) = \langle\psi|\hat{n}|\psi\rangle\,. \tag{2.13}$$

Here $\hat{n} = \sum_i \delta(\mathbf{r} - \mathbf{r}_i)$ is the density operator, which contains a Dirac delta function for every position in space. From this description, it can be seen that the electron density is a function of only three variables (the three Cartesian components of $\mathbf{r}$), thereby reducing the complexity of the many-body electronic wave function. This is advantageous for computation as the memory demands associated with storing $n(\mathbf{r})$ scales $\mathcal{O}(M^3)$. For the study of the properties of more realistic materials, the electron density is much more numerically and computationally tractable than the electronic wave function. The following section describes how to utilise this quantity with Density Functional Theory.

2.2 Density Functional Theory

2.2.1 The Hohenberg-Kohn theorems

Following from the discussion of the Born-Oppenheimer approximation in Section 2.1.1, it is known that the Coulomb potential arising from interactions with the nuclei are treated by a fixed external potential

$$V_{\text{ext}}(\mathbf{r}_i) = -\sum_{I}^{N_n} \frac{Z_I}{|\mathbf{r}_i - \mathbf{R}_I|}. \tag{2.14}$$

The other components of the electronic Hamiltonian, which are universally held for all N-electron systems, can be grouped together such that $\hat{H}_{el} = \hat{F} + \hat{V}_{\text{ext}}$, where

$$\hat{F} = -\frac{1}{2}\sum_{i}^{N_e} \nabla^2_{\mathbf{r}_i} + \sum_{i}^{N_e}\sum_{j>i}^{N_e} \frac{1}{|\mathbf{r}_i - \mathbf{r}_j|}. \tag{2.15}$$

The energy of the electronic state, denoted $|\psi\rangle$, is the expectation value

$$\begin{aligned} E &= \langle\psi|\hat{H}|\psi\rangle \\ &= \langle\psi|\hat{F}|\psi\rangle + \int \mathrm{d}\mathbf{r}\ V_{\text{ext}}(\mathbf{r})n(\mathbf{r}). \end{aligned} \tag{2.16}$$

Reference [185] highlights several important features of the electronic charge density in what are collectively referred to as the Hohenberg-Kohn (HK) theorems.

The first of the HK theorems states that there is a one-to-one relationship between the external potential and the electron density. Specifically, what is meant by this is that for each $V_{\text{ext}}(\mathbf{r})$, $n(\mathbf{r})$ is uniquely defined and vice versa. Of particular importance, $n(\mathbf{r})$ defines both the Hamiltonian and number of electrons. Furthermore, this means that $n(\mathbf{r})$ also defines the electronic many-body wave function and observables calculable from it. The total energy can therefore be written as a functional of the density

$$E[n] = \langle\psi[n]|\hat{H}|\psi[n]\rangle\,. \tag{2.17}$$

The second HK theorem postulates that the electronic density responsible for minimising $E[n]$ is in fact the ground state electronic density. Thus, the problem of solving the electronic Schrödinger equation can be reformulated into a variational search over all possible densities in the minimisation of $E[n]$.

2.2.1.1 Proof of the first theorem

Suppose that there exist two different external potentials, $V_{\text{ext}}(\mathbf{r})$ and $\tilde{V}_{\text{ext}}(\mathbf{r})$, which give rise to identical ground-state electronic densities $n_0(\mathbf{r}) = \tilde{n}_0(\mathbf{r})$. Then the Hamiltonian operators and electronic wave functions would obey

$$\begin{aligned} E_0 < \langle\tilde{\psi}|\hat{H}|\tilde{\psi}\rangle &= \langle\tilde{\psi}|\hat{H} - \hat{\tilde{H}}|\tilde{\psi}\rangle + \langle\tilde{\psi}|\hat{\tilde{H}}|\tilde{\psi}\rangle \\ &= \tilde{E}_0 + \int \mathrm{d}\mathbf{r}\left[V_{\text{ext}}(\mathbf{r}) - \tilde{V}_{\text{ext}}(\mathbf{r})\right] n(\mathbf{r}) \qquad (2.18a) \\ \tilde{E}_0 < \langle\psi|\hat{\tilde{H}}|\psi\rangle &= \langle\psi|\hat{\tilde{H}} - \hat{H}|\psi\rangle + \langle\psi|\hat{H}|\psi\rangle \\ &= E_0 + \int \mathrm{d}\mathbf{r}\left[\tilde{V}_{\text{ext}}(\mathbf{r}) - V_{\text{ext}}(\mathbf{r})\right] n(\mathbf{r}). \qquad (2.18b) \end{aligned}$$

Addition of Equations (2.18a) and (2.18b) results in the impossible situation where $E_0 + \tilde{E}_0 < E_0 + \tilde{E}_0$. Therefore, by contradiction it is shown that there is a one-to-one mapping between the external potential and the electronic density.

2.2.1.2 Proof of the second theorem

Equation (2.17) shows that the total energy of the system may be written as a functional of the electronic density

$$E[n] = \langle\psi[n]|\hat{H}|\psi[n]\rangle\,.$$

Thence, using Equation (2.16) it is possible to write

$$E[n] = \langle\psi[n]|\hat{F}|\psi[n]\rangle + \langle\psi[n]|\hat{V}_{\text{ext}}|\psi[n]\rangle\,. \qquad (2.19)$$

The variational principle can be applied for the ground state wave function, $|\psi_0\rangle$, and some other wave function, $|\psi\rangle$ that has a density different from the ground state density

$$\langle\psi[n]|\hat{F}|\psi[n]\rangle + \langle\psi[n]|\hat{V}_{\text{ext}}|\psi[n]\rangle > \langle\psi_0[n]|\hat{F}|\psi_0[n]\rangle + \langle\psi_0[n]|\hat{V}_{\text{ext}}|\psi_0[n]\rangle \qquad (2.20)$$

For the same Hamiltonian, $\hat{V}_{\text{ext}}$ will be the same so that

$$E[n] > E[n_0]. \qquad (2.21)$$

2.2.2 The Kohn-Sham equations

The HK theorems permit an exact solution of the ground state electronic many-body problem via the electronic density. In spite of its confirmed existence, the lack of a known global functional $F[n]$ initially presented a serious problem for the application of DFT. Specifically, there are no known density functional expressions for the (quantum mechanical) kinetic, $T[n]$, and electron-electron internal potential, $V_{\text{int}}[n]$, energies. The KS framework offers a convenient method for making use of DFT and the HK theorems whilst maintaining exchange and correlation effects associated with $T[n]$ and $V_{\text{int}}[n]$ [180].

The ingenuity of the KS method is the mapping of the interacting N-electron system onto a system of non-interacting fermions [180]. For this KS system, the kinetic energy is a well-defined functional of the density

$$T_s[n] = -\frac{1}{2}\sum_i^N f_i \int \mathrm{d}\mathbf{r}\ \varphi_i^*(\mathbf{r})\nabla^2\varphi(\mathbf{r}); \tag{2.22}$$

$\varphi(\mathbf{r})$ are the non-interacting single particle eigenfunctions, otherwise known as KS states, f_i are the KS-state occupations. Moreover, the remaining quantum effects associated with the true interacting system are collected in a separate functional of the density denoted the exchange-correlation (XC) functional $E_{xc}[n]$. Perhaps most importantly, the fictitious system of non-interacting fermions exactly reproduces the density of the real interacting system

$$n(\mathbf{r}) = \sum_i^N f_i|\varphi_i(\mathbf{r})|^2. \tag{2.23}$$

In this representation the HK-minimisation scheme can be rewritten as the first variation

$$\delta\left[F[n] + \int \mathrm{d}\mathbf{r}\ V_{\text{ext}}(\mathbf{r})n(\mathbf{r}) - \mu\left(\int \mathrm{d}\mathbf{r}\ n(\mathbf{r}) - N\right)\right] = 0, \tag{2.24}$$

where μ is a Lagrange multiplier that enforces a total electron count constraint, which is a requirement for a closed system; in practice μ describes the chemical potential of the system. The KS functional, $F[n]$, is

$$F[n] = T_s[n] + \frac{1}{2}\iint \mathrm{d}\mathbf{r}\mathrm{d}\mathbf{r}'\ \frac{n(\mathbf{r})n(\mathbf{r}')}{|\mathbf{r}-\mathbf{r}'|} + E_{xc}[n]. \tag{2.25}$$

Given the general definition of the functional derivative in terms of a function J [181, 186, 187]

$$\delta J[p] = \int \frac{\delta F}{\delta p}(x)\phi(x)\mathrm{d}x = \left[\frac{\mathrm{d}}{\mathrm{d}\varepsilon}F[p+\varepsilon\phi]\right]_{\varepsilon=0}, \tag{2.26}$$

where $\frac{\delta F}{\delta p}(x)$ is the functional derivative, $\phi(x)$ is an arbitrary function and ε is the infinitesimal variation, Equation (2.24) reduces to the Euler-Lagrange equation

$$\frac{\delta T_s[n]}{\delta n}(\mathbf{r}) + V_{\mathrm{KS}}(\mathbf{r}) = \mu. \tag{2.27}$$

The KS potential, V_{KS}, is implicitly defined in Equation (2.27)

$$V_{\mathrm{KS}}[n] = \int \frac{n(\mathbf{r}')}{|\mathbf{r}-\mathbf{r}'|}\,\mathrm{d}\mathbf{r}' + V_{xc}[n] + V_{ext}(\mathbf{r}), \tag{2.28}$$

here $V_{xc}[n]$ is the exchange-correlation potential

$$V_{xc}[n] = \frac{\delta E_{xc}[n]}{\delta n}(\mathbf{r}). \tag{2.29}$$

Led by the definition of $T_s[n]$ in terms of the single particle Kohn-Sham orbitals in Equation (2.22), it is convenient to also solve Equation (2.27) for those N-states. Towards this end, one can write the Kohn-Sham equations, which are a set of N single particle Schrödinger-like equations:

$$\left[\hat{T}_s + \hat{V}_{\mathrm{KS}}(\mathbf{r})\right]\varphi_i(\mathbf{r}) = \epsilon_i\varphi_i(\mathbf{r}) \tag{2.30}$$

The states $\varphi_i(\mathbf{r})$ define the operators $\hat{T}_s$ and $\hat{V}_{\mathrm{KS}}$, therefore the total energy of the N-electron system can be obtained via a self-consistent iteration over Equations (2.30). By initialising a trial charge density, i.e. a trial $\varphi_i(\mathbf{r})$ (see Equation (2.23)), as input for the Kohn-Sham equations it is possible to calculate a set of KS orbitals. These orbitals then serve as the basis for an updated charge-density (calculated using Equation (2.23)), which is in turn used to construct an updated Hamiltonian. The latter is then diagonalised to yield the KS-states for the next iteration. Convergence is reached when the input and output densities are identical, to within a numerical threshold.

2.2.3 Exchange-correlation functionals

The KS equations as presented in Section 2.2.2 are formally exact. They capture by construction, all of the quantum components of the kinetic energy ($T[n] - T_s[n]$), and static Coulomb interactions ($U[n] - U_H[n]$) collectively within the exchange-correlation functional, $E_{xc}[n]$. The caveat is that in spite of over fifty years of research, no exact expression for $E_{xc}[n]$ has been found; in order to make use of the KS formalism, approximations to account for the electron exchange and correlation must be introduced. These approximations take various forms that can be stacked in complexity into what is commonly known as Jacob's ladder of increasing accuracy for exchange-correlation functionals [188]:

unoccupied $\psi_\alpha(\mathbf{r}')$: Exact-exchange and exact partial correlation

occupied $\psi_\alpha(\mathbf{r}')$: Exact-exchange and compatible correlation

$\nabla^2 n(\mathbf{r})$: *Meta*-generalised gradient approximation

$\nabla n(\mathbf{r})$: Generalised gradient approximation

$n(\mathbf{r})$: Local density approximation

At each "rung" on the ladder the accuracy of the result is thought to increase at the cost of complexity and computational effort. This Thesis makes exclusive use of the generalised gradient approximation, which provides an acceptable level of accuracy given the computational loading. In the following sections the local density approximation, generalised gradient approximation and the incorporation of long-ranged interactions will be introduced.

2.2.3.1 The local density approximation

By its position on Jacob's ladder, the Local Density Approximation (LDA) is the simplest form of exchange-correlation functional. Despite being the first approximation to E_{xc} [180], the LDA is surprisingly reliable (for systems with slowly varying densities) and still occasionally finds use in modern simulations [189,190]. The most notable parametrisation (that of Perdew and Zunger) of the LDA XC-functional fits Monte Carlo data and analytical expressions in the high density limit [191–193]. Importantly, the LDA assumes that, locally, the electronic density can be represented by a homogeneous electron gas that has an equal density to that isolated volume. The LDA functional of Kohn and

Sham can be derived analytically, and is written [180]

$$\begin{aligned} E_x^{\mathrm{LDA}}[n] &= \int \mathrm{d}\mathbf{r}\ n(\mathbf{r})\varepsilon_{xc}[n], \\ &= \frac{3}{4}\left(\frac{3}{\pi}\right)^{\frac{1}{3}} \int \mathrm{d}\mathbf{r}\ n(\mathbf{r})^{\frac{4}{3}}, \end{aligned} \tag{2.31}$$

$\varepsilon_{xc}[n]$ is the exchange-correlation energy per electron in a homogeneous electron gas with density $n(\mathbf{r})$. Using the relation

$$\frac{\delta}{\delta f}(x)F_1F_2 = \frac{\delta F_1}{\delta f}(x)F_2 + F_1\frac{\delta F_2}{\delta f}(x),$$

which is reported in multiple outlets [181, 186, 187], the exchange correlation potential can be derived as

$$V_{xc}^{\mathrm{LDA}}[n] = \varepsilon_{xc}[n]\left(n(\mathbf{r}) + n(\mathbf{r})\frac{\delta\varepsilon_{xc}[n]}{\delta n}(\mathbf{r})\right). \tag{2.32}$$

2.2.3.2 The generalised gradient approximation

The LDA can be practically useful for systems whose density varies slowly; it is generally inadequate for the description of materials with non-homogeneous densities. More than that, due to spurious self-interactions, it is well established that LDA functionals underestimate experimental bond lengths and band gaps. To reconcile these problems, one can introduce gradient expansions of the density into the $E_{xc}[n]$. This leads to the class of density functionals second on Jacob's ladder, those which make use of the generalised gradient approximation GGA. Recalling the general formula for the LDA: Equation (2.31), the GGA functionals are constructed

$$E_{xc}^{\mathrm{GGA}}[n] = \int \mathrm{d}\mathbf{r}\ f\left[n(\mathbf{r})\right], \nabla n(\mathbf{r})). \tag{2.33}$$

Parametrisation of the function $f(n(\mathbf{r}), \nabla n(\mathbf{r}))$ has proven difficult, and over many years of study has given rise to an abundance of flavours of GGA-functional [194]. By taking into account derivatives of the density, the effects of density-fluctuations are also considered within GGA functionals. Resultantly they provide a better picture than the LDA for total energies, energy barriers and structural energy differences. Although, it should be noted that GGA functionals have a tendency to over-soften bonding interactions. Furthermore, GGAs are well known for their underestimation of band gaps owning to prediction of the valence band edges too high in energy and the conduction

band edges too low in energy [195–200] This work, makes extensive use of the Perdew-Burke-Ernzerhof (PBE) parametrisation [201] for the simulations reported in Chapters 3, 4 and 5.

2.2.3.3 Exchange and correlation for sparse matter

The exact exchange-correlation functional will contain a full description of the long ranged van der Waals (VDW) interactions that are important in the description of layered materials, surface-molecule interfaces and for inter- and intra-molecular interactions. The local (LDA) and semilocal (GGA) exchange-correlation schemes outlined above fail to capture any long ranged interactions where there is little or no overlap of the electronic density. As such, there is great impetus to derive density functionals that account correctly for these important energetic contributions. In DFT, VDW forces are typically addressed via an empirical correction to the exchange-correlation energy [202–207] or via self-consistent minimisation of an intrinsically non-local correlation functional [208–215].

Perhaps the most trivial way to introduce long-ranged interactions into the DFT simulations is to additively correct the total energy using interatomic VDW interaction energies. This is the dispersion-corrected DFT approach, otherwise referred to as DFT-D, that uses a summation over atomic pair $C_{6,IJ}$ coefficients to correct the energy

$$E_{\mathrm{DFT-D}} = E_{\mathrm{DFT}} - s_6 \sum_{I}^{N_n} \sum_{I>J}^{N_n} f_{\mathrm{damp}}(\mathbf{R}_{IJ}) \frac{C_{6,IJ}}{\mathbf{R}_{IJ}^6}. \tag{2.34}$$

Depending on the underlying exchange-correlation functional, s_6 is a scaling factor, $\mathbf{R}_{IJ} = |\mathbf{R}_I - \mathbf{R}_J|$ is the interatomic distance and $f_{\mathrm{damp}}(\mathbf{R}_{IJ})$ is a function introduced to dampen the strength of the interaction at different interatomic distances. Determination of the $C_{6,IJ}$ coefficients is non-trivial and beyond the realms of this work [204,205]. They are obtained from the homoatomic $C_{6,I}$ quantities on the basis of known experimental or ab-initio values. For this reason DFT-D represents only an empirical VDW-correction.

Not only do the $C_{6,IJ}$ coefficients vary between different DFT-D corrections, the form of $f_{\mathrm{damp}}(\mathbf{R}_{IJ})$ is also correction-dependent. Ultimately this means that, as shown in Figure 2.1, the added correction is different. One must therefore, carefully consider the results obtained via dispersion-corrected simulations. In Chapter 4 of this Thesis a direct comparison of the use of the empirical corrections of Elstner [204] and Grimme [206] for

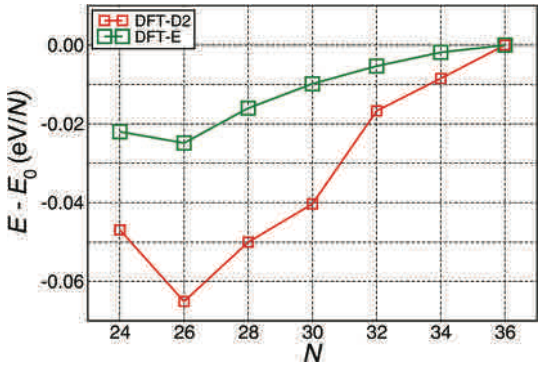

Figure 2.1: For illustrative purposes, a plot showing the different total energy corrections produced by the Elstner (DFT-E [204]) and Grimme (DFT-D2 [206]) models for a range of differently sized methylated aluminosilicate nanotubes (See Chapter 4).

the set of methyl containing NTs of Figure 1.8 and 2.1 is presented.

Non-empirical self-consistent non-local exchange correlation functionals take the form

$$E_{xc}[n] = E_x^{\mathrm{GGA}}[n] + E_c^{\mathrm{new}}[n], \tag{2.35}$$

where $E_x^{\mathrm{GGA}}[n]$ is a pre-existing semilocal exchange functional and $E_c^{\mathrm{new}}[n]$ is a modified non-local correlation functional [213]. Self-consistency is obtained by minimising the $E_c^{\mathrm{new}}[n]$ functional within the variational Kohn-Sham process as part of Kohn-Sham potential [212]. The correlation function is split into two parts, relating to short- and long-ranged interactions

$$E_c^{\mathrm{new}}[n] = E_c^{\mathrm{LDA}}[n] + E_c^{\mathrm{nl}}[n]. \tag{2.36}$$

Local correlation interactions are treated in the LDA approximation, whilst the non-local contributions are computed via

$$E_c^{\mathrm{nl}}[n] = \int \mathrm{d}\mathbf{r}\mathrm{d}\mathbf{r}'\; n(\mathbf{r})\Phi(q,q')n(\mathbf{r}') \tag{2.37}$$

The kernel, $\Phi(q,q')$, contains the expressions for the non-local interactions, where $q = q(n(\mathbf{r}), \nabla n(\mathbf{r}))$ depends on the density and its gradient.

In Chapter 4 three different self-consistent exchange-correlation functionals are utilised:

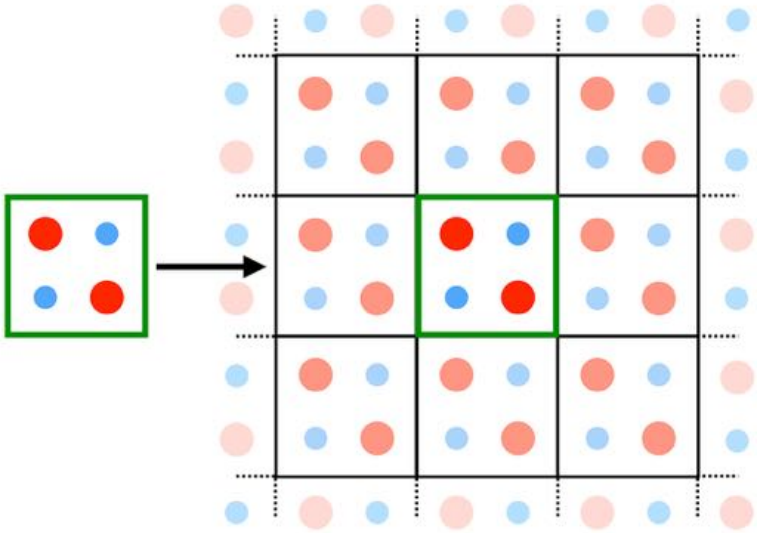

Figure 2.2: Representation of a simplistic single cell (green box) infinitely repeated under periodic boundary conditions.

VDWDF [210–212], OPTPBE [214,215] and OPTB88 [214,215]. Each of these functionals is constructed according to Equations (2.35), (2.36) and (2.37); they differ in the calculation and parametrisation of the exchange energy. The VDWDF functional, which can be regarded as the original self consistent non-local functional, uses the revPBE [216] parametrisation of the exchange energy. It has been noted that revPBE may not be the optimal representation of the exchange energy and therefore additional VDW-type functionals have been developed: the OPTPBE and OPTB88 functionals instead make use of the PBE [201] and Becke88 [217] exchange parametrisation. The exchange components of these non-local functionals have been subsequently reparametrisation for the S22 set of molecules [214, 218].

2.2.4 Periodic boundary conditions in DFT

The application of periodic boundary conditions within DFT can be used to reduce the size of the computed system to a single unit cell or manageable supercell. Under periodic boundary conditions the extended system is represented on an infinitely periodic lattice, Figure 2.2. The justification for such an approach is provided by Bloch's theorem [219].

For a periodic system, the Kohn-Sham potential at a particular $\mathbf{r}$ in space has the

property

$$V_{\mathrm{KS}}(\mathbf{r}+\mathbf{R}) = V_{\mathrm{KS}}(\mathbf{r}), \tag{2.38}$$

where $\mathbf{R} = n_1\mathbf{a}_1 + n_2\mathbf{a}_2 + n_3\mathbf{a}_3$ is the crystal lattice vector, a function of the Cartesian unit vectors $\mathbf{a}_i$. Defining an operator for translation, $\hat{T}_{\mathbf{R}}$, such that it translates the potential

$$\hat{T}_{\mathbf{R}} V_{\mathrm{KS}}(\mathbf{r}) = V_{\mathrm{KS}}(\mathbf{r}+\mathbf{R}), \tag{2.39}$$

and

$$\hat{T}_{\mathbf{R}}\hat{T}_{\mathbf{R}'} V_{\mathrm{KS}}(\mathbf{r}) = V_{\mathrm{KS}}(\mathbf{r}+\mathbf{R}+\mathbf{R}'), \tag{2.40}$$

then the $\hat{T}_{\mathbf{R}}$-translated single particle Schrödinger equation reads

$$\begin{aligned} \hat{T}_{\mathbf{R}}\left[\hat{H}(\mathbf{r})\psi(\mathbf{r})\right] &= \hat{H}(\mathbf{r}+\mathbf{R})\psi(\mathbf{r}+\mathbf{R}) \\ &= \hat{H}(\mathbf{r})\hat{T}_{\mathbf{R}}\psi(\mathbf{r}). \end{aligned} \tag{2.41}$$

The commutator $\left[\hat{H}, \hat{T}_{\mathbf{R}}\right] = 0$ for all $\mathbf{R}$, thence the eigenvalues of both the Hamiltonian and translation operators can be obtained on the basis of common eigenfunctions, and

$$\hat{T}_{\mathbf{R}}\psi(\mathbf{r}) = c(\mathbf{R})\psi(\mathbf{r}). \tag{2.42}$$

On the basis of Equation (2.40) it can be asserted that the eigenvalues $c(\mathbf{R})$ obey

$$c(\mathbf{R}+\mathbf{R}') = c(\mathbf{R})c(\mathbf{R}'). \tag{2.43}$$

This exponential identity leads to the conclusion that the natural representation of $c(\mathbf{R})$ is

$$c(\mathbf{R}) = e^{i\mathbf{k}\cdot\mathbf{R}}. \tag{2.44}$$

This analysis introduces the wave vector $\mathbf{k} = x_1\mathbf{b}_1 + x_2\mathbf{b}_2 + x_3\mathbf{b}_3$, which has the property $\mathbf{a}_i \cdot \mathbf{b}_j = 2\pi\delta_{ij}$; $\mathbf{b}_i$ are the reciprocal lattice vectors.

The function $u_{i\mathbf{k}}(\mathbf{r}) = \exp(-i\mathbf{k}\cdot\mathbf{r})\psi_{i\mathbf{k}}(\mathbf{r})$, which is an eigenfunction of the Hamilto-

nian translates as:

$$\begin{aligned} \hat{T}_{\mathbf{R}} u_{i\mathbf{k}}(\mathbf{r}) &= e^{-i\mathbf{k}\cdot(\mathbf{r}+\mathbf{R})}\psi_{i\mathbf{k}}(\mathbf{r}+\mathbf{R}) \\ &= e^{(-i\mathbf{k}\cdot\mathbf{r})}\psi_{i\mathbf{k}}(\mathbf{r}) = u_{i\mathbf{k}}(\mathbf{r}). \end{aligned} \tag{2.45}$$

Thus, Bloch's theorem states that the eigenfunctions of the Hamiltonian may be expressed in terms of the unit cell periodic function, $u_{\mathbf{k}}(\mathbf{r})$, and the wave vector, $\mathbf{k}$.

2.2.5 The pseudopotential approximation

The pseudopotential approximation reduces the computational demands associated with the treatment of electrons that reside in core levels [220–222]. Generally, these are the most energetically bound states, spatially localised at the atomic nucleus. The core-level electrons are responsible for shielding the valence electrons from the nuclear charge. Therefore, where the valence eigenstates are characterised by their bonding environment and orbital hybridisation, the core states are qualitatively unaffected by changes in the bonding environment. Orthogonality between the valence and core eigenstates leads to rapid oscillations in the valence states close to the nuclei. The representation of the wave function within the core region is therefore costly and requires exceptionally high plane wave cut offs or large numbers of basis functions. As it is widely accepted that (i) the core states have a minimal contribution to chemical bonding and (ii) the core states only experience a small perturbation during changes to the chemical bonding, it is acceptable to replace the rapidly oscillating function with a smooth pseudo wave function in the core region. This is known as the pseudopotential approximation.

Supposing that the valence state wave function, $|\varphi\rangle$, can be expressed in terms of a smooth pseudo-function, $|\tilde{\varphi}\rangle$, less a summation, of coefficients a_n, of the core states [220], $|\chi\rangle$,

$$|\tilde{\varphi}\rangle = |\varphi\rangle - \sum_{n}^{\text{core}} a_n |\chi_n\rangle : \tag{2.46}$$

then the orthogonality of the valence and core eigenstates leads to,

$$\langle\chi_n|\tilde{\varphi}\rangle = -a_n, \tag{2.47}$$

thence,

$$|\varphi\rangle = |\tilde{\varphi}\rangle - \sum_{n}^{\text{core}} |\chi_n\rangle \langle\chi_n|\tilde{\varphi}\rangle \,. \tag{2.48}$$

If a Schrödinger equation for the valence states can be written $\hat{H}\,|\varphi\rangle = E\,|\varphi\rangle$, then a similar expression must also hold for the pseudo-state,

$$\left[\hat{H} + \hat{V}^{\text{nl}}\right] |\tilde{\varphi}\rangle = E\,|\tilde{\varphi}\rangle \,, \tag{2.49}$$

where,

$$\hat{V}^{\text{nl}} = \sum_{n}^{\text{core}} (E - E_n)\,|\chi_n\rangle \langle\chi_n| \,, \tag{2.50}$$

is an energy dependent operator that ensures smoothness inside the core region, and is named the pseudopotential.

The energy of the eigenstates will vary as a function of the atomic environment, however, in practice E (in $\hat{V}^{\text{nl}}$) is fixed at the energy of the valence eigenvalue for that isolated atom. This approximation is valid in the limit where the core and valence states are separated by a large energy gap. Norm-conserving pseudopotentials are constructed subject to the constraints that (i) the pseudo valence states accurately the reproduce eigenvalues obtained in an all-electron calculation and (ii) the pseudo-wave functions and all-electron wave functions are identical outside a given core region r_c. These constraints ensure the transferability of the pseudopotentials created [223–227].

Spin polarised (magnetic) species with 3d or higher energy/ angular momentum electrons present a problem for the pseudopotential approximation that has been presented above. The electronic densities of the core, $n_c^{(\sigma)}$, and valence states, $n_v^{(\sigma)}$, overlap in space. For these species, the exchange-correlation potential does not vary linearly with the charge density or magnetisation. Consequently, within the core region, residual valence contributions to the exchange-correlation are observed,

$$V_{\text{xc}}^{(\sigma)}\left[n_v + n_c, \xi\right] - V_{\text{xc}}^{(\sigma)}\left[n_v, \xi_v\right] \neq 0. \tag{2.51}$$

The residual contribution arises from the differences between the the pseudo valence

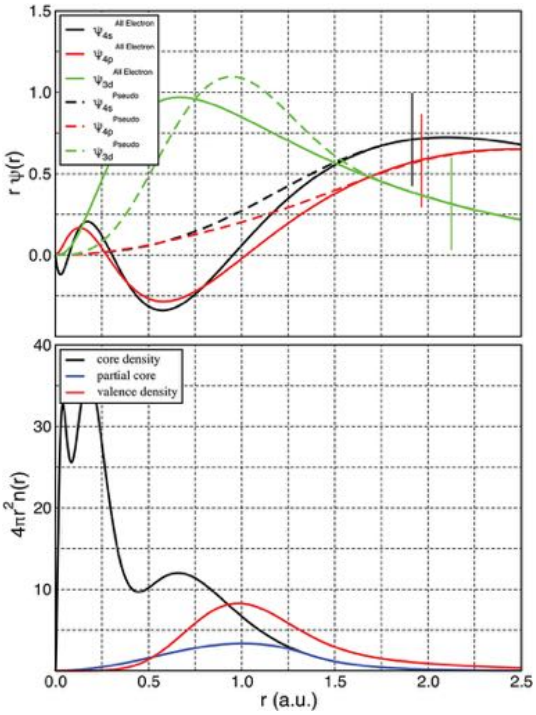

Figure 2.3: An example pseudopotential for Cobalt, generated by the Opium code [228]. In the top panel a plot the probability amplitudes of the all-electron and pseudo wave functions is shown. In the bottom panel the density distributions for the core, partial core and valence states are plotted.

function spin-polarisation,

$$\xi_v = \frac{n_v^{(\uparrow)}(\mathbf{r}) - n_v^{(\downarrow)}(\mathbf{r})}{n_v(\mathbf{r})}, \tag{2.52}$$

and the all-electron spin-polarisation,

$$\xi = \frac{n_v^{(\uparrow)}(\mathbf{r}) - n_v^{(\downarrow)}(\mathbf{r})}{n_c(\mathbf{r}) + n_v(\mathbf{r})}. \tag{2.53}$$

To correct for this, it is convenient to use nonlinear core corrections (NLCC) [229]. In the NLCC during the computation of the exchange-correlation potential a fraction of the core charge spin density, referred to as the partial core, is added to the valence spin density. This has been shown to improve the transferability of pseudopotentials for use in spin polarised and magnetic systems [229].

Although more computationally efficient methods to the core-valence hybridisation exist such as the projector augmented wave method, which enables the use of lower energetic cutoffs, these have only recently been implemented within the ONETEP code [230] and have not been used for this research. That is why NLCC-pseudopotentials have been used in the treatment of 3d containing elements such as Fe in Chapter 6.

2.2.6 Atomic forces and geometry optimisation

First principles based simulations are generally employed as methods for obtaining expectation values of quantum mechanical operators for a given arrangement of atoms. The observables are properties of the system and may include total energies, band structure, density of states or information pertaining to magnetic ordering. Yet, for the data obtained to be meaningful, there must be some importance placed on having the *correct* relaxed thence populated arrangement of those atoms. As such, in most available DFT packages, modules and subroutines are dedicated to obtaining not just the minimum energy density, but also the coordinates for which those atoms have an adiabatic potential energy minimum.

There are numerous strategies that one can utilise in order to obtain such a minimum energy atomic configuration. Born-Oppenheimer and *ab-initio* molecular dynamics based approaches offer seemingly physical solutions to the problem by considering the time evolved mechanical response to the initial estimated configuration [231]. Here, the

problem is equated to that of minimising an arbitrary multidimensional function. Common methods for solving a problem like this include conjugate gradient and quasi-Netwon (QN) methods [232]. Owing to their favourable accuracy at reasonable computational cost, both have been implemented in a variety of DFT codes. This work deals with the use of the quasi-Newton scheme implemented in the ONETEP code [230].

2.2.6.1 Mathematical background: Newton method

Given an arbitrary multi-dimensional function, $f(\mathbf{x}) = |\mathbf{F}\rangle$, one can apply Newton's method to find the stationary points that satisfy

$$\frac{\partial f}{\partial \mathbf{x}} = 0. \tag{2.54}$$

If inputting $|\mathbf{x}_i\rangle$ returns the result $|\mathbf{F}_i\rangle$ then the Taylor's series expansion of $|\mathbf{F}\rangle$ to second order about this point is

$$|\mathbf{F}\rangle = |\mathbf{F}_i\rangle + (|\mathbf{x}\rangle - |\mathbf{x}_i\rangle)\frac{\partial}{\partial \mathbf{x}}|\mathbf{F}_i\rangle + \frac{1}{2}(\langle\mathbf{x}| - \langle\mathbf{x}_i|)\mathcal{A}(|\mathbf{x}\rangle - |\mathbf{x}_i\rangle). \tag{2.55}$$

The Hessian matrix, $\mathcal{A}$, is the square matrix whose elements are the functions second derivatives $\left(\mathcal{A}_{ij} = \frac{\partial^2|\mathbf{F}\rangle}{\partial \mathbf{x}_i \partial \mathbf{x}_j}\right)$. Taking the derivative of the approximated $|\mathbf{F}\rangle$, and rearranging according to Equation (2.54) yields

$$|\mathbf{x}\rangle - |\mathbf{x}_i\rangle = -\mathcal{A}^{-1}\frac{\partial}{\partial \mathbf{x}}|\mathbf{F}_i\rangle\,. \tag{2.56}$$

This result provides a method for finding the stationary points for the initial function, through iteration of $|\mathbf{x}_i\rangle$. Focusing on finding the minimum of the function, it is easily seen that $\mathcal{A}^{-1}$ should be a positive definite matrix (the eigenvalues of $\mathcal{A}^{-1}$ are real and positive) to yield decreasing $|\mathbf{F}_i\rangle$. This is because the scheme proceeds by line search, and the fact that $\mathcal{A}^{-1}$ is positive definite means that the search direction will always be descending towards the minima [232].

2.2.6.2 Quasi-Newton Method

By calculating $\mathcal{A}$ at $|\mathbf{x}_i\rangle$, there can be no way of ensuring that $\mathcal{A}^{-1}$ is in fact a positive definite matrix, especially in the cases where the initial point is far from the global (or

local) minimum, or the function is not quadratic i.e. the electronic potential energy surface. In the Quasi-Newton (QN) scheme, instead an estimate to the inverse Hessian, $\mathcal{H}^{(i)}$ is provided such that it is always positive definite and has the property

$$\lim_{i\to\infty} \mathcal{H}^{(i)} \quad = \quad \mathcal{A}^{-1}, \tag{2.57}$$

where the bracketed superscript is the geometry optimisation iteration step. In the minimisation of $|\mathbf{F}\rangle$, one can envisage from Equation (2.56) that the stepwise update using the approximated inverse Hessian is given by

$$|\Delta\mathbf{x}_i\rangle \quad = \quad \mathcal{H}^{(i)} \frac{\partial}{\partial \mathbf{x}} |\Delta\mathbf{F}_i\rangle \,. \tag{2.58}$$

The terms $|\Delta\mathbf{x}_i\rangle$ and $|\Delta\mathbf{F}_i\rangle$ are $(|\mathbf{x}_i\rangle - |\mathbf{x}_{i-1}\rangle)$ and $(|\mathbf{F}_i\rangle - |\mathbf{F}_{i-1}\rangle)$ respectively. The update of $\mathcal{H}^{(i)}$ can be handled in different ways [233]. Two important approaches to the Hessian Update include the Davidon-Fletcher-Powell (DFP) method and its successor the Broyden-Fletcher-Goldfarb-Shanno (BFGS) update. In the BFGS update, the approximated inverse Hessian matrices proposed at each sequential iteration are given by

$$\begin{aligned} \mathcal{H}^{(i)} \quad &= \quad \mathcal{H}^{(i-1)} + \frac{|\Delta\mathbf{x}_i\rangle \langle\Delta\mathbf{x}_i|}{\langle\Delta\mathbf{x}_i|\Delta\mathbf{F}_i\rangle} - \frac{\left(\mathcal{H}^{(i-1)} |\Delta\mathbf{F}_i\rangle\right)\left(\mathcal{H}^{(i-1)} \langle\Delta\mathbf{F}_i|\right)}{\langle\Delta\mathbf{F}_i|\mathcal{H}^{(i-1)}|\Delta\mathbf{F}_i\rangle} \\ &+ \quad \langle\Delta\mathbf{F}_i|\mathcal{H}^{(i-1)}|\Delta\mathbf{F}_i\rangle \, |U\rangle \langle U| \,, \end{aligned} \tag{2.59}$$

where

$$|U\rangle = \frac{|\Delta\mathbf{x}_i\rangle}{\langle\Delta\mathbf{x}_i|\Delta\mathbf{F}_i\rangle} - \frac{\mathcal{H}^{(i-1)} |\Delta\mathbf{F}_i\rangle}{\langle\Delta\mathbf{F}_i|\mathcal{H}^{(i-1)}|\Delta\mathbf{F}_i\rangle}. \tag{2.60}$$

The superiority of the BFGS update when compared to the DFP method arises from its ability to more efficiently correct the eigenvalues of the $\mathcal{H}^{(i-1)}$ [234]. For this reason, the BFGS algorithm has found widespread use in unconstrained optimisation problems including electronic structure theory.

Implementation of the QN method for geometry optimisation is provided in reference [235]. In this publication, it is highlighted that the BFGS algorithm can be applied to the ionic relaxations of the crystal structures. The praxis of the BFGS scheme rests upon the computation of the forces on each ion, since it is the force vector, $\langle\Delta\mathbf{F}_i|$, that makes it possible to minimise a structure possessing the coordinates $\langle\Delta\mathbf{R}_i|$. This is

achieved making use of the Hellman-Feynman theorem [236, 237], which has been shown to uphold in both all-electron and pseudopotential approaches [238, 239].

The enthalpy is expressible in terms of the total energy of the system, E, and the unit cell volume, Ω

$$H = E + p\Omega, \tag{2.61}$$

where p is an applied pressure. By noticing that the forces are related to H, according to

$$\mathbf{F} \quad = \quad -\left(\frac{\partial H}{\partial \mathbf{R}}\right)_p, \tag{2.62}$$

one can establish the geometry optimisation problem to be a minimisation of the enthalpy per unit cell. Following Equation (2.55) and expanding the change in enthalpy, δH, as a Taylor series:

$$\delta H = \frac{1}{2}\left(\langle \mathbf{R}| - \langle \mathbf{R}_i|\right)\mathcal{A}\left(|\mathbf{R}\rangle - |\mathbf{R}_i\rangle\right). \tag{2.63}$$

To facilitate the algorithm, H is considered to be a function of both the strain and atomic coordinates, thereby, defining a (9+3N) vector space comprised of the 9 elements of the stress tensor and each of the $3N$ degrees of freedom. In this notation the coordinate update is given b

$$|\mathbf{R}_i\rangle \quad = \quad |\mathbf{R}_{i-1}\rangle + \lambda \mathcal{H}^{(i-1)}\,|\mathbf{F_{i-1}}\rangle\,, \tag{2.64}$$

where λ is the step length, a parameter which is obtained through line search. In practice, the Hessian matrix is updated according to (2.59) until the atomic forces are smaller than a set convergence threshold. This work has made extensive use of the BFGS scheme as described here, although alternative methods such as the LBFGS are available.

2.3 Linear-scaling Density Functional Theory in ONETEP

Favourable accuracy-viability trade-offs, fuelled by the efficient design and implementation of codes and ever improving academic access to better computational hardware, have led to DFT becoming the go-to strategy for the routine modelling of materials containing hundreds of atoms. The framework outlined in Section 2.2 readily allows the

simulation of diverse complex properties far beyond the electronic structure of bulk materials, such as the simulation of surfaces, two dimensional materials and nanoparticles. However, the current shift in scientific interest towards functional nanomaterials, biological systems and processes at surface-reactant-medium interfaces, all of which expectedly involve the simulation of thousands of atoms, demands even better performance of DFT software. Avenues that can be explored in order to overcome these limitations include the derivation of better scaling theories [178], more efficient parallel implementation and integrated implementations on faster graphical processing units [240–242].

The cost of a conventional DFT calculation scales as $\mathcal{O}(N^3)$ with the number of atoms in the system (N). This imposes serious restrictions on the size of the system that can be viable considered. As a consequence, DFT-investigations often rely upon the transferability of smaller idealised models as representations of experiments. Processes such as geometry optimisation and computation of electronic, dynamic or optical properties of systems with more that a few hundred atoms are restricted. Cubic scaling in DFT arises from the forced orthogonality of the KS-states as obtained by explicit diagonalisation of the Hamiltonian matrix. On top of the overall scaling factor it is worth noting that, a significant proportion of any (plane-wave) DFT simulation involves calculating Fast Fourier transforms (FFT) between real and reciprocal space, and these processes scale as $\mathcal{O}(N\log(N))$ [243].

Overcoming the cubic scaling barrier has been a target for DFT developers for some time. In particular, there has been a large focus on the development of linear-scaling $\mathcal{O}(N)$-DFT. LS-DFT centres around the so-called quantum mechanical property of "nearsightedness" [244]. Nearsightedness postulates that each particle in a quantum system, which is comprised of many interacting particles, experiences a potential that is overwhelmingly dominated by local interactions. The locality of these interactions depends on the electronic nature of the system. In metallic systems the interaction decays as a power series, whereas for insulating and semiconducting materials the decay is exponential. This condition can be expressed on the basis of the single particle density matrix as:

$$\rho(\mathbf{r}, \mathbf{r}') \approx e^{-\gamma|\mathbf{r}-\mathbf{r}'|}, \tag{2.65}$$

where $\mathbf{r}$ and $\mathbf{r}'$ are the positions in space. The exponential factor, $\gamma \propto \sqrt{E_g}$, is a non-negative quantity related to the size of the band gap, E_g. The locality of the systems

ensures that it is possible to work within a non-orthogonal representation, enforce spatial cutoffs and maintain sparse matrix algebra, all of which contribute towards a working LS-DFT implementation with the ONETEP code.

2.3.1 Density matrix formulation of DFT

The ONETEP program is a LS-DFT code that is formulated in terms of the aforementioned single particle density matrix, $\rho(\mathbf{r}, \mathbf{r}')$ [179,245–251]. For details of the properties of $\rho(\mathbf{r}, \mathbf{r}')$ the interested reader is referred to reference [252]. Density matrix theory is well established and it has already been mentioned that for materials with a band gap the elements of $\rho(\mathbf{r}, \mathbf{r}')$ decay exponentially with distance, Equation (2.65) [253]. This property, so called quantum nearsightedness, is what allows the formulation of linear-scaling methods. The next Section explains the utilisation of density matrix based approaches.

2.3.1.1 Density matrix theory

In the density matrix formulation of DFT, the density operator

$$\hat{\rho} \;=\; \sum_{n} f_n \left|\phi_n\right\rangle \left\langle\phi_n\right|, \tag{2.66}$$

is expressed in terms of the orthonormal KS states and their occupancies f_n. In a non-orthogonal basis representation, instead, one can write

$$\hat{\rho} \;=\; \sum_{\alpha\beta} \left|\phi_\alpha\right\rangle K^{\alpha\beta} \left\langle\phi_\beta\right|, \tag{2.67}$$

making use of the Einstein summation convention over repeated indices. The basis functions $|\phi_\alpha\rangle$, that shall be discussed in Section 2.3.2, are non-orthogonal generalised Wannier functions, and $K^{\alpha\beta}$ is the density kernel. The non-orthogonal representation necessitates a complete tensorial formulation (see Appendix A) [254], with a dual basis defined as

$$\left|\phi^\alpha\right\rangle = \sum_{\beta} \left|\phi_\beta\right\rangle S^{\beta\alpha}, \tag{2.68}$$

for the calculation of the density kernel

$$K^{\alpha\beta} = \left\langle\phi^\alpha\right|\hat{\rho}\left|\phi^\beta\right\rangle. \tag{2.69}$$

Here, the overlap matrix, $S^{\beta\alpha} = \langle \phi^{\beta} | \phi^{\alpha} \rangle$, is analogous to the metric tensor [254], converting between the (localised) co-variant and (delocalised) contra-variant representation of the basis-functions. Within this basis, $\rho(\mathbf{r}, \mathbf{r}')$ can be written in separable form in terms of the atomic coordinates

$$\rho(\mathbf{r}, \mathbf{r}') = \sum_{\alpha\beta} \phi_{\alpha}(\mathbf{r}) K^{\alpha\beta} \phi^{*}_{\beta}(\mathbf{r}'). \tag{2.70}$$

Exploiting the nearsightedness principle, the basis set, ϕ_{α} can be localised if the system has a band gap, and $\rho(\mathbf{r}, \mathbf{r}')$ will be sparse, i.e.

$$\rho(\mathbf{r}, \mathbf{r}') = 0,$$

for $|\mathbf{r} - \mathbf{r}'| > r_{\text{cut}}$, where r_{cut} is spatial cutoff. Then, one can also impose the following constraints. Firstly that the the density matrix be idempotent

$$\rho(\mathbf{r}, \mathbf{r}') \quad = \quad \int d\mathbf{r}'' \rho(\mathbf{r}, \mathbf{r}'') \rho(\mathbf{r}'', \mathbf{r}') \tag{2.71}$$

and secondly that $\rho(\mathbf{r}, \mathbf{r}')$ is normalised such that

$$N = \sum_{\mathbf{r}} \rho(\mathbf{r}, \mathbf{r}). \tag{2.72}$$

Density matrix idempotency states that $\rho(\mathbf{r}, \mathbf{r}')^2 = \rho(\mathbf{r}, \mathbf{r}')$ and ensures that all of the KS state occupancies are 0 or 1, a requirement of the Pauli exclusion principle. Normalisation instead ensures that the number of electrons in the system is conserved throughout an energy minimisation. Idempotency of $\rho(\mathbf{r}, \mathbf{r}')$ can be maintained by adding an additional term to the energy minimisation step that penalises deviation from non-integer occupancies

$$\tilde{E}[\hat{\rho}] \quad = \quad E[\hat{\rho}] + \alpha P[\hat{\rho}], \tag{2.73}$$

$$P[\hat{\rho}] \quad = \quad \text{Tr}\left((\hat{\rho} - \hat{\rho}^2)^2 \right). \tag{2.74}$$

It is worth noting in passing that in the ONETEP code $\rho(\mathbf{r}, \mathbf{r}')$ idempotency is achieved via a combination of the purification schemes of McWeeny and of Li, Nunes and Vanderbilt (LNV). Their details are beyond the scope of this Thesis but can be found in references [255–257]. The LNV purification scheme also drives the trace of $\rho(\mathbf{r}, \mathbf{r}')$ to normalisation. In accordance with $\rho(\mathbf{r}, \mathbf{r}')$ theory, in this formulation, the normalisation

of the $\rho(\mathbf{r},\mathbf{r}')$ can be cast as

$$N = \mathrm{Tr}(KS), \tag{2.75}$$

and the total energy as

$$E = \mathrm{Tr}(KH). \tag{2.76}$$

The formulation outlined above shows that, as long as idempotency and normalisation can be maintained, in the presence of a band gap the DM is sparse. Accordingly, and based on Equation (2.70) this sparsity may be exploited by enforcing spatial cutoffs on the basis set, $\{\phi_\alpha\}$, and truncating the density kernel without jeopardising the accuracy of the result.

2.3.2 Non-orthogonal generalised Wannier functions

The previous section briefly introduced the non-orthogonal basis set implemented within ONETEP. The nearsightedness principle means that expectation values of (DFT) operators do not depend on distant regions of the system and can instead be evaluated locally [244]. In this Section discussions are focused on the implementation and advantages of the NGWF basis set, as well as standard practices that should be adhered to when initialising new simulations.

Wannier functions are a reformulation of the periodic Bloch wave functions, $\psi^{(\sigma)}_{i\mathbf{k}}(\mathbf{r})$, with specific relevance to localised properties [258–260]. Central to the ONETEP approach, the nonorthogonal generalised Wannier functions (NGWFs) are strictly localised atom centred functions (expressed with spin notation suppressed) [261, 262],

$$|\phi_{\alpha\mathbf{R}}\rangle = \left(\frac{\Omega_{\mathrm{cell}}}{(2\pi)^3}\right)^{\frac{1}{2}} \int_{1^{st}BZ} d\mathbf{k}\; e^{i\mathbf{k}\cdot\mathbf{R}} \sum_{i=1}^{N} |\psi_{i\mathbf{k}}\rangle \left[M_i^{\dagger\beta}(\mathbf{k}) S_{\beta\alpha}\right]. \tag{2.77}$$

The NGWFs are characterised by a transformation of the subspace by the matrix,

$$M_i^{\alpha}(\mathbf{k}) = \int d\mathbf{r}\; \phi^{\alpha}_{\mathbf{k}}(\mathbf{r}) \psi_{i\mathbf{k}}(\mathbf{r}) \tag{2.78}$$

Locality is imposed by means of a user defined cut off radius, r_α. Each NGWF is initialized, centred on a nuclear coordinate; for coordinates within the simulation cell where $|\mathbf{r}-\mathbf{r}_0| > r_\alpha$ the value of the basis set is by definition zero. As r_α is a user de-

fined quantity, it is important to converge the total energy with respect to each NGWF radius, bearing in mind that computational overheads increase with larger basis sets. In Chapter 3 explicit demonstration of the protocol for optimising the balance between NGWF size, convergence of the total energy and computational viability are discussed.

2.3.2.1 The psinc basis grid

To avoid complications with the use of atom-centred basis set [263], the NGWFs are expanded over a real space grid as a linear combination of delocalised bandwidth limited delta functions, otherwise known as periodic sine cardinal functions, psincs:

$$\phi_\alpha(\mathbf{r}) = \sum_{k=0}^{N_1-1} \sum_{l=0}^{N_2-1} \sum_{m=0}^{N_3-1} C_{klm,\alpha} D(\mathbf{r} - \mathbf{r}_{klm}). \tag{2.79}$$

Here k, l & m are the Cartesian components of the psinc at each grid point, N_1, N_2 & N_3 are the total number of grid points in the simulation cell along each axis direction and $C_{klm,\alpha}$ are the expansion coefficients for the NGWFs, optimised $C_{klm,\alpha}$ are obtained via a minimisation of the energy using the conjugate gradient algorithm [264].

The psinc functions are orthonormal and closely related to plane waves,

$$D(\mathbf{r} - \mathbf{r}_{klm}) = (N_1 N_2 N_3)^{-1} \sum_{p=-J_1}^{J_1} \sum_{q=-J_2}^{J_2} \sum_{r=-J_3}^{J_3} e^{i(p\mathbf{b}_1 + q\mathbf{b}_2 + s\mathbf{b}_3)\cdot(\mathbf{r}-\mathbf{r}_{klm})}, \tag{2.80}$$

where $\mathbf{b}_1$, $\mathbf{b}_2$ and $\mathbf{b}_3$ are the reciprocal lattice vectors and J_1, J_2 and J_3 are the grid points. Advantageously, the psincs are disconnected from the nuclear coordinates, this lends to the approach some of the added advantages of plane wave methods: it is possible, by increasing the fineness of the psinc grid, to increase the accuracy of the result. Furthermore, no Pulay forces arise if the atoms move [263]. This is because the fineness of the grid is related to an energetic cutoff, similar to the way that the energy cutoff defines the number of basis functions in plane wave DFT.

2.3.3 Fast Fourier transforms in ONETEP

With the orthogonality constraint lifted, $\mathcal{O}(N)$ scaling can be achieved by overcoming the $\mathcal{O}(N\log N)$ FFT scaling barrier. FFTs are required in the calculation of many facets

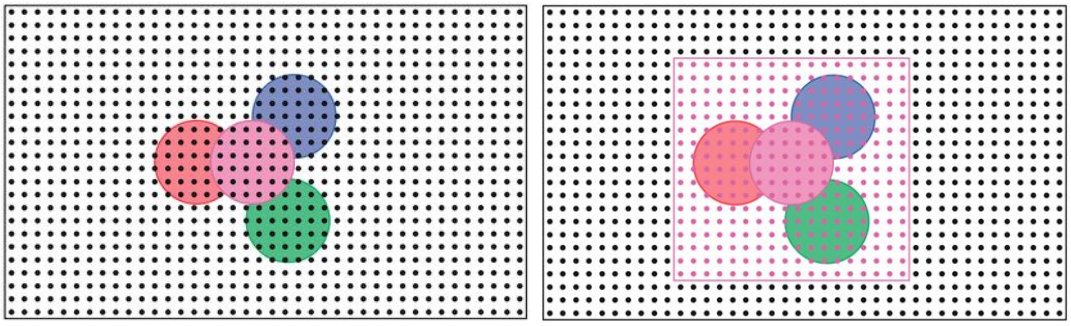

Figure 2.4: Representation of the psinc grid covering the entire simulation cell and overlapping, localised, NGWF spheres (left). The pink FFTbox (right) illustrates the smaller subspace in which FFTs can be safely calculated due to the localisation of the basis set. Images have been reproduced from reference [247]
.

of the system such as the kinetic energy, charge density and local potential integral [246]. As the NGWFs are localised real space functions, their respective reciprocal space functions are smooth. This means that, unlike in the case of plane waves, the FFTs can be partitioned and performed on smaller subspaces of the total simulation cell; each of these partitions is called an FFTbox.

The simulation cell is divided into equally sized FFTbox parallelepipeds, each containing an equal number of psinc grid points and being commensurate with the size of the simulation cell. As shown in Figure 2.4, the FFTboxes are constructed so that they totally encompass adjacent overlapping NGWFs, making the evaluation of FFTs independent of the simulation cell size. The NGWFs are projected into the FFTbox via,

$$O \approx \langle \phi_\beta | \hat{\mathcal{P}}^\dagger_{(\beta\alpha)} \, \hat{O} \, \hat{\mathcal{P}}_{(\beta\alpha)} | \phi_\alpha \rangle \,, \tag{2.81}$$

where O is the result of some operator $\hat{O}$ and $\hat{\mathcal{P}}$ is the projector, centred in the FFTbox for overlapping NGWFs $(\beta\alpha)$.

Once the calculation of the expectation value is complete, resultant values can be back-projected into the simulation cell. The computation iterates over all of the FFTboxes until the (real) space spanned by the NGWFs has been accounted for completely, in this way increasing the size of the vacuum region does not lead to an increase in computational load as would be the case for plane wave DFT where FFTs are carried out on

the entire simulation cell. Furthermore, the fact that the FFTboxes are not dependent on the size of the cell, but on the the size of the system, means that the number of computational operations to be carried out scales with the number of atoms. Therefore through the use of localised non-orthogonal basis functions and FFTboxes $\mathcal{O}(N)$ scaling can be achieved.

2.3.4 Calculation of the total energy

In ONETEP the total energy, which is a functional of the $\rho(\mathbf{r}, \mathbf{r}')$, is optimised via two nested loops, see Figure 2.5,

$$E^0 = \min_{\hat{\rho}} E\left[\hat{\rho}\right], \tag{2.82}$$

$$= \min_{\{C_{klm,\alpha}\}} \varepsilon\left[\{C_{klm,\alpha}\}\right], \tag{2.83}$$

where,

$$\varepsilon\left[\{C_{klm,\alpha}\}\right] \equiv \min_{\{K^{\alpha\beta}\}} E\left[\{K^{\alpha\beta}\}; \{C_{klm,\alpha}\}\right]. \tag{2.84}$$

In the outer loop the expansion coefficients, $C_{klm,\alpha}$ see Equation (2.79), of the NGWFs are optimised while the $K^{\alpha\beta}$ is fixed. Variational minimisation of $C_{klm,\alpha}$ allows ONETEP to optimise the basis set in-situ. This means that although the NGWFs are initialised as atom centred functions, their optimisation on a non nuclei-coordinate dependent grid allows them to evolve to account optimally for the various electronic hybridisation states and chemical bonding environments. For sufficiently large cutoff radii this enables simulation accuracy equivalent to plane waves. In the inner loop, the $K^{\alpha\beta}$ is pushed towards idempotency by the purification schemes [255–257]. These two loops are iterated to a user specified self-consistency threshold for the ground state total energy.

2.3.5 Calculation of Pulay forces

According to the Hellmann-Feynman theorem [236, 237], the force acting on a nucleus, $\mathbf{F}_{\mathbf{R}_\mathcal{I}}$, is obtainable from the derivative of the energy with respect to atomic coordinate

$$\mathbf{F}_{\mathbf{R}_\mathcal{I}} = -\frac{\partial E}{\partial \mathbf{R}_\mathcal{I}} \tag{2.85}$$

The Hellmann-Feynman theorem holds for the true ground-state electronic wave function, an object that can only be numerically approximated via the variational DFT

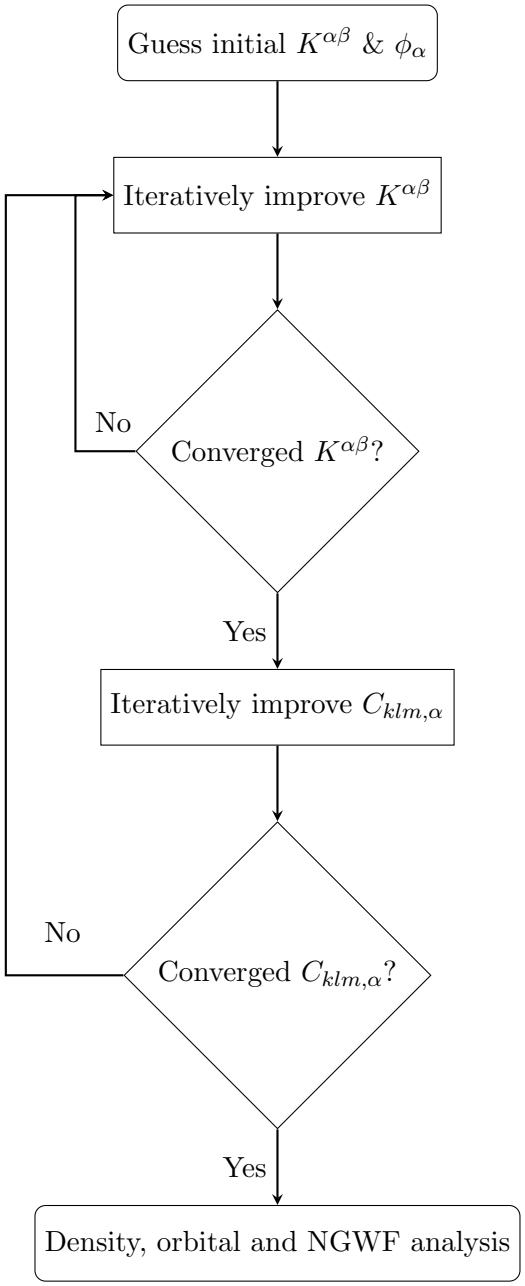

Figure 2.5: A flow diagram highlighting the optimisation of the total energy during a ONETEP calculation via a nested loop. In the inner loop, the $K^{\alpha\beta}$ is optimised with fixed ϕ_α subject to idempotency and normalisation. In the outer loop, the expansion coefficients $C_{\alpha\beta}$ of the ϕ_α are optimised with respect to $K^{\alpha\beta}$

approach. Instead, as noted in [265], for some trial wave function expanded in a basis

$$|\varphi_{\text{trial}}(\mathbf{r})\rangle = \sum_i c_i \, |\phi_i\rangle \, , \tag{2.86}$$

the energy derivative is somewhat more complex

$$\mathbf{F}_{\mathbf{R}_\mathcal{I}} = -\frac{\mathrm{d}E}{\mathrm{d}\mathbf{R}_\mathcal{I}} = -\left[\frac{\partial E}{\partial \mathbf{R}_\mathcal{I}} + \sum_i \frac{\partial E}{\partial c_i}\frac{\partial c_i}{\partial \mathbf{R}_\mathcal{I}} + \sum_i \int \mathrm{d}\mathbf{r} \frac{\delta E}{\delta \phi}(\mathbf{r}) \frac{\partial \phi(\mathbf{r})}{\partial \mathbf{R}_\mathcal{I}}\right]. \tag{2.87}$$

The additional terms, called Pulay forces, that arise from the numerical representation of the wave function, are terms containing derivatives with respect to the basis set expansion coefficients and the basis functions. In cases where the basis functions are independent from the nuclear coordinates, i.e. in plane wave DFT

$$\frac{\partial \phi(\mathbf{r})}{\partial \mathbf{R}_\mathcal{I}} = 0. \tag{2.88}$$

Furthermore, for sufficiently converged calculations the following condition is also true:

$$\frac{\partial c_i}{\partial \mathbf{R}_\mathcal{I}} = 0. \tag{2.89}$$

Therefore, in plane wave simulations the terms corresponding to the Pulay forces vanish and the atomic forces can be calculated using Equation (2.85).

In the ONETEP formalism that has been built up in this Chapter, the total force (containing all Pulay terms) is written in terms of the density kernel and psinc expansion coefficients [266]

$$\frac{\mathrm{d}E}{\mathrm{d}\mathbf{R}_\mathcal{I}} = -\left[\frac{\partial E}{\partial \mathbf{R}_\mathcal{I}} + \sum_i \frac{\partial E}{\partial K^{\alpha\beta}}\frac{\partial K^{\alpha\beta}}{\partial \mathbf{R}_\mathcal{I}} + \sum_\alpha \sum_{klm} \frac{\partial E}{\partial C_{klm,\alpha}}\frac{\partial C_{klm,\alpha}}{\partial \mathbf{R}_\mathcal{I}}\right]. \tag{2.90}$$

Leveraging the tight purification of $\rho(\mathbf{r}, \mathbf{r}')$ by the LNV algorithm [256, 257], and the ensuing convergence of $K^{\alpha\beta}$ with respect to the total energy [267]

$$\frac{\partial K^{\alpha\beta}}{\partial \mathbf{R}_\mathcal{I}} = 0. \tag{2.91}$$

For fully delocalised NGWFs expanded on the psinc grid spanning the entire simulation cell, electronic convergence would mean that the derivative of the expansion coefficients

with respect to the nuclear positions is zero. This is equivalent to the condition for plane waves. Strict localisation of the NGWFs leads to a small, but non-negligible energy gradient [262]. Thence, the Pulay forces that must be calculated at each ionic iteration in order to obtain accurate ionic forces in ONETEP are

$$\mathbf{F}_{\mathbf{R}_\mathcal{I}}^{\text{Pulay}} = \sum_{\alpha} \sum_{klm} \frac{\partial E}{\partial C_{klm,\alpha}} \frac{\partial C_{klm,\alpha}}{\partial \mathbf{R}_\mathcal{I}}. \tag{2.92}$$

When the convergence threshold for the atomic forces is very tight, $\partial E / \partial C_{klm,\alpha} = 0$. This means that $\mathbf{F}_{\mathbf{R}_\mathcal{I}}^{\text{Pulay}}$ become negligible [266].

2.3.6 Optimisation of conduction states in ONETEP

The scheme outlined in the previous Sections jointly ensures the accuracy of plane-wave calculations and the speed of minimal basis approaches. The total energy and electronic density of a given system are obtained from the density matrix and NGWFs. Additionally eigenvalues for each of the occupied states can be accurately determined via a one-off diagonalisation of the Hamiltonian within the optimised NGWF basis. However, the eigenvalues corresponding to empty Kohn-Sham states cannot be accurately computed in this way because the DFT energy minimisation in ONETEP acts directly on occupied Kohn-Sham states only.

In spite of this, it is possible to optimise a second set of NGWFs that describe the unoccupied Kohn-Sham states using the density operator as a projector [268–270].

$$\hat{H} - \hat{\rho}\hat{H}\hat{\rho} \tag{2.93}$$

The operator is employed in such a way that it selectively zeros the energy of the valence states. To ensure optimisation of the conduction states, a rigid energetic shift is applied to make them more favourable.

$$\hat{H} - \hat{\rho}(\hat{H} - \sigma)\hat{\rho} \tag{2.94}$$

The benefit of this projection is that no energy reference is required and the density matrix, which has already been calculated for the valence state optimisation, is readily available.

The newly defined conduction overlap matrix, valence-conduction cross overlap ma-

trix, $T = \langle \phi_\alpha | \chi_\beta \rangle$, unprojected and projected conduction Hamiltonian, $(H_\chi^{(\mathrm{proj})})_{\alpha\beta}$, conduction density kernel and conduction density matrix are all represented by sparse matrices ensuring asymptotical linear-scaling computational effort.

$$(H_\chi^{\mathrm{proj}})_{\alpha\beta} = \langle \chi_\alpha | \hat{H} - \hat{\rho}(\hat{H} - \sigma)\hat{\rho} | \chi_\beta \rangle \quad (2.95)$$

$$= (H_\chi)_{\alpha\beta} - (T^\dagger K H_\phi K T) + \sigma (T^\dagger K S_\phi K T)_{\alpha\beta} \quad (2.96)$$

Minimisation of the energy expression is achieved through optimisation of the conduction NGWFs and conduction kernel following the same procedure outlined in previous sections.

$$E = \mathrm{tr}\left[M H_\chi^{\mathrm{proj}} \right] \quad (2.97)$$

2.3.6.1 Computation of optical spectra via Fermi's golden rule

Access to the optimised conduction KS states, as noted in reference [268], enables the computation of the optical absorption spectra. In ONETEP, this is achievable via linear-response time-dependent DFT (LR-TDDFT) or through the application of Fermi's golden rule [271]. Limitations of the adiabatic LDA prevent the simulation of periodic unit cells [272], meaning that in this Thesis LR-TDDFT is not considered.

Optical spectra can be calculated from the imaginary component of the dielectric function [268], $\varepsilon_2(\omega)$, as

$$\varepsilon_2(\omega) = \sum_{\alpha\beta} |\langle \chi_\beta(\mathbf{r}) | \mathbf{q} \cdot \mathbf{r} | \phi_\alpha(\mathbf{r}) \rangle|^2 \, \delta(E_\beta - E_\alpha - \hbar\omega), \quad (2.98)$$

where E_α (E_β) are the energies of the valence (conduction) states and $\mathbf{q}$ is the direction of the photon ($\hbar\omega$) polarisation. The definition of the operator $\mathbf{r}$ undefined for systems subject to periodic boundary conditions since $\varphi(\mathbf{r} + \mathbf{L}) = \varphi(\mathbf{r})$, where $\mathbf{L}$ is the system periodicity. In ONETEP $\varepsilon_2(\omega)$ is computed in the momentum space representation which can be related to the position space representation according to [268]

$$\langle \chi_\beta | \mathbf{r} | \phi_\alpha \rangle = \frac{1}{i\omega m} \langle \chi_\beta | \mathbf{p} | \phi_\alpha \rangle + \frac{1}{\hbar\omega} \langle \chi_\beta | \left[\hat{V}_{\mathrm{nl}}, \mathbf{r} \right] | \phi_\alpha \rangle \, . \quad (2.99)$$

Here $\mathbf{p}$ is the momentum operator and the commutator $\left[\hat{V}_{\mathrm{nl}}, \mathbf{r} \right]$ accomodates for the use of non-local pseudopotentials [273].

2.3.7 Hybrid MPI-OpenMP parallel implementation within ONETEP

2.3.7.1 Message passing interface and open multi-processing

To expand the use of DFT for large scale simulations on high performance computing (HPC) facilities, careful consideration of the parallelisation and scalability of the code must be taken. This means that (i) the computational tasks outlined in the previous Sections must be partitioned and computed by different processors in tandem. (ii) As the size of the computation increases to larger numbers of cores, there should minimal loss of efficiency, this is the so-called *weak scaling*. (iii) There should be minimal loss of efficiency for increasing core counts at fixed problem size, this is known as *strong scaling*. This section will discuss how, through a combination of parallel strategies, ONETEP achieves strong scaling up to the point of multiple cores per atom.

Modern DFT codes make use of multi-node and multicore HPC architectures by means of parallel code, generally using the message-passing interface (MPI) [274, 275]. MPI is a divide-and-conquer parallel programming approach, where recursive serial tasks are broken up and passed to processes that execute the same block of code simultaneously. In the simplest form, each MPI process is allocated one core for computation. However, depending on memory demands and subject to performance optimisation, other configurations are possible. Once the parallel computation is complete the data is collected and the root process continues. Importantly, each MPI process is allocated its own memory, and performs computation on its own data, with intercore communication strictly controlled by the code. MPI implementations allow (DFT-)codes to scale well up to thousands of processes, however, for fixed problem size the performance saturates at large core counts.

To overcome this limitation, ONETEP employs an additional layer of open Multi-Processing (OpenMP) over the existing MPI parallelisation [276]. OpenMP is a different parallelisation strategy, which upon execution spawns threads that work simultaneously and all have shared memory [277,278]. Rather than making extensive use of the OpenMP features, the parallelisation in ONETEP is limited to specific pragmas that address the performance of computational bottlenecks within the code. In Figure 2.6, the different OpenMP pragmas used are represented diagrammatically. Thread spawning is controlled by the initialisation of an OpenMP do loop: `!$OMP PARALLEL DO`, the optional tag `NUM_THREADS()` allows the user to strictly control the number of threads spawned for that specific parallel block. Thread merging operation is controlled by the analogous

`!$OMP END PARALLEL`. The solid red line at represents the operation for thread blocking, in Figure 2.6 specified as `!$OMP CRITICAL$`. In the critical region only one of the threads may work at any time while the remaining threads wait; this inputs a temporary serial region within a parallel part of the code.

2.3.7.2 Implementation in ONETEP

During any given simulation, a large proportion of the total simulation time is spent performing FFTs between real space and reciprocal space. For example, both the evaluation of the charge density and calculation of local potential integrals utilise FFTs [246]. As FFTs constitute such a large portion of the calculation, it makes sense that they should be optimised in the hybrid code.

In the MPI-only and hybrid MPI-OpenMP approaches, a space-filling curve is used to populate the underlying MPI processes [251], this controls the distribution of data pertaining to the system across the available MPI ranks. Moreover, where possible the stored data is reordered to construct block diagonal matrices, with non-zero elements along the matrix-diagonal [279]. Part of this distribution are the FFTboxes, which are grouped into batches and partitioned evenly across the MPI ranks. Rather than iterating over the whole FFT-box batch, as would be the case in the MPI-only code, the FFT-box batch is acted upon by an additional layer of OpenMP threading. Where memory and core numbers permits, nested OpenMP threading can then be used to carry out individual FFT-box operations as shown in Figure 2.6.

By understanding the underlying parallel implementation it is possible, as a user, to enhance the performance of a given simulation [276]. The overall calculation performance is architecture specific and the parameters that relate to the OpenMP threading must be tuned to the different node and memory structures. Specifically, it is important to consider that, when assigning threads, the allocated data relating to the FFTbox batches must not exceed to the total memory of each core and that the total number of threads should be lower than the total number of cores to avoid any instances of hyperthreading, which can have a dramatic negative impact on the simulation time.

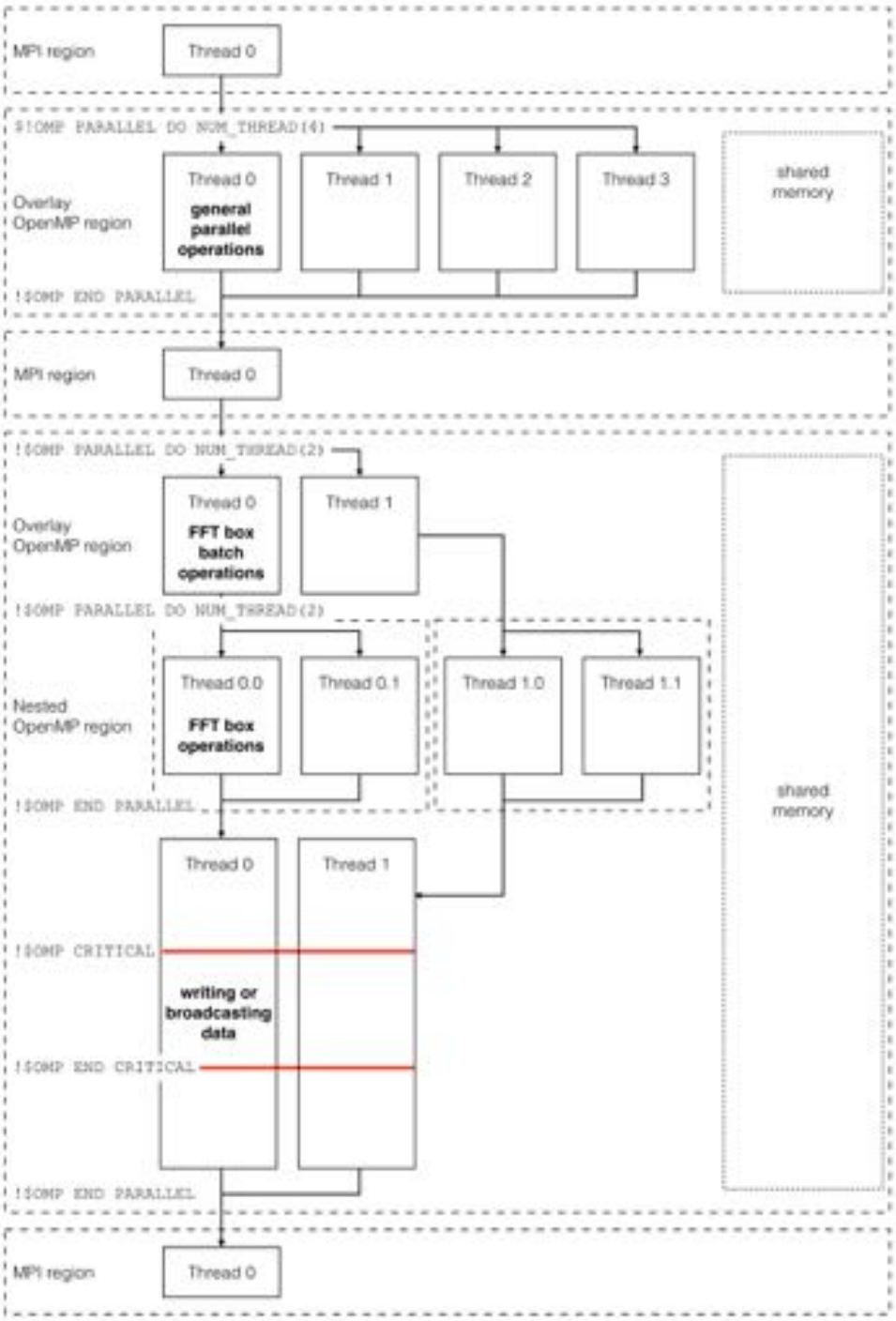

Figure 2.6: Diagrammatic representation of the OpenMP pragmas used within ONETEP showing how it is possible to spawn and merge threads and how to sequentially execute parallel code using critical regions. For each of the levels of parallelisation the associated task within ONETEP is highlighted in Thread 0.

Chapter 3

Large scale simulation of Imogolite nanotubes

Abstract

Simulation of the family of Imogolite nanotubes has been hindered by the fact that their respective unit cells range in size from 300 to 2200 atoms. This poses a challenge, especially for standard electronic structure based methods which at best scale $\mathcal{O}(N^3)$. Building on the theoretical foundations introduced in Chapter 2, this Chapter aims to show how LS-DFT can be applied to these inorganic nanotubes with favourable accuracy-viability trade offs. For two systems: (a) a one dimensional warped Aluminosilicate fragment; (b) a methylated Aluminosilicate nanotube unit cell ($N = 24$, $AlSi_{24}$-Me NT), convergence of pivotal computational parameters: the kinetic energy cutoff and geometric optimisation thresholds are shown. Furthermore, and specific to the adopted linear-scaling DFT method, investigations of the basis-set localisation radius and number of empty states which must be optimised to achieve converged band-gaps and conduction band edges are carried out. Finally, in the last section of this Chapter the smallest possible nanotube model capable of simultaneous description of a bulk-like *core* and *termination* regions is investigated.

The work in this Chapter is coauthored by E. Poli and J. Elliott and was published in March 2015 [280]. J. Elliott's contribution to the work includes the simulations relating to the aluminosilicate nanotube fragment and methylated aluminosilicate nanotube. With regards to the simulation of the terminated models, the simulations have been split evenly, however the geometric analysis has been carried out by E. Poli.

3.1 Introduction

Chapter 1 provided a detailed overview of the experimental and theoretical research into Imogolite based NTs. Experimental progress in understanding and controlling the synthesis and development of new functionalities AlSi NTs is currently unmatched by the materials modelling community. While it is true that theoretical studies have provided insight into the NT growth mechanism [128, 131], the properties of periodic defect-free AlSi and AlGe NT models [166, 168–172] and speculation into the possible formation of phosphorous- and arsenic-based analogues [281], of the work published only three DFT contributions, focused on point-defects and Fe-doping in AlSi and AlGe NTs [169, 171, 174], are available.

This leaves questions surrounding the impact of the functionalisation of the tube walls, the introduction of dopant atoms and termination-induced relaxations at the tube extremities on the properties of the NTs and prospective applications in photocatalysis unresolved. Furthermore, the polarisation of the AlSi and AlGe NT walls [177] that was recently linked to a separation of the VBE and CBE on different sides of the NT cavity [170, 171] has not yet been studied in detail. Meaning that the potential strengthening or weakening of these properties through the substitution of surface hydroxyls [144–148, 150], the encapsulation of one NT inside another of different radii in DW-AlGe NTs [137, 139, 140], cation-vacancy induced defects [282] or by the interactions with different solvents are also unknown.

The challenge associated with modelling the different members of the Imogolite family can be attributed to the size of the basic unit cells, which have more than 300 atoms for the smallest system ($AlSi_{24}$: 336 atoms [127]). This has slowed the progress that could have been made through the application of electronic structure based methods. A survey of the accessible literature highlights the detrimental accuracy-viability compromises that must be made in order to perform the simulations: DFT investigations have been restricted to one single unit cell, and in cases to fractions of the NT circumference [128, 131, 166, 168–172, 174, 281]. To reduce the overall computational resources required, simulation strategies include employment of fixed, minimally optimised basis sets [168–170, 174], exploitation of the system symmetry [172] and rest on the parametrisation of TB-DFT for analogous systems [166, 281]. There is significant input required before it will be possible to routinely simulate the nanotubes, including the effects of defects, dopants and the tube terminations accurately.

This Chapter illustrates for the first time the applicability of LS-DFT as implemented in the ONETEP code [179, 247, 251, 266] to Imogolite nanotubes, detailing the existing accuracy-viability compromises and introducing practices to maximise the efficiency of the simulations without affecting their accuracy. These results will lay the foundation for the remainder of this Thesis as well as for the future study of extended metal oxide nanostructures. The Chapter is organised as follows: First, a brief overview of the computational parameters is provided in Section 3.2. In Sections 3.3, 3.4 & 3.5 detailed derivations of the convergence of parameters critical to the adopted LS-DFT method and the size of the NT repeat unit are given. Finally, to explore the limits of the linear scaling method, this Chapter considers the minimum size of NT model needed in order to study the electronic properties of the NT extremities which provides a platform for the future investigations of longitudinal band bending effects.

3.2 Computational details

In this Chapter, calculations have all been performed making use of the PBE exchange correlation (XC-)functional [201]. Separable, Kleinman-Bylander norm-conserving pseudopotentials [283] constructed using the open source opium code [228] have been used. A kinetic energy cutoff of 1000 eV has been applied and based on the number of valence orbitals present on each atom, 4(9) valence and conduction NGWFs were used for O(Si, Al) unless stated otherwise. One NGWF has been used for H atoms. In all cases, no truncation of the density kernel has been enforced. Leveraging convergence tests carried out within the Chapter, the localisation radii of the NGWFs is 8 a_0.

Optimisation of the models has been achieved via the quasi-Newton optimisation scheme, making use of the BFGS algorithm [235]. Because of the use of non-orthogonal basis sets [263], corrections for Pulay forces have been included in geometry optimisations [267]. To prevent interactions between periodically repeated images a vacuum buffer of 15 Å has been used.

3.3 Convergence with respect to kinetic energy cutoff and NGWFs localisation radius

As explained in Chapter 2, the numerical precision of the ONETEP approach in solving the Kohn-Sham problem depends on the number and localisation radius (R_α) of the

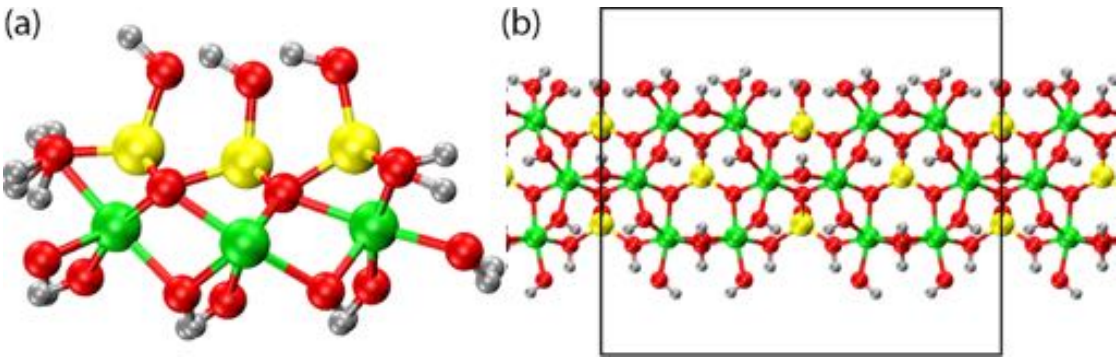

Figure 3.1: Front (a) and top (b) view of the 1-D periodic $Al_{12}Si_6O_{52}H_{44}$ AlSi NT warped fragment used for NGWFs-convergence tests. The black rectangle in (b) indicates the periodic unit cell.

NGWFs used to represent the single particle density matrix, $\rho(\mathbf{r}, \mathbf{r}')$, as well as the kinetic energy cutoff, which is used to set up the real-space grid for the psinc expansion of the NGWFs [245, 262, 284]. To fine tune the balance between simulation accuracy and costs, it is thus necessary to study the convergence of the DFT energy with respect to these computational parameters. This is especially important when modelling a material with ONETEP for the first time, as is the case for the Imo-NTs considered in this Thesis.

Our tests have been performed on the basis of two systems. The first is a model fragment of the AlSi NT with the stoichiometry $Al_{12}Si_6O_{52}H_{44}$, which was extracted from the plane-wave DFT optimised structure in Ref [171] and kept fixed in order to preserve the curvature of the NT system, Figure (3.1). Peripheral hydroxyls were replaced with H_2O molecules to maintain overall electroneutrality of the system. The second model is the periodic $AlSi_{24}$-Me NT discussed in Chapter 1 and displayed in Figure 1.8.

Starting with the NT fragment, use of a 1000 eV kinetic energy cutoff and 8 a_0 R_α for the NGWFs yields a final DFT energy converged to within 1 meV with respect to results for a 1400 eV cutoff (Table 3.1). Although tighter levels of convergence are achievable, they are obtained at the cost of increased computation time so that on balance 1000 eV cutoff emerges as a reasonable compromise.

A similar convergence rate is found for the DFT energy for R_α in the range 8-10 a_0. Owing to the the use of 4(9) NGWFs on each O (Al, Si) atom in the system, increase to R_α impacts on the simulation time more heavily than the energetic cutoff because of the

Cutoff, R (eV, a_0)	ΔE (meV Atom^{-1})	N_{it}	Δt (%)
800, 8	26.16	19	-50
1000, 8	1.09	18	-26
1200, 8	0.72	17	-17
1400, 8	0.00	15	0
1000, 8	0.91	18	-69
1000, 9	0.03	20	-58
1000, 10	0.00	32	0

Table 3.1: Convergence of the DFT energy for the one-dimensional periodic $Al_{12}Si_6O_{52}H_{44}$ fragment as a function of the kinetic energy cutoff (eV) and the NGWFs-localisation radius (R_α, a_0). Here ΔE is the change in energy with respect to the most accurate result (1400 eV for the top half, 10 a_0 for the bottom half), N_{it} is the number of iterations required to reach NGWF convergence and Δt is the percentage speed up obtained.

larger number of psinc grid points included in the multiple NGWF localisation regions, and the ensuing increase in the number of steps required to optimise the coefficients of the NGWFs. Based on these results, use of 8 a_0 NGWFs R_α and kinetic energy cutoff of 1000 eV appears to provide the optimal trade-off between precision of the DFT solution and computation time. Timings have been measured for calculations carried out with 12 MPI processes and 2 OpenMP threads per MPI process, they have been performed on two 2.7 GHz, 12 core E5-2697-v2 (Ivy Bridge) series processors. It should be noted that observed performances may be hardware dependent, and that further refinement of the MPI-OpenMP parallelism [276] should be carried out for other HPC architectures.

The dependence of the computed DFT energy on the kinetic energy cutoff has been investigated for the inner surface methylated $AlSi_{24}$ NT that has 24 Al atoms in its circumference (R_α = 8 a_0), Figure 3.2. The results obtained for the range of cutoff energies: 800, 1000, 1300 and 1500 eV, suggests acceptable convergence (2 meV per atom) at 1000 eV. Whilst convergence to within 0.5 meV per atom can be obtained for kinetic energy cutoffs exceeding 1200 eV, it should be noted that this leads to increases of the computation time. Therefore, on the basis of these results, in the remainder of this work, unless explicitly stated, it can be assumed that the kinetic energy cutoff employed is 1000 eV and R_α is 8 a_0.

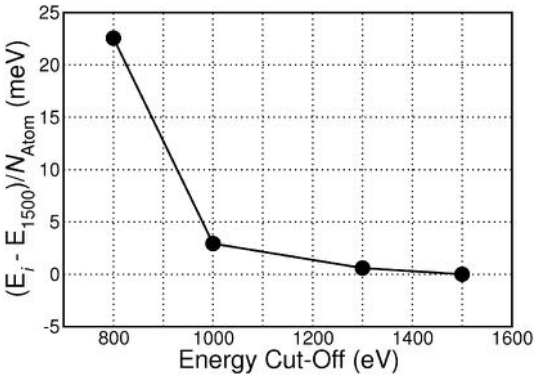

Figure 3.2: Convergence of the $AlSi_{24}$-Me NT DFT energy with respect to the adopted kinetic energy cutoff.

3.4 Optimisation of the NT periodic unit

Using the set of parameters that have been derived in Section 3.3 makes it possible to optimise repeat length along the NT axis in ONETEP, focusing on the $AlSi_{24}$ NT. Based on earlier plane-wave DFT reports regarding a weak dependence of this parameter on the reciprocal-space sampling in the simulations, with optimal convergence obtained for $2k$ points along the NT periodic direction [164], in these tests the adopted set-up is equivalent, based on a $\times 2$ supercell of the $AlSi_{24}$-Me NT along the tube axis, the number of atoms in the simulation cell is 768. The localisation radius of the NGWF was set to 8 a_0, on the basis of the convergence tests in Table 3.1.

In order to maintain the translational invariance of the system with respect to the discretised psinc grid (avoiding the emergence of the so-called *egg-box* effect [285, 286], which is the breakdown of translational symmetry through the representation of continuous functions on discretized grids), and following reference [249] the unit cell length along the tube axis was expanded and contracted in multiples of the psinc spacing. In each case all of the atomic positions were optimised to within a 0.05 eV $Å^{-1}$ convergence threshold.

The energy for the optimised geometries is plotted in Figure (3.3) as a function of the unit cell vector along the NT axis, c. Quadratic fitting of the calculated values suggests an energy minimum for $c = 8.62 \pm 0.01$ Å, which is very close to the optimised c-value for the $AlSi_{24}$ NT (8.68 ± 0.01 Å [171]), suggesting a predominant role

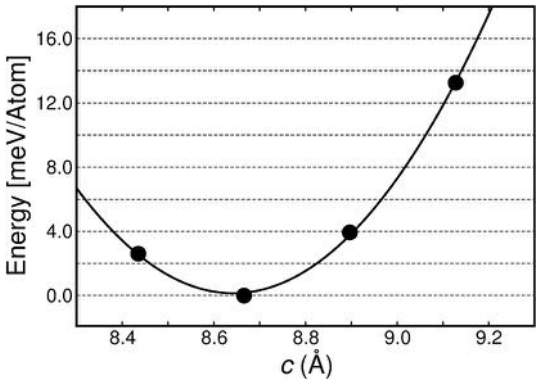

Figure 3.3: Plot of the energy of the optimised $AlSi_{24}$-Me NT as a function of the tube repeat unit length c. The continuous line shows the result of a quadratic fitting to the computed energies.

of the aluminium-hydroxide backbone rather than the interior-silanol hydrogen bonding network or methyl groups in controlling the optimised length of the tube, at least at PBE-level. In-line with experimental results [145], optimisation of the c-parameter and atomic positions for AlSi-Me NTs of different diameter (N) reveals the occurrence of a shallow energy minimum for diameters larger ($28 < N < 32$, depending on adopted DFT-functional and ensuing treatment of dispersion interactions) than for the $AlSi_{24}$-Me NT. These results will be reported in Chapter 4.

It is found that the geometries optimised to within an 0.1 eV $Å^{-1}$ force tolerance are converged within $< 10^{-5}$ eV $atom^{-1}$ with respect to the results of the 0.05 eV $Å^{-1}$ optimisation, suggesting an 0.1 eV $Å^{-1}$ optimisation threshold as viable for Imogolite NTs.

3.5 Optimisation of the nanotube conduction band and band gap

As described in Chapter 2, optimisation of empty KS states in ONETEP is achieved via dedicated post-processing of the optimised valence density matrix and KS states. The user has control over the number of empty KS states to be optimised as well as the number and localisation radius of the conduction NGWFs χ_α used to represent them, with fewer states and smaller NGWFs requiring less computational resources at the potential cost of accuracy [268]. This section present results on the convergence of the

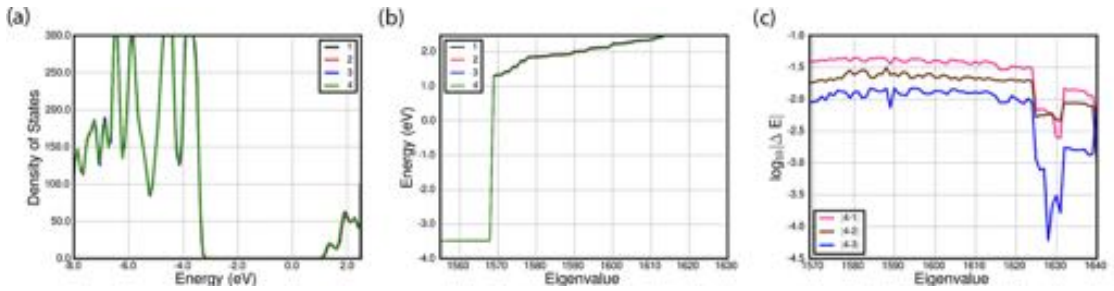

Figure 3.4: Calculated density of states for the $AlSi_{24}$-Me following optimisation of different numbers of conduction-KS states. (a) 1-4 indicate results for 10 (1), 20 (2), 30 (3) and 40 (4) optimised conduction-KS states. The energy of each KS eigenvalue is reported in (b). Panel (c) displays on a logarithmic scale, the eigenvalue energy differences between data sets 1-3 and 4.

$AlSi_{24}$-Me NT band-gap with respect to the number of empty KS states optimised for a $\times 1$ supercell at the minimum energy c-value, Figure 3.3.

The convergence of the band-gap computed in the joint valence (ϕ_α) and conduction (χ_α) representation have been tested following optimisation of 10, 20, 30 and 40 empty KS states. The results are displayed in Figure (3.4). The low-energy edge of the CB obtained with 30 optimised KS states is found to deviate by < 9 meV with respect to the results for 40 optimised empty KS states. Optimisation of 20 (10) empty KS states leads to poorer convergence of 18 (32) meV for the computed CB edge. The converged band-gap for the low energy CB edge and high energy VB edge with 40 empty KS states optimised is 4.75 eV, 0.18 eV wider than for the pristine $AlSi_{24}$ NT at the same level of theory. Thus methylation of the AlSi NT leads to an increase of the NT band-gap with respect to the hydroxylated case. Electrostatic alignment between AlSi and AlSi-Me NTs reveals a negative shift of -0.34 eV (-0.16 eV) for the VB (CB) with respect to the AlSi NT results, suggesting methylation of Imo-NTs as an effective strategy towards engineering band-gaps and band-alignments for these materials [249].

3.6 Structural relaxation of the nanotube termination and its dependence on the size of the model

With the exception of the (non-atomically resolved) transmission electron microscopy images for AlSi and AlGe NT thin-films reported in reference [126], very little is currently

known on the structure of the tubes open-ended extremities. As a result, the available insight into termination-induced effects on the NTs electronic properties and chemical reactivity or into the possible segregation of point-defects [282] at the tube extremities is effectively non-existent. Unlike in carbon NTs, which present buckyball closure of the tube ends, the AlSi and AlGe NTs are thought to remain open at the NT extremities allowing access to the inner cavity.

Although the atomic structure and electronic properties of NT extremities could, in principle, be elucidated via DFT modelling, the size of the models necessary to realistically capture the tube extremities *in vacuo* or, even more challenging, in solvent phase, has so far prevented any advance along these lines. However, DFT modelling of the tube terminations can be viably and accurately performed by exploiting the ONETEP approach. To this end the (idealised) extremities of the $AlSi_{24}$ NT are considered.

Owing to the composition of the structural unit, $(Al_2SiO_7H_4)_N$, two neutral terminations are possible for the AlSi NTs (Figure 3.5). In one case, referred to as the Al-termination from here onwards, the aluminium-hydroxide network of the NT is truncated and the terminal under-coordinated Al atoms saturated with one H_2O molecule (instead of one hydroxyl) to maintain global electroneutrality. In the other, referred to as the Si-termination, the NT ends with two hydroxyls connected to the fourfold coordinated terminal Si-atom, resulting in a Si-termination. In addition, in this case, the second hydroxyl is needed to maintain electroneutrality.

In order to simulate NT ends, a suitable model should be clearly finite (i.e. not 1-D periodic as used so far for Imo-NTs [166, 168–172, 174, 281]) and large enough to allow accurate description of both the *core* and *terminal* regions of the NT model. Although in reality, Imogolite NTs are up to 20 nm long depending on their composition [126], it is reasonable to expect the relaxation of the tube terminations to involve no more than a few nanometres from the tube end. Accordingly, rather than attempting simulation of $>$ 20 nm models, it is desirable to define the smallest possible system capable of simultaneous description of the *core* and *termination*. To this end, several models were set up on the basis of the periodically optimised NT structure. As shown in Figure 3.6, for both Al- and Si-terminations, we considered models of increasing size measured by the number of complete Al-hexagons present along the NT axis, which are accordingly labelled *hex*-3, 5 & 7. The overall stoichiometry and number of atoms is reported in Table 3.2. To prevent the occurrence of large longitudinal polarisations [287] which may

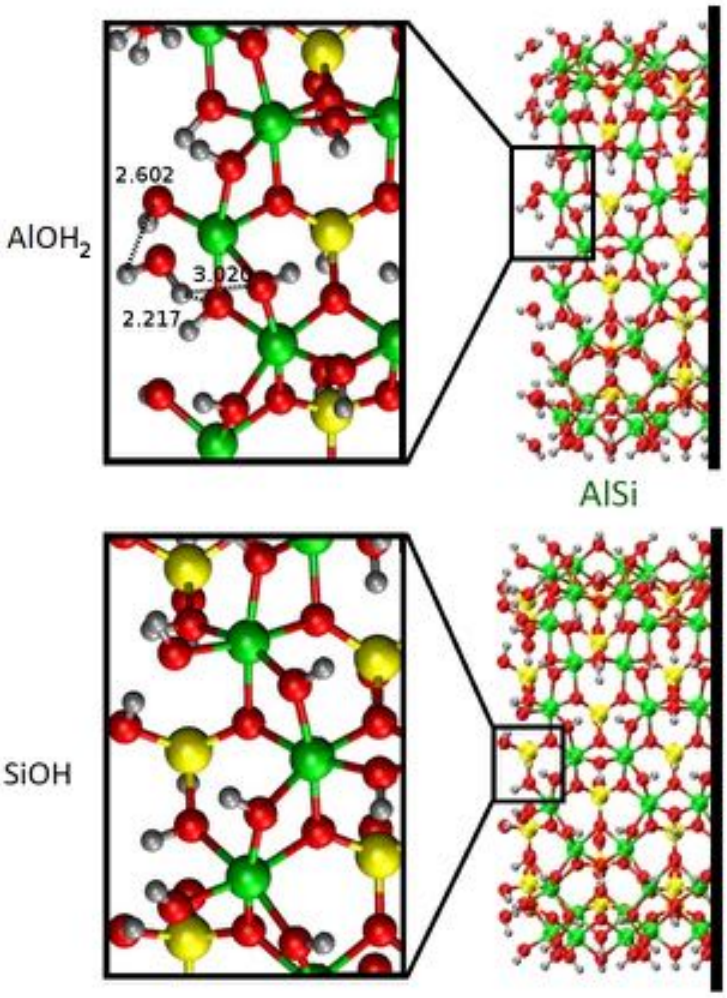

Figure 3.5: Side view of the two optimised electroneutral truncations of the AlSi NT: Al-termination (top) and Si-termination (bottom). The insets display a close-up of the terminal Al and Si atoms. In the case of Al-termination, the shortest distances (Å) between H atoms of the coordinated H_2O and the bridging hydroxyls have been marked as broken lines

	Al-Termination	Si-Termination
hex-3	$Al_{96}Si_{36}O_{348}H_{264}$ (744)	$Al_{96}Si_{60}O_{396}H_{264}$ (816)
hex-5	$Al_{144}Si_{60}O_{516}H_{360}$ (1080)	$Al_{144}Si_{84}O_{564}H_{360}$ (1152)
hex-7	$Al_{192}Si_{84}O_{684}H_{456}$ (1416)	$Al_{192}Si_{108}O_{732}H_{456}$ (1488)

Table 3.2: Stoichiometry of the considered models of the Al- and Si-terminations of the $AlSi_{24}$ NTs. The total number of atoms is reported in the brackets

affect the geometry optimisation of the systems, all finite NT models were symmetric with respect to a plane containing the innermost Si-ring (Ring 0 Figure 3.6).

The geometry of the AlSi NT finite models was optimised relaxing all the atoms of the models, apart from the Si atoms in the central ring ($R = 0$ in Figure 3.6). The latter were kept fixed at the periodically optimised geometry and used as a reference for measuring the distortion of the tube along its axis.

The NT relaxation was monitored according to three geometrical descriptors: the first one is the average ring displacement, $\langle \Delta r(R) \rangle$, defined as:

$$\langle \Delta r(R) \rangle = \frac{1}{N} \sum_{i}^{N} |\mathbf{r}_i(R) - \mathbf{r}_i^b(R)|. \tag{3.1}$$

Where $\mathbf{r}_i$ is the position of the i^{th} atom in the R^{th} (Figure 3.6) ring in the finite NT model, and $\mathbf{r}_i^b$ is the position of the same atom in the periodically repeated NT model. N refers to the number of atoms in a given ring, where a ring is defined as the group of longitudinally equivalent Si (Al) atoms and bridging OH groups plus the closest OH groups facing the tube ends. For the central ring ($R = 0$ Figure 3.6) only longitudinally equivalent Si-atoms and bridging OH were considered in computing $\langle \Delta r(0) \rangle$. For Al-terminated NTs, terminal H_2O molecules were not considered in the calculation of the average ring displacement. Negligible $\langle \Delta r \rangle$ values correspond to negligible relaxation of the ring structure from the periodically optimised geometry and are used to identify the separation between *core* and *terminal* regions of the model.

The second geometrical descriptor quantifies the radial distortion of the NT, leading to changes in the diameter of the NT rings. The average layer-resolved ring diameter $\langle D(j, R) \rangle$, calculated as,

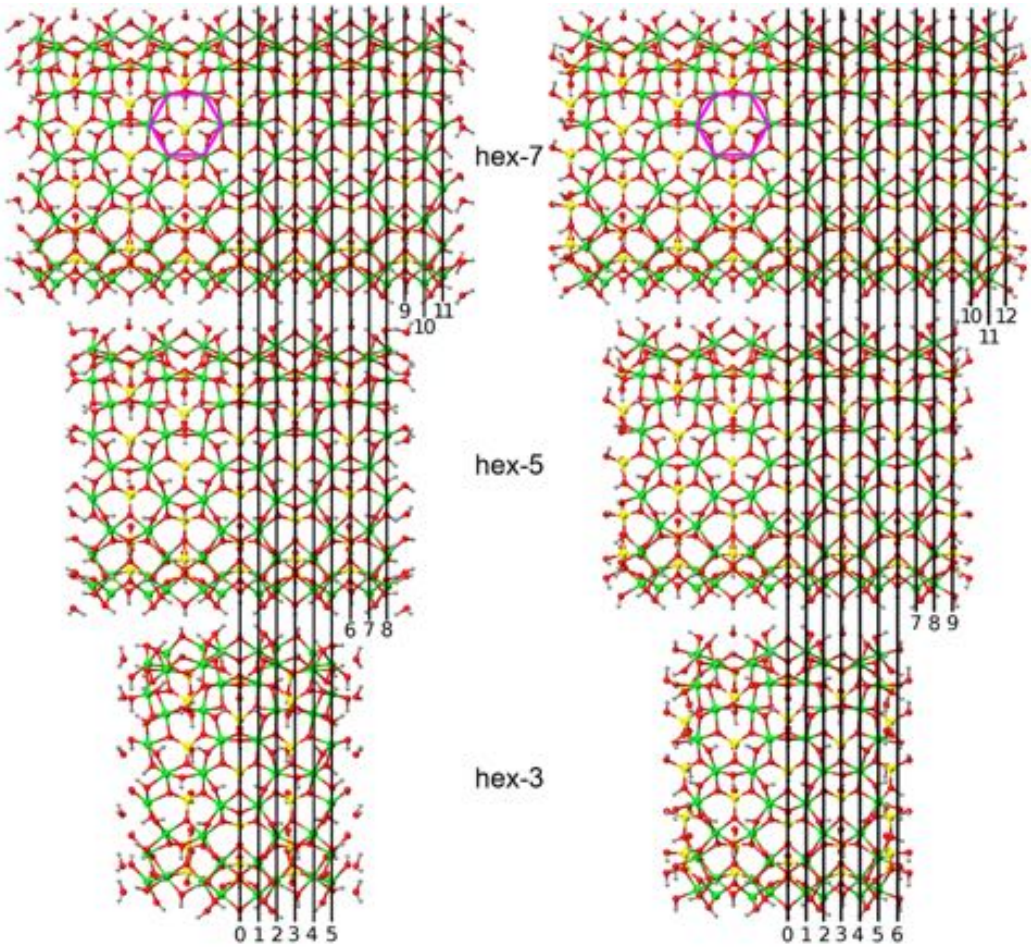

Figure 3.6: The optimised atomic structure of the considered finite models for the Al- (left) and Si- (right) terminations. The models are labelled according to the number of complete Al-hexagons present along the structure axis, this has been illustrated in the top panels via pink highlighting. Black vertical lines mark the positions of the tube rings (R = -12, ..., 0 ..., 12 from left to right) with R corresponding to the inner most Si ring. Marks for negative rings have been omitted for clarity.

$$\langle D(j,R)\rangle \;=\; \frac{1}{M}\sum_{i}^{M} d_i(j,R), \tag{3.2}$$

where $d_i(j,R)$ indicates the layer-resolved (j: H_1, O_2,..., H_7) diameter for the i^{th} pair of atoms in the R^{th} ring. Each $d_i(j,R)$ was in turn calculated as the distance between opposite atoms in the j^{th} layer of the R^{th} ring. $M = \frac{N}{2}$ is the number of layer-equivalent atom pairs in a given ring.

The third geometrical descriptor used to measure the overall longitudinal relaxation of the NT models is the tube length (L) along the NT axis (parallel to the c direction) calculated as the difference in the c-coordinate between the terminal Al (Si) rings of the Al- and Si-terminations:

$$L \;=\; \frac{1}{n}\sum_{i}^{n} \left[z_i(R_{\max}) - z_i(R_{\min})\right], \tag{3.3}$$

with n referring to the number of atoms in the Al(Si) terminal rings (twelve for the considered systems).

With an average ring displacement ($\langle\Delta r\rangle$, figure 3.7) > 0.1 Å for the inner most rings, the *hex*-3 models turns out to be too small to accommodate converged relaxation of the tube extremities in the presence of a structurally unperturbed core region. This conclusion holds regardless of the Al- or Si-termination composition. Conversely, the negligible average ring displacement ($\leq 10^{-3}$ Å) for at least the 3 (5) inner most rings of the *hex*-5 (*hex*-7) models demonstrates that the larger models are indeed suitable for describing the relaxations of the tube ends in the presence of a bulk-like *core*. It is interesting to note that, both for the *hex*-5 and *hex*-7 models, the Al-termination is calculated to induce larger structural relaxation that the Si-termination, because of the larger disruption to the aluminium-hydroxide framework and NT-VB [169].

Layer- and ring-resolved analysis of the relaxed diameters ($\langle D(j,R)\rangle$, Figure 3.8) reveals an overall tendency for the NT ends to relax inwards, making the cavity narrower at the extremities. The simulations for the larger *hex*-5 (*hex*-7) models suggest the tube-end relaxation mechanism to be affected by the specific Al- or Si-termination, leading

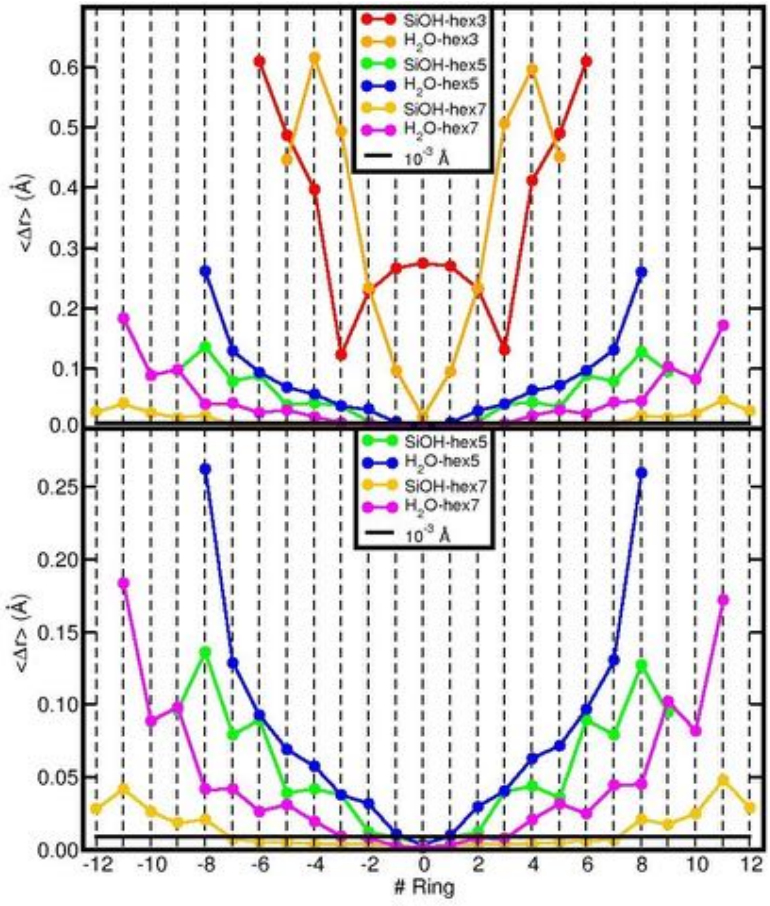

Figure 3.7: Ring-resolved average displacement ($\langle \Delta r \rangle$, Å) for the finite models of the Al- and Si-terminations (top). Close-up view of the data pertaining to *hex*-5 and -7 terminations (bottom). The black horizontal line marks the 10^{-3} Å displacement threshold.

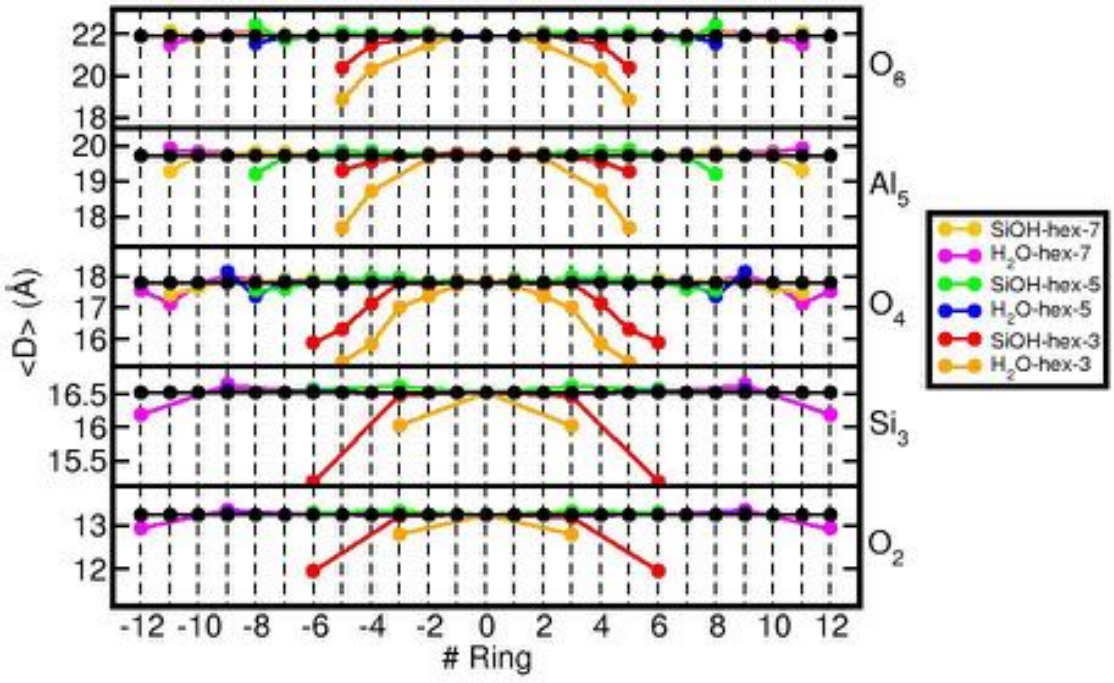

Figure 3.8: The layer-resolved ($O_{2,4,6}$, Si_3, Al_5) average ring diameter ($\langle D \rangle$, Å) for the finite models of the Al- and Si-terminations. Results for periodically optimised NT are displayed as black circles.

to different changes for radially different atoms. Whereas relaxation of the (*hex*-7) Al-termination proceeds via major contraction of the O_2, Si_3 and O_4 diameters, geometry optimisation of the Si-termination is found to affect mainly the Al_5 and O_6 layers.

In line with the calculated $\langle \Delta r \rangle$ also the calculated $\langle D(j,R) \rangle$ points out severe biases in the optimisation of the smallest *hex*-3 models. with deviations up to > 2 Å (O_4 layer) from the *hex*-5 (7) optimised terminal diameters, the *hex*-3 model turns out to be clearly too small to accurately capture the cavity narrowing at the tube extremities. These results strengthen the conclusion that, if interested in modelling termination effects in AlSi NTs in the presence of a *core* bulk-like region of the tube, the smallest viable model should be at least as long as the *hex*-5. Additionally, it should be noted that the reduction in the NT diameter (Figure 3.8) at the extremities is significantly lower for the *hex*-5 and -7 models, this supports the idea that, at least for these idealised compositions, the AlSi NTs would be open ended.

	Al-Termination	Si-Termination
hex-3	14.40 (+0.01)	16.15 (+1.16)
hex-5	23.07 (+0.01)	26.00 (+0.00)
hex-7	31.68 (+0.05)	34.35 (+0.02)

Table 3.3: Optimised length (L, Å) of the finite models of the Al- and Si-terminations. The change with respect to the length of the corresponding models (ΔL, Å) is reported in brackets. Axial NT contraction (expansion) corresponds to negative (positive) values of ΔL.

Turning to the variation in the NT length (L) following relaxation of its extremities, Table 3.3 shows the difference in the tube length between the optimised finite models and the periodically repeated counterparts (ΔL). With ΔL values < 0.05 Å, it is found that relaxation of the tube terminations to negligibly affect the length (Equation 3.3) of *hex*-5 and *hex*-7 models, regardless of the Al- or Si-termination. These results are in qualitative agreement with the appearance of the AlSi NT terminations in thin-films, as reported by TEM in reference [123], however, it should be noted that the resolution of the experimental images does not allow quantitative comparison between experiment and simulation.

In contrast to the *hex*-5 and *hex*-7 cases, the simulations suggest the specific termination of the *hex*-3 models to more strongly affect the relaxed NT length. Where as the calculated ΔL for the Al-terminated *hex*-3 model is negligibly small ($\Delta L = 0.01$ Å), the axial distortion for the Si-termination is substantially larger ($\Delta L = 1.16$ Å) as a consequence of the displacement induced on the terminal Si-atoms by reorganisation of the silanol H-bonding network at the tube extremities, Figure 3.9.

Overall the results indicate that *hex*-5 models are sufficiently extended to suitably account for the termination-induced relaxations in AlSi-NTs in the presence of a bulk-like region at the core of the model. They also demonstrate that smaller models, such as *hex*-3, can severely bias the simulation. Further work will explore the effects of terminal relaxations on the AlSi NTs electronic structure and wall-polarisation and similarities and analogies between end-relaxations in AlSi, AlGe and AlSi-Me NTs.

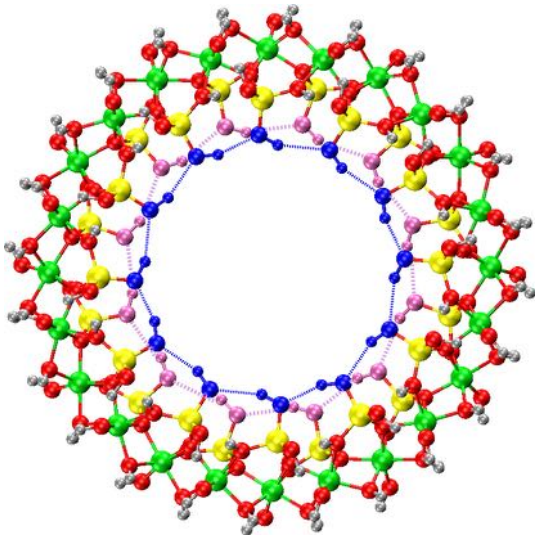

Figure 3.9: Front view of the geometry optimised Si-termination of the *hex*-3 models. The outer most (blue) and second outer most (pink) H-bonding networks between pending silanol groups have been marked by dotted lines.

3.7 Conclusions

This Chapter illustrates the applicability of the linear-scaling, *in-situ* optimised basis set, ONETEP approach to the emerging class of inorganic open-ended AlSi-based Imo-NTs. Study of accuracy-viability trade offs for representative systems of the Imo-NTs family suggests the use of 1000 eV kinetic energy cutoff and 8 a_0 localisation spheres for the optimised basis set to provide optimal accuracy-viability compromises for the geometrical relaxation of the systems. Optimisation of empty KS states requires 30 states in order for convergence of the calculated band-gap to within < 10 meV. Analysis of the optimised structure for different-sized models of the tube extremities reveal heavy biases in the simulation for systems < 2 nm (≈ 1100 atoms), making use of highly efficient DFT implementation a requirement for accurate simulation of the NT terminations. Overall, the results show that the NT extremities relax inwards leading to a narrower cavity at the tube extremities, with minimal effects on the NT length. The results presented in this Chapter will be used for the LS-DFT investigation of other members of the Imo-NT family throughout this Thesis, as well as for the future simulation of other AlSi-based functional materials.

Chapter 4

Polarisation tuning in organic-Imogolite nanotubes

Abstract

In this Chapter, theoretical insight into the recently discovered AlSi NTs with inner surface methyl functionalisation is provided. Using six exchange-correlation (XC) functionals, each differently corrected for long-range dispersion interactions (as per Chapter 2), it is shown that the energy profile for the diameter of the functionalized nanotube has a broad minimum, in line with experimental results. Results indicate that depending on the size of the diameter the nanotube band-gap increases by 0.26-0.31 eV after methylation. However, the real space separation of the valence and conduction band edges remains qualitatively unaffected with respect to the pristine tubes. For the first time for this class of materials, comparative, large-scale simulations for six different dispersion corrected XC-functionals are given. These calculations demonstrate that although there is little impact on the geometry of the tube, the choice of XC-functional can have a larger bearing on the energetic alignment of the eigenstates close to the band-gap. Lastly, the Chapter investigates the size and compositional factors governing the NT wall dipole and analyse in detail the geometric factor, the tunable nature of the Imogolite polarisation and its dependence on the NT radius. These results should be useful for better informed development of polarised-enhanced photo-catalysis.

The work in this Chapter has recently been accepted for publication in *Advanced Science* [175].

4.1 Introduction

The basic requirements of effective, visible-light, photo-catalysts were outlined in Chapter 1. These include sufficient photon absorbance energies coincidental with the visible spectrum, or ideally the Sun radiance peak (1.6-2.1 eV) [30], a propensity to separate the photo-generated electron-hole (e-h) pairs, independent *e*-*h* migration pathways to the surfaces of the catalyst and fast photo-catalyst-reactant charge transfer kinetics. Depending on the desired reaction scheme, reactants could plausibly be different for the electron (e) & hole (h) and may be situated at different surface adsorption sites, introducing additional complexity and possibilities to the engineering of candidate catalysts. Furthermore, the structuring of the photo-catalytic interfaces with the medium could also play a role in determining the catalytic activity and should not be overlooked in the development of new materials. Cheap and scalable materials that cater for these requirements are yet to be uncovered. This is, in part, due to a knowledge-gap surrounding the interplay of photo-catalyst structures, atomic compositions and properties, as well as the solvent-dependent interactions with reactants.

Chapter 1 discussed at length the different design routes to photo-catalytic materials. It is worth reiterating here that: a) structuring differently functionalized semiconducting materials in the form of one-dimensional nanotubes, nanorods and nanowires has been shown to induce anisotropies in the substrate potential [33–35]. These lead to observed enhancement in reactivity due to increased *e*-*h* separation. b) The permanent polarisation of ferroelectric substrates is understood to be advantageous for superior *e*-*h* separation and diffusion [102–104, 288]. Exploitation of this polarisation in photo-ferroelectric (ferroelectric-photovoltaic) materials results in improved photo-catalytic performance, this is especially true if the polarisation can be maintained under illumination. c) Confinement of reactants and intermediates inside nanoporous photo-catalysts is observed to markedly benefit the reaction selectivity [31, 62–64, 289–291]. These avenues represent large advances in the development of photo-catalytic technologies, yet progress along these different lines has been disconnected, and the links between polarisation-enhanced *e*-*h* separation and the selectivity of the *e* & *h* transfer processes effectively overlooked. In a first attempt to bridge this gap, the following Chapter examines how the benefits of 1-D structuring, paired with local permanent polarisations and reactant nanoconfinement could possibly be integrated into one solution based on the emerging hybrid organic-inorganic Imogolite-type AlSi-Me NTs [142, 145, 147, 150, 151].

The experimental understanding and control of Imogolite NTs has grown noticeably [123, 125, 126, 128–131, 134–137, 139, 140, 292], in particular with the definition of routes to surface-selective functionalization by organic groups [145, 147], post-synthesis functionalization [144,146,148] and synthetic strategies governing the formation of mixed $AlSi_xGe_{1-x}$ Imogolite NTs [142]. The occurrence of hydrophobic organic cavities within otherwise hydrophilic NTs gives rise to a natural chemical separation mechanism with superior performance [142, 145–148, 150, 151]. The integration of chemical separation and the proposed photo-catalytic z-scheme (see Section 1.4) opens up the potential for the design of new classes of photo-catalyst based on hybrid organic-inorganic materials. As of yet, the functionalization-induced changes to the NT curvature, polarisation and ensuing VBE-CBE separation, band alignment and optical properties have not been considered.

Chapter 4 has been organised as follows: the computational details are provided in Section 4.2. The results of the simulations are presented in Section 4.3, with the energetic profiling of different sized NTs and XC-functionals in 4.3.1 and the electronic characterisation of the tubes in 4.3.2. The evaluation of the NT wall dipole, resultant surface polarisation and comparison with current state of the art photo-ferroelectric materials is reported in Section 4.3.3.

4.2 Computational Details

In this Chapter, all simulations have been carried out using the ONETEP program [179, 266], and following the results of benchmark simulations described in the previous Chapter and [280]. For Al, Si, C and O atoms we have used four 8 a_0 NGWFs, whereas for H one single NGWF is used. The psinc basis set energy cutoff used for these simulations was 1000 eV with no truncation of the density kernel enforced. Kleinman-Bylander norm-conserving pseudopotentials [283], generated using the opium code [228], have been used to represent the core electrons. Periodic boundary conditions have been used with at least 15 Å of vacuum separating replicated images along non-periodic axes. The NGWF convergence threshold was 1×10^{-4} eV/atom and geometry has been optimised using the quasi-Newton minimisation scheme with corrections for Pulay forces, to within a force threshold of 0.05 eV/Å. Along the NT axis, the repeat length has been optimised at PBE level (8.666 Å) for all systems considered and found to be constant for the range of N (the number of units in the NT circumference). On the basis of Equation (2.98) and reference [268] the empty conduction state NGWFs have been optimised and

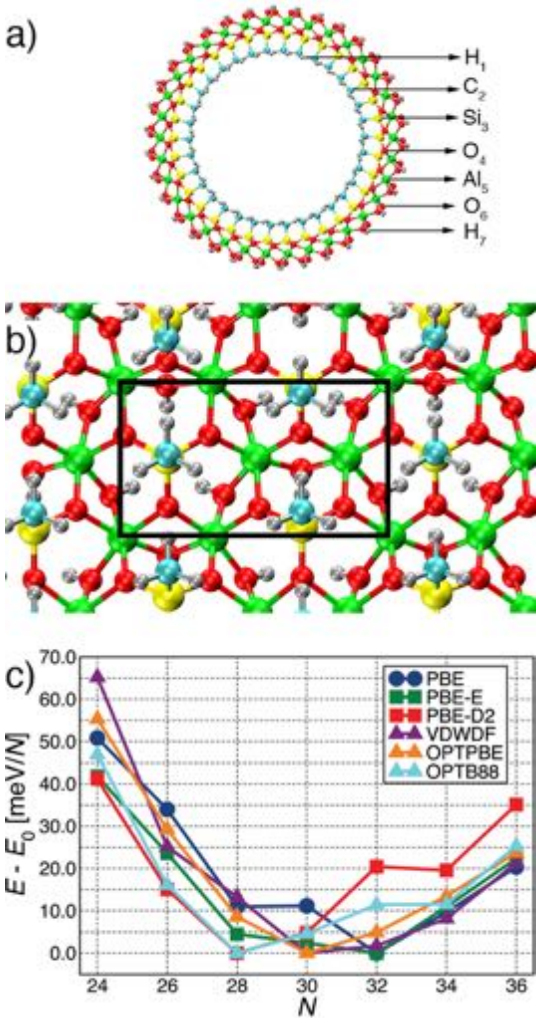

Figure 4.1: (a) Front view and adopted labelling scheme for AlSi-Me NTs, and (b) side view from inside the cavity of the $AlSi_{34}$-Me NT. The black rectangle outlines the periodic unit. (c) Relative DFT energy as a function of the number of radially non-equivalent Al atoms in the tube circumference, reference to the computed minimum for each XC-functional tested.

optical spectra calculated by means of the Fermi golden rule.

To explore the shortcomings of the PBE functional [201] in the description of long range interactions, given the presence of polarisable CH_3 groups, a complete spectrum of simulations for several dispersion corrected XC-functionals have been computed: Elstner (PBE-E) [204,207] and Grimme (PBE-D2) [206] empirical corrections and self-consistent dispersion functionals VDWDF [210,211], OPTPBE and OPTB88 [214].

4.3 Results and Discussion

4.3.1 Structural optimisation and energetic characterisation

Geometry optimisation of the AlSi-Me NTs with 24 to 36 Al-atoms (N) in the circumference uncovers a broad and relatively shallow energy minimum between $N = 28$ ($AlSi_{28}$-Me from now on) and $N = 34$ ($AlSi_{34}$-Me). This result is independent of the choice of XC-functional as seen in Figure 4.1c. For comparison to experiment, the computed inner diameters of the $AlSi_{28}$-Me and $AlSi_{34}$ NTs are 15.33 and 20.11 Å respectively. These values bracket the pore-size distributions derived from N_2 absorption isotherms, which peak at 20 Å [145], and fitting from SAX data (18.2 Å) [142]. This confirms that the AlSi-Me NTs have a larger diameter than the pristine AlSi NTs (SAXS diameter 14.8 Å [142]). The complete layer-resolved average radii for each of the XC-functionals considered are reported in Table 4.1, the average bond lengths within the AlSi-Me NTs have also been considered and are presented in Table 4.2. Despite changes in the fine-details of the $E(N)$ profile, the optimised NTs' diameter and bond-lengths are negligibly (± 0.01 Å) affected by changes to the XC-functional: covalent bonding of the aluminium hydroxide layer dominates over the dispersion interactions for the structuring of the methylated NTs. This conclusion is corroborated by the also negligible deviations (≤ 0.01 Å) between the bond-lengths in the aluminium hydroxide layers of the pristine $AlSi_{24}$ and methylated $AlSi_{24}$-Me NTs, Table 4.2.

	H_1	C_2	Si_3	O_4	Al_5	O_6	H_7
$N = 24$							
PBE	12.48 ± 0.01	13.24 ± 0.01	16.90 ± 0.01	18.17 ± 0.04	20.08 ± 0.01	22.25 ± 0.05	23.45 ± 0.04
PBE-E	12.48 ± 0.01	13.24 ± 0.01	16.90 ± 0.01	18.17 ± 0.04	20.08 ± 0.01	22.25 ± 0.05	23.45 ± 0.04
PBE-D2	12.48 ± 0.01	13.24 ± 0.01	16.90 ± 0.01	18.17 ± 0.04	20.08 ± 0.01	22.25 ± 0.05	23.45 ± 0.04
VDWDF	12.48 ± 0.01	13.24 ± 0.01	16.90 ± 0.01	18.17 ± 0.04	20.08 ± 0.01	22.24 ± 0.05	23.46 ± 0.04
OPTPBE	12.48 ± 0.01	13.24 ± 0.01	16.90 ± 0.01	18.17 ± 0.04	20.08 ± 0.01	22.24 ± 0.05	23.45 ± 0.04
OPTB88	12.48 ± 0.01	13.24 ± 0.01	16.90 ± 0.01	18.17 ± 0.04	20.08 ± 0.01	22.24 ± 0.05	23.45 ± 0.04
$N = 26$							
PBE	13.73 ± 0.00	14.48 ± 0.00	18.15 ± 0.00	19.43 ± 0.04	21.36 ± 0.00	23.54 ± 0.04	24.71 ± 0.05
PBE-E	13.73 ± 0.00	14.48 ± 0.00	18.15 ± 0.00	19.43 ± 0.04	21.36 ± 0.00	23.54 ± 0.04	24.71 ± 0.05
PBE-D2	13.73 ± 0.00	14.49 ± 0.00	18.15 ± 0.00	19.43 ± 0.04	21.36 ± 0.00	23.53 ± 0.04	24.71 ± 0.05
VDWDF	13.73 ± 0.00	14.49 ± 0.00	18.15 ± 0.00	19.43 ± 0.04	21.37 ± 0.00	23.53 ± 0.04	24.71 ± 0.05
OPTPBE	13.73 ± 0.00	14.50 ± 0.00	18.16 ± 0.00	19.44 ± 0.04	21.36 ± 0.00	23.53 ± 0.04	24.71 ± 0.05
OPTB88	13.73 ± 0.00	14.50 ± 0.00	18.16 ± 0.00	19.43 ± 0.04	21.36 ± 0.00	23.52 ± 0.04	24.71 ± 0.04
$N = 28$							
PBE	15.33 ± 0.03	16.10 ± 0.02	19.77 ± 0.01	21.04 ± 0.04	22.97 ± 0.01	25.15 ± 0.05	26.33 ± 0.03
PBE-E	15.33 ± 0.03	16.10 ± 0.02	19.77 ± 0.01	21.04 ± 0.04	22.97 ± 0.01	25.15 ± 0.05	26.33 ± 0.03
PBE-D2	15.35 ± 0.01	16.11 ± 0.01	19.78 ± 0.00	21.04 ± 0.04	22.97 ± 0.01	25.14 ± 0.04	26.32 ± 0.02
VDWDF	15.34 ± 0.01	16.11 ± 0.01	19.78 ± 0.01	21.05 ± 0.03	22.98 ± 0.01	25.14 ± 0.04	26.35 ± 0.03
OPTPBE	15.34 ± 0.02	16.11 ± 0.01	19.77 ± 0.01	21.04 ± 0.03	22.97 ± 0.01	25.14 ± 0.04	26.33 ± 0.03
OPTB88	15.34 ± 0.02	16.11 ± 0.01	19.78 ± 0.01	21.04 ± 0.03	22.97 ± 0.01	25.13 ± 0.04	26.33 ± 0.03
$N = 30$							
PBE	16.93 ± 0.02	17.68 ± 0.01	21.35 ± 0.00	22.61 ± 0.05	24.55 ± 0.00	26.72 ± 0.04	27.90 ± 0.05
PBE-E	16.93 ± 0.01	17.70 ± 0.01	21.39 ± 0.01	22.64 ± 0.03	24.58 ± 0.01	26.76 ± 0.04	27.95 ± 0.02
PBE-D2	16.94 ± 0.01	17.69 ± 0.01	21.36 ± 0.00	22.61 ± 0.04	24.54 ± 0.00	26.71 ± 0.04	27.88 ± 0.04
VDWDF	16.97 ± 0.02	17.74 ± 0.02	21.42 ± 0.02	22.67 ± 0.04	24.61 ± 0.02	26.77 ± 0.04	27.98 ± 0.03
OPTPBE	16.96 ± 0.02	17.73 ± 0.02	21.41 ± 0.02	22.58 ± 0.04	24.58 ± 0.02	26.75 ± 0.04	27.94 ± 0.03
OPTB88	16.93 ± 0.01	17.69 ± 0.01	21.35 ± 0.00	22.61 ± 0.05	24.53 ± 0.00	26.70 ± 0.04	27.89 ± 0.05
$N = 32$							
PBE	18.55 ± 0.02	19.32 ± 0.02	23.01 ± 0.01	24.26 ± 0.03	26.19 ± 0.01	28.37 ± 0.04	29.56 ± 0.03
PBE-E	18.53 ± 0.02	19.30 ± 0.02	22.99 ± 0.01	24.24 ± 0.03	26.18 ± 0.01	28.36 ± 0.04	29.55 ± 0.01
PBE-D2	18.53 ± 0.03	19.29 ± 0.02	22.96 ± 0.00	24.20 ± 0.05	26.14 ± 0.01	28.32 ± 0.04	29.49 ± 0.06
VDWDF	18.55 ± 0.02	19.32 ± 0.02	23.01 ± 0.02	24.26 ± 0.04	26.20 ± 0.02	28.36 ± 0.04	29.56 ± 0.02
OPTPBE	18.56 ± 0.02	19.32 ± 0.02	23.00 ± 0.01	24.24 ± 0.04	26.16 ± 0.02	28.33 ± 0.04	29.52 ± 0.02
OPTB88	18.54 ± 0.05	19.30 ± 0.02	22.96 ± 0.00	24.21 ± 0.05	26.13 ± 0.01	28.30 ± 0.04	29.50 ± 0.05
$N = 34$							
PBE	20.11 ± 0.01	20.88 ± 0.01	24.56 ± 0.01	25.79 ± 0.04	27.73 ± 0.01	29.91 ± 0.03	31.07 ± 0.04
PBE-E	20.12 ± 0.01	20.88 ± 0.01	24.56 ± 0.01	25.79 ± 0.04	27.73 ± 0.01	29.90 ± 0.03	31.07 ± 0.04
PBE-D2	20.11 ± 0.01	20.87 ± 0.01	24.56 ± 0.01	25.80 ± 0.03	27.73 ± 0.01	29.90 ± 0.03	31.07 ± 0.04
VDWDF	20.10 ± 0.01	20.87 ± 0.01	24.56 ± 0.01	25.80 ± 0.03	27.74 ± 0.01	29.91 ± 0.03	31.10 ± 0.04
OPTPBE	20.12 ± 0.01	20.88 ± 0.01	24.56 ± 0.01	25.80 ± 0.04	27.73 ± 0.01	29.90 ± 0.03	31.08 ± 0.04
OPTB88	20.12 ± 0.01	20.89 ± 0.01	24.56 ± 0.01	25.80 ± 0.04	27.72 ± 0.01	29.89 ± 0.03	31.07 ± 0.04
$N = 36$							
PBE	21.69 ± 0.02	22.46 ± 0.01	26.15 ± 0.01	27.38 ± 0.04	29.32 ± 0.01	31.50 ± 0.04	32.70 ± 0.05
PBE-E	21.69 ± 0.02	22.46 ± 0.01	26.15 ± 0.01	27.38 ± 0.04	29.32 ± 0.01	31.50 ± 0.04	32.70 ± 0.05
PBE-D2	21.72 ± 0.00	22.48 ± 0.01	26.16 ± 0.01	27.38 ± 0.04	29.32 ± 0.01	31.49 ± 0.03	32.67 ± 0.03
VDWDF	21.70 ± 0.01	22.47 ± 0.01	26.15 ± 0.01	27.39 ± 0.03	29.33 ± 0.01	31.50 ± 0.03	32.71 ± 0.04
OPTPBE	21.71 ± 0.01	22.48 ± 0.01	26.16 ± 0.01	27.39 ± 0.04	29.32 ± 0.01	31.49 ± 0.03	32.70 ± 0.04
OPTB88	21.70 ± 0.01	22.47 ± 0.01	26.15 ± 0.01	27.39 ± 0.04	29.32 ± 0.01	31.48 ± 0.03	32.70 ± 0.05

Table 4.1: Average atom-resolved diameters and standard deviation (Å) for the optimised NT-models and considered XC-functionals. The adopted labelling corresponds to the atom element and radial layer, see Figure 4.1a. N is the number of radially nonequivalent Al-atoms contained within the NT circumference.

	H_1-$C(O)_2$	$C(O)_2$-Si_3	Si_3-O_4	O_4-Al_5	Al_5-O_6	O_6-H_7
$AlSi_{24}$ PBE	0.97 ± 0.00	1.65 ± 0.00	1.65 ± 0.01	1.94 ± 0.02	1.89 ± 0.01	0.96 ± 0.00
$N = 24$						
PBE	1.09 ± 0.00	1.84 ± 0.00	1.66 ± 0.01	1.95 ± 0.01	1.90 ± 0.01	0.96 ± 0.00
PBE-E	1.09 ± 0.00	1.84 ± 0.00	1.66 ± 0.01	1.95 ± 0.01	1.90 ± 0.01	0.96 ± 0.00
PBE-D2	1.09 ± 0.00	1.84 ± 0.00	1.66 ± 0.01	1.95 ± 0.01	1.90 ± 0.01	0.96 ± 0.00
VDWDF	1.08 ± 0.00	1.84 ± 0.00	1.66 ± 0.01	1.95 ± 0.01	1.90 ± 0.01	0.96 ± 0.00
OPTPBE	1.09 ± 0.00	1.84 ± 0.00	1.66 ± 0.01	1.95 ± 0.01	1.90 ± 0.01	0.96 ± 0.00
OPTB88	1.09 ± 0.00	1.84 ± 0.00	1.66 ± 0.01	1.95 ± 0.01	1.90 ± 0.01	0.96 ± 0.00
$N = 26$						
PBE	1.09 ± 0.00	1.85 ± 0.00	1.66 ± 0.01	1.94 ± 0.01	1.89 ± 0.01	0.96 ± 0.00
PBE-E	1.09 ± 0.00	1.85 ± 0.00	1.66 ± 0.01	1.94 ± 0.01	1.89 ± 0.01	0.96 ± 0.00
PBE-D2	1.09 ± 0.00	1.85 ± 0.00	1.66 ± 0.01	1.94 ± 0.01	1.89 ± 0.01	0.96 ± 0.00
VDWDF	1.08 ± 0.00	1.83 ± 0.00	1.66 ± 0.01	1.95 ± 0.01	1.89 ± 0.01	0.96 ± 0.00
OPTPBE	1.09 ± 0.00	1.85 ± 0.00	1.66 ± 0.01	1.94 ± 0.01	1.89 ± 0.01	0.96 ± 0.00
OPTB88	1.09 ± 0.00	1.84 ± 0.00	1.66 ± 0.01	1.94 ± 0.01	1.89 ± 0.01	0.96 ± 0.00
$N = 28$						
PBE	1.09 ± 0.00	1.85 ± 0.00	1.66 ± 0.01	1.94 ± 0.01	1.89 ± 0.01	0.96 ± 0.00
PBE-E	1.09 ± 0.00	1.85 ± 0.00	1.66 ± 0.01	1.94 ± 0.01	1.89 ± 0.01	0.96 ± 0.00
PBE-D2	1.09 ± 0.00	1.85 ± 0.00	1.66 ± 0.01	1.94 ± 0.01	1.89 ± 0.01	0.96 ± 0.00
VDWDF	1.08 ± 0.00	1.85 ± 0.00	1.66 ± 0.01	1.95 ± 0.01	1.89 ± 0.01	0.96 ± 0.00
OPTPBE	1.09 ± 0.00	1.85 ± 0.00	1.66 ± 0.01	1.94 ± 0.01	1.89 ± 0.01	0.96 ± 0.00
OPTB88	1.09 ± 0.00	1.85 ± 0.00	1.66 ± 0.01	1.94 ± 0.01	1.89 ± 0.01	0.96 ± 0.00
$N = 30$						
PBE	1.09 ± 0.00	1.85 ± 0.00	1.66 ± 0.01	1.95 ± 0.01	1.89 ± 0.01	0.96 ± 0.00
PBE-E	1.09 ± 0.00	1.85 ± 0.00	1.66 ± 0.01	1.95 ± 0.01	1.89 ± 0.01	0.96 ± 0.00
PBE-D2	1.09 ± 0.00	1.85 ± 0.00	1.66 ± 0.01	1.94 ± 0.01	1.89 ± 0.01	0.96 ± 0.00
VDWDF	1.08 ± 0.00	1.85 ± 0.00	1.66 ± 0.01	1.95 ± 0.01	1.89 ± 0.01	0.96 ± 0.00
OPTPBE	1.09 ± 0.00	1.85 ± 0.00	1.66 ± 0.01	1.95 ± 0.01	1.89 ± 0.01	0.96 ± 0.00
OPTB88	1.09 ± 0.00	1.85 ± 0.00	1.66 ± 0.01	1.94 ± 0.01	1.89 ± 0.01	0.96 ± 0.00
$N = 32$						
PBE	1.09 ± 0.00	1.85 ± 0.00	1.67 ± 0.01	1.95 ± 0.01	1.89 ± 0.01	0.96 ± 0.00
PBE-E	1.09 ± 0.00	1.85 ± 0.00	1.67 ± 0.01	1.95 ± 0.01	1.89 ± 0.01	0.96 ± 0.00
PBE-D2	1.09 ± 0.00	1.85 ± 0.00	1.67 ± 0.01	1.95 ± 0.01	1.89 ± 0.01	0.96 ± 0.00
VDWDF	1.08 ± 0.00	1.85 ± 0.00	1.66 ± 0.01	1.95 ± 0.01	1.89 ± 0.01	0.96 ± 0.00
OPTPBE	1.09 ± 0.00	1.85 ± 0.00	1.66 ± 0.01	1.95 ± 0.01	1.89 ± 0.01	0.96 ± 0.00
OPTB88	1.09 ± 0.00	1.85 ± 0.00	1.66 ± 0.01	1.95 ± 0.01	1.88 ± 0.01	0.96 ± 0.00
$N = 34$						
PBE	1.09 ± 0.00	1.85 ± 0.00	1.67 ± 0.01	1.95 ± 0.01	1.88 ± 0.01	0.96 ± 0.00
PBE-E	1.09 ± 0.00	1.85 ± 0.00	1.67 ± 0.01	1.95 ± 0.01	1.88 ± 0.01	0.96 ± 0.00
PBE-D2	1.09 ± 0.00	1.85 ± 0.00	1.67 ± 0.01	1.95 ± 0.01	1.89 ± 0.01	0.96 ± 0.00
VDWDF	1.08 ± 0.00	1.85 ± 0.00	1.66 ± 0.01	1.95 ± 0.01	1.89 ± 0.01	0.96 ± 0.00
OPTPBE	1.09 ± 0.00	1.85 ± 0.00	1.66 ± 0.01	1.95 ± 0.01	1.88 ± 0.01	0.96 ± 0.00
OPTB88	1.09 ± 0.00	1.84 ± 0.00	1.66 ± 0.01	1.95 ± 0.01	1.88 ± 0.01	0.96 ± 0.00
$N = 36$						
PBE	1.09 ± 0.00	1.85 ± 0.00	1.67 ± 0.01	1.95 ± 0.01	1.88 ± 0.01	0.96 ± 0.00
PBE-E	1.09 ± 0.00	1.85 ± 0.00	1.67 ± 0.01	1.95 ± 0.01	1.88 ± 0.01	0.96 ± 0.00
PBE-D2	1.09 ± 0.00	1.85 ± 0.00	1.67 ± 0.01	1.95 ± 0.01	1.89 ± 0.01	0.96 ± 0.00
VDWDF	1.08 ± 0.00	1.85 ± 0.00	1.67 ± 0.01	1.95 ± 0.01	1.88 ± 0.01	0.96 ± 0.00
OPTPBE	1.09 ± 0.00	1.85 ± 0.00	1.67 ± 0.01	1.95 ± 0.01	1.88 ± 0.01	0.96 ± 0.00
OPTB88	1.09 ± 0.00	1.85 ± 0.00	1.67 ± 0.01	1.95 ± 0.01	1.88 ± 0.01	0.96 ± 0.00

Table 4.2: Average layer-resolved bond lengths and their standard deviations (Å) for optimised NT models and considered XC-functionals. The adopted labelling corresponds to the atom element and the subscript suffix numbers the radial layer (see Figure 4.1a. N is the number of radially non-equivalent Al-atoms in the NT-circumference. The PBE results for the pristine $AlSi_{24}$ NT are reported for comparison.

4.3.2 Electrostatic alignment of band edges and electronic characterisation

Appropriate alignment between the electronic bands of a photo-catalyst and the e (h) acceptor states of reactants is critical for viable e (h) transfer and possible photo-reduction (oxidation) chemistry. Although interface structuring and charge redistribution can greatly affect the electronic alignment between photo-catalysts and reactants [20, 293–299], the position of the photo-catalyst band edges with respect to the vacuum level can be used as a first approximation to the photo-catalyst photo-oxidation (reduction) energy drive, especially if compared to the results of known photo-catalysts.

Figure 4.2a shows the vacuum-aligned VBEs and CBEs for the considered $AlSi_N$-Me NTs. Within deviations of 0.09 eV or less, the computed VBEs and CBEs for the $AlSi_N$-Me NTs, and the corresponding energy drive towards photo-reduction and oxidation, are found to depend weakly on the NT diameter and curvature. Despite negligible effects on the optimised geometry (Tables 4.1 & 4.2), explicitly non-local dispersion XC-functionals (vdwDF, OPTPBE and OPTB88) yield band edges downshifted by roughly 0.2-0.3 eV with respect to the results of the (empirically corrected) semi-local functionals.

At the PBE level, the computed band gaps for the considered $AlSi_N$-Me NTs (4.70-4.75 eV depending on N, Figure 4.2) is 0.31-0.26 eV larger than for the pristine AlSi ($N = 24$) system (4.4 eV). Thus, despite the substitution of more polar hydroxyls by less polar methyl units, methylation of the AlSi NT cavity increases the systems band gap. A non-negligible, weakly diameter dependent, transfer of roughly 0.3 e/CH_3 from the aluminium hydroxide backbone to the (negatively charge) methyl groups accompanies the band gap opening Table B.1 (see Appendix). Although the computed band gaps, underestimated by the semi-local approximations to the adopted XC-functionals [195–200], are well beyond the visible light spectrum (1.6-3.1 eV), transfer of existing AlSi and AlGe Fe-doping strategies [141, 155, 158, 165] to the considered AlSi-Me NTs could be effective in reducing the AlSi-Me NT band gap to the visible range. Furthermore, when gauged against demanding selectivity and separation requirements, use of UV light (> 3.1 eV) may be profitably considered. [31, 62–64, 289–291]

Figure 4.2 compares the vacuum-aligned $AlSi_N$-Me NT band edges with those of rutile and anatase TiO_2, whose mixture is known to lead to effective H_2O photolysis [300, 301]. Notably, the $AlSi_N$-Me NTs VBEs are at least 1.59 eV (2.06 eV) higher

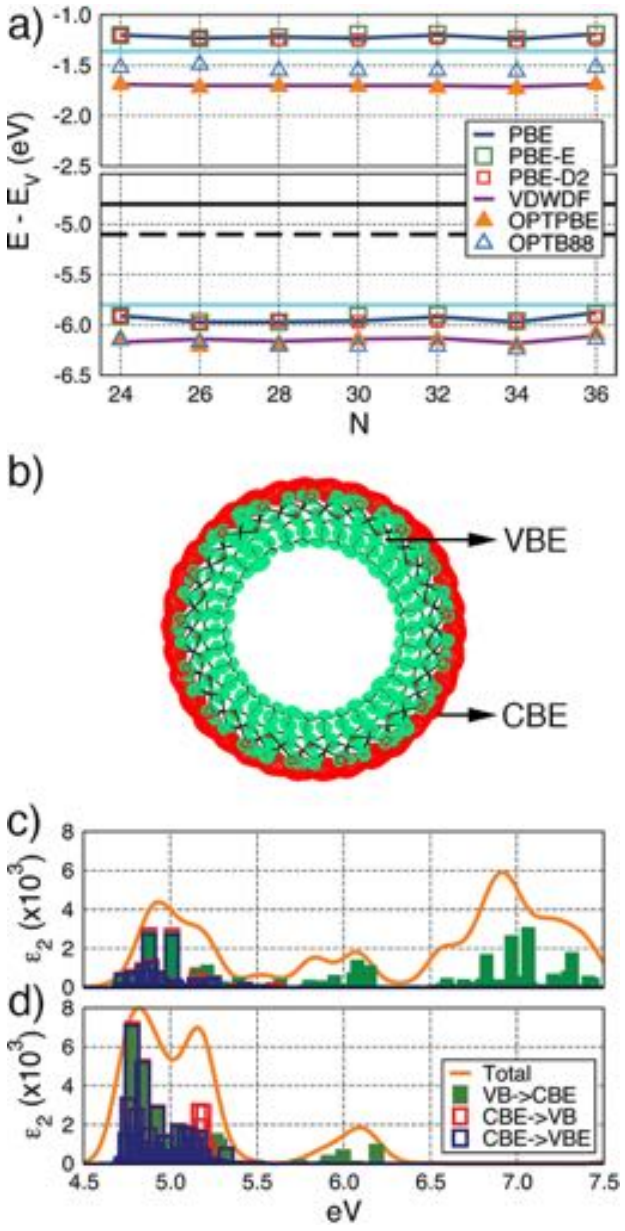

Figure 4.2: (a) Vacuum aligned VBE and CBE of the $AlSi_N$-Me NTs for the range of adopted XC-functionals. Values for the TiO_2 CBEs are marked with solid (rutile) and dashed (anatase) black horizontal lines [300]. The VBE and CBE of $AlSi_{24}$ NT (PBE) is marked by a blue horizontal line. (b) Real-space separation of the VBE (green) and CBE (red) of $AlSi_{34}$-Me NT. The imaginary component of the dielectric function (ε_2) with single-electron transition resolved analysis for $AlSi_{28}$-Me (c) and $AlSi_{34}$-Me (d).

than the rutile (anatase) VBEs. Likewise, the $AlSi_N$-Me NTs CBEs are at least 3.07 eV (3.40 eV) higher than the rutile (anatase) CBEs. Neglecting the photo-catalyst-reactant-medium interface structuring and electron transfer kinetics, these results suggest a lower (higher) H_2O direct photo-oxidation (reduction) drive for $AlSi_N$-Me NTs with respect to TiO_2. While detrimental to their possible use as a photo-oxidant, the noticeably high-energy VBEs of the $AlSi_N$-Me NTs (-6.24/-5.88 eV depending on the XC-functional, Figure 4.2a) suggests that grafting a molecular or nanoparticle photo-catalyst to the Imogolite-NTs may be a rewarding strategy to enhance *e-h* separation by promoting h-transfer and relaxation from the grafted photo-catalyst to the NT.

The weak dependence of the $AlSi_N$-Me NT band gap and absolute band alignment on the NT-diameter indicate that, while potentially beneficial for separation purposes, control of the NT-diameter by varying the ionic strength of the synthetic solution [130] does not allow band engineering for Imogolite-NTs, at least for the considered composition and range of N.

Pristine AlSi and AlGe Imogolite NTs present an intriguing real-space separation of the VBE and CBE [170,171,177], which may also be beneficial for *e-h* separation via optical charge transfer excitations across the NT walls. Results show that the separation to be qualitatively unaffected by the methylation process, the diameter of the NTs and the adopted XC-functional, Figure 4.2b and B.1. Consistent with the real-space distribution of the VBE and CBE, layer resolved analysis of the local density of states (LDOS) in Figures B.2-B.7 indicates major contributions by the C_2/O_4 (H_7) layers to the VBE (CBE).

To explore the occurrence of the optically active charge-transfer excitations across the NT-wall, the optical spectra are simulated for the $AlSi_{28}$-Me and $AlSi_{34}$-Me NTs which bracket experimental pore size distributions [142, 145, 147, 150, 151]. Notably, optical transitions involving states at the VBE and CBE on different sides of the NT-cavity (Figure 4.2b) are found to contribute strongly to the low-energy absorbance peak, Figure 4.2c, suggesting the existence of charge-transfer excitations across the tube wall. These excitations, and prospective enhancement to e-h separation (across the NT wall which has a thickness of roughly 1.1 Å) may be beneficial to sustain photostatic reactivity. Given the limitations of the adopted XC-functionals and approximations in evaluating the optical spectra, the transition energy is expected to be underestimated and possible excitonic effects missed [272]. Nevertheless, the simulated optical activity for the differently localised states of the band-edge should be meaningful.

4.3.3 Nanotube wall dipole & polarisation

Experimental and DFT results [170,171,177] indicate that, due to accumulation of negative (positive) charge on the inner (outer) tube surface, the AlSi and AlGe walls are permanently polarised. The extent to which the wall-polarisation is jointly affected by the functionalization and curvature of the NT has not been previously considered for Imogolite-NTs or, to the best possible knowledge, any NT.

4.3.3.1 Polarisation from the potential step in a co-axial cylindrical capacitor

As shown in Figure 4.3a, in spite of the NT-wall polarisation, and owing to the NT cylindrical symmetry and overall charge neutrality, the NTs present a flat electrostatic potential ($V(\mathbf{r})$) inside and outside the NT-cavity. Since the electrostatic field ($\vec{\mathbf{E}}$) is given by the negative gradient of the electrostatic potential,

$$\vec{\mathbf{E}} \;=\; -\nabla V(\mathbf{r}), \tag{4.1}$$

no electrostatic field is present inside and outside the tube. As a result, it is possible to model the electrostatics of the NT on the basis of an overall neutral co-axial (hollow) cylindrical capacitor. Gauss' theorem relates the flux of the $\vec{\mathbf{E}}$ across the closed surface S to the charge Q contained inside that surface:

$$\frac{Q}{\epsilon_0} \;=\; \oint_S \vec{\mathbf{E}}\ \mathbf{d\hat{s}}. \tag{4.2}$$

Here ϵ_0 is the vacuum permittivity and $\mathbf{d\hat{s}}$ a unit vector, locally normal to the infinitesimal surface element. Using Equation 4.2 it is possible to define three electrostatic regions within the co-axial capacitor:

Region 1: For $r < R_{\text{in}}$, where R_{in} is the radius of the inner cylinder, the electric field is 0 since the Gaussian surface of radius r' does not contain any net charge.

Region 2: For $R_{\text{in}} < r < R_{\text{out}}$, where R_{out} is the radius of the outer cylinder, the electric field is not zero since the Gaussian surface of radius r'' does contain a net charge. As the hollow cylinders are taken to be in electrostatic equilibrium,

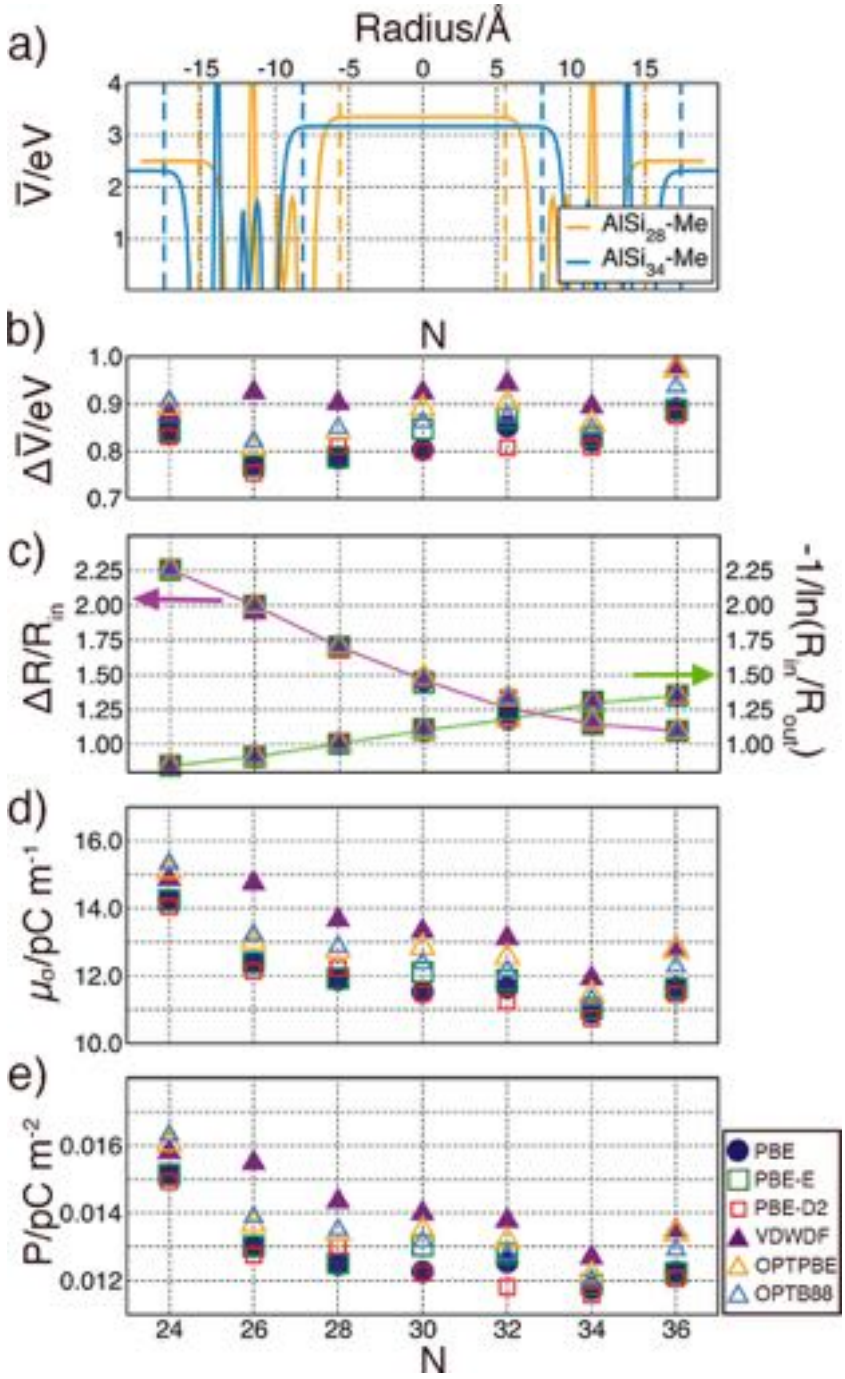

Figure 4.3: (a) (PBE) average electrostatic potential ($\bar{V}$) along the NT radius for $AlSi_{28}$-Me and $AlSi_{34}$-Me NTs. The dotted vertical lines mark the inner (R_{in}) and outer (R_{out}) NT radii as defined by the onset of the vacuum electrostatic plateaus. (b) Computed NT-wall potential step ($\Delta\bar{V}$, (c) geometric factors $\Delta R/R_{\text{in}}$ and $[-\ln(R_{\text{in}}/R_{\text{out}})]^{-1}$, (d) surface dipole density μ_σ and (e) polarisation, P, for the $AlSi_N$-Me NTs as a function of N and XC-functional.

with no net transfer of charge, the electrostatic field must lie parallel to the tube radius, with zero components along the lateral tube surface.

Region 3: For $r > R_{\text{out}}$ the electric field is zero since the Gaussian surface of radius r''' does not contain any net charge with the cylindrical capacitor being overall charge neutral.

Focus is on Region 2 to calculate the electric field and potential difference between R_{in} and R_{out} by Gauss' Flux theorem. To begin, expanding and rearranging both sides and of Equation 4.2 it can be written that

$$\frac{Q}{\epsilon_0} = -\frac{2\pi R_{\text{in}} L \sigma^{(-)}}{\epsilon_0}, \tag{4.3}$$

$$\oint_S \vec{\mathbf{E}}\ \mathbf{d\hat{s}} = 2\pi r'' L E, \tag{4.4}$$

$$-\frac{R_{\text{in}}\sigma^{(-)}}{\epsilon_0 r''} = \frac{\mathrm{d}V}{\mathrm{d}r''}. \tag{4.5}$$

Here ϵ_0 is the vacuum permittivity, L is the length of the coaxial cylinders of radius R_{in} and R_{out} and $\sigma^{(-)}$ gives the charge at the surface R_{in}. In deriving Equation 4.4 the fact that $\vec{\mathbf{E}}$ is locally parallel to $\mathbf{d\hat{s}}$ has been exploited and that between the two cylinders $\vec{\mathbf{E}}$ has to be directed parallel to the surface normal with zero components along the cylinder axis. The rearrangement to Equation 4.5 allows the integration of the electrostatic potential between R_{in} and R_{out},

$$\Delta V = V(R_{\text{in}}) - V(R_{\text{out}}), \tag{4.6}$$

$$= -\frac{R_{\text{in}}\sigma^{(-)}}{\epsilon_0} \int_{R_{\text{in}}}^{R_{\text{out}}} \frac{\mathrm{d}r''}{r''}, \tag{4.7}$$

$$= \frac{R_{\text{in}}\sigma^{(-)}}{\epsilon_0} \ln\left(\frac{R_{\text{in}}}{R_{\text{out}}}\right). \tag{4.8}$$

At this point it is worth mentioning that the overall negative sign of ΔV is consistent with $\vec{\mathbf{E}}$ being directed from the outer, positively charged, to inner, negatively charged, cylinder.

In analogy with the treatment of the surface dipole density (μ_σ) due to two opposite charged surfaces (of surface charge density σ) locally parallel and separated by a distance

d

$$\lim_{d\to 0} \sigma d \quad = \quad \mu_\sigma, \tag{4.9}$$

for infinitesimally small separation $\Delta R = R_{\text{out}} - R_{\text{in}}$, leading to $R_{\text{in}} = R_{\text{out}}$ and $|\sigma^{(-)}| = \sigma^{(+)} = \sigma$, the separation in surface charge density (σ) between the inner and outer cylinders can be described via a surface dipole density as

$$\lim_{\Delta R\to 0} \sigma \Delta R \quad = \quad \mu_\sigma. \tag{4.10}$$

This in turn can be used to write

$$\sigma = \frac{\mu_\sigma}{\Delta R} \tag{4.11}$$

Although Equation 4.9 is strictly verified for infinitesimally small separations (d) between charge-layers, it is routinely used in the modelling of potential steps due to bi-dimensional interface dipole densities in finite thickness ($d \neq 0$) junctions between different semiconductors. It should be possible to resort to the same approximation and compute the potential step across the dipole density of the NT wall of atomically finite thickness $\Delta R \neq 0$. Accordingly, and based on Equation 4.11, Equation 4.8 can be rearranged to

$$\Delta V \quad = \quad 4\pi R_{\text{in}} \frac{\mu_\sigma}{\Delta R} \ln\left(\frac{R_{\text{in}}}{R_{\text{in}} + \Delta R}\right), \tag{4.12}$$

leveraging the fact that in atomic units $\frac{1}{\epsilon_0} = 4\pi$.

For consistency with the convention in some DFT codes when calculating the electrostatic potential (Figure 4.3a) of using the electron as test charge, leading to lower (higher) electrostatic potentials for electron rich (poor) regions, the sign of ΔV needs to be changed such that,

$$\Delta V \quad = \quad -4\pi R_{\text{in}} \frac{\mu_\sigma}{\Delta R} \ln\left(\frac{R_{\text{in}}}{R_{\text{in}} + \Delta R}\right), \tag{4.13}$$

which correctly describes regions of high (low) electrostatic potential for the electron rich (poor) side of the NT cavity. Equation 4.13 allows computation of the dipole density from the step in the electrostatic potential across the NT-wall. Given the solution to the DFT problem via discretised grids, the far from homogeneous electrostatic potential

inside (and immediately outside) any material, and in analogy with standard procedure for planar dipole densities, it is convenient to angularly and longitudinally average the electrostatic potential,

$$\bar{V}(r) = \frac{1}{2\pi L}\int_0^{2\pi} \mathrm{d}\phi \int_0^{L} \mathrm{d}L\ V(r,\phi,L), \tag{4.14}$$

obtaining,

$$\Delta\bar{V} = \bar{V}(R_{\mathrm{in}}) - \bar{V}(R_{\mathrm{out}}) \tag{4.15}$$

$$= -4\pi R_{\mathrm{in}} \frac{\mu_\sigma}{\Delta R} \ln\left(\frac{R_{\mathrm{in}}}{R_{\mathrm{in}}+\Delta R}\right). \tag{4.16}$$

This last equation is used to compute μ_σ on the basis of the potential step ($\bar{V}$) between the electrostatically derived R_{in} and R_{out}, Figure 4.3.

The derivation of Equation 4.16 makes it possible to explore the influence of both the geometric factor and the interplay between R_{in} and ΔR in damping μ_σ and $\Delta\bar{V}$. As shown in Figure 4.4 large values of R_{in} and small values of ΔR maximise the surface dipole density. Furthermore, by increasing R_{in} it is possible to recover, at the asymptotic limit: $\Delta\bar{V}/\mu_\sigma = 4\pi$.

4.3.3.2 Size and composition dependence of nanotube polarisation

Rearranging Equation 4.16 it is possible to obtain an expression for μ_σ,

$$\mu_\sigma = -\frac{\Delta\bar{V}}{4\pi}\frac{\Delta R}{R_{\mathrm{in}}}\frac{1}{\ln\left(\frac{R_{\mathrm{in}}}{R_{\mathrm{in}}+\Delta R}\right)} \tag{4.17}$$

with the inner (R_{in}) and outer (R_{out}) radii obtained from the onset of the vacuum-electrostatic plateaus inside and outside the NT (Figure 4.3a). $\Delta R = R_{\mathrm{out}} - R_{\mathrm{in}}$ is the electrostatic thickness of the NT-wall. For the sign convention used, positive μ_σ values indicate accumulation of negative (positive) charge at the inner (outer) surface of the NT wall, with creation of electronegative (electropositive) environment inside (outside) the NT-cavity.

The potential step, geometric factors and μ_σ for $AlSi_N$-Me are shown in Figures 4.3b-d. There is a small dependence (< 0.15 eV) of $\Delta\bar{V}$ on both the N (NT-radius) and the

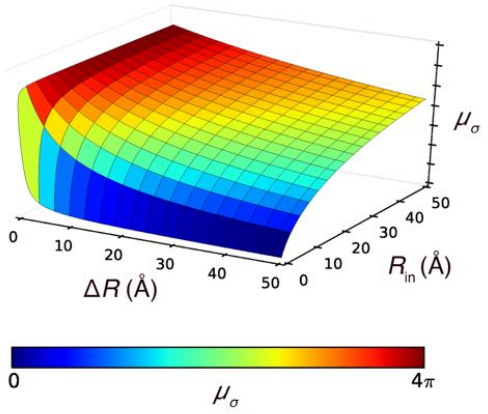

Figure 4.4: Two dimensional plot of equation 4.16, which shows the asymptotic tendency of the $\mu_\sigma/\Delta\bar{V}$ ratio for the cylindrical capacitor as a function of R_{in} and ΔR. For increasingly large R_{in} values the asymptotic value (4π) for the planar capacitor is recovered.

functional used, with explicitly non-local dispersion XC-functionals (VDWDF, OPTPBE and OPTB88) yielding slightly larger potential steps than (empirically corrected) PBE (Figure 4.3b). The sub-meV convergence of the change in $\Delta\bar{V}$ with N as a function of the psinc-grid energy cutoff and NGWF-radius rules out any numerical artifact in the computed trends presented in Chapter 2. Therefore, despite the roughly constant $\Delta\bar{V}$, and due to the decrease of the $\Delta R/R_{\text{in}}$ geometric factor with NT radius (N) dominating the increase of the $[-\ln(R_{\text{in}}/(R_{\text{in}}+\Delta R))]^{-1}$ term (Figure 4.3c), μ_σ is found to decrease for $AlSi_N$-Me NTs of larger radius (Figure 4.3d). Thus, the walls of the larger NTs are less polarised than the smaller ones. The positive value of μ_σ indicates that, as for the AlSi and AlGe systems [170, 171, 177], the $AlSi_N$-Me NTs present accumulation of negative (positive) charge inside (outside) the NT cavity. The decrease of μ_σ with N is coupled with a depletion of negative charge on the inner methyl group as N increases (Table B.1).

In line with chemical intuition, substitution of more polar hydroxyls by less polar methyl groups inside the cavity of the $AlSi_{24}$ NT reduces μ_σ substantially (-42%) from 22.48 pC m^{-1} ($AlSi_{24}$ NT) to 14.24 pC m^{-1} ($AlSi_{24}$-Me NT, Figure 4.3d). Based on the observed correspondence between system polarisation and favourable e-h separation [102–104, 288], the latter should be enhanced in pristine (not methylated) AlSi NTs. Maximisation of μ_σ towards enhanced e-h separation in Imogolite-NTs should accordingly target use of strongly electron attracting (donating) constituents on the inner

(outer) side of the NT-cavity. To this end, the use of chloromethyl- or other halogenated substituents, rather than methylsilane precursors, [142, 145, 147, 150, 151] may be profitably explored to enhance μ_σ while maintaining the overall hydrophobic cavity of the hybrid organic-inorganic Imogolite-NTs.

To quantitatively discuss the charge-separation in AlSi-Me NTs with respect to state-of-the-art photo-ferroelectrics and provide a better estimate of their *e*-*h* separation propensity, discussions turn to the charge separation per unit of (medium-excluded) volume i.e. the polarisation, P. To this end, the surface dipole density is integrated over the surface of the NT dipole-layer ($S = 2\pi R_{\text{av}} L$, L is the tube length) calculated from the average electrostatic radius ($R_{\text{av}} = \frac{1}{2}(R_{\text{in}} + R_{\text{out}})$, taken as the centre of the warped dipole layer.) Dividing the result by the tube volume ($V = \pi(R_{\text{out}}^2 - R_{\text{in}}^2)L$) yields the NT-dipole per unit of volume or P:

$$P = \frac{\mu_\sigma S}{V} \tag{4.18}$$

$$= \mu_\sigma \frac{2\pi \frac{1}{2}(R_{\text{in}} + R_{\text{out}})L}{\pi(R_{\text{out}}^2 - R_{\text{in}}^2)L} \tag{4.19}$$

$$= \mu_\sigma \frac{(R_{\text{in}} + R_{\text{in}} + \Delta R)}{(R_{\text{in}} + \Delta R)^2 - R_{\text{in}}^2} \tag{4.20}$$

$$\frac{\mu_\sigma}{\Delta R} = -\frac{\Delta \bar{V}}{4\pi} \frac{1}{R_{\text{in}}} \left[\ln\left(\frac{R_{\text{in}}}{R_{\text{in}} + \Delta R} \right) \right]^{-1} \tag{4.21}$$

Figure 4.3e shows that the AlSi_N-Me polarisation is one order of magnitude smaller than for standard photo-ferroelectrics ($BaTiO_3$: 0.26-0.34 C m^{-2} [302], $KNbO_3$: 0.55 C m^{-2} [100]). Given the roughly constant ΔR for the considered AlSi_N-Me NTs, the dependence of P and μ_σ on the N (NT-radius) is very similar.

Notably, the AlSi_N-Me polarisation is achieved by way of abundant and light elements (H, C, O, Al, Si) in a warped layer roughly 1 nm thick. In contrast, state of the art cubic photo-catalytic $BaTiO_3$ nanoparticles have sides on the order of 7.5 nm [103]. This may be beneficial for cost-effective use of materials in creating polarised interfaces. In addition, the non-negligible P-values for AlSi_N-Me NTs suggest use of overall dipole-free 1-D nanostructures with chemically heterogeneous 1 nm thick walls as an effective strategy to circumvent critical thickness issues in ferroelectric substrates [303–305].

Besides being potentially beneficial for e-h separation, the NTs μ_σ leads to markedly different electrostatic environments on either side of the NT-cavity ($\Delta\bar{V} \neq 0$). This can be used to modulate NT-reactants (or nanoconfined photo-catalyst-reactant) electronic alignments and affect e (h) transfer kinetics [20, 293–299]. Equation 4.17 compactly provides directions for future synthetic efforts aimed at increasing μ_σ (to the benefit of e-h separation) while simultaneously influencing the NT-reactant electronic alignment towards enhanced e (h) transfer kinetics. Owing to the geometric factors in equation 4.17, the same surface dipole density differently arranged in space can lead to a different potential step across the NT-wall. As shown in Figure 4.4 large R_{in} and small ΔR values allow maximisation of $\Delta\bar{V}$ for a given μ_σ. Conversely, the same μ_σ can lead to smaller $\Delta\bar{V}$ values, provided that R_{in} (ΔR) is decreased (increased). The extent to which this result is affected by the presence of a medium of variable ionic strength remains to be quantified and requires further research that may be stimulated with this work.

4.4 Conclusions and outlook

In conclusion, LS-DFT with six different semi-local and dispersion-corrected functionals has been used to elucidate the interplay between chemical functionalization, curvature, local permanent polarisations, band-gap, band-separation, band-alignment and the occurrence of charge-transfer excitations in an existing class of hybrid organic-inorganic nanotubes with hydrophobic interior and hydrophilic exteriors: methylated aluminosilicate Imogolite NTs. Strategies based on the generated insight have been suggested to increase the NT polarisation to values comparable with state of the art ferroelectric photo-catalytic, and to tune NT-reactant electronic alignments by altering the NT-radius and wall thickness. These results on the potential of (hybrid organic-inorganic) nanotubes for polarisation enhanced photo-catalytic applications may stimulate further experimental interest and investigations.

Chapter 5

The (co-)photocatalytic potential of Imogolite nanotubes

Abstract

The following Chapter extends the discussion of Chapter 4 by reporting on the geometric and electronic properties of Imogolite nanotubes (Imo NTs) with different compositions. The results presented illustrate the compositional dependence of the nanotubes properties, with double-walled Aluminogermanate NTs found to have the smallest band gap and largest surface dipole density and the methylated aluminosilicate nanotubes found to have the largest band gap and smallest surface dipole density. This Chapter reports on the absolute vacuum aligned band edges, and draws comparisons with the TiO_2 polymorphs rutile and anatase. To assess the capacity for photolysis by the NTs, idealised H_2O-Imo NT interfaces are considered. Results indicate a substantial energetic drive for photo-reduction of outer surface adsorbed water molecules for all of the NT compositions (excluding the DW-AlGe NTs). Furthermore, for non-methylated NTs, the simulations presented point towards photo-oxidation of H_2O molecules inside the NT cavity.

The results of this Chapter were published in January 2016 [173] and selected as a research highlight for the Institute of Physics' Lab Talk. The work has been co-authored with Emiliano Poli who was responsible for the software for analysis of the simulated optical spectra. Simulations of the nanotube models have been split evenly, J. Elliott is responsible for the computation and analysis of the NT wall surface dipole densities.

5.1 Introduction

Experimental characterisation techniques that provide time- and atom-resolution can be both extremely challenging and costly. Consequently, ever greater importance is being placed on rapidly improving accuracy and scalability of first principles simulation methods [306–310], which has become a fundamental tool for the modelling of photo-catalysts and their interfaces [33, 311–317]. This is because, with increasing accuracy and computational viability, modelling can relatively inexpensively access the atomic and electronic factors that underpin a photo-catalysts physical and chemical functionality. In addition, as highlighted by the work presented in this Chapter, computational simulations can be also used to hone in on elements otherwise inaccessible to experimental analysis. Therefore, utilisation of the computational methods could suggest new routes for the the development of novel photocatalytic strategies.

Chapter 1 outlines several experimental reports suggesting that an increased aspect ratio, present in one dimensional nanostructures (specifically nanorods), can be linked to enhanced photocatalytic activity. It is suspected that this is because of a highly anisotropic diffusion of separated e-h pairs within the materials [65, 66, 70]. The benefits of one dimensional structuring with respect to the bulk material and thin-films are also demonstrated in [67, 72, 73] whilst investigations of coated and asymmetrically functionalized one dimensional nanostructured substrates, still in their infancy, have appealing prospects for the development of enhanced photocatalytic strategies [35, 68, 69, 71, 74–80, 107].

Effective separation of the excited e-h pair plays a fundamental role in determining the viability of photocatalytic processes, this has brought about the development of photo-active ferroelectric substrates. Ferroelectric materials possess an intrinsic permanent polarisation that, in photocatalytic applications, may be used to bias the e-h relaxation resulting in efficient separation and diffusion of the charge carriers towards the photo-catalyst surfaces, these effects are now being reported in the literature [92, 100, 102–104, 318, 319] prompting growing interest in this field. Currently, the use of one dimensional ferroelectrics for photo-catalysis has not been explored, that is in spite of several studies of one dimensional ferroeletric nanotubes (NTs) and nanorods present in the literature [305, 320–334].

Alongside catalyst efficiency, cost and scalability, the chemical selectivity of the

photo-catalyst towards a specific reactant and product is a key factor that must be controlled for industrially viable synthesis and in conversion of fine-chemicals and feed-stock. Seminal work on the highly selective methane activation by microporous beta-zeolite via deep-UV photo-catalysis [31] has brought to the forefront the concept of nanoconfinement-assisted photo-catalysis. This has also now begun to receive serious attention from both experimental and theoretical communities [62–64, 289–291].

As explained in Chapter 1, these three different avenues represent highly innovative progress towards the design of photocatalytic material, yet this progress has been largely disconnected. This poses the question as to whether these three concepts could be integrated in one solution, ideally based on cheap and abundant materials. The previous two Chapters have attempted to initiate investigations along these lines by laying out methods for the simulation- and characterisation of a candidate material and rigorously exploring the curvature (strain) induced changes in the magnitude of surface polarisations. This has led to speculation on whether local polarisation of overall dipole-free nanostructures, rather than the macroscopic polarisations present in ferroelectrics, could be equally, if not more, effective in promoting e-h separation and enhanced photocatalytic activity.

In an attempt to provide, for the first time, exploration of these concepts, this Chapter investigates the electronic and optical properties of multiple members of the Imogolite (Imo) NT family that have received recent interest. In addition, this Chapter also explores the local-polarisation induced effects on interacting H_2O molecules, which can provide a preliminary insight into their photocatalytic viability.

The Chapter is organised as follows: Building on (some of) the results in Chapter 3, Section 5.2 briefly summarises the specific details of computational work carried out in this Chapter. Section 5.3 provides the results and discussions for the simulations carried out, this is split into four parts. Firstly, for the simulation of the different compositions, structural analysis is provided. Secondly, the impact of the composition on the magnitude of the NT-wall polarisation is considered. Thirdly, a characterisation of the electronic structure, absolute band alignment and optical properties of the pristine AlSi NTs as well as AlSi-Me, AlGe and DW AlGe NTs is carried out, making use of different exchange-correlation (XC-)functionals. In the final part, this work investigates the effects of the differently polarised inner and outer NT surfaces on the absolute alignment of H_2O electron acceptor and donor states for highly idealised NT/H_2O interfaces.

5.2 Computational methods

Simulations in this Chapter have been performed using the hybrid OpenMP-MPI parallel code ONETEP [179, 247, 251, 266, 276]. Modelling of the AlSi and (DW-)AlGe NTs has been carried out using the PBE XC-functional [201]. Building on the results presented in Chapter 4, methyl containing NTs have been optimised using three different XC-functionals, each differently corrected for long-ranged interactions: PBE, PBE with empirical dispersion corrections according to Grimme's D2 parametrisation [206] (PBE-D2) and via the self-consistent dispersion functional OPTB88 [214, 215]. In all cases, separable (Kleinman-Bylander) norm-conserving pseudopotentials constructed with the opium code have been used [228, 283].

The adopted kinetic energy cutoff and number of valence and conduction NGWFs, following Chapter 3 and reference [280], was 1000 eV and 4 (9) for O (Al,Si) atoms, 1 NGWF was used for H atoms. In all cases, no truncation of the density kernel has been enforced. The localisation radius for the valence (conduction) NGWFs was 8 a_0 (15 a_0). Periodic boundary conditions are applied, ensuring at least 15 Å of vacuum separation between virtual images along the non-periodic directions. Conduction NGWF optimisation has been performed on $1 \times 1 \times 2$ super-cells that are replicated along the NT axis to accommodate their extended localisation radius. The length of the periodic unit for the AlSi, AlSi-Me, AlGe and DW-AlGe NTs has previously been optimised, [171, 280] (SW-AlSi: 8.666 Å, SW-AlSi-Me: 8.666 Å, SW-AlGe: 8.627 Å, DW-AlGe: 8.627 Å).

To remove the possibility of artificial dipole formation in the simulation cells due to biases from the asymmetric distribution of H_2O molecules inside and outside the NTs, vacuum-aligned KS states have been computed for 1D-periodic simulations with truncated electrostatics in the two directions perpendicular to the tube axis, this is the cylindrical Coulomb cutoff [335, 336] approach as implemented in the ONETEP code [337]. The truncation radii (AlSi: 57.2 Å, AlSi-Me: 77.9 Å, SW-AlGe: 76.2 Å, DW-AlGe: 102.7 Å) have been checked to yield sub-meV convergence of the results.

5.3 Results and discussion

5.3.1 Characterisation of the Imogolite structures

The minimisation of the Imo NTs total energy and internal strain as a function of the number of units in the tube circumference, N, has already been thoroughly investigated

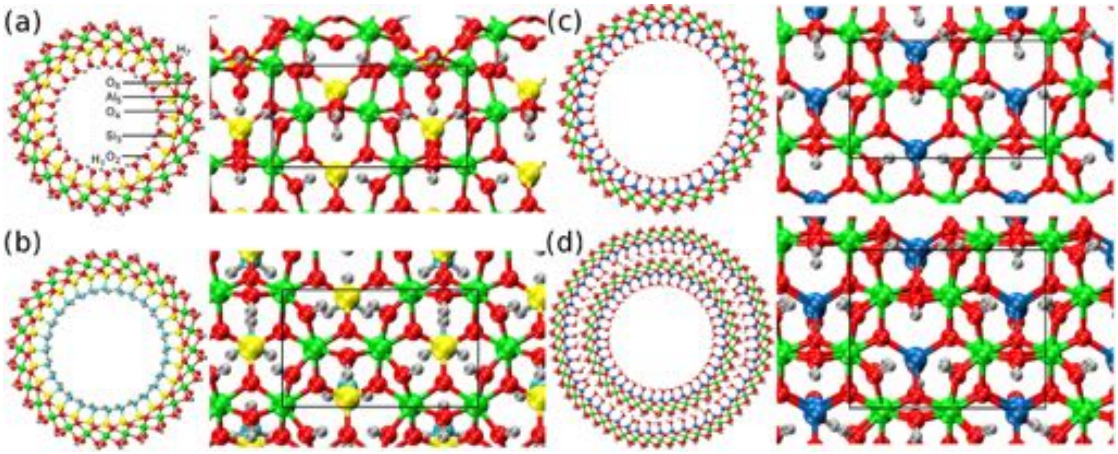

Figure 5.1: Cross section and side view of the geometry optimised (a) $AlSi_{24}$, (b) $AlSi_{28}$-Me, (c) $AlGe_{36}$ and (d) DW-$AlGe_{36,54}$ NTs. The zig-zag periodic unit along the NT axis is highlighted by the black rectangle. As has been the case in other Chapters, the adopted labelling is based on the radial layer and is displayed in panel (a), with O_2 substituted by C_2 in (b). Si_3 is substituted by Ge_3 in (c), and by $Ge_{3,in}$ and $Ge_{3,out}$ in (d). The atomic colouring scheme is Al: green, Si: yellow, Ge: blue, O: red, H: silver, C: cyan.

both computationally and experimentally. As reported in Table 1.2, these studies have often led to conflicting results [126, 134–137, 139, 166, 167, 170, 172], due to the use of different computational approaches and approximations used as well as to the different synthetic experimental protocols. Together with Chapter 1, reference [167] provides a comprehensive table highlighting disparities between different methods. The aim of this Chapter is not to contribute towards this ongoing debate, especially in the absence of atomically resolved experimental data for Imo NTs structure. Instead, the focus is to build upon the initial exploration of the relationships between Imo NTs composition, structure, polarisation and bands alignment that was introduced within the previous Chapter. To achieve this, five archetype Imo NT models have been considered, namely i) AlSi ($N = 24$, $AlSi_{24}$ from now), ii) AlSi-Me ($N = 28$, $AlSi_{28}$-Me), iii) AlSi-Me ($N = 34$, $AlSi_{34}$-Me), iv) AlGe ($N = 36$, $AlGe_{36}$), and v) DW-AlGe ($N_{in} = 36$, $N_{out} = 54$, DW-$AlGe_{36,54}$) NTs, their respective structures are shown in Figure 5.1.

For this work, the $AlSi_{24}$ and $AlGe_{36}$ NTs were selected on the basis of earlier optimisations of the AlSi (AlGe) NT-strain for tubes with $N = 24(36)$ [127, 128, 166]. The $AlSi_{28}$-Me and $AlSi_{34}$-Me were selected on the basis of results presented in Chapter 4

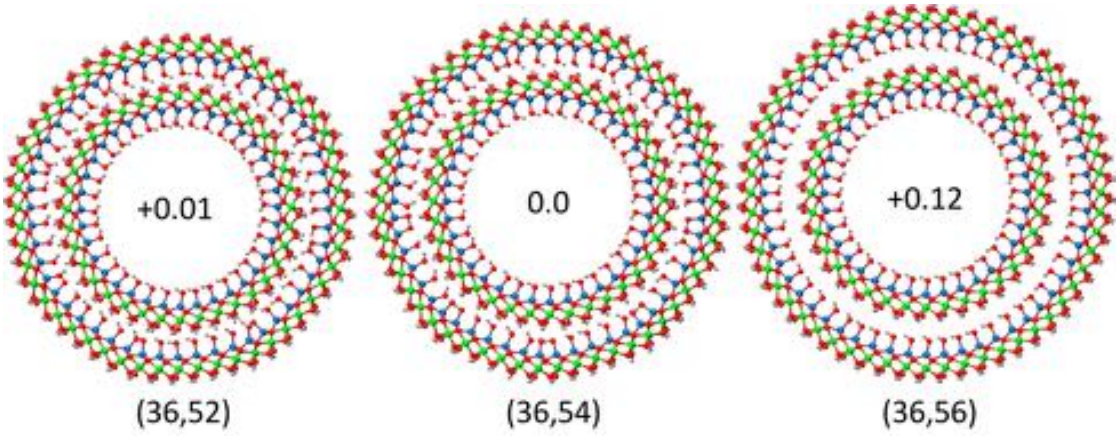

Figure 5.2: Front view of the optimised DW AlGe (N_{in}, N_{out}) NT models screened. The relative energy per ($Al_2GeO_7H_4$) unit (eV) is shown inside each NT-model.

and those of [145], since the computationally optimised diameters reported in Tables 4.1 and 5.1) brackets the peaks in the experimental pore-size distribution. Finally, the DW-$AlGe_{36,54}$ has been selected after a minimal energy screening of the $AlGe_{36}$ NT encased within differently sized outer NTs, shown in Figure 5.2. This screening at PBE level, finds that the energetically favoured DW-$AlGe_{36,54}$ NT has $N_{\text{out}} - N_{\text{in}} = 18$ (9-unit according to the labelling in [167]), in agreement with recent TB-DFT suggestions for zig-zag DW AlSi and AlGe NTs [167].

Following the detailed analysis presented in Table 4.1, Table 5.1 provides a layer-resolved (Figure 5.1) analysis of the diameters obtained for the geometry optimised NT-models. These results, in line with an earlier ultrasoft pseudopotential plane-wave PBE-DFT study [171], show that the optimised outer (H_7, Figure 5.1) diameter for the $AlSi_{24}$ (23.11 Å) and $AlGe_{36}$ (33.18 Å) NTs is in good agreement with reported values (23 Å) [126] and (30-38 Å) [126, 134–137, 139, 140] respectively. The optimised outer diameter for the DW-$AlGe_{36,54}$ NT ($O_{6,\text{out}}$: 45.37 Å, $H_{7,\text{out}}$: 46.38 Å) also aligns well with the documented values (40-43 Å [135, 139, 167]). The DW-$AlGe_{36,54}$ NT modelled is not expected to be an energy minimum for DW-AlGe NTs, which is the reason for the more noticeable deviations from the experimentally derived diameter-ranges.

For the case of the DW-$AlGe_{36,54}$ NT, it is worthwhile considering the average inter-tube hydrogen bonding distances. This analysis is inclusive of both hydrogen bonding patterns: $H_{7,\text{in}}$-$O_{2,\text{out}}$ and $O_{6,\text{in}}$-$H_{1,\text{out}}$. The average distance is 2.23 ± 0.46 Å, the fairly

	H_1	$O(C)_2$	Si_3	O_4	Al_5	O_6	H_7
$AlSi_{24}$ (PBE)	12.37 ± 0.02	13.25 ± 0.01	16.52 ± 0.01	17.81 ± 0.04	19.73 ± 0.02	21.91 ± 0.06	23.11 ± 0.04
$AlSi_{28}$-Me (PBE)	15.33 ± 0.03	16.10 ± 0.02	19.77 ± 0.01	21.04 ± 0.04	22.97 ± 0.01	25.15 ± 0.05	26.33 ± 0.02
$AlSi_{28}$-Me (PBE-D2)	15.35 ± 0.01	16.11 ± 0.01	19.78 ± 0.01	21.04 ± 0.04	22.97 ± 0.01	25.14 ± 0.04	26.32 ± 0.02
$AlSi_{28}$-Me (OPTB88)	15.34 ± 0.02	16.11 ± 0.01	19.78 ± 0.01	21.04 ± 0.04	22.96 ± 0.01	25.13 ± 0.04	26.33 ± 0.02
$AlSi_{34}$-Me (PBE)	20.25 ± 0.02	20.79 ± 0.01	24.45 ± 0.01	25.82 ± 0.01	27.77 ± 0.01	29.89 ± 0.01	30.92 ± 0.01
$AlSi_{34}$-Me (PBE-D2)	20.25 ± 0.02	20.78 ± 0.01	24.45 ± 0.01	25.82 ± 0.01	27.77 ± 0.01	29.89 ± 0.01	30.92 ± 0.01
$AlSi_{34}$-Me (OPTB88)	20.25 ± 0.02	20.80 ± 0.03	24.45 ± 0.01	25.82 ± 0.01	27.76 ± 0.01	29.88 ± 0.01	30.92 ± 0.01
$AlGe_{36}$ (PBE)	22.01 ± 0.02	22.79 ± 0.03	26.40 ± 0.03	27.80 ± 0.05	29.79 ± 0.02	31.95 ± 0.04	33.18 ± 0.02
In-$AlGe_{36,54}$ (PBE)	22.08 ± 0.05	22.87 ± 0.06	26.40 ± 0.06	27.83 ± 0.09	29.81 ± 0.06	31.94 ± 0.13	33.02 ± 0.38
Out-$AlGe_{36,54}$ (PBE)	35.09 ± 0.06	36.19 ± 0.12	39.69 ± 0.10	41.25 ± 0.11	43.24 ± 0.11	45.37 ± 0.11	46.38 ± 0.55

Table 5.1: Calculated average layer-resolved diameters and standard deviations in Å for the optimised NT-systems XC-functionals used. The labelling scheme is provided in Figure 5.1. Results for the DW-$AlGe_{36,54}$ are reported independently for each tube using the prefixes In- ($N = 36$) and Out- ($N = 54$).

large standard deviation is a result of the non-circular section of the NTs that act to maximise to the inter-tube interactions. Geometric variation of the NT cross-sections have been previously observed for AlGe NTs organised in bundles [338], in these cases a circular to hexagonal transition is observed, showing that inter-tube interactions can significantly affect the cross-sectional symmetry of SW- and DW-AlGe NTs.

The agreement between computed and experimentally reported diameters, though promising, does not factor in the role of the ionic strength of the solution in determining the size of each of the Imo AlSi NTs [130]. Therefore, any comparison drawn between these vacuum exposed results and experimentally measured diameters should not be considered conclusive. To this end, atomically resolved X-ray scattering or Atomic Force Microscopy would be extremely beneficial and timely for the communities with interest in Imo NTs.

5.3.2 The impact of composition on Imogolite wall polarisation

The accumulation of negative and positive charge at the inner and outer NT surfaces, resulting in the polarisation of the NT wall of has previously been noted for AlSi and AlGe NT [171,177]. Moreover, in the last Chapter, the impact of methylation highlighted that not only the NT-curvature, but also the NT-composition can lead to great variation in the magnitude of the ensuing surface dipole density. This section analyses the extent to which μ_σ is affected by the different tube compositions, including the formation of multi-walled Imo NTs.

Following the methodology laid out in Chapter 4, μ_σ is obtainable from the difference between the vacuum-plateaus of the angularly and longitudinally averaged electrostatic (ionic plus Hartree) potential, $\Delta\bar{V}$, inside and outside the NT-cavity

$$\mu_\sigma = -\frac{\Delta\bar{V}}{4\pi}\frac{\Delta R}{R_{\text{in}}}\frac{1}{\ln\left(\frac{R_{\text{in}}}{R_{\text{in}}+\Delta R}\right)}. \tag{5.1}$$

The inner and outer radii, R_{in} and R_{out}, of the NT are defined as the onset of the electrostatic plateaus corresponding to regions of vacuum. These are given by the radii at which the oscillations of the local potential (V) are lower than the 5×10^{-3} eV threshold employed. In line with previous analysis, the adopted sign convention means that

	μ_σ (mD Å^{-2})	$\Delta\bar{V}$ (eV)	R_{in} (Å)	R_{out} (Å)
$AlSi_{24}$ (PBE)	67.53	1.40	4.52	13.45
$AlSi_{28}$-Me (PBE)	35.68	0.78	5.59	15.11
$AlSi_{28}$-Me (PBE-D2)	26.69	0.81	5.59	14.99
$AlSi_{28}$-Me (OPTB88)	38.64	0.85	5.59	15.11
$AlSi_{34}$-Me (PBE)	32.75	0.82	8.09	17.37
$AlSi_{34}$-Me (PBE-D2)	32.23	0.81	8.09	17.37
$AlSi_{34}$-Me (OPTB88)	33.90	0.85	8.09	17.49
$AlGe_{36}$ (PBE)	63.54	1.62	8.73	18.28
$AlGe_{36,54}$ (PBE)	136.11	2.89	8.79	25.29

Table 5.2: The computed surface dipole densities, inner-outer vacuum-plateau differences, and electrostatically-derived inner and outer NT radii for the considered NT compositions and various XC-functionals employed.

positive μ_σ values are obtained when the direction of polarisation (+ve to -ve) occurs from the outer NT surface towards the inner NT surface. The computed surface dipole densities, potential steps and inner and outer NT radii are reported in Table 5.2

The substitution of inner hydroxyl groups with methyl groups (here $AlSi_{28/34}$-Me NTs) has already been found to leave the direction of wall polarisation unchanged with respect to the AlSi NTs. The substitution has been shown to be accompanied by a reduction in the magnitude of the computed μ_σ. The decrease for $AlSi_{28}$-Me (-47.2%) is slightly smaller than for $AlSi_{34}$-Me (-51.5 %), this is a result of the different geometrical factor $\Delta R/R_{in}$, defined in Equation (5.1), for $AlSi_{28}$-Me and $AlSi_{34}$-Me. The previous Chapter dealt with the analogous $AlSi_{24}$-Me NT, confirming that the smaller observed wall-polarisation is a direct consequence of the less polar methyl groups.

Remarkably, the DW-$AlGe_{36,54}$ is computed to have the largest μ_σ, which is more than double the next largest SW-$AlSi_{24}$ NT. This can be attributed to the large $\Delta\bar{V}$ value observed that maximises the value of the surface dipole density. The $AlSi_{24}$ and $AlGe_{36}$ NTs have a roughly equal calculated dipole density in spite of different potential step, this is due to the different geometric factors in Equation (5.1). Overall these results reinforce the earlier conclusions that by tuning Imo NTs composition and diameter

(i.e. curvature), it is possible to control the polarisation of the NT walls. The ability to tune the surface dipoles may open up the potential selective absorption of molecules inside and outside the NT walls based on their affinities for electro-positive and negative environments.

5.3.3 Electronic structure and absolute band alignment

Chapter 1 outlines that in order to viably photo-catalyse a given reaction, it is necessary for the the energetic-position of an semiconductor or insulators valence band edge (VBE) and conduction band edge (CBE) to match the energies of the h- or e- acceptor states in the reactants. Moreover, that there should be an effective separation of the photo-generated e-h pair [17–30]. In light of these requirements, for consideration of Imo NTs as photo-catalysts, consideration should be given to the absolute vacuum aligned band edges of the isolated in vacuo NTs as well as the distribution of those states near the band edges in real-space. Here, going one step further, the positions of the NT VBE and CBE are discussed in the context of recent results for bulk-phases of two more conventional photocatalytic materials: anatase and rutile TiO_2 [300]. Specifically, Section 1.2.2.4 points out that energetically viable e transfer between the photo-catalyst and the reagent requires that the empty e acceptor state is lower in energy than the e donor state. In other words the CBE, occupied by the photo-excited e, should be higher in energy than the reactant LUMO. The converse is true for h-transfer, thus the photo-catalyst VBE must be lower in energy than the reacting HOMO state [17–29].

Any analysis based on the semi-local XC-functionals adopted [201, 206, 214, 215] should be treated with care. It is expected that the over- and underestimation of computed VBE and CBE energies, ultimately leads to an overall underestimation of the band gap [195–200]. Therefore, reported values for the NTs VBE and CBE are regarded as upper and lower bounds to the actual vacuum aligned band edges. Also not yet considered, are the photo-catalyst-reactants-medium interface relaxations, and their role in determining the electrostatic properties (and ensuing band alignments) of the systems considered.

	VBE	CBE	BG
$AlSi_{24}$ (PBE)	-5.80	-1.36	4.44
$AlSi_{28}$-Me (PBE)	-5.97	-1.22	4.75
$AlSi_{28}$-Me (PBE-D2)	-5.96	-1.24	4.72
$AlSi_{28}$-Me (OPTB88)	-6.21	-1.54	4.67
$AlSi_{34}$-Me (PBE)	-5.97	-1.23	4.74
$AlSi_{34}$-Me (PBE-D2)	-5.97	-1.26	4.71
$AlSi_{34}$-Me (OPTB88)	-6.24	-1.56	4.68
$AlGe_{36}$ (PBE)	-5.74	-1.39	4.35
$AlGe_{36,54}$ (PBE)	-4.30	-1.49	2.81
$AlGe_{36,54}$-inner (PBE)	-4.30	-0.93	3.37
$AlGe_{36,54}$-outer (PBE)	-4.92	-1.49	3.43
TiO_2 Rutile[a]	-7.83	-4.80	3.03
TiO_2 Anatase[a]	-8.30	-5.10	3.20

Table 5.3: The computed vacuum-aligned VBE, CBE and band gaps (BG) for the different Imo NTs and DFT-functionals in eV. [a]Reference [300]

5.3.3.1 The band-gap and band alignment in Imogolite NTs

Firstly, the Density of States (DOS) have been aligned via their vacuum levels, as defined by the onset of plateaus in the radially averaged electrostatic potential, they are plotted in Figure 5.3, Table 5.3 collects their respective VBEs, CBEs and band gaps. As stated in Chapter 4, the computed band gaps for the $AlSi_{28}$-Me and $AlSi_{34}$-Me (4.67-4.75 eV depending on the adopted functional) are 0.23-0.31 eV larger than for the pristine $AlSi_{24}$: in spite of the reduced polarity of the methyl units introduced, the NT band gap is increased. Again, restating the findings of Chapter 4, a breakdown of the population by Mulliken analysis [339] (Appendix B) highlights that the observed opening of the NT band gap is coincidental with a transfer of 0.30 ± 0.01 e/CH_3 (XC-functional dependent) from the aluminium hydroxide backbone to the methyl groups. Therefore, the methyl groups in the Imo NTs can be said to be negatively charged, consistent with the polarisation gradient across the NT wall.

The band gap obtained in this work for the $AlGe_{36}$ NT is in good agreement with

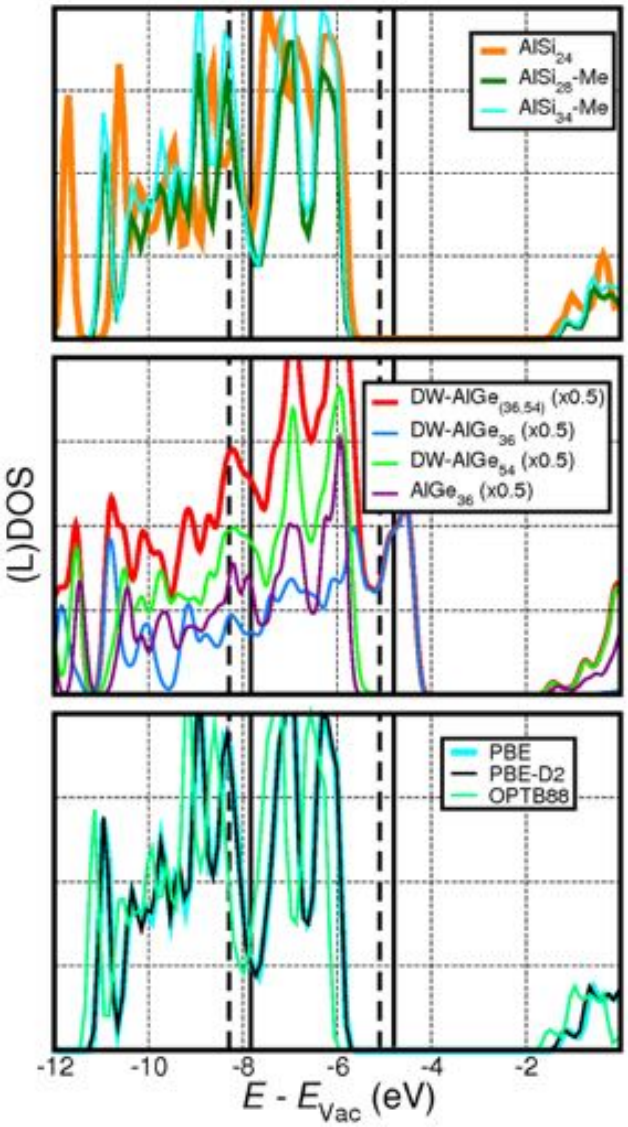

Figure 5.3: Plots of the vacuum-aligned DOS and tube-projected LDOS for the different Imo NTs and XC-functionals. For comparison, in vertical dotted (continuous) lines, the VBE and CBE of bulk anatase (rutile) TiO_2 are marked [300].

previously simulated values at the PBE level of theory [168, 172]. Notably, the energy gap computed for the DW-$AlGe_{36,54}$ (2.81 eV) is considerably smaller (-1.54 eV) than the SW-analogue. This can be understood by considering the inner- and outer-tube resolved local DOS (LDOS [287]) in Figure 5.3; the large reduction of the band gap stems from the complimentary polarisation gradients of the inner and outer tubes, which leads to an upward shift of the inner NT bands and a simultaneous downward shift of the outer NT electronic bands. As noted above, the DW-$AlGe_{36,54}$ NT band gap is underestimated due the limitations associated with the PBE functional, however, the reduction in gap upon introducing the multi-walled structure should be qualitatively significant.

Concerning the absolute values of the NTs bands, vacuum alignment at PBE-level reveals that the $AlSi_{28/34}$-Me NT and the DW-$AlGe_{36,54}$ NT have the lowest (-5.97 eV) and highest (-4.30) VB edges respectively. For the CB, the lowest energy band edges (-1.49 eV) are found to occur in the DW-$AlGe_{36,54}$ NTs, the highest (-1.22/-1.23) in the $AlSi_{28/34}$-Me NTs. A depletion of the charge in the aluminosilicate framework, brought about by the presence of the methyl group (0.3 e/CH_3), is responsible for the 0.2 eV lowering (0.15 eV increase) of the $AlSi_{28/36}$-Me VBE (CBE) in comparison to the $AlSi_{24}$ NT. At the present moment, work is being undertaken to investigate whether this mechanism exists for hybrid methyl-Si/Ge Imo NTs [142]. Direct comparison of the absolute alignment of the bands in the SW-$AlGe_{36}$ and DW-$AlGe_{36,54}$ NTs suggests that an encapsulation effect is capable of inducing large (1.44 eV) upward shifts in the energy of the VBE. Furthermore, this is accompanied by a (smaller) lowering (0.1 eV) of the CBE that, overall leads to a significant reduction (-1.54 eV) to the global band gap. As discussed previously (see Chapter 4), in spite a very negligible effect of the optimised geometries the different treatment of long-ranged interactions in the XC-functional can have a profound affect (up to nearly 0.3 eV) on the absolute position of the VBE and CBE. Therefore, care must be taken to avoid making comparisons between simulations carried out with different non-local (PBE) or self-consistent dispersion corrected (OPTB88) DFT-functionals.

DFT simulations of AlSi and AlGe NTs highlight an intriguing real-space separation of the VBE and CBE [170, 171], that is the foundation of any supposed *e*-*h* separation mechanism. The extent to which this peculiar property is affected by methylation was addressed in the previous Chapter, however the encapsulation effects of the DW-AlGe NTs have not yet been addressed. The simulations presented in this Thesis point towards a consistency, that the across-wall separation of the NT bands is a feature of all Imo-type

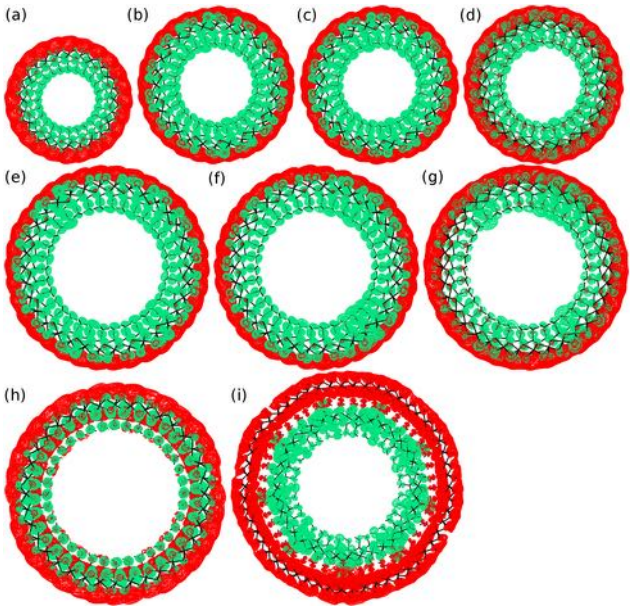

Figure 5.4: Plots of the band decomposed VBE (green) and CBE (red) separation in real space, ordered by NT diameter, Table 5.1: (a) $AlSi_{24}$ (PBE), (b) $AlSi_{28}$-Me (PBE), (c) $AlSi_{28}$-Me (PBE-D2), (d) $AlSi_{28}$-Me (OPTB88), (e) $AlSi_{34}$-Me (PBE), (f) $AlSi_{34}$-Me (PBE-D2), (g) $AlSi_{34}$-Me (OPTB88), (h) $AlGe_{36}$ (PBE), (i) DW-$AlGe_{36,54}$ (PBE). For visual clarity, (i) has been reduced by a factor of 1.5.

NTs. Band decomposed charge density distributions plotted in Figure 5.4 show that this is true, at least for the systems considered here (also for more imaginative Imo-systems as demonstrated by the -CF_3 substituted NTs in the SI of [175]). In particular, in line with the tube-projected and layer-resolved DOS analysis for DW-$AlGe_{36,54}$ (Figure 5.3 and Appendix B), the VBE and CBE of the DW-$AlGe_{36,54}$ are localised on the inside and outside tube respectively. This result raises the possibility for photo generated *e-h* relaxation on different faces of different AlGe NTs. The real-space distribution of the VBEs and CBEs presented in Figure 5.4 are in good agreement with layer-resolved, NGWF-projected [287], LDOS analysis provided in Appendix B. These LDOS plots show large contributions to the VBE by the O_2 and O_4 layers and H_7 layers to the CBE in the case of $AlSi_{24}$ NTs. Likewise, the VB (CB) edge of the methylated NTs is found to be characterised by C_2 and O_4 (H_7) layers. Following directly from the result in Figure 5.3, the DW-$AlGe_{36,54}$ expectedly has leading contributions to the CBE and VBE edges from the inner tube O_2 and O_4 layers and outer tube Al_5 and H_7 layers respectively. Somewhat different from the other NTs, the $AlGe_{36}$ NT show larger contributions from the Ge_3 (O_6) layer to the CB (VB) band edges. Yet this is also manifested in Figure 5.3, where the real-space separation for $AlGe_{36}$ NT is less pronounced.

5.3.3.2 Comparison between Imogolite NTs and TiO_2

In addition to the results obtained for the considered Imo NTs, Figures 5.3 and 5.5 and Table 5.3 also report the vacuum-aligned band edges and band gaps of rutile and anatase TiO_2, obtained in reference [300], by adding the experimental optical band gap to the simulated ionisation potential. The mixture of these two polymorphs is known to lead to effective water photolysis [301]. Contrasting the relative energies of the TiO_2 with the computed Imo NTs band edges, facilitates an estimation of the possible increased or reduced photocatalytic drive towards H_2O reduction or oxidation.

This work finds that vacuum-aligned VBEs of the $AlSi_{28/34}$ NTs, which are found to have the lowest energy of the NTs considered, are still 1.86 eV (2.33 eV) higher than the reported VBEs for rutile (anatase). Therefore, on the basis of a weaker energy drive in comparison to the TiO_2, a lower H_2O photo-oxidation propensity should be expected for all of the Imo NTs. Looking instead at the relative energies of the CBEs, the results (omitting data obtained via non-local XC-functionals) show that the DW-AlGe NT, the Imo NT, with the lowest energy CBE is 3.31 eV and 3.61 eV higher in energy than the rutile and anatase TiO_2 respectively. This suggests a higher drive for H_2O photo-

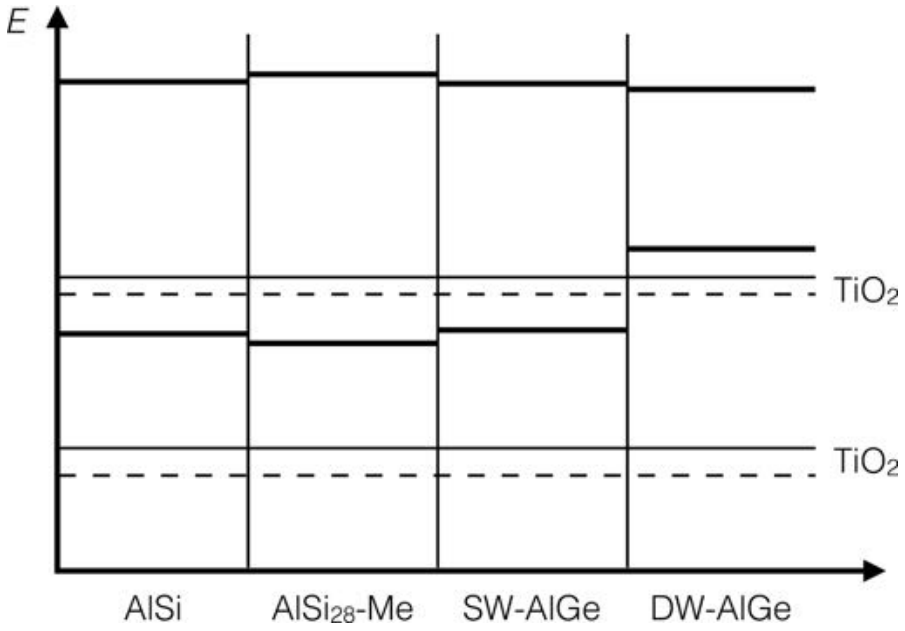

Figure 5.5: To scale visual comparison between the energies of the computed NT and TiO_2 band edges. The rutile (anatase) band edges are represented by the continous solid (dashed) line. Each segment along the x-axis represents a different NT composition, the upper and lower horizontal lines are the CB and VB edges.

reduction by the different Imo NTs compared with TiO_2. Whilst the comparatively high energies of the VBE are detrimental for the possible use of Imo NTs as a photo-oxidant, one avenue that may be explored is grafting a molecular or nanoparticle photo-catalyst on to the Imo-NT. In such an approach, enhanced e-h separation may be achieved by promoted h-transfer and relaxation from the grafted photo-catalyst onto the NT.

The conclusions drawn here rest on the assumption that the polarisation of the Imo NT walls has no affect on the energies of the H_2O HOMO and LUMO states. The validity of this assumption is explored in detail in the following Section.

5.3.3.3 Optical properties of Imogolite NTs

The pace of experimental and theoretical research into Imo NTs is increasing as new potential applications emerge. However, despite growing research interests, the optical absorption properties of the different Imo NTs are yet to be fully characterised. Thus far, there are only three published UV-visible absorption spectrum available [128, 153, 155]. To contribute to this current knowledge gap, optical spectra of the one dimensional periodic Imo-NT models have been computed using Fermi golden rule. Figure 5.6 plots the values of the computed imaginary component of the dielectric function, ε_2 [268, 270], for the different NT models. Larger values of ε_2 indicate a larger absorbance of the system. Given the interest in a comparison of the possible differences between the considered Imo NTs, the spectra have been calculated at PBE level. Recalling that as a result of the limitations of the adopted XC-functional and approximations for the evaluation of optical spectra, Chapter 2, expectations are that the energy of the optical transitions will be underestimated.

The profile of the synthetic AlGe NTs absorbance has a main peak at 6.2 eV, a broad shoulder in within the range 5-5.4 eV and a secondary peak at 3.9 eV [128]. In light of the anticipated underestimation of the $AlGe_{36}$ band gap, the simulated main 5 eV peak in Figure 5.6 can be tentatively assigned to the 6.2 eV peak in the experimental spectra. By decomposition of the optical matrix elements, in Figure 5.7, the transition responsible for the absorbances can be analysed. This analysis indicates that not only are the transitions between deep VB and CB KS states optically active, but they also strongly contribute towards the calculated spectra. Figure 5.6 suggests that the lower energy absorbance, comparable with the 5-5.4 eV shoulder observed in experiment, stems from

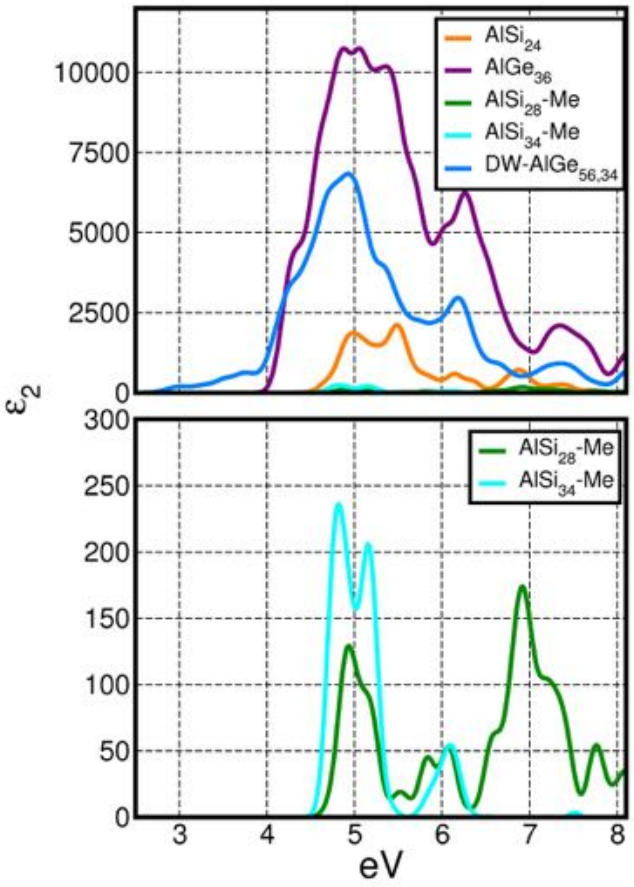

Figure 5.6: The imaginary component of the dielectric function ε_2 computed for the Imo NTs. For comparison, spectra are normalised to N. The lower panel provides a view of the spectra obtained for the $AlSi_{28}$-Me and $AlSi_{34}$-Me NTs that are found to absorb considerably less than the non-methylated tubes.

transitions involving the states at the VBE and CBE, those that are localised on different sides of the NT cavity, Figure 5.4. In terms of maximal effective separation of the e and h, these optically active inside-outside charge-transfer excitations could possibly lead to longer recombination times since the excited particles would have to decay against the wall-polarisation Table 5.2. The calculated spectra for the $AlGe_{36}$ NT model in Figure 5.6 do are not consistent with the appearance of a secondary absorbance peak detached at lower energy. However, since that peak in the experimental spectrum is lower in energy than the already underestimated PBE-gap 4.35 eV, Table 5.3, there is a suggestion that the experimental 3.9 eV peak could be the result of excitonic effects in AlGe NTs [128, 171] that cannot be captured by single-electron approximations to the optical spectra [272] employed in this work. In addition to the deficiencies associated with computation of optical spectra by Fermi golden rule [268], the disparity between experiment and predictions made in this work might also be linked to absorbances by point-defects similar to those reported for AlSi NTs [282], the restructuring of the tube-terminations, the presence of unreacted precursors or photo-active side-products or NT-aggregates in the synthetic solution monitored in [128].

Figure 5.6 also highlights the fact that the normalised optical absorbance of the $AlGe_{36}$ and DW-$AlGe_{36,54}$ NTs are nearly six and four times larger than $AlSi_{24}$ NT respectively. The absorbance of the methylated $AlSi_{28}$-Me and $AlSi_{34}$-Me NTs are significantly lower than the other tubes. This work shows that the calculated absorbance per Imo unit decreases as a function of NT composition in the order SW $AlGe_{36}$, DW-$AlGe_{36,54}$, $AlSi_{24}$, $AlSi_{28}$-Me and $AlSi_{34}$-Me NTs. In spite of the fact that the low-energy ε_2 peak is found to only vary weakly with changing NT composition, 4.83 eV ($AlSi_{34}$-Me) up to 4.94 eV ($AlSi_{24}$), the emergence of an additional absorption shoulder in the range 3-4 eV for the DW-$AlGe_{36,54}$ NTs suggests that the use of DW NTs may be a potential strategy for introducing lower-energy (near-UV) absorption. More than that, the lower-energy absorbance observed for the DW-$AlGe_{36,54}$ case is overwhelmingly dominated by charge-transfer excitations between the two different tubes, see Figure 5.7. This could be extremely effective for e*-h separation because of the increased separation between inner and outer NTs (H_7,in-H_1,out: 2.07 , H_1,in-H_7,out: 24.03 , see Table 5.1).

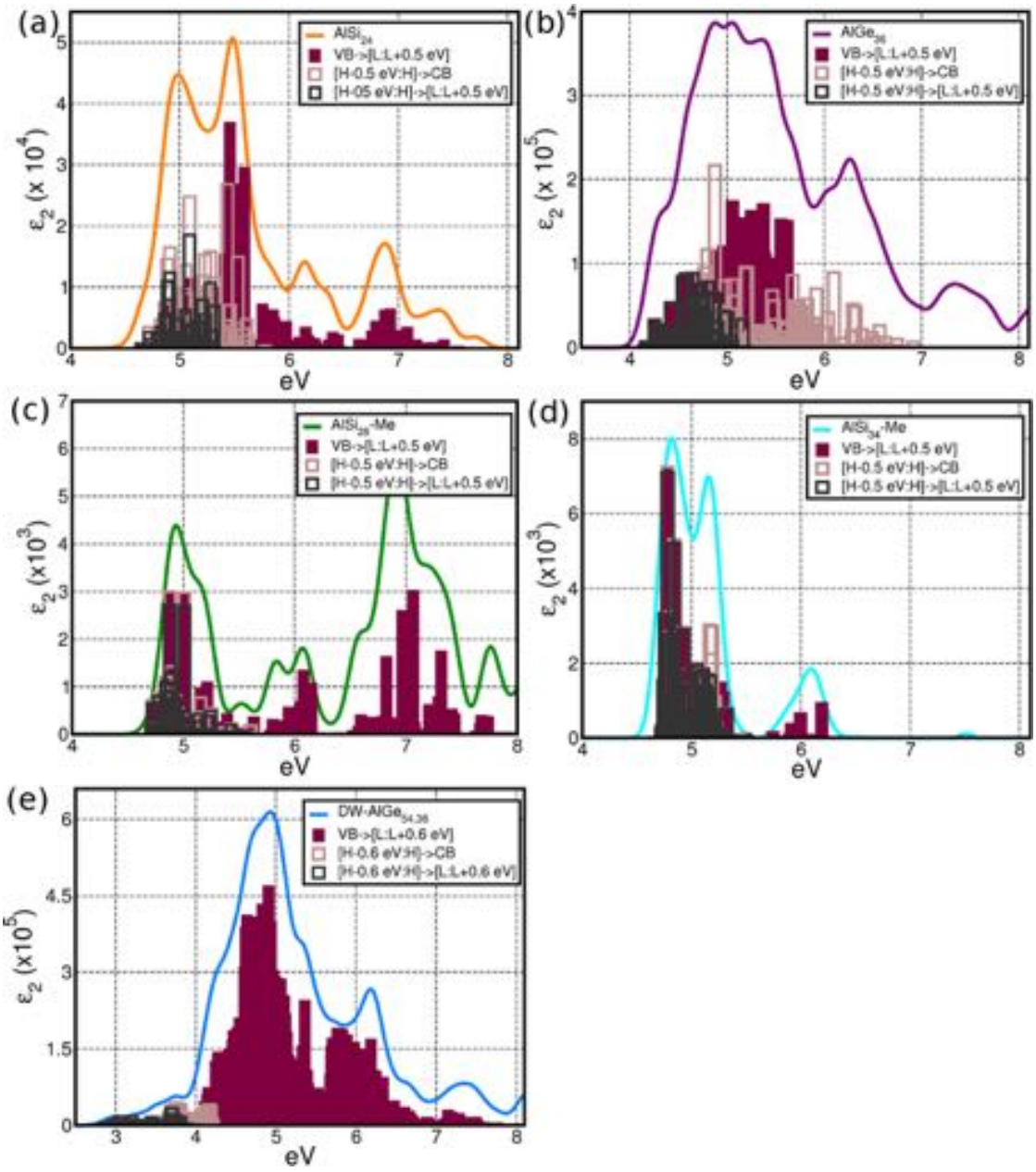

Figure 5.7: Plots showing the resolved contribution of the KS states to the low energy values of ε_2: (a) $AlSi_{24}$, (b) $AlGe_{36}$, (c) $AlSi_{28}$-Me, (d) $AlSi_{34}$-Me, (e) DW-$AlGe_{36,54}$. H and L are the HOMO and LUMO states, the VB and CB have been defined as any states within 0.5 eV (0.6 eV for DW-AlGe36,54) of the HOMO and LUMO. The excitations between these defined states has been marked with an arrow.

5.3.4 Polarisation mediated photo-catalyst-reactant band alignment

The importance of the electronic alignment between a photo-catalyst band-edges and the reactant e and h acceptor states was discussed in Chapter 1. At this point is should be restated that on the basis of Equation (1.12) this alignment is crucial for viable photo-induced e or h transfer between the photo-catalyst and reactants. Consequently, strategies such as band engineering, that strive to match photo-catalyst and reactant e and h acceptor states dominate much of research in the field [17–30]. Two avenues that are yet to be explored extensively, are whether through the tuning of the NT cavity electrostatics, i) reactants can be altered such that the HOMO and LUMO match the VBE and CBE of a (polarising) photo-catalyst and ii) the confinement of differently polarised photo-catalysts and reactants in a polarising environment can be used as a method for the tuning of the electronic alignment between a prospective photo-catalytic and given reactant(s). The inner diameters of the Imo NTs, which range from 12 to 22 Å (Table 5.1), offer significantly different electrostatic environments on the inside and outside of the NT cavity (Table 5.2), and offer and ideal model-system for the exploration of such concepts. To this end, the final section of this Chapter reports on investigations into the effects of the NT wall-polarisation on H_2O molecules interacting with inner and outer surface of the considered Imo NTs (Figure 5.8). The models have been intialised in a configuration that maximises hydrogen bonding (or dispersion interactions for methylated NTs). Along the z-axis the H_2O molecules are aligned with the inner (outer) hydroxyl (or methyl) groups. Geometry optimisation is not found to lead to deviations in the molecules along the NT axis. For the DW-AlGe NT (i, Figure 5.8), energy minimisation leads to an alternate H-bonding configuration that could be due to the omission of long range interactions within the exchange-correlation functional.

Geometry optimisation of each of the considered $2H_2O$@NT models highlights the larger (shorter) absorption distances for molecules at the inner (outer) NT surface. The inner distances, reported in Table 5.4, are between 14 and 19% larger than the outer distances for the SW-AlSi and SW-AlGe NTs indicative of a much weaker hydrogen bonding interaction under the influence of the negatively polarised NT cavity, see Table 5.2. On the other hand, the hydrogen bonding distances obtained for the H_2O inside and outside the DW-AlGe NT cavity, which is significantly more polarised than the SW-analogues, are equivalent. These results hint towards a more complex trade off between NT polarisation and wall curvature in the determination of the reactant absorption geometry. The substitution for methyl groups on the inside of the NT-cavity yields only

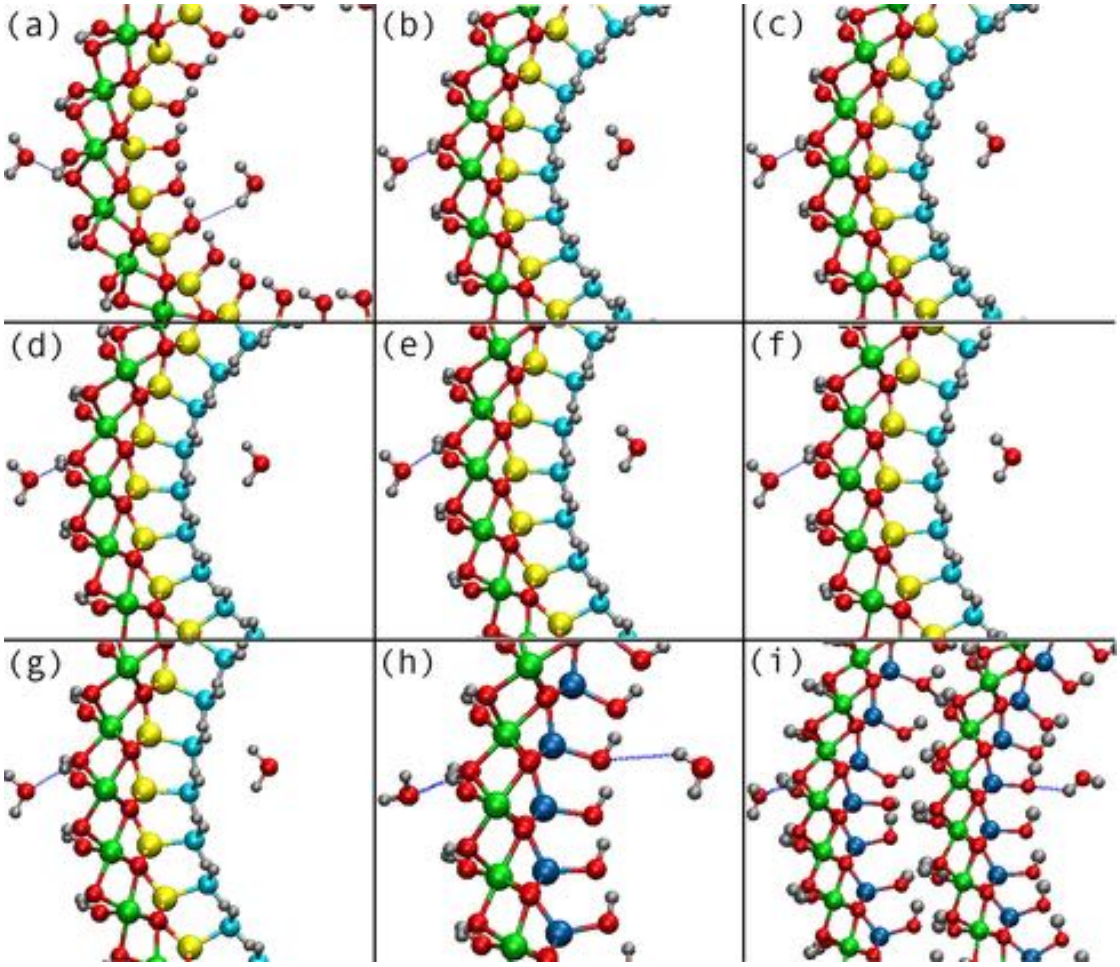

Figure 5.8: The optimised geometry of the different $2H_2O$@Imo NTs models considered, with the different XC-functionals used. (a) $AlSi_{24}$ (PBE), (b) $AlSi_{28}$-Me (PBE), (c) $AlSi_{28}$-Me (PBE-D2), (d) $AlSi_{28}$-Me (OPTB88), (e) $AlSi_{34}$-Me (PBE), (f) $AlSi_{34}$-Me (PBE-D2), (g) AlSi34-Me (OPTB88), (h) $AlGe_{36}$ (PBE), (i) DW-$AlGe_{36,54}$ (PBE). The shortest H_2O-NT H-bonding distances (see also Table 5.4) are highlighted by dotted lines. Same atom-colour labelling as in Figure 5.1

	d (Å)	q (e)
$AlSi_{24}$ (PBE)	2.38 (2.09)	-0.01 (+0.05)
$AlSi_{28}$-Me (PBE)	2.32 (2.08)	+0.01 (+0.05)
$AlSi_{28}$-Me (PBE-D2)	2.32 (2.08)	+0.01 (+0.05)
$AlSi_{28}$-Me (OPTB88)	2.40 (2.00)	+0.00 (+0.07)
$AlSi_{34}$-Me (PBE)	2.34 (2.10)	+0.01 (+0.04)
$AlSi_{34}$-Me (PBE-D2)	2.28 (2.20)	+0.01 (+0.05)
$AlSi_{34}$-Me (OPTB88)	2.31 (2.13)	+0.00 (+0.05)
$AlGe_{36}$ (PBE)	2.49 (2.09)	+0.00 (+0.02)
$AlGe_{36,54}$ (PBE)	2.09 (2.11)	-0.01 (+0.05)

Table 5.4: The minimum H_2O-Imo NT hydrogen bonding distances (d, Å) and computed Mulliken charges (q, e) of the H_2O molecules inside (outside) the NT cavity for the XC-functionals considered.

minimal changes in the hydrogen bonding distances at the outer surface. Varying the treatment of the long-ranged interactions, the absorption height of the H_2O molecule inside the cavity is found to be sensitive up to 0.08 Å difference. The results highlight a difference between the PBE, PBE-D2 and OPTB88 absorption geometries for the $AlSi_{28}$-Me and $AlSi_{34}$-Me NTs, which can be interpreted as meaning that both a combination of the polarisation of the tube wall (Table 5.2) and size of the dispersion interactions contribute to the adsorption of H_2O on the NT inner methylated surface.

Table 5.4 also reports the Mulliken charge analysis [339] for all of the considered systems. In each case, the interaction of the H_2O molecule adsorbed on the outer NTs surface brings about a small, but non-negligible, electronic charge depletion, the result of which is partial positive charging ($0.02 \rightarrow 0.07\ e$) of the adsorbed molecule. Simulations also find a negligible charge transfer ($\approx 0.00\ e$) for the H_2O molecule inside the cavity. Drawing comparisons with other nanostructures, it has been recently highlighted that similar H_2O adsorption on the outer surface of carbon nanotubes (CNTs) results in a negligible ($< 10^{-4}e$/molecule) electron transfer between H_2O and the CNT [340]. Therefore, in contrast and likely due to the possibility for forming hydrogen-bonding with the Imo NTs which is not available with the CNT, the results presented here show the interactions of H_2O and Imo-NTs to be accompanied by a non-negligible charge transfer. It should be taken into account that the modelling of small periodically repeated H_2O/NT

rings likely lead to deviations from the results obtained for effectively isolated adsorbates [340]. However, the trends that arise amongst the Imo NTs considered should be robust.

Figure 5.9 reports the simulated, vacuum-aligned LDOS plots for the H_2O@Imo NT systems, which allow examination of the effects induced upon the H_2O molecules by the NT polarisation. Irrespective of the NT size, composition or the XC-functional employed, the presence of the electronegative (positive) environments at the inner (outer) NT surface yields a significantly large shift in the energy of the HOMO for the H_2O molecule inside the tube cavity. The largest shifts are understandably observed where the polarisation of the NT walls is greatest, an increase of approximately 3 eV for $AlSi_{24}$, $AlGe_{36}$ and DW-$AlGe_{36,54}$ NTs. This is accompanied by a smaller downwards shift in energy for the HOMO of the molecules situated outside the NT, in the electropositive environment. Upward and downward shifts are also observed for the LUMO states of the molecules inside and outside the NT. The results presented strongly endorse the idea that the local polarisation of the NT wall is capable of inducing marked changes in the electronic alignment of adsorbed H_2O. Furthermore, early indications suggest that qualitatively similar results are also observed for other adsorbates.

Considering a comparison between the vacuum-aligned energies of the H_2O HOMOs in the adsorbed case and in an isolated molecule in vacuo (vertical orange lines Figure 5.9): depending on the choice of adsorption side, and in the absence of electron transfer kinetics considerations, there is a favourable energetic drive for oxidation of the adsorbed inner H_2O molecule as a consequence of the high HOMO level. More than that, resulting directly from the interactions with the positively charged outer surface, the LUMO of the outer H_2O molecule is computed below the vacuum energy. Promisingly, this leads to a positive electron affinity for the adsorbed H_2O molecule, in contrast with the negative affinity in the isolated case [341].

The energetic alignment of the HOMO of the H_2O inside the tube and the LUMO of the H_2O outside the tube with the top and bottom of the $AlSi_24$ NT VBE and CBE is conveniently compatible with a photo-induced oxidation/ reduction scheme as illustrated in Chapter 1. The slightly higher-than-VB energy HOMO means that an energetically viable photo-oxidation process may also be available for the H_2O molecule inside the $AlGe_{36}$ and DW-$AlGe_{36,54}$ NT. However, the position of the LUMO, above the CB-edge suggests that the opposing photo-reduction process outside the cavity is not viable. In

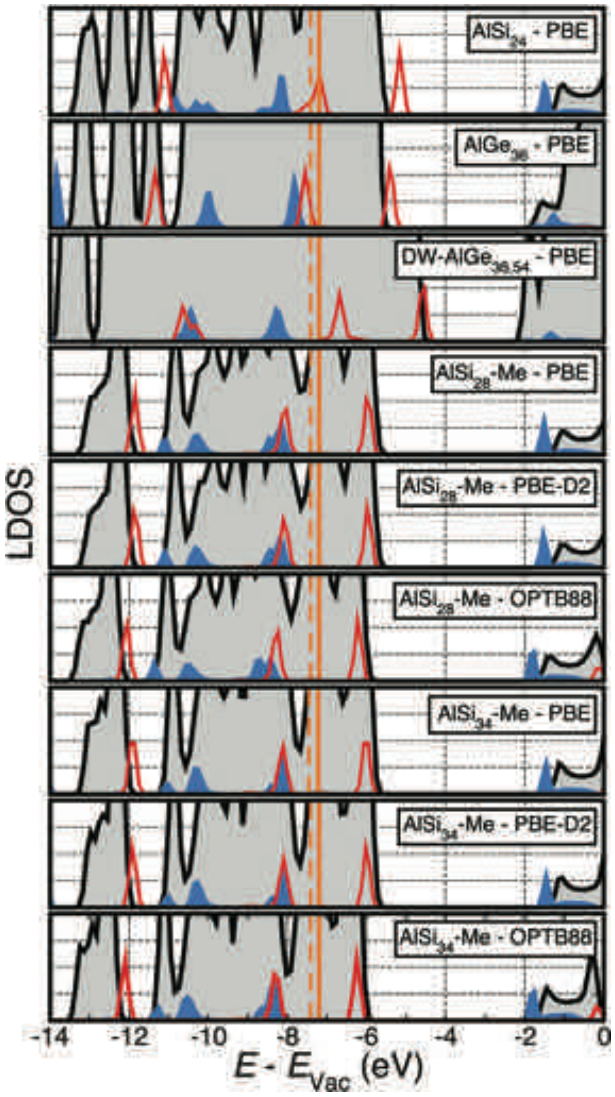

Figure 5.9: Vacuum aligned LDOS plots of the optimised $2H_2O$@NT systems and different XC-functionals. The total DOS is filled grey, with the inner site H_2O molecules displayed in red and the outer in blue. Vertical solid (dashed) orange lines represent the HOMO energy of a single isolated H_2O molecule computed at the PBE and PBE-D2 (OPTB88) level. In accordance with experimental results [341] The LUMO levels for the isolated molecule are computed above the vacuum.

spite of this set back the reduction process should not be ruled out since population of deep (higher energy) CB-states through high energy optical excitations, as reported in Figure 5.7, could lead to a de-excitation pathway compatible with photo-reduction of the outer H_2O molecule. For all of the XC-functionals screened in this Chapter, both the small and large AlSi-Me NTs also offer suitable electronic alignment for photo-reduction of the outer H_2O molecule, as the energy of the HOMO is lower than the CBE. At odds with the findings for the unfunctionalised cases, the AlSi-Me NTs do not have favourable alignment for the oxidation process inside the NT cavity. Although, given the predictions made for increased polarisation at larger NT diameters (in the previous Chapter) and the possibility for templated Imo NT synthesis reported in [131], it may be possible to generate NTs with a large enough polarisation to make the oxidation process more energetically viable. Ultimately, all of these processes will be subject to the competition between the kinetics of CB e-relaxation and NT$\rightarrow$$H_2O$ e-transfer, topics that are currently set aside for future investigation.

These findings should not be considered without first taking into account the following considerations. As already stated, this analysis rests only on energetic contributions and wholly neglect any of the important e and h charge transfer kinetics [111]. This means that despite favourable electronic alignments between donor and acceptor states, the respective rates of e and h transfer between those states may still be prohibitively slow as a consequence of the electronic coupling and Frank-Condon factors discussed in Chapter 1. The analysis given is based on the optimised geometries of (although LS-DFT has been applied, still comparatively small when compared to what would realistically be required) ideal models in vacuo. Undoubtedly, these models will fail to capture all of the real photo-electro-chemistry present within the defect containing, full-solvated and bundled NTs. For instance, the polarisation of the NT walls may be differently screened in different media that could lead to a significant deviation from the computed energetic alignments of the H_2O molecules. On the basis of 0 K simulations, it is impossible to draw any insight into the temperature-induced fluctuations [342–344] of the NTs-H2O electronic line-ups. The arguments made, have been based on KS states; again neglecting the limitations of the XC-functional, only the highest occupied KS state possesses strong physical significance in terms of molecular acceptor and donor states [195, 345–347].

Taking into account these objective limitations, universally shared with the current DFT-based theoretical production on PC materials [33, 311–317], this body of work represents an initial contribution that could lead to further input by communities with

an interest in photo-catalysis and photocatalytic materials.

5.4 Conclusions

To summarise the work of this Chapter, simulations have been extended to other members of the Imogolite family. SW-$AlSi_{24}$, SW-$AlSi_{28}$-Me, SW-$AlSi_{34}$-Me, SW-$AlGe_{36}$ and DW-$AlGe_{36,54}$ have been considered, and in keeping with the results presented in Chapter 4, different formulations of long-ranged exchange correlations have been employed for NTs with methyl functionalisation. The Imo NTs have been considered as either isolated entities or interacting with two H_2O molecules.

Importantly, the NT composition and SW- or DW-nature does not affect qualitatively the presence of NT wall polarisations or the localisation of the VBE and CBE in real space; computation reveals that the inner (outer) NT surface always accumulates negative (positive) charge, with the VBE at the inner surface and the CBE at the outer surface. The results presented suggest that experimental control over composition, as well as the curvature, could enable the NT wall-polarisation to be increased fourfold in going from SW $AlSi_{28}$-Me to DW-$AlGe_{36,54}$ NTs. Similarly, independent of the composition and SW- or DW-structure, the NTs considered in this Chapter are all found to behave as insulators. The band gaps span the range 2.81 eV for the DW-$AlGe_{36,54}$ NT to 4.75 eV for the $AlSi_{28}$-Me NT.

Alignment of the NT band edges reveals the relatively high energy of the VBE that may be exploited for its hole-scavenging propensity. Of all of the systems considered, the DW-$AlGe_{36,54}$ NT is found to have the highest VBE (-4.30 eV). Additionally, the vacuum-aligned CBEs are also high in energy, which precedes a possible photo-reduction propensity. The SW-$AlSi_{28}$Me NT is observed to have the highest CBE (-1.22 eV). Comparison with the TiO_2 polymorphs rutile and anatase shows that the Imo NTs have noticeably higher VB and CBEs. Within the Fermi golden rule based spectral analysis, the Imo NTs display a wide variety of optical activity, with the largest absorbances calculated for SW-$AlGe_{36}$ and DW-$AlGe_{36,54}$ NTs, noticeably larger than SW-$AlSi_{24}$ NTs, which in turn are significantly more active than methylated analogues.

Finally, the calculated polarisation of the NT wall can be correlated to the electronic alignment of H_2O molecules interacting at the different surfaces. Computed alignment of the low energy edge of the CB points towards an energetically viable photo-reduction of

H_2O on the NT-outer surface for all of Imo NT models, with the exception of the DW-$AlGe_{36,54}$ NT. An energetic drive for the opposing photo-oxidation process is present inside the NT-cavity where the high energy edge of the VB is positioned in energetic favourability for the non-methylated Imo NTs. The analysis presented, although promising, does not consider the electron transfer kinetics that were outline in Chapter 1, the role of additional solvent molecules in screening the NT polarisation or temperature induced fluctuation of the H_2O-NT relative band-alignment.

Chapter 6

Optimisation of the Hubbard-U for Fe-Imogolite

Abstract

This Chapter investigates the application and optimisation of the Hubbard U correction in linear-scaling Density Functional Theory (LS-DFT) for future screening and characterisation of transition metal doped Imogolite nanotubes (Imo NTs). The Chapter considers an idealised AlSi NT model with two isomorphic Fe/Al substitutions arranged opposite to each other in the NT circumference. Results obtained with a standard GGA exchange correlation functional have been compared with different Hubbard-U corrections. Values of U are derived from the literature, an internally consistent formulation based on linear response theory and a fully self-consistent value derived via a series of linear response calculations. The simulations indicate that the NT geometry and characteristic separation of the VBE and CBE is unaffected by the choice of LS-DFT+U correction. Expectedly, the system band gap and absolute vacuum-aligned band edges are sensitive to the applied correction, with the GGA functional found to give a qualitatively different picture with respect to all values of U. Results for the internally consistent and fully self-consistent corrections are comparable and would be appropriate for more extended simulation of the Fe-containing NTs. The idealised NT model considered is found to have a visible-light band gap (2.3 eV) and the vacuum aligned band edges are consistent with those found for other members of the Imogolite family. These results should provide a novel methodological basis for future investigation in this area.

6.1 Introduction

6.1.1 The problem of the Imogolite band gap

So far in this Thesis, the the novel linear-scaling Density Functional Theory (LS-DFT) code ONETEP has been successfully applied to different members of the Imogolite (Imo) family. It has been shown that it is possible to study systems containing thousands of atoms: enabling first principles investigation of Imo NT termination effects (Chapter 3), energetic profiling of the previously unexplored methyl-functionalized tube (Chapter 4) and the electronic properties of double walled AlGe NTs (Chapter 5). This has also made it possible to explore the reported polarisation and band separation effects that are of particular interest for charge-separation and catalyst-reactant band alignment, two crucial aspects for photo-catalysis. So far, the work has overlooked the fact that the Imo NTs band gap is unsuitably large for visible-light photo-catalysis. In spite of the documented evidence that UV-light based photo-catalysis can be favourable for sustainable energy applications [31, 62–64], the reader should be acutely aware that this is a large drawback since the profitability of any energy technology is massively enhanced by the ability to make use of renewable energy resources, in this case solar radiation. To this end, this Thesis will now focus on Fe-doped AlSi NTs (Fe-AlSi NTs), the previous experimental and computational characterisation of which was reported in Chapter 1.

The synthesis of Fe-AlSi NTs can be traced back to the publication of [153] in 2006. In the time since, there has been a scarcity of further investigations into Fe-doped Imogolite type materials, limited to just 7 research publications [141, 153–157, 174]. This is in spite of the fact that, rather promisingly, Fe-AlSi NTs are reported to have visible light absorbance in the region 1.9-2.8 eV [153, 155, 158, 174]. The emergence of an appropriately sized band gap, combined with reports that Fe-doped NTs maintain the structural properties and high pore size monodispersity of pristine Imogolite NTs, and the fact that they are known to catalyse the oxidation reactions of aromatic hydrocarbons [153, 154, 158], makes them a highly attractive candidate for possible heterogeneous (visible-light) photo-catalysis. Ultimately, the success of such an application will rely heavily on factors already discussed at length throughout this Thesis. Namely, the availability of a direct gap excitation and ensuing large light-absorbance, effective charge carrier separation (potentially facilitated by the polarisation of the NT wall) and suitably fast charge transfer kinetics between the NT and reactants.

The only previous DFT-modelling of the Fe-AlSi NTs supports the experimental

evidence that the HOMO-LUMO gap reduces significantly with respect to the pristine tubes [174]. However, the models investigated in [174] are at odds, in terms of the number of circumferential repeat units ($N = 20$), with the currently accepted value for AlSi-NT structure ($N = 24$ [170]). Furthermore, limited by the cubic scaling of plane wave DFT, simulations have been carried out on a single $AlSi_{20}$ NT unit cell, no doubt resulting in large defect-defect interactions between periodic images. This Chapter explores the application and system-specific optimisation of the linear-scaling DFT+U method for overcoming these obstructions. This offers a new approach for the characterisation of the electronic properties of (isolated, see Appendix) Fe^{3+}/Al^{3+} substitutions in AlSi NTs that can be extended to other members of the Imogolite family or other large scale metal oxide systems.

6.1.2 Density Functional Theory for strongly correlated materials

Transition metals oxides, and the ensuing presence of $d(f)$ electrons, historically pose one of the greatest challenges for DFT modelling. Within both the LDA and GGA frameworks, the insulating nature of transition metal oxides can be completely missed: simulations offer instead a qualitatively incorrect metallic ground state for these systems. The reason for such inadequate results is the poor description of the strongly-correlated transition metal d-electrons by the exchange-correlation functionals. Notably, both the LDA and GGA also fail to capture these effects for lanthanoid f-electrons as well. Such a large failure of DFT has stimulated different improvements to the existing method including the use of Hubbard-U corrections and Dynamic Mean Field Theory. In the description of Fe-AlSi NTs, this work will focus on the Hubbard-U (DFT+U) approach, which was devised in order to overcome, at a very favourable computational cost, some of the limitations associated with the exchange-correlation functional that result in the incorrect picture of transition metal oxides [348–350].

The DFT+U approach builds on the spatial localisation of $d(f)$ electrons in the core-region, the energy and potential for these states is corrected locally in order to account for correlation effects by means of a projector operation (via Hubbard projectors). When accounting for this correction, the total energy can be expressed as:

$$E_{\mathrm{DFT}+U}[n(\mathbf{r})] = E_{\mathrm{DFT}}[n(\mathbf{r})] + E_{\mathrm{Hub}}[\{n_m^{I\sigma}\}] - E_{\mathrm{DC}}[\{n_m^{I\sigma}\}], \tag{6.1}$$

where the occupations of the Hubbard sites (as obtained via projection of the Kohn-Sham states into the atomic "core" region described by the Hubbard projectors) are

given by $n_m^{I\sigma}$. In summary, a Hubbard type correction, E_{Hub} , is appended to the total energy. In addition, to prevent any double counting of electrons that are treated in a mean field within the DFT functional and explicitly in the Hubbard correction, a double counting term, E_{DC}, must also be included. This ultimately means that the DFT+U correction term is

$$E_U[\{n_{mm'}^{I\sigma}\}] = E_{\text{Hub}}[\{n_{mm'}^{I\sigma}\}] - E_{\text{DC}}[\{n^I\}] \tag{6.2}$$

A rotationally invariant, isotropic, formulation of the DFT+U correction functional is reported in [351, 352]

$$\begin{aligned} E_U[\{n_{mm'}^{I\sigma}\}] &= \frac{U}{2}\sum_{I,\sigma}\sum_{m}\left(n_{mm}^{I\sigma} - \sum_{m'} n_{mm'}^{I\sigma} n_{m'm}^{I\sigma}\right), & (6.3)\\ &= \frac{U}{2}\sum_{I,\sigma}\text{Tr}[\mathbf{n}^{I\sigma}(1-\mathbf{n}^{I\sigma})]. & (6.4) \end{aligned}$$

For localised orbitals, diagonalisation of the occupation matrices in the representation

$$\mathbf{n}^{I\sigma}\mathbf{v}_i^{I\sigma} = \lambda_i^{I\sigma}\mathbf{v}_i^{I\sigma};\ 0 \leq \lambda_i^{I\sigma} \leq 1, \tag{6.5}$$

makes it possible write the energy correction as

$$E_U[\{n^{I\sigma}\}] = \frac{U}{2}\sum_{I,\sigma}\sum_{i}\lambda_i^{I\sigma}(1-\lambda_i^{I\sigma}). \tag{6.6}$$

Therefore, the correction is a penalty function on non-integer occupancy of the Hubbard site orbitals, scaled by the size of U; the DFT+U solution preferentially disproportionates towards filled or empty states. This is a physical effect, lacking within the GGA/LDA DFT exchange-correlation functionals owing to the self-interaction error present in the latter.

On the interpretation of the U, the energy of a given system, expressed as a function of its electron occupation should be linear between integer points [352]. This is because the electron cannot be divided, therefore the energy of a system with non-integer occupancy must be given as a linear combination (having no curvature) of the integer occupancy states. Exact DFT should be capable of reproducing this physical behaviour. However, as a result of the self-interaction error, the GGA and LDA approximations yield an unphysical curvature with non-integer occupation at the extrema, see Figure

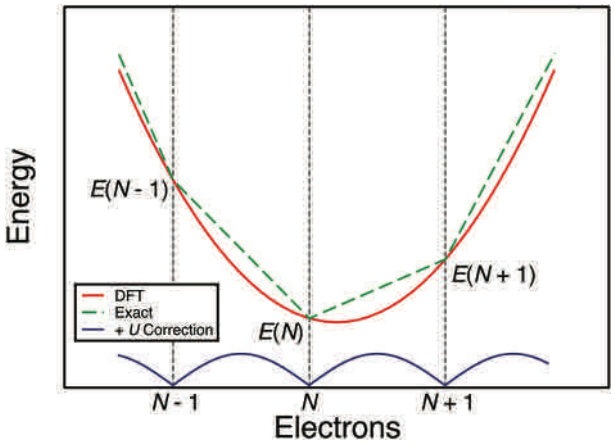

Figure 6.1: Adapted from [352], the total energy of a closed system as a function of the number of electrons, highlighting the artificial curvature of DFT, red, and the linear piecewise exact solution, green. Additionally, the DFT+U penalty for non-integer occupancy is plotted in blue.

6.1. The Hubbard correction method presented above, therefore represents a computationally convenient way of recovering the physical behaviour of the system. Importantly, it should be stated that U is not a tunable parameter that can be manipulated in order to recover properties of the system such as the band gap, but a measure of the unphysical curvature present in the approximated DFT calculation.

6.2 Computational details

Simulations of the Fe-AlSi NTs have been performed leveraging the results presented in Chapter 3. For Al and Si atoms nine 8 a_0 NGWFs have been used, whereas for O four 8 a_0 NGWFs are used and for H one 8 a_0 NGWF is used. To guarantee energetic convergence, in the absence of strict testing, nine larger 12 a_0 NGWFs are used for the Fe atoms. The kinetic energy cutoff was 1000 eV with no truncation of the density kernel. Kleinman-Bylander, norm-conserving pseudopotentials [283] generated using the Opium code [228] have been used. In the case of Fe, non-local core corrections [229] (discussed in Chapter 2) have been applied.

For the NT models, supercells have been constructed from the periodic pristine AlSi NT with a lattice periodicity of 8.66 Å [171]. Furthermore, in non-periodic directions

a 15 Å vacuum-buffer is included. The geometries have been optimised via the quasi-Newton scheme with BFGS Hessian matrix updates [235]. For all DFT+U simulations the forces are computed as well as the energy [353], furthermore, corrections to the Pulay forces have also been considered [267].

The PBE XC-functional [201] has been applied with Hubbard-U [348] corrections to account for the unphysical energy-electron count curvature. Corrections are derived within the text, the applied values are: $U = 0.00,\ 5.00,\ 7.63$ and 7.74 eV.

6.3 Results and discussion

6.3.1 Obtaining an internally consistent DFT+U correction

A number of strategies exist for the calculation of the Hubbard-U correction to DFT [348, 352,354–356]. These approaches all rest on the variation of the total energy functional as a function of the localised Hubbard site occupations. This can be computed employing a constrained density functional method [357,358]:

$$E[\{q_I\}] = \min_{n(\mathbf{r}),\alpha_I} \left\{ E[n(\mathbf{r})] + \sum_I \alpha_I (n_I - q_I) \right\}. \tag{6.7}$$

Constrained-DFT makes it possible to put a restriction on the occupation of the Hubbard sites, n_I, via Lagrange multipliers, α_I, which act as constraining potentials for each site. Thence, by varying these constraining potentials it is possible to compute numerically the associated curvature in the total energy. The curvature measures the energetic cost of localising electrons at the specific Hubbard-corrected sites.

Within the Kohn-Sham (KS) regime that is described in Chapter 2, the constrained-DFT expression is given by

$$E^{\mathrm{KS}}[\{q_I\}] = \min_{n(\mathbf{r}),\alpha_I^{\mathrm{KS}}} \left\{ E^{\mathrm{KS}}[n(\mathbf{r})] + \sum_I \alpha_I^{\mathrm{KS}} (n_I - q_I) \right\}. \tag{6.8}$$

This KS total energy functional possesses a different curvature to that of Equation (6.7) owing to the emergent re-hybridisation of the KS states as the occupation varies. Therefore, the DFT+U correction is given by the curvature of the interacting system

minus the curvature of the non-interacting KS system:

$$U = \frac{\partial^2 E[\{q_I\}]}{\partial q_I^2} - \frac{\partial^2 E^{\mathrm{KS}}[\{q_I\}]}{\partial q_I^2}. \tag{6.9}$$

Janak's theorem states that $\partial E/\partial n_i = \varepsilon_i$ [345]. This in turn means that U can be formulated as [348, 349]

$$U = \frac{\partial \varepsilon_I}{\partial q_I} - \frac{\partial \varepsilon_I^{\mathrm{KS}}}{\partial q_I}. \tag{6.10}$$

For constrained systems it is also possible to write $\partial E/\partial n_i = -\alpha_i$, where α_i is the constraint [359]. Linear response theory provides access to these two different gradients through the relationship between on-site occupations and the enforced constraining potential. In reference [352] it is shown that the interacting (χ_{IJ}) and non-interacting (χ^0_{IJ}) response functions are given by

$$\chi_{IJ} = \frac{\partial^2 E[\{q_I\}]}{\partial \alpha_I \partial \alpha_J} = \frac{\partial n_I}{\partial \alpha_J}, \tag{6.11}$$

and

$$\chi^0_{IJ} = \frac{\partial^2 E^{\mathrm{KS}}[\{q_I\}]}{\partial \alpha_I^{\mathrm{KS}} \partial \alpha_J^{\mathrm{KS}}} = \frac{\partial n_I}{\partial \alpha_J^{\mathrm{KS}}}. \tag{6.12}$$

leaving the internally consistent DFT+U correction, U_0, computable via

$$U_0 = \left(\chi_0^{-1} - \chi^{-1}\right)_{II}. \tag{6.13}$$

For illustrative purposes, the stepwise process for calculating an internally consistent value of the DFT+U correction is: (i) Perform an unconstrained DFT calculation with a null constraining potential at each site, $\alpha_I = 0$. (ii) Using the solution to the unconstrained system, add small perturbative, $\alpha_I \neq 0$, potentials to compute the variation of the occupancies for each Hubbard site. (iii) For χ_{IJ}, the KS system should be allowed to iterate to self-consistency, so that it is possible to capture the screening response to the perturbation. (iv) Instead, χ^0_{IJ} is computed at the first iteration step in order to calculate the immediate deviation from (i).

In the method outlined [352], χ^0_{IJ} and χ_{IJ} are the unscreened and screened responses to the constraining potential. They are calculated from explicit diagonalisation of the

Hamiltonian after a single self-consistency cycle (unscreened response) and after calculation of the perturbed system ground state electronic configuration (screened response). Implementation within the LS-DFT software ONETEP is problematic since it is not immediately clear at which stage during the calculation the unscreened response function should be calculated because of the immediate preconditioning of the state occupancies for the purification of the density kernel. To overcome this problem, the unscreened response function is calculated from the average change in the Kohn-Sham potential with respect to the occupancy of the Hubbard projectors

$$\chi^0_{IJ} = \frac{\mathrm{d}\,\langle V_{\mathrm{KS}}\rangle}{\mathrm{d}\mathrm{Tr}[n]}, \tag{6.14}$$

where $\mathrm{Tr}[n]$ is the trace of the Hubbard projector occupations matrix [360, 361].

This work represents the first attempt to calculate an internally consistent DFT+U correction in Fe-containing Imogolite NTs, to do so, the pristine $AlSi_{24}$ NT is used. Extensive simulations of varying Fe^{3+}/Al^{3+} substitution concentrations, inner surface Fe absorption and outer surface Fe absorption as documented in [153, 158, 174], together with a systematic study of the role of the tube-curvature and dopant-concentration for the energy-favoured magnetic ordering, represent future endeavours; this preliminary work will focus on a minimally sized supercell for isolated Fe^{3+}/Al^{3+} substitutions with the aim of introducing a methodological advance in the field. On the basis of earlier benchmarks on finite-size effects in Fe-doped NTs, where supercells up to 43 Å in length have been considered, see Appendix C, a simulation supercell with two units along the NT axis, see Figure C.1, has been used. At variance with these earlier calculations, this new supercell contains two Fe(Al) substitutions. The stoichiometry of the considered model is $Fe_2Al_{94}Si_{48}O_{336}H_{192}$, which is close to the $Fe_xAl_{(2-x)}SiO_4H_7$ ($x = 0.025$) NT reported in [155]. The defect sites are symmetrically distributed across the nanotube cross-section, as shown in Figure (6.2), in order to remove any dipole-dipole interactions between periodically repeated images. Spatially, the dopant atoms are circumferentially separated by 31.04 Å, which is significantly larger than the 17.33 Å axial separation already deemed to be sufficient for energetically disconnected defect sites, Appendix. As a result of the odd electron count for Fe^{3+} ions, different magnetic-spin configurations are available to the Fe sites. One recent experimental study suggests that the Fe defects, or the present Fe-cluster contamination, have a high spin configuration in the Fe-AlSi NTs [155]. In this work however, for the calculation of the Hubbard correction this work considers the case where Fe atoms are antiferromagnetically ordered, which leads to

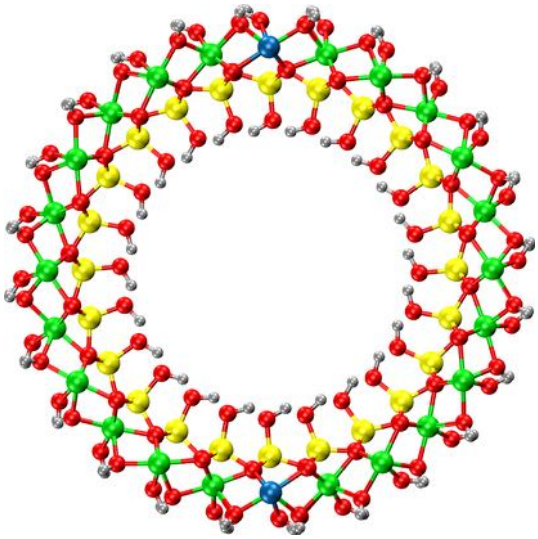

Figure 6.2: Front view of the idealised Fe-$AlSi_{24}$ NT cross section showing the distribution of isomorphic Fe/Al substitutions (Fe atoms coloured blue) across the nanotube diameter.

an optimised low spin configurations; notwithstanding, other spin configurations should not, in the long term, be overlooked since the role of curvature and chemical functionalization for the magnetic ordering in doped Imogolite nanotubes is, to date, yet to be investigated systematically.

Figure 6.3 plots the spin-population-weighted average constraining potential,

$$\bar{\alpha}_{I,\uparrow\downarrow} = \left(\frac{n_{\uparrow}}{n_{\uparrow}+n_{\downarrow}}\right)\alpha_{I,\uparrow} + \left(\frac{n_{\downarrow}}{n_{\uparrow}+n_{\downarrow}}\right)\alpha_{I,\downarrow}, \tag{6.15}$$

as a function of the onsite Hubbard occupation for (i) a converged geometry without Hubbard corrections (circles with dashed line; Opt 1.) and (ii) a converged geometry using the DFT+U correction derived from (i) (squares with solid line; Opt 2.). This work therefore, to the best possible knowledge, is for the first time, analysing the convergence of U as a function of the system geometry for a doped inorganic nanotube. The resultant DFT+U corrections are obtained from the derivatives of these lines by means of finite difference [232].

For Opt. 1, the calculated U_0 correction is the average between the two equivalent Hubbard sites: 7.71 eV. This was used as an initial correction for Opt. 2, the resultant

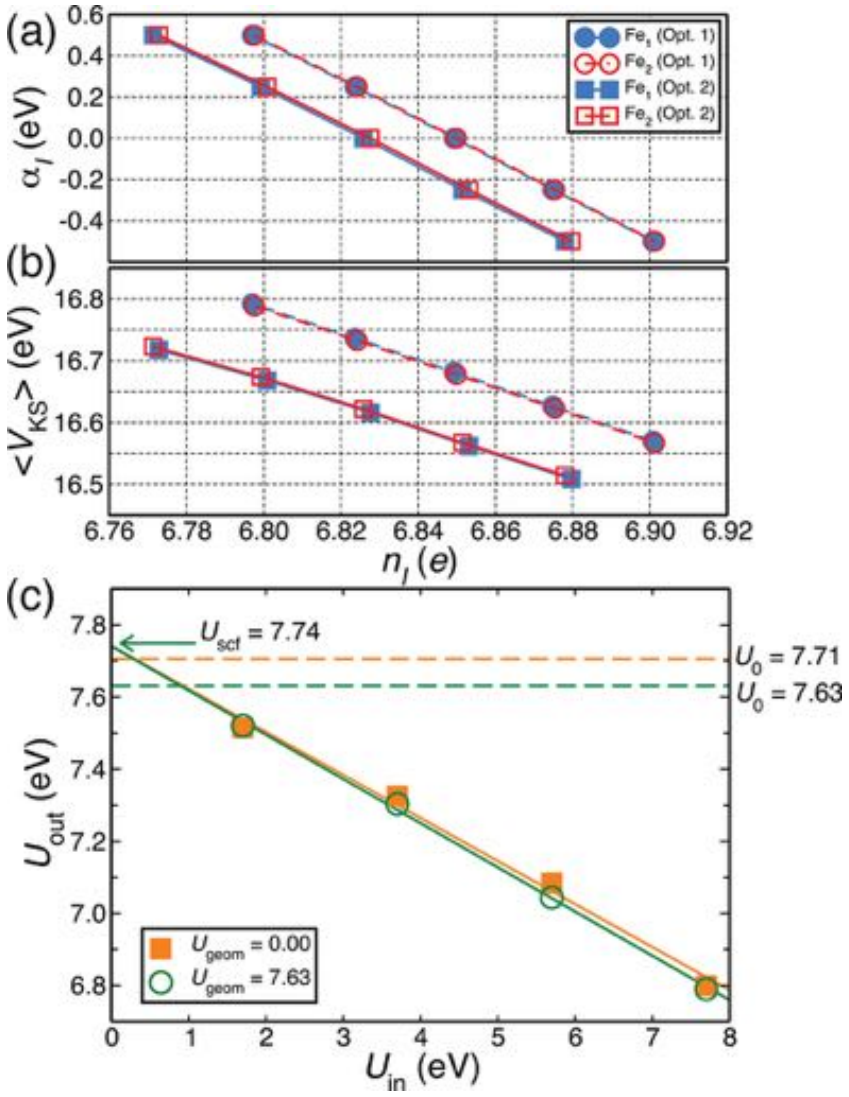

Figure 6.3: (a) Plot of the applied potential, α_I, as a function of the Fe-site occupations for calculation of the screened response function, χ_{IJ}. (b) Plot of the subspace averaged Kohn-Sham potential $\langle V_{\mathrm{KS}} \rangle$, as a function of the onsite Fe occupation for calculation of the unscreened response function, χ^0_{IJ}. Opt 1. Corresponds to geometry optimised with $U = 0$ eV, Opt 2. for the geometry calculated with $U = 7.71$ eV. (c) Self-consistent determination of U from plots of linear response derived U_{in} vs. U_{out}, U_{geom} signifies the correction applied during initial geometry optimisation.

Method	U	Band gap	HOMO	LUMO
GGA	0.00	0.91	-3.74	-2.83
GGA-U_{Lit}	5.00	2.73	-5.45	-2.72
GGA-U_0	7.63	2.31	-5.80	-3.49
GGA-U_{SCF}	7.741	2.29	-5.80	-3.51

Table 6.1: The calculated band gaps and vacuum-aligned HOMO and LUMO energies in eV for the different Hubbard U corrections.

U_0 in that case is found to be 7.63 eV as reported in Table 6.1. Further optimisation of the geometry with updated DFT+U corrections are found to be unnecessary as convergence to within 0.1 eV Å^{-1} (see Chapter 3) is reached at Opt. 2. Computed values of U_0 are notably larger than those previously reported in the literature (5 eV) for Fe atoms in organo-metallic molecules [352, 356, 362]. This discrepancy most likely arises from the vastly different hybridisation environment for the Fe atom within the extended aluminosilicate framework in comparison to the metallic and molecular systems of [352, 356, 362]. This also demonstrates the non-transferability of U values between different DFT codes (implementations) and employed pseudopotentials, and calls into question the erroneous practice of relying on literature based DFT+U corrections, highlights the need for an evaluation of DFT+U corrections specific to the system of interest.

6.3.2 Self-consistent determination of the Hubbard U

Further developments within the field suggest that U should, in fact, not be calculated from uncorrected-DFT level calculations. Instead, a self-consistent value can be obtained directly from a series of DFT+U calculations [356]. The importance of this approach is magnified, it is argued, in cases where the DFT and DFT+U solutions differ on a qualitative basis.

The self-consistent correction is derived by taking the components of the DFT+U total energy functional that have a quadratic dependence on the Hubbard site occupancies, this may written

$$E_{\text{Quad}} = \frac{U_{\text{scf}}}{2} \sum_I \left[\sum_i \lambda_i^I \left(\sum_j \lambda_j^I - 1 \right) \right] + \frac{U_{\text{in}}}{2} \sum_I \sum_i \lambda_i^I \left(1 - \lambda_i^I\right). \tag{6.16}$$

The first term arises from the DFT part of the functional and the second, as shown

above, from the DFT+U part of the functional. U_{SCF} is a measure of the inter-electron interactions at the Hubbard site, present within the DFT functional for a given $U_{\mathrm{in}}(= U_0)$. From the second derivative $\mathrm{d}^2E_{\mathrm{Quad}}/\mathrm{d}(\lambda_i^I)^2$, which is the Linear response U_{out}, is possible to define a relationship for calculating U_{SCF}

$$U_{\mathrm{out}} = U_{\mathrm{scf}} - \frac{U_{\mathrm{in}}}{m}. \tag{6.17}$$

On the basis of several linear response calculations for varying U_{in}, it is possible, as reported in Figure 6.3b, to extrapolate the self-consistent U_{SCF}. In agreement with [356], the results find that U_{SCF} is larger than U_0. Furthermore, we also find that U_{SCF} is independent of the initial geometry. In Figure 6.3b, the data coloured green corresponds to geometry optimisation carried out at U = 0.00 eV and the orange corresponds to U = 7.63 eV (based on the internally consistent approach). Both lead, as reported in Table 6.1, to $U_{\mathrm{SCF}} = 7.74$ eV.

6.3.3 Analysis of Fe-AlSi NTs structure and geometry

It is not clear, based on the current literature [141, 153–157, 174], how the Fe dopant atoms are distributed throughout the aluminosilicate framework, or the role played by the adsorbed Fe_2O_3 clusters (for synthesis at higher $FeCl_3$ concentrations [153, 155]) in determining size and structure of the Fe-AlSi NTs. This requires further, atomically resolved, experimental input and computational energy based screening of many structures that go beyond the realms of this Thesis. The aims of this Chapter are to set out a more informed strategy for the simulation of Fe-containing AlSi NTs with low defect concentrations ($x = 0.021$ for these simulation cells). Since the different Hubbard corrections have been computed in the previous Section, the focus will now turn towards the subtle differences that arise in the NTs geometry computed with different values of U. In addition, the results will also be compared with a value of $U_{\mathrm{Lit}} = 5.00$ eV, taken from previous computation for a different Fe containing system [356, 362].

The insertion of larger Fe atoms into the NT is expected to introduce local disruption to the aluminosilicate framework. Furthermore, given the ensuing changes to the bonding and hybridisation, subtle changes to local geometry might be expected for the different Hubbard-U corrections to the XC-Functional. Detailed analysis of the Fe-AlSi NTs structure and geometry are provided in Table 6.2 and Table 6.3. Table 6.2 reports the layer resolved average radii Table 6.3 reports the average inter-layer bond lengths for the considered Hubbard-U corrections.

	H_1	O_2	Si_3	O_4
$AlSi_{24}$ NT GGA	12.37 ± 0.02	13.25 ± 0.01	16.52 ± 0.01	17.81 ± 0.04
GGA	12.37 ± 0.01	13.26 ± 0.01	16.54 ± 0.01	17.82 ± 0.04
GGA-U_{Lit}	12.37 ± 0.01	13.26 ± 0.01	16.53 ± 0.01	17.82 ± 0.04
GGA-U_0	12.37 ± 0.01	13.26 ± 0.01	16.53 ± 0.01	17.82 ± 0.04
GGA-U_{SCF}	12.37 ± 0.01	13.26 ± 0.01	16.53 ± 0.01	17.82 ± 0.04

	Al_5	Fe_5	O_6	H_7
$AlSi_{24}$ NT GGA	19.73 ± 0.02	-	21.91 ± 0.06	23.11 ± 0.04
GGA	19.74 ± 0.01	19.76 ± 0.00	21.93 ± 0.06	23.12 ± 0.06
GGA-U_{Lit}	19.74 ± 0.01	19.76 ± 0.00	21.93 ± 0.06	23.12 ± 0.06
GGA-U_0	19.74 ± 0.01	19.76 ± 0.00	21.93 ± 0.06	23.12 ± 0.06
GGA-U_{SCF}	19.74 ± 0.01	19.76 ± 0.00	21.93 ± 0.06	23.12 ± 0.06

Table 6.2: The average layer-resolved diameters and standard deviations (Å) for the geometry optimised, DFT+U corrected Fe-doped AlSi NTs.

Changes to the average layer-resolved diameters (Table 6.2) are found to be negligible. The largest deviation (from the $AlSi_{24}$ NT periodic unit) is an 0.12% increase of the Si_3 layer for U_{Lit}, which falls outside the computed standard deviation boundaries. Therefore, for all of the DFT+U corrections considered, the global structure of the (low-concentration) Fe-doped AlSi NTs is quantitatively unaffected by the dopant atoms. At the local level, the Fe_5-$O_{4/6}$ bonds are observed to be (up to 4.1%, O_4–Fe_5; 4.7%, Fe_5–O_6) larger than the Al_5-$O_{4/6}$ bond lengths, as a result of the larger ionic radius of the Fe cation. This work finds that as the value of the DFT+U correction increases: a small, but non-negligible, increase (1.5%) in the size of the Fe-O bond lengths is observed. Mulliken charge analysis [339] shows that this increase is accompanied by a small loss of 0.4 electrons at the Fe ion. Thus, the Fe substituent is computed to be more ionic than the pristine Al-atoms, with an ensuing electron doping of the aluminium-hydroxide backbone.

Overall, the value of the DFT+U correction has a relatively small effect on the structure of the Fe-AlSi NTs considered. For larger defect concentrations (i.e. Fe-0.05-Imo [155] the accumulation of dopant sites, thence changes to the local geometry of the aluminosilicate framework, may present a larger global manifestation and could be responsible for the formation of surface adsorbed Fe_2O_3 clusters. Changes to the nanotube local structure might also be expected if the dopant sites are closer together,

	H_1-O_2	O_2-Si_3	Si_3-O_4	O_4-Al_5
$AlSi_{24}$ NT GGA	0.97 ± 0.00	1.65 ± 0.00	1.65 ± 0.01	1.94 ± 0.02
GGA	0.97 ± 0.00	1.65 ± 0.00	1.65 ± 0.01	1.94 ± 0.01
GGA-U_{Lit}	0.97 ± 0.00	1.65 ± 0.00	1.65 ± 0.01	1.94 ± 0.01
GGA-U_0	0.97 ± 0.00	1.65 ± 0.00	1.65 ± 0.01	1.94 ± 0.01
GGA-U_{SCF}	0.97 ± 0.00	1.65 ± 0.00	1.65 ± 0.01	1.94 ± 0.01

	O_4-Fe_5	Al_5-O_6	Fe_5-O_6	O_6-H_7
$AlSi_{24}$ NT GGA	-	1.89 ± 0.01	-	0.96 ± 0.00
GGA	1.99 ± 0.02	1.89 ± 0.01	1.95 ± 0.23	0.96 ± 0.00
GGA-U_{Lit}	1.99 ± 0.02	1.89 ± 0.01	1.95 ± 0.23	0.96 ± 0.00
GGA-U_0	2.02 ± 0.02	1.89 ± 0.01	1.98 ± 0.38	0.96 ± 0.00
GGA-U_{SCF}	2.02 ± 0.02	1.89 ± 0.01	1.98 ± 0.38	0.96 ± 0.00

Table 6.3: Average layer-resolved bond lengths and their standard deviations (Å) for the geometry optimised, DFT+U corrected Fe-doped AlSi NTs.

this will be the topic of further research.

6.3.4 DFT+U corrections to the electronic structure of Fe-AlSi NTs

Given the severe deficiencies associated with the LDA- and GGA-computed band gaps for materials containing transition metal elements, the exploration of the electronic properties of the Fe-AlSi NTs using DFT+U is important, not only for the implications of transition metal doping Imo NTs, but also for the evaluation of the differently derived values of U (for the first time, based on in-situ basis set optimised LS-DFT calculations). This is because, as has been seen in earlier Chapters, the accuracy of the computed band gaps and vacuum-aligned band edges are vitally important in the investigation and discussion of materials for photo-catalysis. The results presented in this Section on the electronic properties of the Fe-AlSi NTs are discussed in the context of the U corrections applied, but the qualitative conclusions may be transferable to other materials and systems.

The characteristic plots of the band-decomposed charge density distributions suggest that qualitatively, the separation of the VBE and CBE across the NT wall is unaffected for doped AlSi NTs. However, localised states (plotted blue in Figure 6.4) are observed, these correspond to the substituted Fe ions. In real space, the Fe-centred states bridge the gap between the VBE and CBE suggesting that the Fe atoms may potentially act as

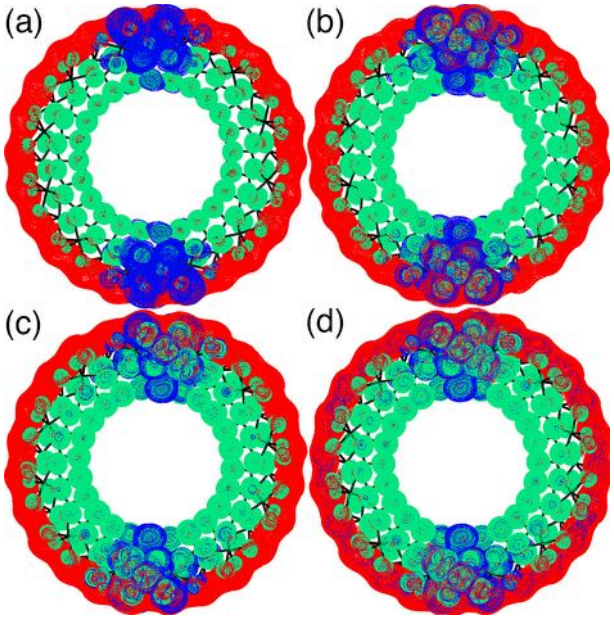

Figure 6.4: Real-space plots of the band-decomposed charge density distributions for the Fe-AlSi NTs computed at (a) GGA (b) $U_{\mathrm{Lit}} = 5.00$ (c) $U_0 = 7.63$ and (d) $U_{\mathrm{SCF}} = 7.74$ eV. The VBE and CBE of the AlSi NT are plotted in green and red respectively, the localised (occupied and unoccupied) Fe-states are plotted in blue.

e-*h* recombination centres inside the Imo NTs. This effect, that was discussed in Chapter 1, has also been observed for other transition metal doped semiconducting metal oxide materials. In agreement with the geometrical analysis (Table 6.2 and 6.3), the real-space distribution of the VBE, CBE and localised Fe states is qualitatively unaffected for the range of U considered.

Analysis of the vacuum-aligned Local Density of States (LDOS) (Figure 6.5), computed band gaps and vacuum aligned band edges (Table 6.1) suggest that the Fe-AlSi NTs have a visible light band gap. As expected, the GGA-only ($U = 0$ eV) simulation underestimates the experimental band gap by at least 1 eV [153, 158]; the DFT+U corrected systems all have band gaps aligned with experimentally reported values (1.9-2.8 eV [153, 155, 158]). Inspection of the LDOS plots (Figure 6.5) highlights the contradictory results for GGA and DFT+U simulations. Results for obtained via the GGA functional suggest that the occupied Fe states are fully detached from the VBE with the HOMO +3.5 eV above AlSi NT valence band. In contrast, the Hubbard-U corrected functionals each yield qualitatively similar pictures: highest occupied Fe-states are situ-

ated at the top of the nanotube valence band, the empty Fe-states are in the middle of the band gap and at the bottom edge of the conduction band. Despite similar energetic profiles, simulation results for U_{Lit} and U_0 give notably different band gaps and absolute vacuum aligned valence band edges, with the U_{Lit} band gap is 0.42 eV larger, and the valence band edge 0.45 eV higher in energy. Given that the linear response derived and self-consistent DFT+U corrections differ by only a small amount 0.11 eV, it is not surprising that the computed LDOS, band gaps and alignments are negligibly different. Consistent with the negligible differences in the nanotubes local and global geometries, the analysis of the electronic structure suggests that for Fe-doped AlSi NT systems it may be sufficient to use the U_0, obtained from a single linear response based simulation for computation of properties of interest.

The results presented give some insight into the behaviour of Fe-doped AlSi NTs, but this work is primarily an exploration of the LS-DFT+U method. The results obtained for the nanotubes are far from conclusive and neglect many factors. As such, a complete survey of transition metal doped Imo NTs, that provides an energetic screening of the different Imo compositions and NT sizes, dopant concentrations and magnetic orderings is planned. Furthermore, given the scalability of the adopted method, the presence of transition metal clusters adsorbed onto the NT surface should also be considered. Investigations along these lines will inevitably rely on recalculation of the Hubbard-U, but will enable computation of more representative electronic properties and additional the optical spectra, wall polarisations and the influence of differently doped NTs on the energy of electron-acceptor and donor states in reagent molecules.

6.4 Summary and conclusions

In summary, this Chapter explored the potential future investigation of transition metal doping in Imo NTs by means of (self-consistent) Hubbard-U corrected LS-DFT. This has been achieved by considering a highly idealised AlSi NT model, two unit cells in length, with two isomorphic Fe/Al substitutions arranged opposite each other in the NT circumference. For this system the standard PBE-GGA functional has been evaluated as well as three different Hubbard-U corrections: (a) based on a literature derived value (5.00 eV [356, 362]) (b) an internally consistent value obtained via a single GGA linear response calculation (7.63 eV) and (c) a fully self-consistent value derived via a series of linear response calculations (7.74 eV). Methods for obtaining the linear response val-

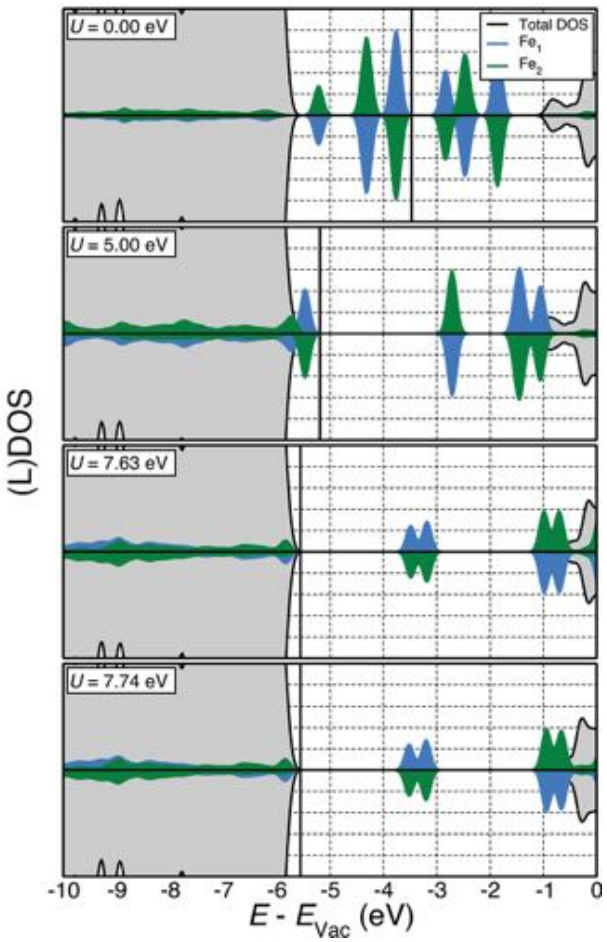

Figure 6.5: Plots of the spin-polarised local Density of States for Fe-AlSi NTs computed with different DFT+U corrections. For GGA, $U_{\mathrm{Lit}} = 5.00$, $U_0 = 7.63$ and $U_{\mathrm{SCF}} = 7.74$ eV. Total density of states are filled grey, the two (identical) Fe sites are plotted in blue and green. The vertical black continuous line mark separates occupied states (on its left) from empty ones (on its right).

ues based on ONETEP calculations (see Equations (6.11) & (6.14)) have been developed outside of this Thesis and the corresponding manuscript is being reviewed. In this Chapter, the computed internally and fully self-consistent values of U are similar, but larger than previously reported, although previous works have considered chemically different systems.

The U correction is not found to significantly alter the geometry of the NTs or the qualitatively separation of the VBE and CBE of the underlying AlSi NT. In addition, U also does not alter the spatial distribution of the localised Fe-states, which are found to bridge the gap between the VBE and CBE. Where the choice of U is found to have a large impact in the computation of the system band gap and absolute vacuum-aligned band edges. In this respect the GGA functional is found to give a qualitatively different picture with respect to all values of U. Furthermore, where the internally and fully self-consistent values of U are employed the electronic properties of the considered system are (i) highly comparable with each other (ii) significantly different from results obtained with the literature value of U, suggesting that either U_0 or U_{SCF} would be appropriate for simulation of the Fe-containing NTs.

Concerning the Fe containing tubes, results for the fully-self consistent U_{SCF}, suggest the presence of a visible-light band gap (2.3 eV) in good agreement with experimental values, and band alignments consistent with those found for other members of the Imogolite family. These conclusions must be taken with extreme caution as they fail to consider more realistic dopant concentrations, the presence of surface adsorbed clusters and adatoms or the potential for Fe atoms to induce size changes to the NT. In spite of the objective limitations these results are however promising and lay a novel methodological basis for future investigation in this area.

Chapter 7

Conclusions

7.1 Summary of this Thesis

This Thesis has studied the different members of the Imogolite family in the context of polarisation-assisted photo-catalysis. This exploration has been conducted by means of the linear-scaling Density Functional Theory formalism implemented within the ONETEP code.

Previous experimental and theoretical investigations have highlighted the versatility of Imogolite nanotubes in terms of their ease of synthesis, functionalisation and doping. They have uncovered, but not fully explored, the emergence of a permanent local polarisation across the nanotube wall and an observed separation of the valence and conduction band edges in real space. The work presented here builds upon these results, uncovering, for the first time, the relationship between the size and composition of the nanotube and the magnitude of the surface polarisation, the influence of the nanotube polarisation on the energetic distribution of the states of reactant molecules and insight into the optical transitions present in nanotubes with varying compositions. The results presented begin to bridge the knowledge gap that exists between experiment and theory of inorganic nanotubes as a result of the difficulty encountered when simulating systems with large numbers of atoms. Furthermore, they invite future investigations of the different Imogolite nanotubes by experiment and simulation.

The first part of the Thesis provides the background necessary for developing new photo-catalysts, driven by the properties of the photo-catalyst, as well as the theoretical foundation needed for the investigation of materials by linear-scaling Density

Functional Theory simulations. Chapter 1 discusses the requirements for viable, visible light photo-catalysis, highlighting the need for a band gap suitable to the given application, mechanism for effective e and h separation and independent migration to the photo-catalyst surfaces, and fast charge transfer between the photo-catalyst and reactant at the interfaces. Leveraging these key requirements the Chapter describes theory that underpins photo-catalysis by semiconducting materials. The absorbtion process was outlined, stressing the advantage of direct band gap over indirect gap semiconductors and possible routes to e-h recombination. The theoretical rate constant for charge-transfer was introduced; its formulation allowed a discussion of the optimal conditions for electron transfer between the photo-catalyst and reactant, namely suitable alignment of the bands of the photo-catalyst with the donor and acceptor states of the molecule, strong electronic coupling between the electron-donor and electron-acceptor states and overlap between the initial and final state nuclear wavefunctions.

A brief account of the current "state-of-the-art" techniques for band tuning and engineering were presented to show that, while capable of providing suitable band gaps and alignment with reactant states, the challenges associated with current research in the field are yet to be overcome. This leads to a discussion of innovative strategies, based on photo-catalyst design. Properties found to be of particular interest are the nanoporosity of zeolite based materials, the permanent polarisation and ensuing electric field gradients of ferroelectric materials and the large aspect ratios and electrostatic potential anisotropies introduced by one dimensional nanostructuring. Each of these avenues has previously been found to be beneficial for photo-catalysis, therefore, in order to bring them together into one material Imogolite nanotubes are introduced. The final part of Chapter 1 explains the structure and properties of the various Imogolite nanotubes, highlighting potential exploits for photo-catalysis. These include the visible light band gap observed for Fe-doped aluminosilicate nanotubes, the open ended nature of the nanotubes and potential reactant access to the 1 nm pores and the permanent polarisation of the nanotube walls that could be useful for e-h separation. Finally a mechanism for nanoconfined, polarisation enhanced photo-catalysis is proposed on the basis of the properties of the Imogolite nanotubes.

Chapter 2 provides the formulation of linear-scaling Density Functional Theory as implemented in the ONETEP code. The underlying theory was recounted first, starting from basic many-body quantum theory. This shows the practical impossibility of solving the time-dependent many-body Schrödinger Equation for any meaningful system,

and the need for approximate solutions. As a background to the linear-scaling theory, Kohn-Sham Density Functional Theory is introduced. A derivation of Hohenberg-Kohn theorems demonstrates that the wavefunction may be replaced by the electronic density as a variable for calculations, reducing the complexity of the problem. The derivation of the Kohn-Sham equations provides a variational approach for the computation of the total energy of the system.

Linear-scaling Density Functional Theory relies on the nearsightedness of quantum matter and the imposition of spatial and energetic cutoffs on the basis functions. This is well represented by the single particle density matrix. The Section relating to linear-scaling Density Functional Theory begins with a description of density matrix theory and how to abstract information from the single particle density matrix. Specific theory relating to ONETEP is presented, including the use of non-orthogonal generalised Wannier functions, and underlying periodic sine cardinal basis and partitioned Fast Fourier Transforms (that only span occupied regions of the simulation cell). These are the elements that enable the linear-scaling in ONETEP. More than just a theoretical formulation, Chapter 2 also provides some practical considerations for simulations. In particular, for optimal performance across different computational clusters and architectures, insight into the Hybrid OpenMP-MPI parallelisation is given.

In the second part of the Thesis the results of the simulations carried out are presented. In order for those simulations to be carried out, extensive testing of the linear-scaling approach is required. This testing is detailed in Chapter 3, which reports on the computational parameters and accuracy-viability compromises needed for the simulation of Imogolite nanotubes. Two systems are considered for the evaluation of key computational parameters: a small curved fragment of the aluminosilicate nanotube circumference terminated with hydrogen atoms and a methylated ($N = 24$) aluminosilicate nanotube. On this basis, the required kinetic energy cutoff, NGWF localisation radius and required number of empty states for viable energetic and band gap convergence are obtained. Additionally, Chapter 3 also reports on the lattice parameter and geometric convergence thresholds for the methylated aluminosilicate nanotubes. To test the adopted linear-scaling method for description of more realistic materials, the Chapter analyses the minimum model size required for simultaneous description of the aluminosilicate nanotube termination and bulk phase. The results presented suggest that, depending on the termination composition, models should be at least 23 Å in length.

Chapter 4 combines an energetic screening and characterisation of the selectively inner surface methylated aluminosilicate nanotubes with an investigation into the size (and exchange-correlation functional) dependence of the nanotube wall polarisation. Owing to the presence of polarisable methyl groups, the investigation takes into consideration several different exchange correlation functionals. The results indicated that the methylated nanotubes are larger than the pristine nanotubes, and the broad energetic minima found brackets the experimental pore size distribution. It is reported that whilst the choice of exchange-correlation functional does not largely affect the geometry, the use of self-consistent van der Waals corrected functionals (VDWDF, OPTPBE and OPTB88) reduces the energies of the computed band edges and widens the band gap. Moreover, these exchange correlation functionals also result in slightly higher computed polarisations.

Following the derivation of the surface dipole density on the basis of the associated step in the electrostatic potential, the polarisation of the methylated nanotubes is found to decrease as a function of the diameter. Given that the potential step is found to be constant for the range of nanotube diameters considered, this result is explained in terms of the geometric factor associated with warped surface-dipole layers. In the last Section, the Chapter provides generalisable strategies for the development of more polarised nanotubes, for better *e*-*h* separation, based on the radii and surface functionalisations.

Building on these results, Chapter 5 extends the electronic characterisation of the Imogolite nanotubes to the aluminosilicate, aluminogermanate and double-walled aluminogermanate nanotubes. In addition, Chapter 5 presents results on the photocatalytic potential of the Imogolite nanotubes. Each of the considered nanotube compositions provides (qualitatively) the same electronic properties, namely a wide band gap, separation of the valence and conduction band edges and a permanent polarisation of the nanotube walls. The polarisation is found to vary with nanotube composition, with the methylated (double walled aluminogermante) nanotubes having the smallest (largest) surface dipole densities. Similarly, the band gap and absolute band alignments are also shown to vary with composition with the smallest (largest) gaps observed for the double walled aluminogermanate (methylated) nanotubes. The Chapter compares the vacuum algined band edges with two different TiO_2 polymorphs, this analysis suggests that by comparison the Imogolite tubes have a larger energy drive for H_2O photo-reduction. The influence of the nanotube polarisation on the donor and acceptor states of H_2O molecules inside and outside the nanotube cavity is investigated to gain insight into the

potential for photolysis by the Imogolite nanotubes. Vacuum-alignment suggests an energetic drive for photo-reduction of H_2O outside the cavity by all of the systems except the double-walled aluminogermanate nanotubes. On the other hand, photo-oxidation appeared energetically viable for the H_2O molecules inside non-methylated nanotubes.

The final results Chapter reports on initial attempts to study the properties of Fe containing Imogolite. As a strategy to overcome some of difficulties associated with the computation of materials containing transition metal ions, Chapter 6 introduces the Hubbard U correction, which can be calculated in an internally consistent formulation based on linear response theory and a fully self-consistent value derived via a of series linear response calculations. Comparing these approaches with the uncorrected GGA functional and a U correction taken from the literature, the Chapter shows that the NT geometry and characteristic separation of the VBE and CBE is unaffected. The system band gap and absolute vacuum-aligned band edges are shown to be sensitive to the applied correction, with the GGA functional found to give a qualitatively different picture with respect to all values of U. The two linear response optimised approaches are found to give similar results and both could be considered appropriate for simulation of the Fe-containing NTs. The idealised NT model considered is found to have a visible-light band gap (2.3 eV) and the vacuum aligned band edges are consistent with those found for other members of the Imogolite family. These results should provide a novel methodological basis for future investigation in this area.

7.2 Future work

Before concluding this Thesis, some consideration will be given to the further work that could be carried out, building on the results presented, in both the short and long term.

The results presented in Chapter 3 show that the linear scaling formulation can be successfully applied to complex metal oxide nanotubes containing thousands of atoms. The approach could also be extended to other (wide-gap) complex oxide materials providing access to more realistic representations of nanotubes, nanowires, nanoparticles and interfaces. The ONETEP community is currently growing and with this will come its application to many different types of system.

Chapter 4 alluded to the possibility that purposeful functionalisation of the nanotube walls could give rise to smaller or larger polarisations. To this end, several preliminary

calculations have already been carried out on differently functionalised nanotubes with inner surface CF_3 and F in place of OH groups. These early results, for the limited number of nanotube considered ($N = 24, 36$), confirm that the band separation across the walls is maintained and suggest that substitution by more electron withdrawing groups at the inner surface should increase the polarisation of the tube walls potentially allowing for greater *e-h* separation. For a fuller picture, a complete energetic screening of these systems, and other halogenated Imogolites is required and could feasibly be carried out. Investigations along these lines could be used as a tool for the screening of many different Imogolite functionalisations and used to inform experimental syntheses.

On the basis of the results for the H_2O-Imogolite nanotube interfaces presented at the end of Chapter 5, investigation of the photocatalytic potential of the methylated aluminosilicate nanotubes ($AlSi_{28/36}$-Me NTs) has continued. Additional simulations to compute the absolute vacuum alignment of analogous N_2- $AlSi_{28/36}$-Me and CO_2-$AlSi_{28/36}$-Me NTs have been considered. In combination with the results for the molecule interfaces with AlSi, AlGe and DW-AlGe NTs (still to be calculated) a more complete picture of the photocatalytic capability of the Imogolite nanotubes can be obtained. In addition, the extent to which the polarisation of the nanotube walls tunes the energy of the donor and acceptor states of the reagent molecules can also be assessed. More than this, analogous calculations for the aminated AlSi NTs are also planned. In the longer term, to include the screening effects of the solvent on the nanotube polarisation, ab-initio molecular dynamics simulations of full explicitly solvated (in the polar solvent H_2O, and non polar solvent CO_2) Imogolite nanotubes are planned.

The scope for future investigation of transition metal-doped Imogolite nanotubes via Hubbard-U corrected linear-scaling Density Functional Theory is very wide. Recovery of the experimental band gap for the idealised models is promising, however a full energetic screening of the isomorphic Fe/Al substitution sites, diameter of doped nanotube and magnetic ordering should be conducted in order to extend the significance of the study in the field. These results should also be cross checked with respect to the computed U correction which may change as a result of different hybridisation of the Fe site for larger nanotube curvatures or through defect-defect interactions. Pending these results, and similar results for other transition metal elements, the extent to which the surface dipole density of the nanotube wall is affected by the presence of defects would provide an indication of the trade-off between potential polarisation-enhanced *e-h* separation and defect site recombination.

Appendices

Appendix A

Properties of tensors

When working in a non-orthogonal basis, as is the case for simulations in ONETEP, it must appreciated that simply manipulating orthogonal expressions can lead to violations of tensor algebra. Instead, by formulating a tensorially correct theory in the first instance, which reduces to orthogonal basis expressions in the limit where the metric tensor is unit, these violations can be avoided. This Appendix outlines the relevant tensor theory.

In a non-orthogonal basis set, Vectors can be categorised as co-variant, denoted with subscript indices a_i, or contra-variant, denoted with superscript indices a^i. Co-variant vectors usually relate to gradients and other quantities related to derivatives whereas contra-variant vectors instead relate to distances. Specific rules apply to vectors in non-orthogonal basis sets. For example, summation between co-variant and contra-variant vectors cannot be carried out directly and contraction of the vector index can only occur between the indices of co-variant and contra-variant vectors.

For the vector $\mathbf{A} = a_i \mathbf{e}^i$ in the contra-variant basis $\mathbf{e}^i$ and the vector $\mathbf{B} = b^j \mathbf{e}_i$ in the covariant basis $\mathbf{e}_i$, the inner product is defined,

$$\mathbf{A} \cdot \mathbf{B} = a_i \; b^j \; \mathbf{e}^i \cdot \mathbf{e}_j, \tag{A.1}$$

where a_i and b^j represent the co-variant and contra-variant coefficients of $\mathbf{A}$ and $\mathbf{B}$ respectively. Owing to the relationship $\mathbf{e}^i \cdot \mathbf{e}_j = \delta^i_j$ the inner product simplifies to

$$\mathbf{A} \cdot \mathbf{B} = a_i \; b^i. \tag{A.2}$$

The self-product,

$$\mathbf{A} \cdot \mathbf{A} = a_i \; a_j \; \mathbf{e}^i \cdot \mathbf{e}^j, \tag{A.3}$$

$$= a_i \; a_j \; g^{ij}. \tag{A.4}$$

The metric tensor, g^{ij} and its inverse $g_{ij} = \left(g^{ij}\right)^{-1}$, provides the link between covariant and contra-variant vector representations, in that it makes it possible to lower or raise the vector indices:

$$a^j = g^{ji} \; a_i \tag{A.5}$$

$$a_j = g_{ji} \; a^i. \tag{A.6}$$

Appendix B

Further electronic characterisation of Imogolite nanotubes

This Appendix provides further electronic characterisation of the different Imogolite nanotubes (Imo NTs) considered in this Thesis. Specifically, Table B.1 gives a breakdown of the Mulliken charge analysis [339] for the CH_3 groups at the inner surface of the methylated Imo NTs for each of the exchange correlation (XC-)functionals considered in Chapter 4. Figure B.1 also compares the performance of the XC-functionals for the real space separation of the Imo NT valence and conduction band edges. Finally Figures B.2 to B.10 are the layer resolved local density of states for all of the NT compositions considered in this Thesis.

N	PBE	PBE-E	PBE-D2	VDWDF	OPTPBE	OPTB88
24	-0.3076	-0.3080	-0.3086	-0.3184	-0.3129	-0.3197
26	-0.3013	-0.3012	-0.3024	-0.3115	-0.3067	-0.3128
28	-0.2934	-0.2933	-0.2938	-0.3088	-0.2990	-0.3109
30	-0.2876	-0.2896	-0.2856	-0.3022	-0.2961	-0.2985
32	-0.2818	-0.2838	-0.2833	-0.2986	-0.2889	-0.2938
34	-0.2720	-0.2730	-0.2765	-0.2942	-0.2816	-0.2919
36	-0.2753	-0.2758	-0.2729	-0.2932	-0.2836	-0.2884

Table B.1: Muliken charges (e) for the methyl groups at the inner surface for each of the XC-functionals adopted.

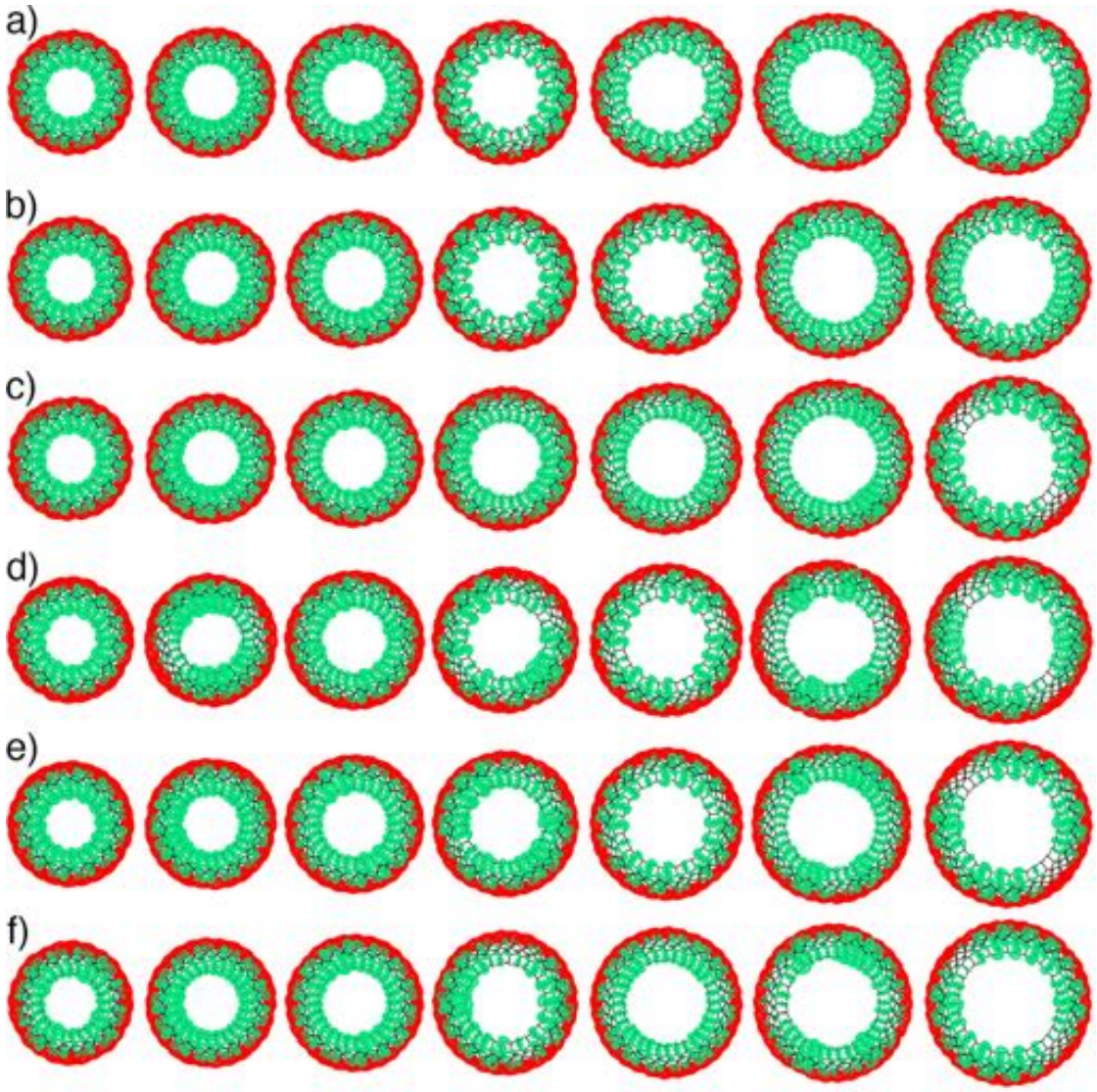

Figure B.1: Real space separation of the VBE (green) and CBE (red) for the considered $AlSi_N$-Me NTs in the range $N = 24$ to $N = 36$ (left to right) and for each adopted XC-functional: (a) PBE (b) PBE-E (c) PBE-D2 (d) VDWDF (e) OPTPBE (f) OPTB88

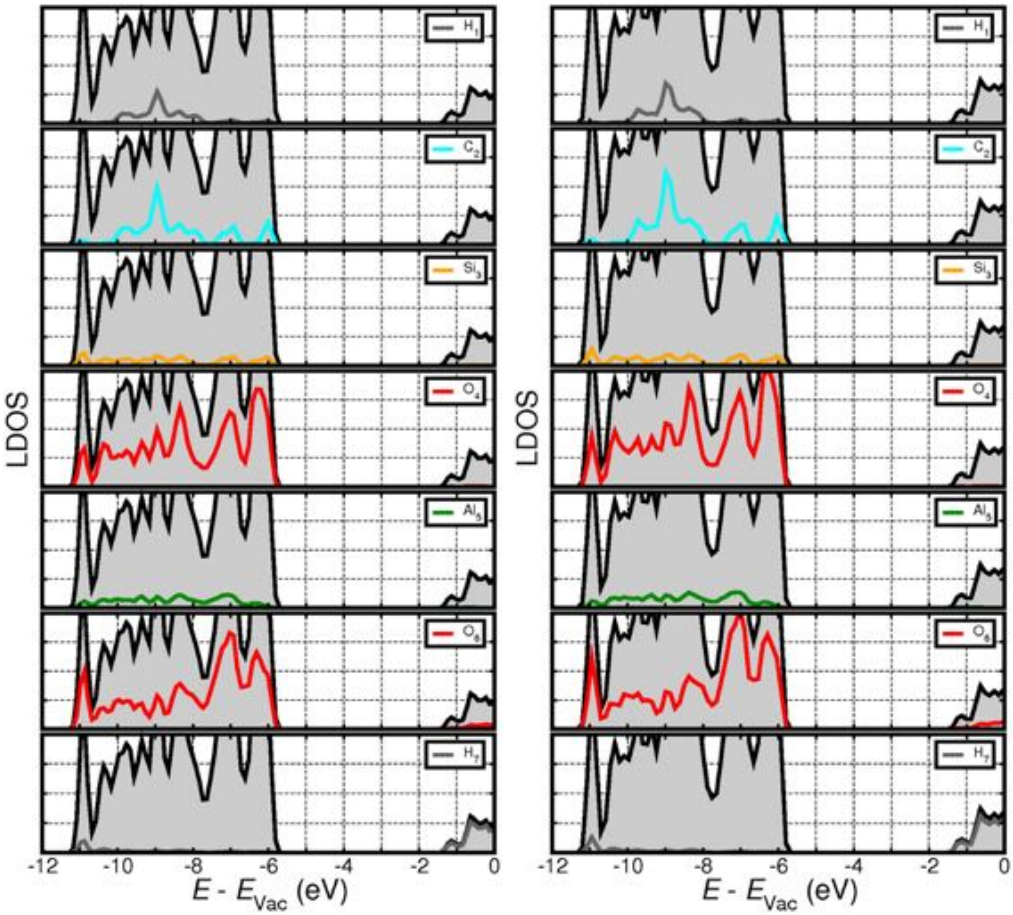

Figure B.2: The vacuum aligned layer resolved LDOS plot for $AlSi_{28}$-Me, left, and $AlSi_{34}$-Me, right, NTs calculated with the PBE XC-functional. The total DOS is filled grey.

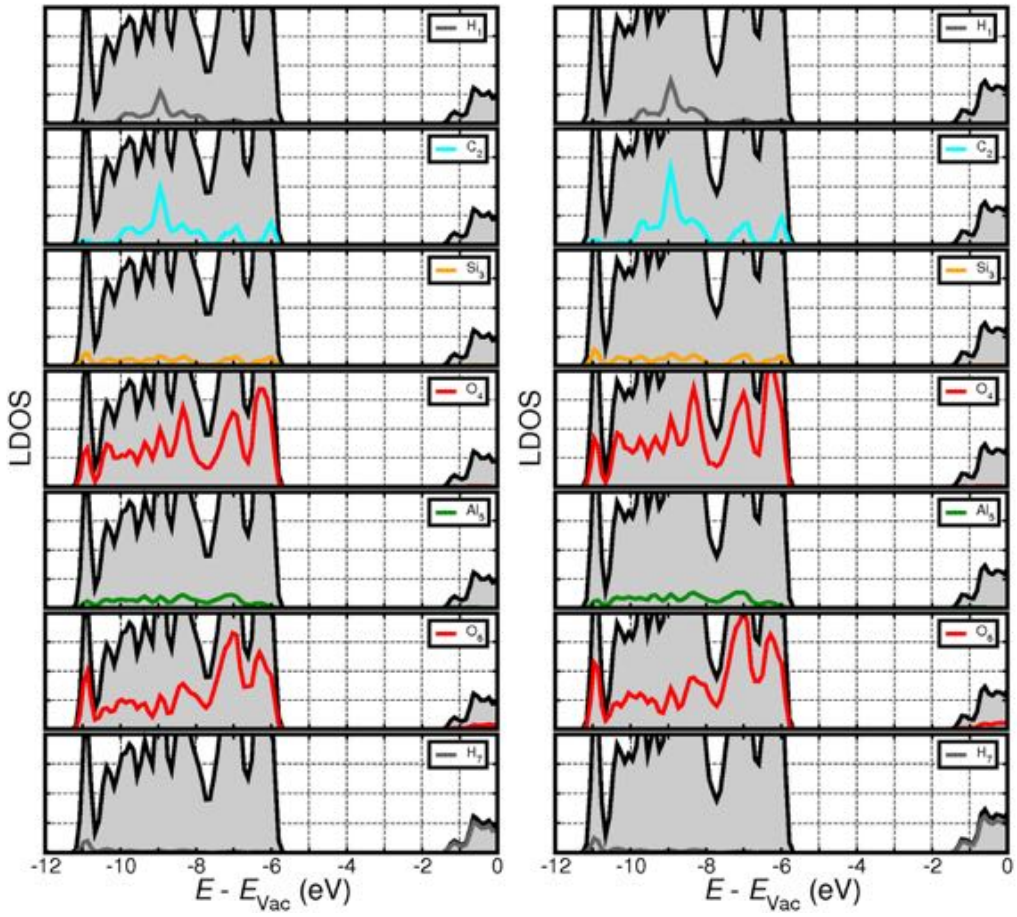

Figure B.3: The vacuum aligned layer resolved LDOS plot for $AlSi_{28}$-Me, left, and $AlSi_{34}$-Me, right, NTs calculated with the PBE-E XC-functional. The total DOS is filled grey.

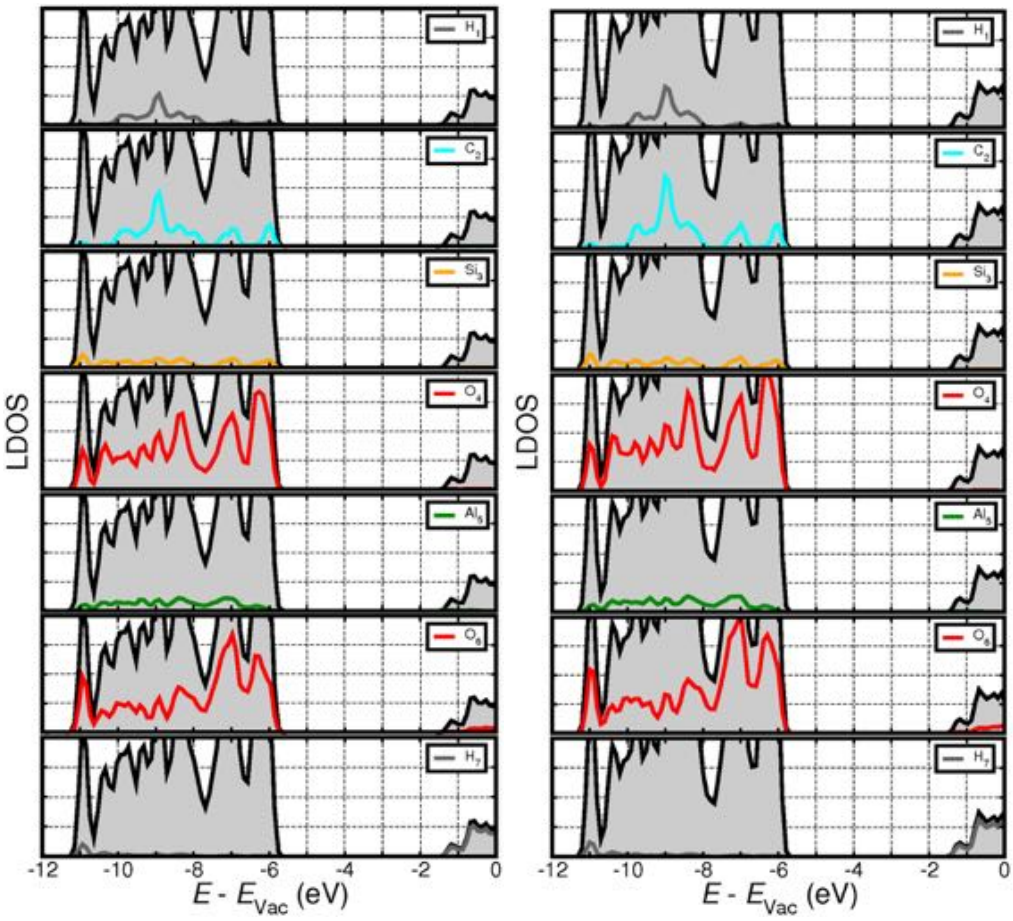

Figure B.4: The vacuum aligned layer resolved LDOS plot for $AlSi_{28}$-Me, left, and $AlSi_{34}$-Me, right, NTs calculated with the PBE-D2 XC-functional. The total DOS is filled grey.

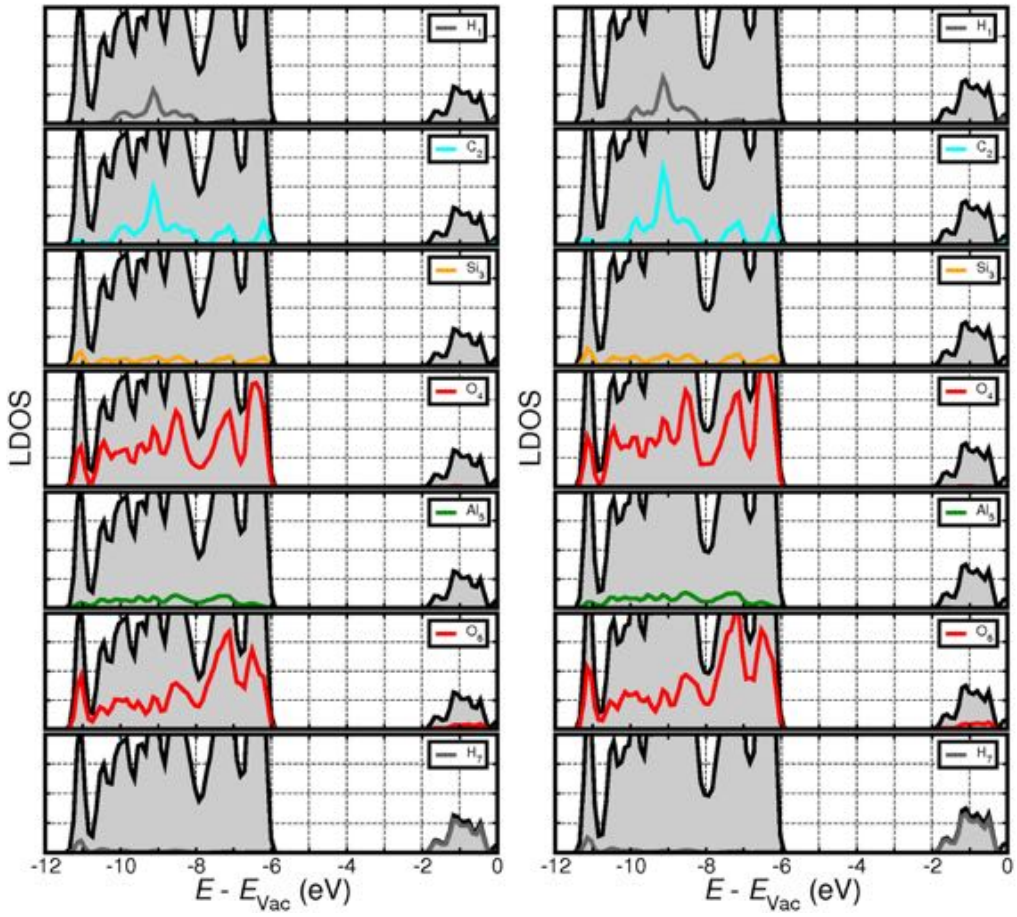

Figure B.5: The vacuum aligned layer resolved LDOS plot for $AlSi_{28}$-Me, left, and $AlSi_{34}$-Me, right, NTs calculated with the VDWDF XC-functional. The total DOS is filled grey.

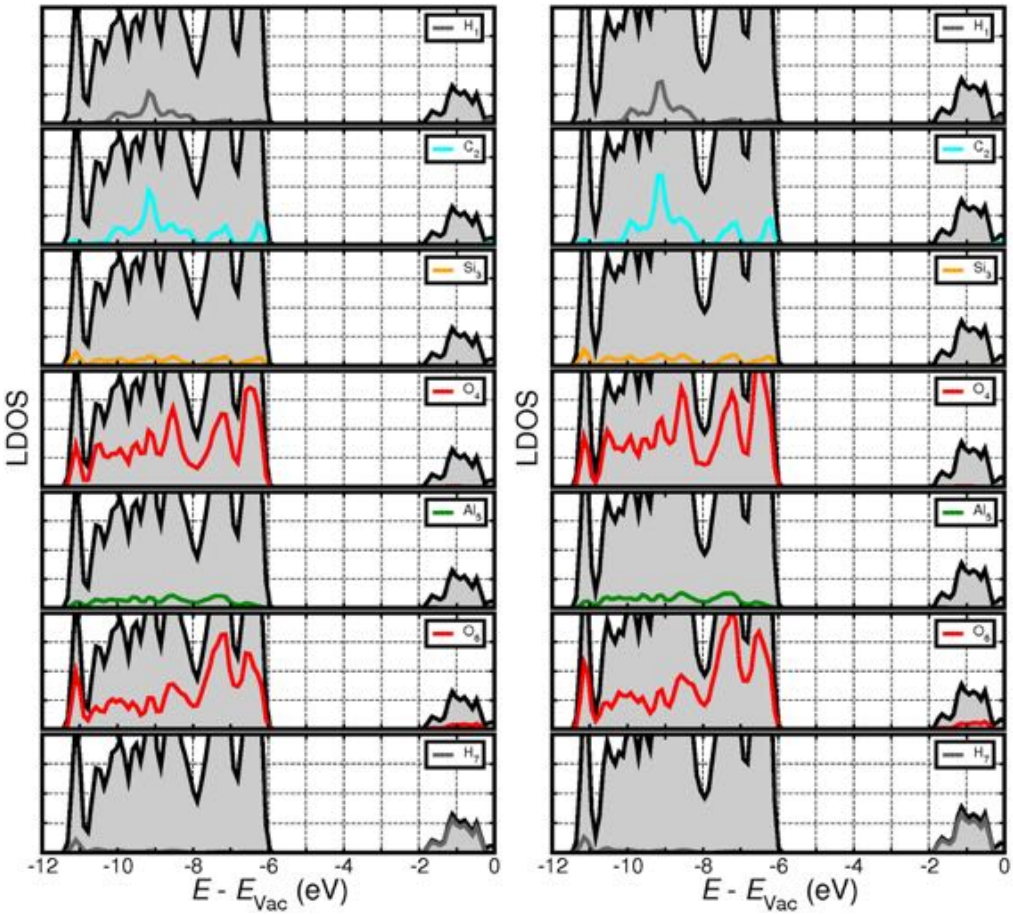

Figure B.6: The vacuum aligned layer resolved LDOS plot for $AlSi_{28}$-Me, left, and $AlSi_{34}$-Me, right, NTs calculated with the OPTB88 XC-functional. The total DOS is filled grey.

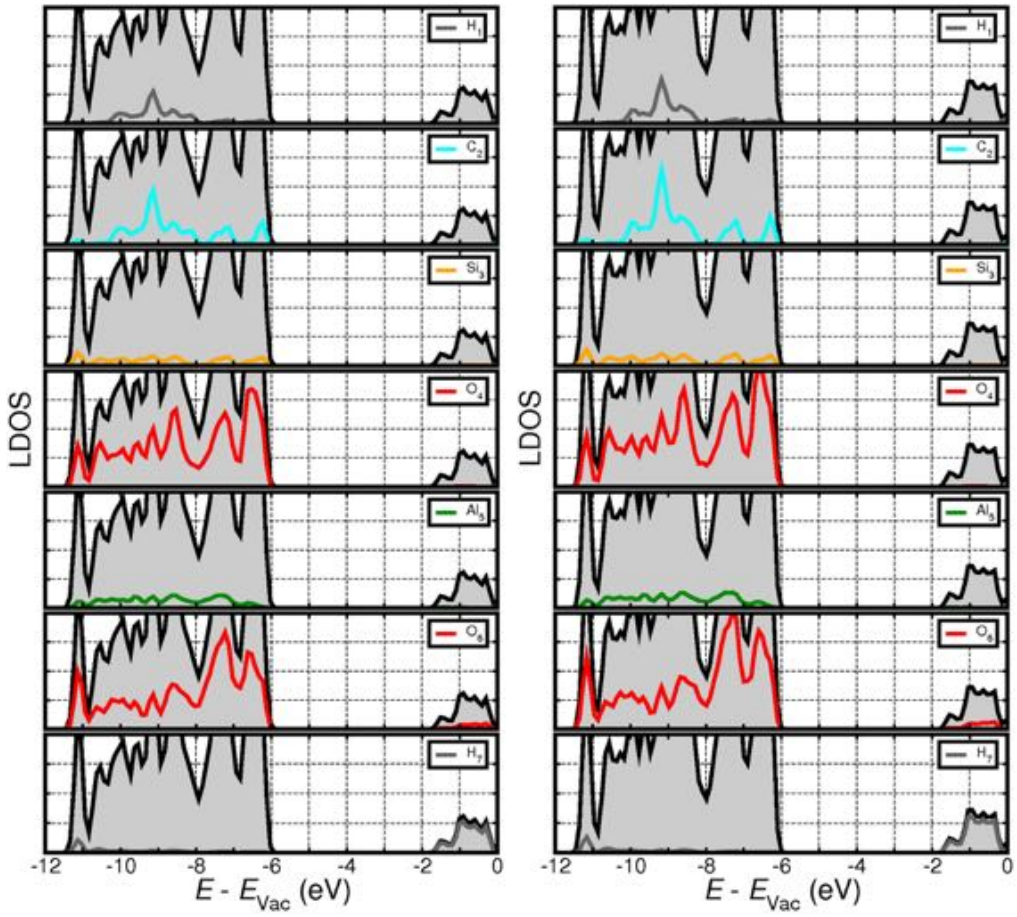

Figure B.7: The vacuum aligned layer resolved LDOS plot for $AlSi_{28}$-Me, left, and $AlSi_{34}$-Me, right, NTs calculated with the OPTB88 XC-functional. The total DOS is filled grey.

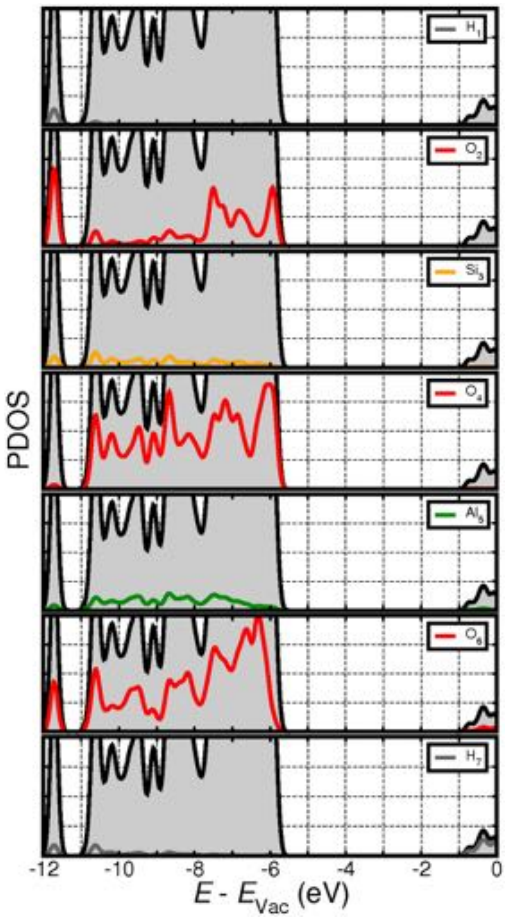

Figure B.8: The vacuum aligned layer resolved LDOS plot for $AlSi_{36}$ NT, calculated with the PBE XC-functional. The total DOS is filled grey.

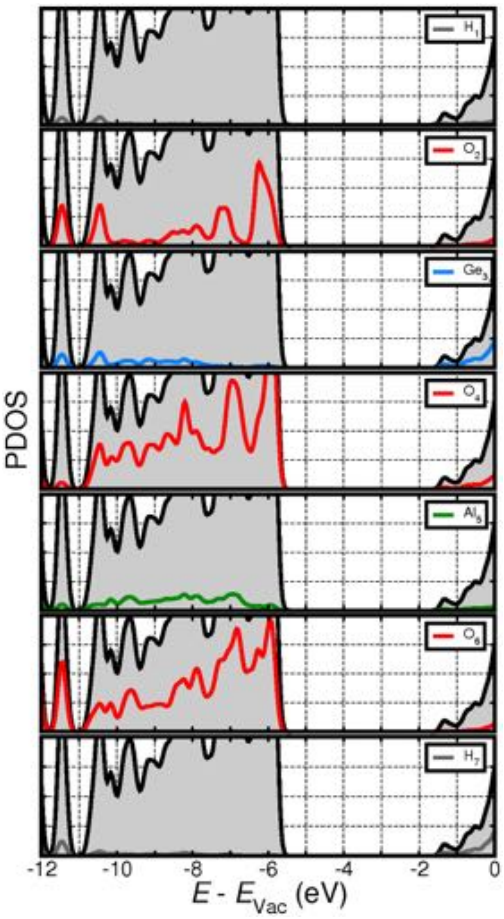

Figure B.9: The vacuum aligned layer resolved LDOS plot for $AlGe_{36}$ NT, calculated with the PBE XC-functional. The total DOS is filled grey.

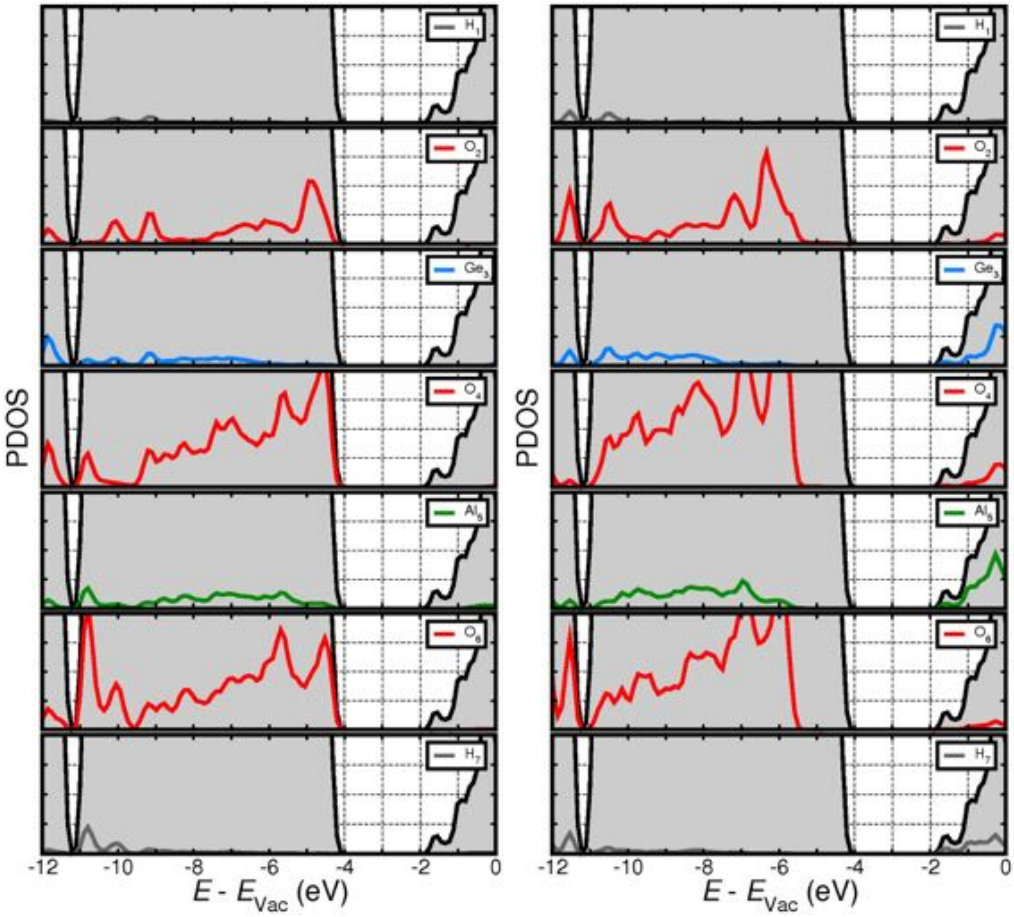

Figure B.10: The vacuum aligned layer resolved LDOS plot for DW-AlGe$_{36,54}$ NT. The inner tube is plotted on the left, and outer tube plotted on the right. NTs calculated with the PBE XC-functional. The total DOS is filled grey.

Appendix C

Convergence of Fe insertion energy in Imogolite

In this Appendix, the energetic convergence of a single isomorphic Fe/Al substitution (Fe insertion) as a function of the overall supercell size, see Figure C.1a is reported.

Fe insertion into the pristine aluminosilicate (AlSi) NT can be described by the chemical scheme:

$$\mathrm{AlSi}_N \ + \ \mathrm{Fe} \rightarrow [\mathrm{Fe}]\mathrm{AlSi}_N \ + \ \mathrm{Al},$$

where, here, N refers to the number of unit cells that the total supercell is comprised of. On this basis the energy of insertion, E_{ins}, can be calculated via

$$E_{\mathrm{ins}} = (E_{[\mathrm{Fe}]\mathrm{AlSi}_N} + E_{\mathrm{Al}}) - (E_{\mathrm{AlSi}_N} + E_{\mathrm{Fe}}). \tag{C.1}$$

where E_X represents the computed energy of species X ($X = [\mathrm{Fe}]\mathrm{AlSi}_N$, AlSi_N, Al and Fe). Here, to prevent the emergence of the egg-box effect [285,286], E_{AlSi_N} represents the energy of an undoped AlSi NT supercell. A plot based on this computation of E_{ins} can be seen in Figure C.1b. Convergence of E_{ins} is obtained for supercells comprised of two AlSi Unit cells (blue markers Figure C.1a).

The results presented in this Appendix suggest that Fe-defects are only weakly energetically coupled when separated by two AlSi NT unit cells. These simulation cells have an axial repeat length of 17.32 Å. This serves a basis for the simulations of Fe-doped Imo NTs reported in Chapter 6.

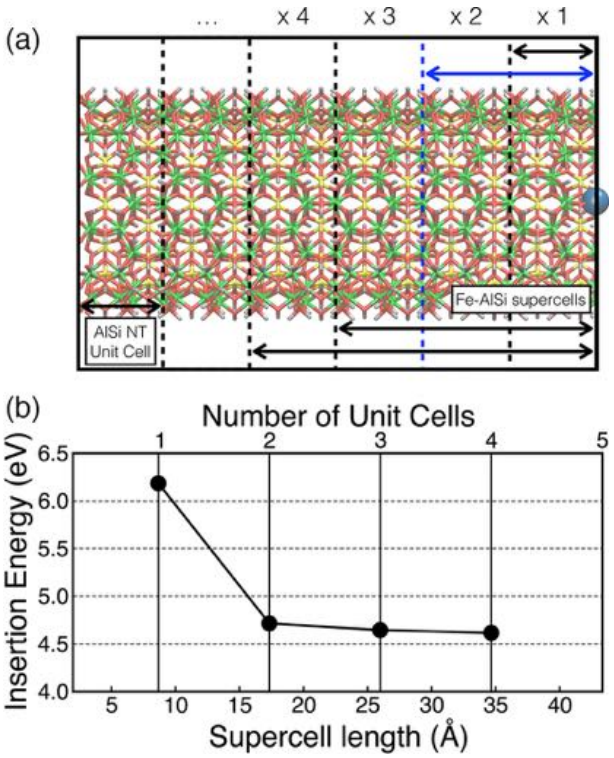

Figure C.1: (a) Schematic representation of the supercell approach used in order to compute the insertion energy of an Fe atom into the $AlSi_2$4 NT. The Fe atom and the supercell size ($1 \times 1 \times 2$) are coloured blue. (b) Plot of the Fe ion insertion energy, E_{ins}, as a function of the supercell size, for the two considered approaches.

Bibliography

[1] *Concise report on the world population situation in 2014* (2014). Department of Economic and Social Affairs Population Division United Nations

[2] *World Population Clock*. URL http://www.worldometers.info/world-population/. Retrieved 25^{th} July 2016

[3] Solomon, S., Ivy, D. J., Kinnison, D., Mills, M. J., Neely, R. R., and Schmidt, A. *Emergence of healing in the Antarctic ozone layer*. Science, **353**, 6296, (2016), 269

[4] Cook, J., Oreskes, N., Doran, P. T., Anderegg, W. R., Verheggen, B., Maibach, E. W., Carlton, J. S., Lewandowsky, S., Skuce, A. G., Green, S. A., *et al. Consensus on consensus: a synthesis of consensus estimates on human-caused global warming*. Environ. Res. Lett., **11**, 4, (2016), 048002

[5] Steinfeld, H., Gerber, P., Wassenaar, T., Castel, V., Rosales, M., and De Haan, C. *Livestock's long shadow*. FAO Rome (2006)

[6] Goodland, R. and Anhang, J. *Livestock and climate change: What if the key actors in climate change are... cows, pigs, and chickens?* World Watch Magazine, **6**, 22, (2009), 10

[7] Tilman, D. and Clark, M. *Global diets link environmental sustainability and human health*. Nature, **515**, 7528, (2014), 518

[8] Scarborough, P., Appleby, P. N., Mizdrak, A., Briggs, A. D., Travis, R. C., Bradbury, K. E., and Key, T. J. *Dietary greenhouse gas emissions of meat-eaters, fish-eaters, vegetarians and vegans in the UK*. Climatic Change, **125**, 2, (2014), 179

[9] Mitchell, J. F. *The "greenhouse" effect and climate change*. Rev. Geophys., **27**, 1, (1989), 115

[10] Thomas, C. D., Cameron, A., Green, R. E., Bakkenes, M., Beaumont, L. J., Collingham, Y. C., Erasmus, B. F., De Siqueira, M. F., Grainger, A., Hannah, L., *et al. Extinction risk from climate change.* Nature, **427**, 6970, (2004), 145

[11] *Annual Fuel Poverty Statistics Report* (2015). URL https://www.gov.uk/government/collections/fuel-poverty-statistics

[12] Schiermeier, Q., Tollefson, J., Scully, T., Witze, A., and Morton, O. *Electricity without carbon.* Nature, **454**, 7206, (2008), 816

[13] Warren, J. *Materials genome initiative.* In *AIP Conf. Proc.* American Institute of Physics, Ste. 1 NO 1 Melville NY 11747-4502 United States (2012)

[14] Jain, A., Ong, S. P., Hautier, G., Chen, W., Richards, W. D., Dacek, S., Cholia, S., Gunter, D., Skinner, D., and Ceder, G. *Commentary: The Materials Project: A materials genome approach to accelerating materials innovation.* Apl. Mater., **1**, 1, (2013), 011002

[15] Fujishima, A. and Honda, K. *Electrochemical evidence for the mechanism of the primary stage of photosynthesis.* B. Chem. Soc. Jpn, **44**, 4, (1971), 1148

[16] Liu, Q., Ding, D., Ning, C., and Wang, X. *Black Ni-doped TiO_2 photoanodes for high-efficiency photoelectrochemical water-splitting.* Int. J. Hydrogen Energ., **40**, 5, (2015), 2107

[17] Fox, M. A. and Dulay, M. T. *Heterogeneous photocatalysis.* Chem. Rev., **93**, 1, (1993), 341

[18] Hagfeldt, A. and Graetzel, M. *Light-induced redox reactions in nanocrystalline systems.* Chem. Rev., **95**, 1, (1995), 49

[19] Hoffmann, M. R., Martin, S. T., Choi, W., and Bahnemann, D. W. *Environmental applications of semiconductor photocatalysis.* Chem. Rev., **95**, 1, (1995), 69

[20] Fujishima, A., Zhang, X., and Tryk, D. A. *TiO_2 photocatalysis and related surface phenomena.* Surf. Sci. Rep., **63**, 12, (2008), 515

[21] Rauf, M. and Ashraf, S. S. *Fundamental principles and application of heterogeneous photocatalytic degradation of dyes in solution.* Chem. Eng. J., **151**, 1, (2009), 10

[22] Hernández-Alonso, M. D., Fresno, F., Suárez, S., and Coronado, J. M. *Development of alternative photocatalysts to TiO_2: challenges and opportunities.* Energy Environ. Sci., **2**, 12, (2009), 1231

[23] Morris, A. J., Meyer, G. J., and Fujita, E. *Molecular approaches to the photocatalytic reduction of carbon dioxide for solar fuels.* Acc. Chem. Res., **42**, 12, (2009), 1983

[24] Chong, M. N., Jin, B., Chow, C. W., and Saint, C. *Recent developments in photocatalytic water treatment technology: a review.* Water Res., **44**, 10, (2010), 2997

[25] Ahmed, S., Rasul, M., Martens, W. N., Brown, R., and Hashib, M. *Heterogeneous photocatalytic degradation of phenols in wastewater: a review on current status and developments.* Desalination, **261**, 1, (2010), 3

[26] Maeda, K. and Domen, K. *Photocatalytic water splitting: recent progress and future challenges.* J. Phys. Chem. Lett., **1**, 18, (2010), 2655

[27] Kitano, M. and Hara, M. *Heterogeneous photocatalytic cleavage of water.* J. Mater. Chem., **20**, 4, (2010), 627

[28] Ji, P., Takeuchi, M., Cuong, T.-M., Zhang, J., Matsuoka, M., and Anpo, M. *Recent advances in visible light-responsive titanium oxide-based photocatalysts.* Res. Chem. Intermediat., **36**, 4, (2010), 327

[29] Yang, Y., Zhong, H., and Tian, C. *Photocatalytic mechanisms of modified titania under visible light.* Res. Chem. Intermediat., **37**, 1, (2011), 91

[30] Hagfeldt, A. and Grätzel, M. *Molecular photovoltaics.* Acc. Chem. Rese., **33**, 5, (2000), 269

[31] Sastre, F., Fornés, V., Corma, A., and García, H. *Selective, room-temperature transformation of methane to C1 oxygenates by deep UV photolysis over zeolites.* J. Am. Chem. Soc., **133**, 43, (2011), 17257

[32] Ciamician, G. *The photochemistry of the future.* Science, **36**, 926, (1912), 385

[33] Tong, H., Ouyang, S., Bi, Y., Umezawa, N., Oshikiri, M., and Ye, J. *Nano-photocatalytic materials: possibilities and challenges.* Adv. Mater., **24**, 2, (2012), 229

[34] Djurišić, A. B., Leung, Y. H., and Ng, A. M. C. *Strategies for improving the efficiency of semiconductor metal oxide photocatalysis.* Mater. Horiz., **1**, 4, (2014), 400

[35] Weng, B., Liu, S., Tang, Z.-R., and Xu, Y.-J. *One-dimensional nanostructure based materials for versatile photocatalytic applications.* RSC Adv., **4**, 25, (2014), 12685

[36] Jacoboni, C., Canali, C., Ottaviani, G., and Quaranta, A. A. *A review of some charge transport properties of silicon.* Solid State Electron., **20**, 2, (1977), 77

[37] Borgarello, E., Kiwi, J., Graetzel, M., Pelizzetti, E., and Visca, M. *Visible light induced water cleavage in colloidal solutions of chromium-doped titanium dioxide particles.* J. Am. Chem. Soc., **104**, 11, (1982), 2996

[38] Herrmann, J.-M., Disdier, J., and Pichat, P. *Effect of chromium doping on the electrical and catalytic properties of powder titania under UV and visible illumination.* Chem. Phys. Lett., **108**, 6, (1984), 618

[39] Karakitsou, K. E. and Verykios, X. E. *Effects of altervalent cation doping of titania on its performance as a photocatalyst for water cleavage.* J. Phys. Chem., **97**, 6, (1993), 1184

[40] Yamashita, H., Ichihashi, Y., Takeuchi, M., Kishiguchi, S., and Anpo, M. *Characterization of metal ion-implanted titanium oxide photocatalysts operating under visible light irradiation.* J. Synchrotron Radiat., **6**, 3, (1999), 451

[41] Kudo, A., Kato, H., and Nakagawa, S. *Water splitting into H_2 and O_2 on new $Sr_2M_2O_7$ (M= Nb and Ta) photocatalysts with layered perovskite structures: factors affecting the photocatalytic activity.* J. Phys. Chem. B, **104**, 3, (2000), 571

[42] Zou, Z., Ye, J., and Arakawa, H. *Structural properties of $InNbO_4$ and $InTaO_4$: correlation with photocatalytic and photophysical properties.* Chem. Phys. Lett., **332**, 3, (2000), 271

[43] Zou, Z., Ye, J., Sayama, K., and Arakawa, H. *Photocatalytic and photophysical properties of a novel series of solid photocatalysts, $BiTa_{1-x}Nb_xO_4$ ($0 \leq x \leq 1$).* Chem. Phys. Lett., **343**, 3, (2001), 303

[44] Zou, Z., Ye, J., and Arakawa, H. *Preparation, structural and optical properties of a new class of compounds, Bi_2MNbO_7 (M= Al, Ga, In).* Mater. Sci. Eng.: B, **79**, 1, (2001), 83

[45] Ye, J., Zou, Z., Arakawa, H., Oshikiri, M., Shimoda, M., Matsushita, A., and Shishido, T. *Correlation of crystal and electronic structures with photophysical properties of water splitting photocatalysts $InMO_4$ (M= V^{5+}, Nb^{5+}, Ta^{5+}).* J. Photochem. Photobiol. A Chem., **148**, 1, (2002), 79

[46] Ishikawa, A., Takata, T., Kondo, J. N., Hara, M., Kobayashi, H., and Domen, K. *Oxysulfide $Sm_2Ti_2S_2O_5$ as a stable photocatalyst for water oxidation and reduction under visible light irradiation ($\lambda \leq 650$ nm).* J. Am. Chem. Soc., **124**, 45, (2002), 13547

[47] Wang, J., Zou, Z., and Ye, J. *Surface modification and photocatalytic activity of distorted pyrochlore-type Bi_2M (M= In, Ga and Fe) TaO_7 photocatalysts.* J. Phys. Chem. Solid., **66**, 2, (2005), 349

[48] Maeda, K., Takata, T., Hara, M., Saito, N., Inoue, Y., Kobayashi, H., and Domen, K. *GaN: ZnO solid solution as a photocatalyst for visible-light-driven overall water splitting.* J. Am. Chem. Soc., **127**, 23, (2005), 8286

[49] Maeda, K., Teramura, K., Takata, T., Hara, M., Saito, N., Toda, K., Inoue, Y., Kobayashi, H., and Domen, K. *Overall Water Splitting on $(Ga_{1-x}Zn_x)(N_{1-x}O_x)$ Solid Solution Photocatalyst: Relationship between Physical Properties and Photocatalytic Activity.* J. Phys. Chem. B, **109**, 43, (2005), 20504

[50] Luan, J., Cai, H., Zheng, S., Hao, X., Luan, G., Wu, X., and Zou, Z. *Structural and photocatalytic properties of novel Bi_2GaVO_7.* Mater. Chem. Phys., **104**, 1, (2007), 119

[51] Zhang, X., Ai, Z., Jia, F., and Zhang, L. *Generalized one-pot synthesis, characterization, and photocatalytic activity of hierarchical BiOX (X= Cl, Br, I) nanoplate microspheres.* J. Phys. Chem. C, **112**, 3, (2008), 747

[52] Chen, X. and Burda, C. *The electronic origin of the visible-light absorption properties of C-, N-and S-doped TiO_2 nanomaterials.* J. Am. Chem. Soc., **130**, 15, (2008), 5018

[53] Bisquert, J. *Interpretation of electron diffusion coefficient in organic and inorganic semiconductors with broad distributions of states.* Phys. Chem. Chem. Phys., **10**, 22, (2008), 3175

[54] Maeda, K. and Domen, K. *Solid Solution of GaN and ZnO as a Stable Photocatalyst for Overall Water Splitting under Visible Light.* Chem. Mater., **22**, 3, (2009), 612

[55] Li, G.-L. and Yin, Z. *Theoretical insight into the electronic, optical and photocatalytic properties of $InMO_4$ (M= V, Nb, Ta) photocatalysts.* Phys. Chem. Chem. Phys., **13**, 7, (2011), 2824

[56] Ohno, T., Bai, L., Hisatomi, T., Maeda, K., and Domen, K. *Photocatalytic water splitting using modified GaN: ZnO solid solution under visible light: long-time operation and regeneration of activity.* J. Am. Chem. Soc., **134**, 19, (2012), 8254

[57] Xu, X., Randorn, C., Efstathiou, P., and Irvine, J. T. *A red metallic oxide photocatalyst.* Nat. Mater., **11**, 7, (2012), 595–598

[58] Shieh, D.-L., Lin, Y.-S., Yeh, J.-H., Chen, S.-C., Lin, B.-C., and Lin, J.-L. *N-doped, porous TiO_2 with rutile phase and visible light sensitive photocatalytic activity.* Chem. Comm., **48**, 19, (2012), 2528

[59] Han, W., Ren, L., Qi, X., Liu, Y., Wei, X., Huang, Z., and Zhong, J. *Synthesis of CdS/ZnO/graphene composite with high-efficiency photoelectrochemical activities under solar radiation.* Appl. Surf. Sci., **299**, (2014), 12

[60] Ding, K., Chen, B., Li, Y., Zhang, Y., and Chen, Z. *Comparative density functional theory study on the electronic and optical properties of $BiMO_4$ (M = V, Nb, Ta).* J. Mater. Chem. A, **2**, 22, (2014), 8294

[61] Luan, J., Guo, N., and Chen, B. *Hydrogen production with Ga_2BiSbO_7, Fe_2BiSbO_7 and Gd_2BiSbO_7 as photocatalysts under visible light irradiation.* Int. J. Hydrogen Energ., **39**, 3, (2014), 1228

[62] Sastre, F., Fornés, V., Corma, A., and García, H. *Conversion of Methane into C1 Oxygenates by Deep-UV Photolysis on Solid Surfaces: Influence of the Nature of the Solid and Optimization of Photolysis Conditions.* Chem. Eur. J., **18**, 6, (2012), 1820

[63] Sastre, F., Corma, A., and García, H. *Deep UV photocatalytic activation of ethane on silica surfaces.* Appl. Catal. B: Environ., **128**, (2012), 84

[64] Sastre, F., Corma, A., and García, H. *185 nm Photoreduction of CO_2 to Methane by Water. Influence of the Presence of a Basic Catalyst.* J. Am. Chem. Soc., **134**, 34, (2012), 14137

[65] Jang, J. S., Joshi, U. A., and Lee, J. S. *Solvothermal synthesis of CdS nanowires for photocatalytic hydrogen and electricity production.* J. Phys. Chem. C, **111**, 35, (2007), 13280

[66] Jung, H. S., Hong, Y. J., Li, Y., Cho, J., Kim, Y.-J., and Yi, G.-C. *Photocatalysis using GaN nanowires.* ACS Nano, **2**, 4, (2008), 637

[67] Huang, J., Ding, K., Hou, Y., Wang, X., and Fu, X. *Synthesis and photocatalytic activity of Zn_2GeO_4 nanorods for the degradation of organic pollutants in water.* ChemSusChem, **1**, 12, (2008), 1011

[68] Bi, Y. and Ye, J. *In situ oxidation synthesis of Ag/AgCl core–shell nanowires and their photocatalytic properties.* Chem. Commun., , 43, (2009), 6551

[69] Wang, L., Wei, H., Fan, Y., Liu, X., and Zhan, J. *Synthesis, optical properties, and photocatalytic activity of one-dimensional CdS@ZnS core-shell nanocomposites.* Nanoscale Res. Lett., **4**, 6, (2009), 558

[70] Kenanakis, G. and Katsarakis, N. *Light-induced photocatalytic degradation of stearic acid by c-axis oriented ZnO nanowires.* Appl. Catal. A: Gen., **378**, 2, (2010), 227

[71] Berr, M., Vaneski, A., Susha, A. S., Rodríguez-Fernández, J., Döblinger, M., Jäckel, F., Rogach, A. L., and Feldmann, J. *Colloidal CdS nanorods decorated with subnanometer sized Pt clusters for photocatalytic hydrogen generation.* Appl. Phys. Lett., **97**, 9, (2010), 093108

[72] Wu, N., Wang, J., Tafen, D. N., Wang, H., Zheng, J.-G., Lewis, J. P., Liu, X., Leonard, S. S., and Manivannan, A. *Shape-enhanced photocatalytic activity of single-crystalline anatase TiO_2(101) nanobelts.* J. Am. Chem. Soc., **132**, 19, (2010), 6679

[73] Liu, Q., Zhou, Y., Kou, J., Chen, X., Tian, Z., Gao, J., Yan, S., and Zou, Z. *High-yield synthesis of ultralong and ultrathin Zn_2GeO_4 nanoribbons toward improved photocatalytic reduction of CO_2 into renewable hydrocarbon fuel.* J. Am. Chem. Soc., **132**, 41, (2010), 14385

[74] Shahid, M., Shakir, I., Yang, S.-J., and Kang, D. J. *Facile synthesis of core–shell SnO_2/V_2O_5 nanowires and their efficient photocatalytic property.* Mater. Chem. Phys., **124**, 1, (2010), 619

[75] Vaneski, A., Susha, A. S., Rodríguez-Fernández, J., Berr, M., Jäeckel, F., Feldmann, J., and Rogach, A. L. *Hybrid colloidal heterostructures of anisotropic semiconductor nanocrystals decorated with noble metals: synthesis and function.* Adv. Funct. Mater., **21**, 9, (2011), 1547

[76] Berr, M. J., Vaneski, A., Mauser, C., Fischbach, S., Susha, A. S., Rogach, A. L., Jäckel, F., and Feldmann, J. *Delayed Photoelectron Transfer in Pt-Decorated CdS Nanorods under Hydrogen Generation Conditions.* Small, **8**, 2, (2012), 291

[77] Berr, M. J., Wagner, P., Fischbach, S., Vaneski, A., Schneider, J., Susha, A. S., Rogach, A. L., Jäckel, F., and Feldmann, J. *Hole scavenger redox potentials determine quantum efficiency and stability of Pt-decorated CdS nanorods for photocatalytic hydrogen generation.* Appl. Phys. Lett., **100**, 22, (2012), 223903

[78] Berr, M. J., Schweinberger, F. F., Doblinger, M., Sanwald, K. E., Wolff, C., Breimeier, J., Crampton, A. S., Ridge, C. J., Tschurl, M., Heiz, U., *et al. Size-selected subnanometer cluster catalysts on semiconductor nanocrystal films for atomic scale insight into photocatalysis.* Nano Lett., **12**, 11, (2012), 5903

[79] Schweinberger, F. F., Berr, M. J., Doblinger, M., Wolff, C., Sanwald, K. E., Crampton, A. S., Ridge, C. J., Jackel, F., Feldmann, J., Tschurl, M., *et al. Cluster size effects in the photocatalytic hydrogen evolution reaction.* J. Am. Chem. Soc., **135**, 36, (2013), 13262

[80] Simon, T., Bouchonville, N., Berr, M. J., Vaneski, A., Adrović, A., Volbers, D., Wyrwich, R., Döblinger, M., Susha, A. S., Rogach, A. L., *et al. Redox shuttle mechanism enhances photocatalytic H_2 generation on Ni-decorated CdS nanorods.* Nat. Mater., **13**, 11, (2014), 1013

[81] Inoue, Y., Okamura, M., and Sato, K. *A thin-film semiconducting titanium dioxide combined with ferroelectrics for photoassisted water decomposition.* J. Phys. Chem., **89**, 24, (1985), 5184

[82] Inoue, Y., Sato, K., Sato, K., and Miyama, H. *Photoassisted water decomposition by ferroelectric lead zirconate titanate ceramics with anomalous photovoltaic effects.* J. Phys. Chem., **90**, 13, (1986), 2809

[83] Inoue, Y., Hayashi, O., and Sato, K. *Photocatalytic activities of potassium-doped lead niobates and the effect of poling.* J. Chem. Soc., Faraday Trans., **86**, 12, (1990), 2277

[84] Ikeda, T., Sasaki, T., and Ichimura, K. *Photochemical switching of polarization in ferroelectric liquid-crystal films.* Nature, **361**, (1993), 428

[85] Langhoff, A. and Giesselmann, F. *Thermodynamics of the photoferroelectric effect in smectic-C* liquid crystals.* J. Chem. Phys., **117**, 5, (2002), 2232

[86] Saipa, A., Osipov, M. A., Lanham, K. W., Chang, C. H., Walba, D. M., and Giesselmann, F. *The intrinsic photoferroelectric effect in the smectic C* phase of a chiral azobenzene.* J Mater. Chem., **16**, 42, (2006), 4170

[87] Harhira, A., Guilbert, L., Bourson, P., and Rinnert, H. *Decay time of polaron photoluminescence in congruent lithium niobate.* Phys. Status Solidi (C), **4**, 3, (2007), 926

[88] Qin, M., Yao, K., and Liang, Y. C. *High efficient photovoltaics in nanoscaled ferroelectric thin films.* Appl. Phys. Lett., **93**, 12, (2008), 2904

[89] Li, D., Zhao, M. H., Garra, J., Kolpak, A., Rappe, A., Bonnell, D., and Vohs, J. *Direct in situ determination of the polarization dependence of physisorption on ferroelectric surfaces.* Nature Mater., **7**, 6, (2008), 473

[90] Zhao, M. H., Bonnell, D. A., and Vohs, J. M. *Effect of ferroelectric polarization on the adsorption and reaction of ethanol on $BaTiO_3$.* Surf. Sci., **602**, 17, (2008), 2849

[91] Zhao, M. H., Bonnell, D. A., and Vohs, J. M. *Influence of ferroelectric polarization on the energetics of the reaction of 2-fluoroethanol on $BaTiO_3$.* Surf. Sci., **603**, 2, (2009), 284

[92] Choi, T., Lee, S., Choi, Y., Kiryukhin, V., and Cheong, S.-W. *Switchable ferroelectric diode and photovoltaic effect in $BiFeO_3$.* Science, **324**, 5923, (2009), 63

[93] Tiwari, D., Dunn, S., and Zhang, Q. *Impact of Zr/Ti ratio in the PZT on the photoreduction of silver nanoparticles.* Mater. Res. Bull., **44**, 6, (2009), 1219

[94] Yang, S., Seidel, J., Byrnes, S., Shafer, P., Yang, C.-H., Rossell, M., Yu, P., Chu, Y.-H., Scott, J., Ager, J., Martin, L., and Ramesh, R. *Above-bandgap voltages from ferroelectric photovoltaic devices.* Nature Nanotechnol., **5**, 2, (2010), 143

[95] Alexe, M. and Hesse, D. *Tip-enhanced photovoltaic effects in bismuth ferrite.* Nature Commun., **2**, (2011), 256

[96] Cao, D., Wang, C., Zheng, F., Dong, W., Fang, L., and Shen, M. *High-efficiency ferroelectric-film solar cells with an n-type Cu_2O cathode buffer layer.* Nano Lett., **12**, 6, (2012), 2803

[97] Fan, H., Li, H., Liu, B., Lu, Y., Xie, T., and Wang, D. *Photoinduced charge transfer properties and photocatalytic activity in Bi2O3/BaTiO3 composite photocatalyst.* ACS Appl. Mater. Interfac., **4**, 9, (2012), 4853

[98] Hengky, C., Moya, X., Mathur, N. D., and Dunn, S. *Evidence of high rate visible light photochemical decolourisation of Rhodamine B with $BiFeO_3$ nanoparticles associated with $BiFeO_3$ photocorrosion.* RSC Adv., **2**, 31, (2012), 11843

[99] Stock, M. and Dunn, S. *Influence of the ferroelectric nature of lithium niobate to drive photocatalytic dye decolorization under artificial solar light.* J. Phys. Chem. C, **116**, 39, (2012), 20854

[100] Grinberg, I., West, D. V., Torres, M., Gou, G., Stein, D. M., Wu, L., Chen, G., Gallo, E. M., Akbashev, A. R., Davies, P. K., *et al. Perovskite oxides for visible-light-absorbing ferroelectric and photovoltaic materials.* Nature, **503**, 7477, (2013), 509

[101] Knežević, M. and Warner, M. *Photoferroelectric solar to electrical conversion.* Appl. Phys. Lett., **102**, 4, (2013), 043902

[102] Cui, Y., Briscoe, J., and Dunn, S. *Effect of Ferroelectricity on Solar-Light-Driven Photocatalytic Activity of $BaTiO_3$: Influence on the Carrier Separation and Stern Layer Formation.* Chem. Mater., **25**, 21, (2013), 4215

[103] Su, R., Shen, Y., Li, L., Zhang, D., Yang, G., Gao, C., and Yang, Y. *Silver-modified nanosized ferroelectrics as a novel photocatalyst.* Small, **11**, 2, (2015), 202

[104] Li, H., Sang, Y., Chang, S., Huang, X., Zhang, Y., Yang, R., Jiang, H., Liu, H., and Wang, Z. L. *Enhanced ferroelectric-nanocrystal-based hybrid photocatalysis by ultrasonic-wave-generated piezophototronic effect.* Nano Lett., **15**, 4, (2015), 2372

[105] Bai, X., Wei, J., Tian, B., Liu, Y., Reiss, T., Guiblin, N., Gemeiner, P., Dkhil, B., and Canero-Infante, I. *Size Effect on Optical and Photocatalytic Properties in $BiFeO_3$ Nanoparticles.* J. Phys. Chem. C, **120**, 7, (2016), 3595

[106] Khan, M., Nadeem, M., and Idriss, H. *Ferroelectric polarization effect on surface chemistry and photo-catalytic activity: A review.* Surf. Sci. Rep., **71**, 1, (2016), 1

[107] Liang, L., Kang, X., Sang, Y., and Liu, H. *One-Dimensional Ferroelectric Nanostructures: Synthesis, Properties, and Applications.* Adv. Sci., **3**, 7, (2016), 1500358

[108] Pankove, J. I. *Optical Processes in Semiconductors.* Courier Corporation (1971)

[109] Scharoch, P., Szatkowski, J., and Pawlikowski, J. M. *Quantum efficiency of internal photoeffects in narrow-gap semiconductor: A model.* J. Appl. Phys., **53**, 8, (1982), 5710

[110] Liang, W. *Excitons.* Phys. Ed., **5**, 4, (1970), 226

[111] Nitzan, A. *Chemical Dynamics in Condensed Phases Relaxation, Transfer and Reactions in Condensed Molecular Systems.* Oxford University Press (2006)

[112] Hsu, C.-P. *The electronic couplings in electron transfer and excitation energy transfer.* Acc. Chem. Res, **42**, 4, (2009), 509

[113] Maggio, E., Martsinovich, N., and Troisi, A. *Evaluating charge recombination rate in dye-sensitized solar cells from electronic structure calculations.* J. Phys. Chem. C, **116**, 14, (2012), 7638

[114] Thiruvenkatachari, R., Vigneswaran, S., and Moon, I. S. *A review on UV/TiO_2 photocatalytic oxidation process (Journal Review).* Korean J. Chem. Eng., **25**, 1, (2008), 64

[115] Bell, N. J., Ng, Y. H., Du, A., Coster, H., Smith, S. C., and Amal, R. *Understanding the enhancement in photoelectrochemical properties of photocatalytically prepared TiO_2-reduced graphene oxide composite.* J. Phys. Chem. C, **115**, 13, (2011), 6004

[116] Besoain, E. *Imogolite in volcanic soils of Chile.* Geoderma, **2**, 2, (1969), 151

[117] Greenland, D., Wada, K., and Hamblin, A. *Imogolite in a volcanic ash from Papua.* Australian J. Sci., **32**, 2, (1969), 56

[118] Wada, K., Henmi, T., Yoshinaga, N., and Patterson, S. H. *Imogolite and allophane formed in saprolite of basalt on Maui, Hawaii.* Clay. Clay Miner., **20**, 6, (1972), 375

[119] Wada, K. and N, Y. *Structure of Imogolite.* Am. Miner., **54**, 1-2, (1969), 50

[120] Russell, J. D., McHardy, W. J., and Fraser, A. R. *Imogolite: a unique aluminosilicate.* Clay Miner., **8**, (1969), 87

[121] Wada, K., Yoshinaga, N., Yotsumoto, K., Ibe, K., and Aida, S. *High resolution electron micrographs of imogolite.* Clay Miner., **8**, (1970), 487

[122] Cradwick, P. D. G., Farmer, V. C., Russell, J. D., Masson, C. R., Wada, K., and Yoshinaga, N. *Imogolite, a hydrated aluminium silicate of tubular structure.* Nature, **240**, 104, (1972), 187

[123] Barron, P. F., Wilson, M. A., Campbell, A. S., and Frost, R. L. *Detection of imogolite in soils using solid state ^{29}Si NMR.* Nature, **299**, 5884, (1982), 616

[124] Farmer, V. C., Fraser, A. R., and Tait, J. M. *Synthesis of imogolite: a tubular aluminium silicate polymer.* J. Chem. Soc., Chem. Comm., , 13, (1977), 462

[125] Wada, S.-I., Eto, A., and Wada, K. *Synthetic allophane and imogolite.* J. Soil Sci., **30**, 2, (1979), 347

[126] Mukherjee, S., Bartlow, V. M., and Nair, S. *Phenomenology of the growth of single-walled aluminosilicate and aluminogermanate nanotubes of precise dimensions.* Chem. Mater., **17**, 20, (2005), 4900

[127] Konduri, S., Mukherjee, S., and Nair, S. *Strain energy minimum and vibrational properties of single-walled aluminosilicate nanotubes.* Phys. Rev. B, **74**, 3, (2006), 033401

[128] Mukherjee, S., Kim, K., and Nair, S. *Short, highly ordered, single-walled mixed-oxide nanotubes assemble from amorphous nanoparticles.* J. Am. Chem. Soc., **129**, 21, (2007), 6820

[129] Kang, D.-Y., Zang, J., Wright, E. R., McCanna, A. L., Jones, C. W., and Nair, S. *Dehydration, dehydroxylation, and rehydroxylation of single-walled aluminosilicate nanotubes.* ACS Nano, **4**, 8, (2010), 4897

[130] Yucelen, G. I., Kang, D.-Y., Guerrero-Ferreira, R. C., Wright, E. R., Beckham, H. W., and Nair, S. *Shaping single-walled metal oxide nanotubes from precursors of controlled curvature.* Nano Lett., **12**, 2, (2012), 827

[131] Yucelen, G. I., Choudhury, R. P., Vyalikh, A., Scheler, U., Beckham, H. W., and Nair, S. *Formation of single-walled aluminosilicate nanotubes from molecular precursors and curved nanoscale intermediates.* J. Am. Chem. Soc., **133**, 14, (2011), 5397

[132] Kolesnikov, A. I., Reiter, G. F., Choudhury, N., Prisk, T. R., Mamontov, E., Podlesnyak, A., Ehlers, G., Seel, A. G., Wesolowski, D. J., and Anovitz, L. M. *Quantum Tunneling of Water in Beryl: A New State of the Water Molecule.* Phys. Rev. Lett., **116**, 16, (2016), 167802

[133] Wada, S.-i. and Wada, K. *Effects on substitution of germanium for silicon in imogolite.* Clay. Clay Miner., **30**, 2, (1982), 123

[134] Levard, C., Rose, J., Masion, A., Doelsch, E., Borschneck, D., Olivi, L., Dominici, C., Grauby, O., Woicik, J. C., and Bottero, J.-Y. *Synthesis of large quantities of single-walled aluminogermanate nanotube.* J. Am. Chem. Soc., **130**, 18, (2008), 5862

[135] Maillet, P., Levard, C., Larquet, E., Mariet, C., Spalla, O., Menguy, N., Masion, A., Doelsch, E., Rose, J., and Thill, A. *Evidence of Double-Walled Al-Ge Imogolite-Like Nanotubes. A Cryo-TEM and SAXS Investigation.* J. Am. Chem. Soc., **132**, 4, (2010), 1208

[136] Levard, C., Rose, J., Thill, A., Masion, A., Doelsch, E., Maillet, P., Spalla, O., Olivi, L., Cognigni, A., Ziarelli, F., and Botterro, J. Y. *Formation and growth mechanisms of imogolite-like aluminogermanate nanotubes.* Chem. Mater., **22**, 8, (2010), 2466

[137] Maillet, P., Levard, C., Spalla, O., Masion, A., Rose, J., and Thill, A. *Growth kinetic of single and double-walled aluminogermanate imogolite-like nanotubes: an experimental and modeling approach.* Phys. Chem. Chem. Phys., **13**, 7, (2011), 2682

[138] Levard, C., Masion, A., Rose, J., Doelsch, E., Borschneck, D., Olivi, L., Chaurand, P., Dominici, C., Ziarelli, F., Thill, A., P, M., and Y, B. J. *Synthesis of Ge-*

imogolite: influence of the hydrolysis ratio on the structure of the nanotubes. Phys. Chem. Chem. Phys., **13**, 32, (2011), 14516

[139] Thill, A., Maillet, P., Guiose, B., Spalla, O., Belloni, L., Chaurand, P., Auffan, M., Olivi, L., and Rose, J. *Physico-chemical control over the single-or double-wall structure of aluminogermanate imogolite-like nanotubes.* J. Am. Chem. Soc., **134**, 8, (2012), 3780

[140] Amara, M.-S., Paineau, E., Bacia-Verloop, M., Krapf, M.-E. M., Davidson, P., Belloni, L., Levard, C., Rose, J., Launois, P., and Thill, A. *Single-step formation of micron long $(OH)_3Al_2O_3Ge(OH)$ imogolite-like nanotubes.* Chem. Commun., **49**, 96, (2013), 11284

[141] Avellan, A., Levard, C., Kumar, N., Rose, J., Olivi, L., Thill, A., Chaurand, P., Borschneck, D., and Masion, A. *Structural incorporation of iron into Ge–imogolite nanotubes: a promising step for innovative nanomaterials.* RSC Adv., **4**, 91, (2014), 49827

[142] Amara, M. S., Paineau, E., Rouzière, S., Guiose, B., Krapf, M.-E. M., Taché, O., Launois, P., and Thill, A. *Hybrid Tunable-Diameter Metal-Oxide Nanotubes for Organic Molecules Trapping.* Chem. Mater., **27**, 5, (2015), 1488

[143] Levard, C., Masion, A., Rose, J., Doelsch, E., Borschneck, D., Dominici, C., Ziarelli, F., and Bottero, J.-Y. *Synthesis of imogolite fibers from decimolar concentration at low temperature and ambient pressure: a promising route for inexpensive nanotubes.* J. Am. Chem. Soc., **131**, 47, (2009), 17080

[144] Kang, D.-Y., Zang, J., Jones, C. W., and Nair, S. *Single-walled aluminosilicate nanotubes with organic-modified interiors.* J. Phys. Chem. C, **115**, 15, (2011), 7676

[145] Bottero, I., Bonelli, B., Ashbrook, S. E., Wright, P. A., Zhou, W., Tagliabue, M., Armandi, M., and Garrone, E. *Synthesis and characterization of hybrid organic/inorganic nanotubes of the imogolite type and their behaviour towards methane adsorption.* Phys. Chem. Chem. Phys., **13**, 2, (2011), 744

[146] Zanzottera, C., Armandi, M., Esposito, S., Garrone, E., and Bonelli, B. *CO_2 Adsorption on Aluminosilicate Single-Walled Nanotubes of Imogolite Type.* J. Phys. Chem. C, **116**, 38, (2012), 20417

[147] Kang, D.-Y., Brunelli, N. A., Yucelen, G. I., Venkatasubramanian, A., Zang, J., Leisen, J., Hesketh, P. J., Jones, C. W., and Nair, S. *Direct synthesis of single-walled aminoaluminosilicate nanotubes with enhanced molecular adsorption selectivity.* Nat. Commun., **5**, 3342, (2014), 1

[148] Zanzottera, C., Vicente, A., Celasco, E., Fernandez, C., Garrone, E., and Bonelli, B. *Physico-chemical properties of imogolite nanotubes functionalized on both external and internal surfaces.* J. Phys. Chem. C, **116**, 13, (2012), 7499

[149] Zanzottera, C., Vicente, A., Armandi, M., Fernandez, C., Garrone, E., and Bonelli, B. *Thermal Collapse of Single-Walled Alumino-Silicate Nanotubes: Transformation Mechanisms and Morphology of the Resulting Lamellar Phases.* J. Phys. Chem. C, **116**, 44, (2012), 23577

[150] Bonelli, B., Armandi, M., and Garrone, E. *Surface properties of alumino-silicate single-walled nanotubes of the imogolite type.* Phys. Chem. Chem. Phys., **15**, 32, (2013), 13381

[151] Bonelli, B., Zanzottera, C., Armandi, M., Esposito, S., and Garrone, E. *IR spectroscopic study of the acidic properties of alumino-silicate single-walled nanotubes of the imogolite type.* Catal. Today, **218**, (2013), 3

[152] Elliott, J. D., Scivetti, I., Poli, E., and Teobaldi, G. *Imogolite Nanotubes with Inner Surface Amine Functionality: A Linear-Scaling Density Functional Theory Investigation* (2016). To be submitted

[153] Ookawa, M., Inoue, Y., Watanabe, M., Suzuki, M., and Yamaguchi, T. *Synthesis and characterization of Fe containing imogolite.* Clay Sci., **12**, S2, (2006), 280

[154] Ookawa, M., Takata, Y., Suzuki, M., Inukai, K., Maekawa, T., and Yamaguchi, T. *Oxidation of aromatic hydrocarbons with H_2O_2 catalyzed by a nano-scale tubular aluminosilicate, Fe-containing imogolite.* Res. Chem. Intermed., **34**, 8, (2008), 679

[155] Shafia, E., Esposito, S., Manzoli, M., Chiesa, M., Tiberto, P., Barrera, G., Menard, G., Allia, P., Freyria, F. S., Garrone, E., and Bonelli, B. *Al/Fe isomorphic substitution versus Fe_2O_3 clusters formation in Fe-doped aluminosilicate nanotubes (imogolite).* J. Nanopart. Res., **17**, 8, (2015), 1

[156] Shafia, E., Esposito, S., Armandi, M., Manzoli, M., Garrone, E., and Bonelli, B. *Isomorphic substitution of aluminium by iron into single-walled alumino-silicate*

nanotubes: a physico-chemical insight into the structural and adsorption properties of Fe-doped imogolite. Micropor. Mesopor. Mat., **224**, (2015), 229

[157] Shafia, E., Esposito, S., Armandi, M., Bahadori, E., Garrone, E., and Bonelli, B. *Reactivity of bare and Fe-doped alumino-silicate nanotubes (imogolite) with H_2O_2 and the azo-dye Acid Orange 7* (2015). In press

[158] Ookawa, M. *Synthesis and characterization of Fe-Imogolite as an oxidation catalyst.* INTECH Open Access Publisher (2012)

[159] Kang, D.-Y., Lydon, M. E., Yucelen, G. I., Jones, C. W., and Nair, S. *Solution-Processed Ultrathin Aluminosilicate Nanotube–Poly (vinyl alcohol) Composite Membranes with Partial Alignment of Nanotubes.* ChemNanoMat, **1**, (2015), 102

[160] Imamura, S., Kokubu, T., Yamashita, T., Okamoto, Y., Kajiwara, K., and Kanai, H. *Shape-selective copper-loaded imogolite catalyst.* J Catal., **160**, 1, (1996), 137

[161] Marzan, L. L. and Philipse, A. P. *Synthesis of platinum nanoparticles in aqueous host dispersions of inorganic (imogolite) rods.* Colloids Surface. A, **90**, 1, (1994), 95

[162] Nakane, J. J., Akeson, M., and Marziali, A. *Nanopore sensors for nucleic acid analysis.* J. Phys.: Condens. Matt., **15**, 32, (2003), R1365

[163] Ohashi, F., Tomura, S., Akaku, K., Hayashi, S., and Wada, S.-I. *Characterization of synthetic imogolite nanotubes as gas storage.* J. Mater. Sci., **39**, 5, (2004), 1799

[164] Ma, W., Yah, W. O., Otsuka, H., and Takahara, A. *Application of imogolite clay nanotubes in organic–inorganic nanohybrid materials.* J. Mater. Chem., **22**, 24, (2012), 11887

[165] Arancibia-Miranda, N., Escudey, M., Pizarro, C., Denardin, J. C., García-González, M. T., Fabris, J. D., and Charlet, L. *Preparation and characterization of a single-walled aluminosilicate nanotube-iron oxide composite: its applications to removal of aqueous arsenate.* Mater. Res. Bull., **51**, (2014), 145

[166] Guimarães, L., Enyashin, A. N., Frenzel, J., Heine, T., Duarte, H. A., and Seifert, G. *Imogolite nanotubes: stability, electronic, and mechanical properties.* ACS Nano, **1**, 4, (2007), 362

[167] Lourenço, M. P., Guimarẽs, L., da Silva, M. C., de Oliveira, C., Heine, T., and Duarte, H. A. *Nanotubes With Well-Defined Structure: Single-and Double-Walled Imogolites.* J. Phys. Chem. C, **118**, 11, (2014), 5945

[168] Alvarez-Ramírez, F. *Ab initio simulation of the structural and electronic properties of aluminosilicate and aluminogermanate natotubes with imogolite-like structure.* Phys. Rev. B, **76**, 12, (2007), 125421

[169] Li, L., Xia, Y., Zhao, M., Song, C., Li, J., and Liu, X. *The electronic structure of a single-walled aluminosilicate nanotube.* Nanotechnology, **19**, 17, (2008), 175702

[170] Zhao, M., Xia, Y., and Mei, L. *Energetic minimum structures of imogolite nanotubes: A first-principles prediction.* J.Phys. Chem. C, **113**, 33, (2009), 14834

[171] Teobaldi, G., Beglitis, N. S., Fisher, A. J., Zerbetto, F., and Hofer, W. A. *Hydroxyl vacancies in single-walled aluminosilicate and aluminogermanate nanotubes.* J. Phys.: Condens. Matt., **21**, 19, (2009), 195301

[172] Demichelis, R., Noël, Y., D'Arco, P., Maschio, L., Orlando, R., and Dovesi, R. *Structure and energetics of imogolite: a quantum mechanical ab initio study with B3LYP hybrid functional.* J. Mater. Chem., **20**, 46, (2010), 10417

[173] Poli, E., Elliott, J. D., Ratcliff, L. E., Andrinopoulos, L., Dziedzic, J., Hine, N. D. M., Mostofi, A. A., Skylaris, C.-K., Haynes, P. D., and Teobaldi, G. *The potential of imogolite nanotubes as (co-)photocatalysts: a linear-scaling density functional theory study.* J. Phys.: Condens. Matt., **28**, 7, (2016), 074003

[174] Alvarez-Ramírez, F. *First principles studies of Fe-containing aluminosilicate and aluminogermanate nanotubes.* J. Chem. Theory and Comput., **5**, 12, (2009), 3224

[175] Elliott, J. D., Poli, E., Scivetti, I., Ratcliff, L. E., Andrinopoulos, L., Dziedzic, J., Hine, N. D. M., Mostofi, A. A., Skylaris, C.-K., Haynes, P. D., and Teobaldi, G. *Polarization Enhanced Photocatalysis without Ferroelectrics and with Tunable Selectivity: the Unrealized Potential of Hybrid Inorganic Nanotubes* (2016). In press

[176] Lee, S. U., Choi, Y. C., Youm, S. G., and Sohn, D. *Origin of the strain energy minimum in imogolite nanotubes.* J. Phys. Chem. C, **115**, 13, (2011), 5226

[177] Gustafsson, J. P. *The surface chemistry of imogolite.* Clays Clay Miner., **49**, 1, (2001), 73

[178] Goedecker, S. *Linear scaling electronic structure methods.* Rev. Mod. Phys., **71**, 4, (1999), 1085

[179] Skylaris, C.-K., Haynes, P. D., Mostofi, A. A., and Payne, M. C. *Introducing ONETEP: Linear-scaling density functional simulations on parallel computers.* J. Chem. Phys., **122**, 8, (2005), 084119

[180] Kohn, W. and Sham, L. J. *Self-consistent equations including exchange and correlation effects.* Phys. Rev., **140**, 4A, (1965), A1133

[181] Parr, R. G. and Yang, W. *Density functional theory of atoms and molecules.* Springer (1980)

[182] Schrödinger, E. *An undulatory theory of the mechanics of atoms and molecules.* Phys. Rev., **28**, 6, (1926), 1049

[183] Szabo, A. and Ostlund, N. S. *Modern quantum chemistry: introduction to advanced electronic structure theory* (1982)

[184] Born, M. and Oppenheimer, R. *Zur quantentheorie der molekeln.* Annalen der Physik, **389**, 20, (1927), 457

[185] Hohenberg, P. and Kohn, W. *Inhomogeneous electron gas.* Phys. Rev., **136**, 3B, (1964), B864

[186] Lanczos, C. *The Variational Principles of Mechanics.* 4. Dover (2012)

[187] Elsgolc, L. D. *Calculus of variations.* Dover (2012)

[188] Perdew, J. P. and Schmidt, K. *Jacob's ladder of density functional approximations for the exchange-correlation energy.* In *AIP Conference Proceedings*, p. 1. IOP INSTITUTE OF PHYSICS PUBLISHING LTD (2001)

[189] Pandey, B. P. and Kumar, V. *Structural and electronic property calculations of $In_xGa_{1-x}As$ alloy based on all electron potentials from first-principle theory.* Indian J. Pure & Appl. Phys., **54**, 01, (2016), 66

[190] Behloul, M., Salmani, E., Ez-Zahraouy, H., and Benyoussef, A. *Theoretical investigation of electronic, magnetic and optical properties of ZnSe doped TM and co-doped with MnTM (TM: Fe, cr, co): AB-initio study* (2016). In press

[191] Perdew, J. P. and Zunger, A. *Self-interaction correction to density-functional approximations for many-electron systems.* Phys. Rev. B, **23**, 10, (1981), 5048

[192] Ceperley, D. M. and Alder, B. *Ground state of the electron gas by a stochastic method.* Phys. Rev. Lett., **45**, 7, (1980), 566

[193] Gell-Mann, M. and Brueckner, K. A. *Correlation energy of an electron gas at high density.* Phys. Rev., **106**, 2, (1957), 364

[194] Marques, M. A., Oliveira, M. J., and Burnus, T. *Libxc: A library of exchange and correlation functionals for density functional theory.* Comput. Phys. Comm., **183**, 10, (2012), 2272

[195] Perdew, J. P., Parr, R. G., Levy, M., and Balduz Jr, J. L. *Density-functional theory for fractional particle number: derivative discontinuities of the energy.* Phys. Rev. Lett., **49**, 23, (1982), 1691

[196] Sham, L. and Schlüter, M. *Density-functional theory of the energy gap.* Phys. Rev. Lett., **51**, 20, (1983), 1888

[197] Heyd, J., Peralta, J. E., Scuseria, G. E., and Martin, R. L. *Energy band gaps and lattice parameters evaluated with the Heyd-Scuseria-Ernzerhof screened hybrid functional.* J. Chem. Phys., **123**, 17, (2005), 174101

[198] Paier, J., Marsman, M., Hummer, K., Kresse, G., Gerber, I. C., and Ángyán, J. G. *Screened hybrid density functionals applied to solids.* J. Chem. Phys., **124**, 15, (2006), 154709

[199] Paier, J., Marsman, M., Hummer, K., Kresse, G., Gerber, I., and Ángyán, J. *Erratum:"Screened hybrid density functionals applied to solids"[J. Chem. Phys. 124, 154709 (2006)].* J. Chem. Phys., **125**, 24, (2006), 9901

[200] Tran, F. and Blaha, P. *Accurate band gaps of semiconductors and insulators with a semilocal exchange-correlation potential.* Phys. Rev. Lett., **102**, 22, (2009), 226401

[201] Perdew, J. P., Burke, K., and Ernzerhof, M. *Generalized gradient approximation made simple.* Phys. Rev. Lett., **77**, 18, (1996), 3865

[202] Böhm, H.-J. and Ahlrichs, R. *A study of short-range repulsions.* J. Chem. Phys., **77**, 4, (1982), 2028

[203] Mooij, W. T., van Duijneveldt, F. B., van Duijneveldt-van de Rijdt, J. G., and van Eijck, B. P. *Transferable ab initio intermolecular potentials. 1. Derivation from methanol dimer and trimer calculations.* J. Phys. Chem. A, **103**, 48, (1999), 9872

[204] Elstner, M., Hobza, P., Frauenheim, T., Suhai, S., and Kaxiras, E. *Hydrogen bonding and stacking interactions of nucleic acid base pairs: a density-functional-theory based treatment.* J. Chem. Phys., **114**, 12, (2001), 5149

[205] Wu, Q. and Yang, W. *Empirical correction to density functional theory for van der Waals interactions.* J. Chem. Phys., **116**, 2, (2002), 515

[206] Grimme, S. *Semiempirical GGA-type density functional constructed with a long-range dispersion correction.* J. Comput. Chem., **27**, 15, (2006), 1787

[207] Hill, Q. and Skylaris, C.-K. *Including dispersion interactions in the ONETEP program for linear-scaling density functional theory calculations.* In *Proceedings of the Royal Society of London A: Mathematical, Physical and Engineering Sciences*, vol. 465, p. 669. The Royal Society (2009)

[208] Rydberg, H., Lundqvist, B. I., Langreth, D. C., and Dion, M. *Tractable nonlocal correlation density functionals for flat surfaces and slabs.* Phys. Rev. B, **62**, 11, (2000), 6997

[209] Rydberg, H., Dion, M., Jacobson, N., Schröder, E., Hyldgaard, P., Simak, S., Langreth, D. C., and Lundqvist, B. I. *Van der Waals density functional for layered structures.* Phys. Rev. Lett., **91**, 12, (2003), 126402

[210] Dion, M., Rydberg, H., Schröder, E., Langreth, D. C., and Lundqvist, B. I. *Van der Waals density functional for general geometries.* Phys. Rev. Lett., **92**, 24, (2004), 246401

[211] Dion, M., Rydberg, H., Schröder, E., Langreth, D. C., and Lundqvist, B. I. *Erratum: Van der Waals Density Functional for General Geometries [Phys. Rev. Lett.* ***92*** *, 246401 (2004)].* Phys. Rev. Lett., **95**, (2005), 109902

[212] Thonhauser, T., Cooper, V. R., Li, S., Puzder, A., Hyldgaard, P., and Langreth, D. C. *Van der Waals density functional: Self-consistent potential and the nature of the van der Waals bond.* Phys. Rev. B, **76**, 12, (2007), 125112

[213] Langreth, D., Lundqvist, B. I., Chakarova-Käck, S. D., Cooper, V., Dion, M., Hyldgaard, P., Kelkkanen, A., Kleis, J., Kong, L., Li, S., *et al. A density functional for sparse matter.* J. Phys.: Condens. Matter, **21**, 8, (2009), 084203

[214] Klimeš, J., Bowler, D. R., and Michaelides, A. *Chemical accuracy for the van der Waals density functional.* J. Phys.: Condens. Matt., **22**, 2, (2009), 022201

[215] Klimeš, J., Bowler, D. R., and Michaelides, A. *Van der Waals density functionals applied to solids.* Phys. Rev. B, **83**, 19, (2011), 195131

[216] Zhang, Y. and Yang, W. *Comment on Generalized gradient approximation made simple.* Phys. Rev. Lett., **80**, 4, (1998), 890

[217] Becke, A. D. *Density-functional exchange-energy approximation with correct asymptotic behavior.* Phys. Rev. A, **38**, 6, (1988), 3098

[218] Jurečka, P., Šponer, J., Černỳ, J., and Hobza, P. *Benchmark database of accurate (MP2 and CCSD (T) complete basis set limit) interaction energies of small model complexes, DNA base pairs, and amino acid pairs.* Phys. Chem. Chem. Phys., **8**, 17, (2006), 1985

[219] Ashcroft, N. and Mermin, N. D. *Solid State Physics.* Holt, Rinehart and Winston (1976)

[220] Herring, C. *A new method for calculating wave functions in crystals.* Phys. Rev., **57**, 12, (1940), 1169

[221] Phillips, J. C. *Energy-band interpolation scheme based on a pseudopotential.* Phys. Rev., **112**, 3, (1958), 685

[222] Phillips, J. C. and Kleinman, L. *New method for calculating wave functions in crystals and molecules.* Phys. Rev., **116**, 2, (1959), 287

[223] Hamann, D., Schlüter, M., and Chiang, C. *Norm-conserving pseudopotentials.* Phys. Rev. Lett., **43**, 20, (1979), 1494

[224] Kerker, G. *Non-singular atomic pseudopotentials for solid state applications.* J. Phys. C: Solid State Phys., **13**, 9, (1980), L189

[225] Hamann, D. *Generalized norm-conserving pseudopotentials.* Phys. Rev. B, **40**, 5, (1989), 2980

[226] Rappe, A. M., Rabe, K. M., Kaxiras, E., and Joannopoulos, J. *Optimized pseudopotentials.* Phys. Rev. B, **41**, 2, (1990), 1227

[227] Fuchs, M. and Scheffler, M. *Ab initio pseudopotentials for electronic structure calculations of poly-atomic systems using density-functional theory.* Comput. Phys. Commun., **119**, 1, (1999), 67–98

[228] http://opium.sourceforge.net/index.html

[229] Louie, S. G., Froyen, S., and Cohen, M. L. *Nonlinear ionic pseudopotentials in spin-density-functional calculations.* Phys. Rev. B, **26**, 4, (1982), 1738

[230] http://www.onetep.org

[231] Car, R. and Parrinello, M. *Unified approach for molecular dynamics and density-functional theory.* Phys. Rev. Lett., **55**, 22, (1985), 2471

[232] Press, W. H. *Numerical Recipes in FORTRAN: The art of scientific computing*, vol. 1. Cambridge University Press (1992)

[233] Polak, E. *Computational Methods in Optimization: A Unified Approach* (1971)

[234] Powell, M. J. D. *How bad are the BFGS and DFP methods when the objective function is quadratic?* Math. Prog., **34**, 1, (1986), 34

[235] Pfrommer, B. G., Côté, M., Louie, S. G., and Cohen, M. L. *Relaxation of crystals with the quasi-Newton method.* J. Comput. Phys., **131**, 1, (1997), 233

[236] Hellmann, H. *Einführung in die quantenchemie: Texte imprimé.* F. Deuticke (1937)

[237] Feynman, R. P. *Forces in molecules.* Phys. Rev., **56**, 4, (1939), 340

[238] Slater, J. C. *Hellmann-Feynman and Virial Theorems in the X(α) Method.* J. Chem. Phys., **57**, 6, (1972), 2389

[239] Ihm, J., Zunger, A., and Cohen, M. L. *Momentum-space formalism for the total energy of solids.* J. Phys. C: Solid State Phys., **12**, 21, (1979), 4409

[240] Andrade, X., Alberdi-Rodriguez, J., Strubbe, D. A., Oliveira, M. J., Nogueira, F., Castro, A., Muguerza, J., Arruabarrena, A., Louie, S. G., Aspuru-Guzik, A., *et al. Time-dependent density-functional theory in massively parallel computer architectures: the octopus project.* J. Phys.: Condens. Matter, **24**, 23, (2012), 233202

[241] Spiga, F. and Girotto, I. *phiGEMM: a CPU-GPU library for porting Quantum ESPRESSO on hybrid systems.* In *2012 20th Euromicro International Conference on Parallel, Distributed and Network-based Processing*, p. 368. IEEE (2012)

[242] Wilkinson, K. and Skylaris, C.-K. *Porting ONETEP to graphical processing unit-based coprocessors. 1. FFT box operations.* J. Comput. Chem., **34**, 28, (2013), 2446

[243] Duhamel, P. and Vetterli, M. *Fast Fourier transforms: a tutorial review and a state of the art.* Sig. Proc., **19**, 4, (1990), 259

[244] Kohn, W. *Density functional and density matrix method scaling linearly with the number of atoms.* Phys. Rev. Lett., **76**, 17, (1996), 3168

[245] Skylaris, C.-K., Haynes, P. D., Mostofi, A. A., and Payne, M. C. *Using ONETEP for accurate and efficient $\mathcal{O}(N)$ density functional calculations.* J. Phys.: Condens. Matt., **17**, 37, (2005), 5757

[246] Skylaris, C.-K., Haynes, P. D., Mostofi, A. A., and Payne, M. C. *Implementation of linear-scaling plane wave density functional theory on parallel computers.* Phys. Status Solidi B, **243**, 5, (2006), 973

[247] Haynes, P. D., Skylaris, C.-K., Mostofi, A. A., and Payne, M. C. *ONETEP: linear-scaling density-functional theory with local orbitals and plane waves.* Phys. Status Solidi B, **243**, 11, (2006), 2489

[248] Mostofi, A. A., Haynes, P. D., Skylaris, C.-K., and Payne, M. C. *ONETEP: linear-scaling density-functional theory with plane-waves.* Mol. Simulat., **33**, 7, (2007), 551

[249] Skylaris, C.-K. and Haynes, P. D. *Achieving plane wave accuracy in linear-scaling density functional theory applied to periodic systems: A case study on crystalline silicon.* J. Chem. Phys., **127**, 16, (2007), 164712

[250] Skylaris, C.-K., Haynes, P. D., Mostofi, A. A., and Payne, M. C. *Recent progress in linear-scaling density functional calculations with plane waves and pseudopotentials: the ONETEP code.* J. Phys.: Condens. Matt., **20**, 6, (2008), 064209

[251] Hine, N. D., Haynes, P. D., Mostofi, A. A., Skylaris, C.-K., and Payne, M. C. *Linear-scaling density-functional theory with tens of thousands of atoms: Expanding the scope and scale of calculations with ONETEP.* Comput. Phys. Commun., **180**, 7, (2009), 1041

[252] Blum, K. *Density matrix theory and applications*, vol. 64. Springer Science & Business Media (2012)

[253] Brouder, C., Panati, G., Calandra, M., Mourougane, C., and Marzari, N. *Exponential localization of Wannier functions in insulators.* Phys. Rev. Lett., **98**, 4, (2007), 046402

[254] White, C. A., Maslen, P., Lee, M. S., and Head-Gordon, M. *The tensor properties of energy gradients within a non-orthogonal basis.* Chem. Phys. Lett., **276**, 1, (1997), 133

[255] McWeeny, R. *Some recent advances in density matrix theory.* Rev. Mod. Phys., **32**, 2, (1960), 335

[256] Li, X.-P., Nunes, R., and Vanderbilt, D. *Density-matrix electronic-structure method with linear system-size scaling.* Phys. Rev. B, **47**, 16, (1993), 10891

[257] Haynes, P. D., Skylaris, C.-K., Mostofi, A. A., and Payne, M. C. *Density kernel optimization in the ONETEP code.* J. Phys.: Condens. Matter, **20**, 29, (2008), 294207

[258] Wannier, G. H. *The structure of electronic excitation levels in insulating crystals.* Phys. Rev., **52**, 3, (1937), 191

[259] Wannier, G. H. *Dynamics of band electrons in electric and magnetic fields.* Rev. Mod. Phys., **34**, 4, (1962), 645

[260] Marzari, N., Souza, I., and Vanderbilt, D. *An introduction to maximally-localized Wannier functions.* Psi-K newsletter, **57**, (2003), 129

[261] Skylaris, C.-K., Mostofi, A. A., Haynes, P. D., Pickard, C. J., and Payne, M. C. *Accurate kinetic energy evaluation in electronic structure calculations with localized functions on real space grids.* Comput. Phys. Commun., **140**, 3, (2001), 315

[262] Skylaris, C.-K., Mostofi, A. A., Haynes, P. D., Diéguez, O., and Payne, M. C. *Nonorthogonal generalized Wannier function pseudopotential plane-wave method.* Phys. Rev. B, **66**, 3, (2002), 035119

[263] Soler, J. M., Artacho, E., Gale, J. D., García, A., Junquera, J., Ordejón, P., and Sánchez-Portal, D. *The SIESTA method for ab initio order-N materials simulation.* J. Phys.: Condens. Matt., **14**, 11, (2002), 2745

[264] Fletcher, R. and Reeves, C. M. *Function minimization by conjugate gradients.* Comput. J., **7**, 2, (1964), 149

[265] Pulay, P. *Ab initio calculation of force constants and equilibrium geometries in polyatomic molecules: I. Theory.* Mol. Phys., **17**, 2, (1969), 197

[266] Hine, N. D. M., Robinson, M., Haynes, P. D., Skylaris, C.-K., Payne, M. C., and Mostofi, A. A. *Accurate ionic forces and geometry optimization in linear-scaling density-functional theory with local orbitals.* Phys. Rev. B, **83**, 19, (2011), 195102

[267] Ruiz-Serrano, Á., Hine, N. D., and Skylaris, C.-K. *Pulay forces from localized orbitals optimized in situ using a psinc basis set.* J. Chem. Phys., **136**, 23, (2012), 234101

[268] Ratcliff, L. E., Hine, N. D., and Haynes, P. D. *Calculating optical absorption spectra for large systems using linear-scaling density functional theory.* Phys. Rev. B, **84**, 16, (2011), 165131

[269] Ratcliff, L. E. and Haynes, P. D. *Ab initio calculations of the optical absorption spectra of C_{60}-conjugated polymer hybrids.* Phys. Chem. Chem. Phys., **15**, 31, (2013), 13024

[270] Ratcliff, L. *Optical absorption spectra calculated using linear-scaling density-functional theory.* Springer Science & Business Media (2013)

[271] Dirac, P. A. *The quantum theory of the emission and absorption of radiation.* In *P. Roy. Soc. Lond. A Mat.*, vol. 114, p. 243. The Royal Society (1927)

[272] Onida, G., Reining, L., and Rubio, A. *Electronic excitations: density-functional versus many-body Greens-function approaches.* Rev. Mod. Phys., **74**, 2, (2002), 601

[273] Read, A. and Needs, R. *Calculation of optical matrix elements with nonlocal pseudopotentials.* Phys. Rev. B, **44**, 23, (1991), 13071

[274] Gropp, W., Lusk, E., and Skjellum, A. *Using MPI: portable parallel programming with the message-passing interface*, vol. 1. MIT press (1999)

[275] Gropp, W., Lusk, E., and Thakur, R. *Using MPI-2: Advanced features of the message-passing interface*, vol. 1. MIT press (1999)

[276] Wilkinson, K. A., Hine, N. D., and Skylaris, C.-K. *Hybrid MPI-OpenMP Parallelism in the ONETEP Linear-Scaling Electronic Structure Code: Application to the Delamination of Cellulose Nanofibrils.* J. Chem. Theory Comput., **10**, 11, (2014), 4782

[277] Chandra, R. *Parallel programming in OpenMP*. Morgan kaufmann (2001)

[278] Chapman, B., Jost, G., and Van Der Pas, R. *Using OpenMP: portable shared memory parallel programming*, vol. 10. MIT press (2008)

[279] Challacombe, M. *A general parallel sparse-blocked matrix multiply for linear scaling SCF theory*. Comp. Phys. Comm., **128**, 1, (2000), 93

[280] Poli, E., Elliott, J. D., Hine, N. D. M., Mostofi, A. A., and Teobaldi, G. *Large-scale density functional theory simulation of inorganic nanotubes: a case study on Imogolite nanotubes*. Materials Research Innovations, **19**, S4, (2015), S272

[281] Guimarães, L., Pinto, Y. N., Lourenço, M. P., and Duarte, H. A. *Imogolite-like nanotubes: structure, stability, electronic and mechanical properties of the phosphorous and arsenic derivatives*. Phys. Chem. Chem. Phys., **15**, 12, (2013), 4303

[282] Yucelen, G. I., Choudhury, R. P., Leisen, J., Nair, S., and Beckham, H. W. *Defect structures in aluminosilicate single-walled nanotubes: A solid-state nuclear magnetic resonance investigation*. J. Phys. Chem. C, **116**, 32, (2012), 17149

[283] Gonze, X., Stumpf, R., and Scheffler, M. *Analysis of separable potentials*. Phys. Rev. B, **44**, 16, (1991), 8503

[284] Haynes, P. D., Skylaris, C.-K., Mostofi, A. A., and Payne, M. C. *Elimination of basis set superposition error in linear-scaling density-functional calculations with local orbitals optimised in situ*. Chem. Phys. Lett., **422**, 4, (2006), 345

[285] Bernholc, J., Briggs, E., Sullivan, D., Brabec, C., Nardelli, M. B., Rapcewicz, K., Roland, C., and Wensell, M. *Real-space multigrid methods for large-scale electronic structure problems*. Int. J. Quantum Chem., **65**, 5, (1997), 531

[286] Artacho, E., Anglada, E., Diéguez, O., Gale, J. D., García, A., Junquera, J., Martin, R. M., Ordejón, P., Pruneda, J. M., Sánchez-Portal, D., *et al. The SIESTA method; developments and applicability*. J. Phys.: Condens. Matt., **20**, 6, (2008), 064208

[287] Hine, N. D., Avraam, P. W., Tangney, P., and Haynes, P. D. *Linear-scaling density functional theory simulations of polar semiconductor nanorods*. In *J. Phys.: Conf. Ser.*, vol. 367, p. 012002. IOP Publishing (2012)

[288] Kreisel, J., Alexe, M., and Thomas, P. A. *A photoferroelectric material is more than the sum of its parts.* Nature Mater., **11**, 4, (2012), 260

[289] Dietl, N., Schlangen, M., and Schwarz, H. *Thermal Hydrogen-Atom Transfer from Methane: The Role of Radicals and Spin States in Oxo-Cluster Chemistry.* Angew. Chem. Int. Ed., **51**, 23, (2012), 5544

[290] Fresno, F., Portela, R., Suárez, S., and Coronado, J. M. *Photocatalytic materials: recent achievements and near future trends.* J. Mater. Chem. A, **2**, 9, (2014), 2863

[291] Baltrusaitis, J., Jansen, I., and Christus, J. S. *Renewable energy based catalytic CH_4 conversion to fuels.* Catal. Sci. Technol., **4**, 8, (2014), 2397

[292] Theng, B., Russell, M., Churchman, G., and Parfitt, R. *Surface properties of allophane, halloysite, and imogolite.* Clay. Clay Miner., **30**, 2, (1982), 143

[293] Kamat, P. V. *Meeting the clean energy demand: nanostructure architectures for solar energy conversion.* J. Phys. Chem. C, **111**, 7, (2007), 2834

[294] Pelaez, M., Nolan, N. T., Pillai, S. C., Seery, M. K., Falaras, P., Kontos, A. G., Dunlop, P. S., Hamilton, J. W., Byrne, J. A., O'shea, M. H., Entezari, and Dionysiou, D. D. *A review on the visible light active titanium dioxide photocatalysts for environmental applications.* Appl. Catal. B: Environ., **125**, (2012), 331

[295] Habisreutinger, S. N., Schmidt-Mende, L., and Stolarczyk, J. K. *Photocatalytic reduction of CO_2 on TiO_2 and other semiconductors.* Angew. Chem. Int. Ed., **52**, 29, (2013), 7372

[296] Navalón, S., Dhakshinamoorthy, A., Álvaro, M., and Garcia, H. *Photocatalytic CO_2 Reduction using Non-Titanium Metal Oxides and Sulfides.* ChemSusChem, **6**, 4, (2013), 562

[297] Maeda, K. *Z-scheme water splitting using two different semiconductor photocatalysts.* ACS Catal., **3**, 7, (2013), 1486

[298] De_Richter, R. K., Ming, T., and Caillol, S. *Fighting global warming by photocatalytic reduction of CO_2 using giant photocatalytic reactors.* Renewable and Sustainable Energy Reviews, **19**, (2013), 82

[299] Ismail, A. A. and Bahnemann, D. W. *Photochemical splitting of water for hydrogen production by photocatalysis: A review.* Sol. Energ. Mat. Sol. C., **128**, (2014), 85

[300] Scanlon, D. O., Dunnill, C. W., Buckeridge, J., Shevlin, S. A., Logsdail, A. J., Woodley, S. M., Catlow, C. R. A., Powell, M. J., Palgrave, R. G., Parkin, I. P., Watson, G. W., Keal, T., Sherwood, P., Walsh, A., and Sokol, A. *Band alignment of rutile and anatase TiO_2.* Nature Mater., **12**, 9, (2013), 798

[301] Li, G. and Gray, K. A. *The solid–solid interface: explaining the high and unique photocatalytic reactivity of TiO_2-based nanocomposite materials.* Chem. Phys., **339**, 1, (2007), 173

[302] Wang, J., Meng, F., Ma, X., Xu, M., and Chen, L. *Lattice, elastic, polarization, and electrostrictive properties of $BaTiO_3$ from first-principles.* J. Appl. Phys., **108**, 3, (2010), 034107

[303] Junquera, J. and Ghosez, P. *Critical thickness for ferroelectricity in perovskite ultrathin films.* Nature, **422**, 6931, (2003), 506

[304] Fong, D. D., Stephenson, G. B., Streiffer, S. K., Eastman, J. A., Auciello, O., Fuoss, P. H., and Thompson, C. *Ferroelectricity in ultrathin perovskite films.* Science, **304**, 5677, (2004), 1650

[305] Shimada, T., Wang, X., Kondo, Y., and Kitamura, T. *Absence of ferroelectric critical size in ultrathin $PbTiO_3$ nanotubes: A density-functional theory study.* Phys. Rev. Lett., **108**, 6, (2012), 067601

[306] Umari, P., Stenuit, G., and Baroni, S. *Optimal representation of the polarization propagator for large-scale GW calculations.* Phys. Rev. B, **79**, 20, (2009), 201104

[307] Umari, P., Stenuit, G., and Baroni, S. *GW quasiparticle spectra from occupied states only.* Phys. Rev. B, **81**, 11, (2010), 115104

[308] Marsili, M., Mosconi, E., De Angelis, F., and Umari, P. *Large scale GW-BSE calculations with N^3 scaling: excitonic effects in dye sensitised solar cells* (2016). ArXiv preprint arXiv:1603.05427, in press

[309] Zuehlsdorff, T. J., Hine, N. D., Spencer, J. S., Harrison, N. M., Riley, D. J., and Haynes, P. D. *Linear-scaling time-dependent density-functional theory in the linear response formalism.* J. Chem. Phys., **139**, 6, (2013), 064104

[310] Zuehlsdorff, T., Hine, N., Payne, M. C., and Haynes, P. D. *Linear-scaling time-dependent density-functional theory beyond the Tamm-Dancoff approximation: Ob-*

taining efficiency and accuracy with in situ optimised local orbitals. J. Chem. Phys., **143**, 20, (2015), 204107

[311] Sato, J., Kobayashi, H., and Inoue, Y. *Photocatalytic activity for water decomposition of indates with octahedrally coordinated d10 configuration. II. Roles of geometric and electronic structures.* J. Phys. Chem. B, **107**, 31, (2003), 7970

[312] Nashed, R., Ismail, Y., and Allam, N. K. *Recent advances in the use of density functional theory to design efficient solar energy-based renewable systems.* J Renew. Sus. Energ., **5**, 2, (2013), 022701

[313] Liu, L.-M., Crawford, P., and Hu, P. *The interaction between adsorbed OH and O_2 on TiO_2 surfaces.* Prog. Surf. Sci., **84**, 5, (2009), 155

[314] Li, Y.-F., Aschauer, U., Chen, J., and Selloni, A. *Adsorption and reactions of O_2 on anatase TiO_2.* Acc. Chem. Res., **47**, 11, (2014), 3361

[315] Di Valentin, C. and Pacchioni, G. *Spectroscopic properties of doped and defective semiconducting oxides from hybrid density functional calculations.* Acc. Chem. Res., **47**, 11, (2014), 3233

[316] Dong, X., Cao, B.-Y., Shao, R., Xiao, Y., He, W., Gao, Y., and Liu, J. *Effect of carbon content and electronic strong correlation on the mechanical and thermodynamic properties of ytterbium carbides.* RSC Adv., **5**, (2015), 103082

[317] Bhatt, M. D. and Lee, J. S. *Recent theoretical progress in the development of photoanode materials for solar water splitting photoelectrochemical cells.* J. Mater. Chem. A, **3**, 20, (2015), 10632

[318] Kirchartz, T., Bisquert, J., Mora-Sero, I., and Garcia-Belmonte, G. *Classification of solar cells according to mechanisms of charge separation and charge collection.* Phys. Chem. Chem. Phys., **17**, 6, (2015), 4007

[319] Chen, Y., Zhao, H., Liu, B., and Yang, H. *Charge separation between wurtzite ZnO polar $\{001\}$ surfaces and their enhanced photocatalytic activity.* Appl. Catal. B: Environ., **163**, (2015), 189

[320] Luo, Y., Szafraniak, I., Zakharov, N. D., Nagarajan, V., Steinhart, M., Wehrspohn, R. B., Wendorff, J. H., Ramesh, R., and Alexe, M. *Nanoshell tubes of ferroelectric lead zirconate titanate and barium titanate.* Appl. Phys. Lett., **83**, 3, (2003), 440

[321] Rørvik, P. M., Grande, T., and Einarsrud, M.-A. *One-Dimensional Nanostructures of Ferroelectric Perovskites.* Adv. Mater., **23**, 35, (2011), 4007

[322] Wang, C., Lu, Z., Yuan, W., Kwok, S., and Teng, B. *Dynamic properties of phase diagram in cylindrical ferroelectric nanotubes.* Phys. Lett. A, **375**, 39, (2011), 3405

[323] Alexe, M. and Hesse, D. *One-dimensional ferroelectrics: nanowires and nanotubes.* Ferroelectrics, **433**, 1, (2012), 53

[324] Yoo, H., Bae, C., Kim, M., Hong, S., No, K., Kim, Y., and Shin, H. *Visualization of three dimensional domain structures in ferroelectric $PbTiO_3$ nanotubes.* Appl. Phys. Lett., **103**, 2, (2013), 022902

[325] Zhao, Y., Miao, J., Meng, X., Weng, F., Xu, X., Jiang, Y., and Wang, S. *Butterfly-shaped multiferroic BiFeO3@BaTiO3 core–shell nanotubes: the interesting structural, multiferroic, and optical properties.* J. Mater. Sci.: Mater. Electron., **24**, 5, (2013), 1439

[326] Han, J. K., Choi, Y. C., Kwak, J. H., and Bu, S. D. *Effects of Wall Thickness on Morphology and Structure of Lead Titanate Nanotubes.* Ferroelectrics, **454**, 1, (2013), 29

[327] Evarestov, R. A., Bandura, A. V., and Kuruch, D. D. *$BaTiO_3$-based nanolayers and nanotubes: First-principles calculations.* J. Comput. Chem., **34**, 3, (2013), 175

[328] Nuraje, N. and Su, K. *Perovskite ferroelectric nanomaterials.* Nanoscale, **5**, 19, (2013), 8752

[329] Wang, J., Xu, T., Shimada, T., Wang, X., Zhang, T.-Y., and Kitamura, T. *Chiral selectivity of improper ferroelectricity in single-wall $PbTiO_3$ nanotubes.* Phys. Rev. B, **89**, 14, (2014), 144102

[330] Li, H., Zhang, G., Zheng, Y., Wang, B., and Chen, W. *Ab initio study on mechanical-bending-induced ferroelectric phase transition in ultrathin perovskite nanobelts.* Acta Mater., **76**, (2014), 472

[331] Bhavanasi, V., Kusuma, D. Y., and Lee, P. S. *Polarization Orientation, Piezoelectricity, and Energy Harvesting Performance of Ferroelectric PVDF-TrFE Nanotubes Synthesized by Nanoconfinement.* Adv. Energ. Mater., **4**, 16

[332] Jeon, C., Lee, Y., Yee, K., Han, J., and Bu, S. *Strain effect on the visible emission in $PbTiO_3$ nanotubes: Template and wall-thickness dependence.* Curr. Appl. Phys., **15**, 2, (2015), 115

[333] Liew, W. H., Mirshekarloo, M. S., Chen, S., Yao, K., and Tay, F. E. H. *Nanoconfinement induced crystal orientation and large piezoelectric coefficient in vertically aligned P(VDF-TrFE) nanotube array.* Sci. Rep., **5**, 9790, (2015), 1

[334] Liu, M. and Wang, J. *Giant electrocaloric effect in ferroelectric nanotubes near room temperature.* Sci. Rep., **5**, 7728, (2015), 1

[335] Jarvis, M., White, I., Godby, R., and Payne, M. C. *Supercell technique for total-energy calculations of finite charged and polar systems.* Phys. Rev. B, **56**, 23, (1997), 14972

[336] Rozzi, C. A., Varsano, D., Marini, A., Gross, E. K., and Rubio, A. *Exact Coulomb cutoff technique for supercell calculations.* Phys. Rev. B, **73**, 20, (2006), 205119

[337] Hine, N. D. M., Dziedzic, J., Haynes, P. D., and Skylaris, C.-K. *Electrostatic interactions in finite systems treated with periodic boundary conditions: Application to linear-scaling density functional theory.* J. Chem. Phys., **135**, 20, (2011), 204103

[338] Amara, M. S., Rouziere, S., Paineau, E., Bacia-Verloop, M., Thill, A., and Launois, P. *Hexagonalization of aluminogermanate imogolite nanotubes organized into closed-packed bundles.* J. Phys. Chem. C, **118**, 17, (2014), 9299

[339] Mulliken, R. S. *Electronic population analysis on LCAO–MO molecular wave functions. I.* J. Chem. Phys., **23**, 10, (1955), 1833

[340] Bell, R. A., Payne, M. C., and Mostofi, A. A. *Does water dope carbon nanotubes?* J. Chem. Phys., **141**, 16, (2014), 164703

[341] Rienstra-Kiracofe, J. C., Tschumper, G. S., Schaefer, H. F., Nandi, S., and Ellison, G. B. *Atomic and molecular electron affinities: photoelectron experiments and theoretical computations.* Chem. Rev., **102**, 1, (2002), 231

[342] Gavartin, J. L. and Shluger, A. L. *Thermal fluctuations, localization, and self-trapping in a polar crystal: Combined shell-model molecular dynamics and quantum chemical approach.* Phys. Rev. B, **64**, 24, (2001), 245111

[343] Troisi, A. and Orlandi, G. *Charge-transport regime of crystalline organic semiconductors: Diffusion limited by thermal off-diagonal electronic disorder.* Phys. Rev. Lett., **96**, 8, (2006), 086601

[344] Sleigh, J. P., McMahon, D. P., and Troisi, A. *Effect of the intermolecular thermal motions on the tail of the electronic density of states in polyacene crystals.* Appl. Phys. A, **95**, 1, (2009), 147

[345] Janak, J. *Proof that $\partial E/\partial n_i = \varepsilon$ in density-functional theory.* Phys. Rev. B, **18**, 12, (1978), 7165

[346] Perdew, J. P. and Levy, M. *Physical content of the exact Kohn-Sham orbital energies: band gaps and derivative discontinuities.* Phys. Rev. Lett., **51**, 20, (1983), 1884

[347] Sau, J. D., Neaton, J. B., Choi, H. J., Louie, S. G., and Cohen, M. L. *Electronic energy levels of weakly coupled nanostructures: C_{60}-metal interfaces.* Phys. Rev. Lett., **101**, 2, (2008), 026804

[348] Anisimov, V. I., Zaanen, J., and Andersen, O. K. *Band theory and Mott insulators: Hubbard U instead of Stoner I.* Phys. Rev. B, **44**, 3, (1991), 943

[349] Anisimov, V. I., Solovyev, I., Korotin, M., Czyżyk, M., and Sawatzky, G. *Density-functional theory and NiO photoemission spectra.* Phys. Rev. B, **48**, 23, (1993), 16929

[350] Solovyev, I., Dederichs, P., and Anisimov, V. *Corrected atomic limit in the local-density approximation and the electronic structure of d impurities in Rb.* Phys. Rev. B, **50**, 23, (1994), 16861

[351] Dudarev, S., Botton, G., Savrasov, S., Humphreys, C., and Sutton, A. *Electron-energy-loss spectra and the structural stability of nickel oxide: An LSDA+ U study.* Phys. Rev. B, **57**, 3, (1998), 1505

[352] Cococcioni, M. and De Gironcoli, S. *Linear response approach to the calculation of the effective interaction parameters in the LDA+U method.* Phys. Rev. B, **71**, 3, (2005), 035105

[353] ORegan, D. D., Hine, N. D., Payne, M. C., and Mostofi, A. A. *Projector self-consistent DFT+ U using nonorthogonal generalized Wannier functions.* Phys. Rev. B, **82**, 8, (2010), 081102

[354] Hybertsen, M. S., Schlüter, M., and Christensen, N. E. *Calculation of Coulomb-interaction parameters for La_2CuO_4 using a constrained-density-functional approach.* Phys. Rev. B, **39**, 13, (1989), 9028

[355] McMahan, A. K., Martin, R. M., and Satpathy, S. *Calculated effective Hamiltonian for La_2CuO_4 and solution in the impurity Anderson approximation.* Phys. Rev. B, **38**, 10, (1988), 6650

[356] Kulik, H. J., Cococcioni, M., Scherlis, D. A., and Marzari, N. *Density functional theory in transition-metal chemistry: A self-consistent Hubbard U approach.* Phys. Rev. Lett., **97**, 10, (2006), 103001

[357] Wu, Q. and Van Voorhis, T. *Direct optimization method to study constrained systems within density-functional theory.* Phys. Rev. A, **72**, 2, (2005), 024502

[358] Kaduk, B., Kowalczyk, T., and Van Voorhis, T. *Constrained density functional theory.* Chem. Rev., **112**, 1, (2011), 321

[359] Dederichs, P., Blügel, S., Zeller, R., and Akai, H. *Ground states of constrained systems: application to cerium impurities.* Phys. Rev. Lett., **53**, 26, (1984), 2512

[360] ORegan, D. D. and Teobaldi, G. *Optimization of Constrained Density Functional Theory* (2016). In press

[361] Moynihan, G., Teobaldi, G., and O'Regan, D. D. *Density-Fuctional Theory cannot be constrained to overcome the self-interaction error* (2016). To be submitted

[362] Kulik, H. J. and Marzari, N. *A self-consistent Hubbard U density-functional theory approach to the addition-elimination reactions of hydrocarbons on bare $FeO+$.* J Chem. Phys., **129**, 13, (2008), 134314